SCATTERED WAVE IMAGING OF THE CRUST AND UPPERMOST MANTLE ALONG STRIKE IN THE ALASKA AND CASCADIA SUBDUCTION ZONES

A Dissertation

Presented to the Faculty of the Graduate School

of Cornell University

In Partial Fulfillment of the Requirements for the Degree of

Doctor of Philosophy

by

Michael E Mann

December 2021

SCATTERED WAVE IMAGING OF THE CRUST AND UPPERMOST MANTLE ALONG STRIKE IN THE ALASKA AND CASCADIA SUBDUCTION ZONES

Michael E Mann, Ph. D.

Cornell University 2021

This dissertation details efforts to image the along-strike continuity of major seismic discontinuities in subduction zones using dense (<20 km spacing) arrays of seismometers. The seismic discontinuities were located using receiver-side *P*-to-*S* and *P*-to-*P* scattered phases from teleseismic (30°<epicentral distance<90°, M_w>~5) earthquake *P* waves. The time series of scattered phases are referred to as "receiver functions" (RFs) though they are slightly different from traditional RFs. Chapter 1 investigates the location and orientation of the subducting Juan de Fuca (JdF) Moho beneath Mount St. Helens (MSH) using RFs from a dense seismometer array that was deployed in a circular area around the volcano. Two-dimensional (2D) migration and three-dimensional (3D) common-conversion point (CCP) stacking imaging methods were used to reveal a continuous JdF slab at 68±2 km beneath MSH, which is the shallowest directly imaged subducting slab beneath an arc volcano in the world. Between 2016 and 2018, we deployed, serviced, and recovered 36 broadband seismometers in a dense array across the road system of southcentral Alaska, which provided the key data for Chapters 2 and 3. RFs from that array and two other dense seismometer deployments across southcentral Alaska were generated using an improved method that accounts for variations in surface geology. 2D migration of the RFs revealed the Yakutat terrane, an oceanic plateau, subducting down to at least 110-km depth on the eastern half of southcentral Alaska. 3D CCP stacking revealed a

continuous LVZ atop the Yakutat terrane for over 450 km along strike, at depths <35 km. Chapter 3 describes the use of RF data from Chapter 2 and data from an older dense seismometer array across central Washington, USA, in estimating the thickness and the ratio of *P* wave velocity to *S* wave velocity (*Vp*/*Vs*) of the LVZ atop the subducting Yakutat terrane in Alaska and the JdF plate in Cascadia. Results show consistent estimates of *Vp*/*Vs* that are lower than those of previous studies. In addition, synthetic seismograms were also generated and used to show that previous measurements of *Vp*/*Vs* may have been biased to higher values.

BIOGRAPHICAL SKETCH

Michael Everett Mann was born in Northern Virginia on April 11, 1993, to Thomas and Diane Mann. He began his academic career in 2011 at North Carolina State University majoring in physics. After two years as a non-scholarship midshipman in Naval Reserve Officer Training Corps at NC State, he quit to focus on academics. Shortly thereafter, he studied the spreading rate of a mixture of cheese mites (*Tyrolichus casei*) and flour with Dr. Karen Daniels as part of a granular physics experiment. After reviewing some of the literature on force chains and friction within granular materials, and visiting an earthquake-devastated Christchurch, New Zealand, he became interested in earthquakes and transitioned to studying geology and geophysics. Recognizing the need to supplement his knowledge of physics with geology, he extended his undergraduate work by a year to prepare him for research in geophysics. He earned a B.S. in physics, with a minor in geology, in 2016.

Michael began to pursue a PhD in 2016 under the guidance of Dr. Geoffrey Abers. The focus has been on seismic imaging of the crust and uppermost mantle beneath Cascadia and Alaska. This dissertation is the culmination of that seismic imaging work done over the last 5 years.

This dissertation is dedicated to all those who fight for liberty in the United States of America and elsewhere, with the sword, not the pen.

ACKNOWLEDGMENTS

I would like to specifically acknowledge and thank my advisor, Dr. Geoffrey Abers, for seeing enough potential in my application to accept me as a graduate student and helping me to reach this point. Being his student has been both challenging and rewarding, and I would not have wanted it any other way. I am indebted to the other members of my special committee: Dr. Katie Keranen, Dr. Greg McLaskey, and Dr. Esteban Gazel. A special thanks is owed to Esteban for helping this young geophysicist begin to understand geochemistry and heavily influencing both of my postdoctoral fellowship applications.

My undergraduate research advisors, Dr. Karen Daniels and Dr. Del Bohnenstiehl, deserve recognition for giving me two opportunities to prove that I could conduct careful scientific research. Karen offered me a research project to gain experience when I needed direction the most. Del has been a great guiding mentor all these years. I am indebted to him for giving me my start in seismology after bothering him for many months. (Additional thanks to Axial volcano for erupting in April 2015, which gave me the opportunity to work with Del.)

I am also grateful to Karen Fischer, Doug Christensen, Ken Creager, and Seth Moran for their encouraging and motivational interactions. I thank my friends and colleagues from Cornell University for making many aspects of graduate school fun, especially (in alphabetical order) Anant Hariharan, Aristides Alfaro, Corey Hensen, Dana Peterson, Diego Lobos, Doyeon Kim, Juan Carlos Garcia, Kayla Jade Crosbie, Kiara Daly, Lester Olivares, Nate Stevens, Paula Bürgi, Paul Morgan, Roque Soto Castañeda, and Sage Mitchell. Special thanks are owed to the Old Guard of Cornell Geological Sciences (I hope they will permit the designation): Muawia Barazangi, George Hade, Sue Kay, Bob Kay, and Larry Brown. They have been patient enough

to share their advice and stories with me. I have not forgotten.

None of this would have been possible without the love and support of Sarah Chaffee and my family. A special thanks to Elliot F. Mann for graciously editing portions of this dissertation. Finally, I must acknowledge the unrequitable investment of the Knoblauch, Mann, Nowak, Smith, and extended families. It takes generations of work to get here and for that I am eternally grateful.

TABLE OF CONTENTS

LIST OF FIGURES

CHAPTER 1

INTRODUCTION

Subduction zones have broad public and scientific importance as the sites of the greatest earthquakes and tsunami, the main regions of mixing between the surface and subsurface, and the drivers of plate tectonics (e.g., Plafker, 1965; Forsyth & Uyeda, 1975). Seismic imaging is the act of using the seismic wavefield to determine or constrain Earth properties. Seismic imaging of lithosphere-scale structures can be conducted using either body or surface waves, in active or passive techniques. Active source seismic imaging techniques use a known source, such as an explosion at the surface, and subsequent transmitted, back-scattered, or refracted arrivals from discontinuities or boundaries in the Earth and their travel times to image and constrain geologic structure. These methods are typically only applicable to the upper ~50 km of the Earth. Passive seismic techniques involve long-term recordings of the seismic wavefield and are sensitive to much greater depths (>700 km), typically waiting for earthquakes to generate sources of seismic energy. This dissertation deals primarily with passive seismic imaging techniques utilizing compressional (*P*) waves from distant earthquakes to image major discontinuity structure in subduction zones.

Passive seismic imaging methods that utilize body waves can be divided into two types: those that involve transmitted seismic waves and those that involve scattered seismic waves. The most common method of seismic imaging using transmitted seismic waves is through the generation of tomographic models of seismic velocity. Tomographic methods involve inverting the differential arrival times of passing (transmitted) seismic waves recorded at the surface for subsurface velocity structure (e.g., Roecker, 1982). In recent years, the proliferation of

seismometers worldwide has yielded large-scale seismic velocity models (e.g., French & Romanowicz, 2015). However, these imaging methods have trouble accurately determining the seismic properties of layers that are thin and/or involve sharp changes in seismic velocity, such as at the boundaries of subducting oceanic crust or lithosphere, often smearing the resulting velocity model (e.g., Jiang et al., 2018). Alternatively, scattering waves detect the sharp variations in geology or lithology themselves and can be used to image smaller scale features or sharp discontinuities.

The passage of a body wave past a seismic or geologic discontinuity produces scattered waves (e.g., Abers, 1998). The arrival times of these scattered waves at the surface are sensitive to the velocity between the scatterer and the receiver, while their amplitudes are sensitive to the velocity on both sides of the discontinuity that caused the scattering. The ability of scattered waves to image structure is dependent on their volume resolution, which is itself dependent on the wavelength of the incident wave and the physical separation of scatterers (Rondenay, 2009).

Scattering from local earthquake body waves provide very high-resolution estimates of scatterer locations but require dense arrays of numerous seismometers to determine the correct source-scatterer-receiver ray paths (e.g., Lin et al., 2020; Lin et al., 2021). Contrastingly, scattering from teleseismic (>25° epicentral distance) earthquake body waves eliminates most of these ambiguities, as the incident waves are approximately planar and their ray parameters are well known (e.g., Vinnik, 1977).

The most common method to extract scattered waves from teleseismic earthquakes is through source-normalization in receiver functions (RFs) (e.g., Langston, 1979). RFs are time series of scattered wave arrivals resulting from the passage of teleseismic body waves, generated from recordings of near-vertically arriving *P* or shear (*S*) body waves from teleseismic

earthquakes with M>~5.5. For *P* waves, the initial arrival on vertical component recordings from a teleseismic earthquake can be taken as a proxy for the incident wave source time function and any source-side scattering and reflections. During that same time period, any energy arriving on the horizontal components can be assumed to be the result of receiver-side *P*-to-*S* scattering (Bostock, 2004). This is possible because *P* waves are longitudinal (i.e., the curl of *P* waves is zero), *S* waves are latitudinal (i.e., the divergence of *S* waves is zero), and their ray paths beneath a distant receiver are mostly vertical.

RFs have been used to image discontinuity structure from the top of the lower mantle (e.g., Schmandt et al., 2014) to shallow sedimentary basins (e.g., Zheng et al., 2005). RF imaging of subduction zones originally involved a careful analysis of teleseismic *P* waves recorded on disparate seismometers (e.g., Langston, 1979). The first dense linear array at a subduction zone was deployed across central Oregon in the 1990s (Li, 1997). The use of seismic arrays such as this permits the isolation of the incident *P* wavefield, giving a better estimate of the source and source-side scattering that can be deconvolved from the three-component wavefield, leaving only the scattered wavefield (e.g., Bostock and Rondenay, 1999; Langston and Hammer, 2001). The time series that result from these array-based deconvolution methods are referred to as "receiver functions" here but there are some important differences, namely the lack of a zero-lag peak representing the incident *P* wave arrival and the isolation of both the *P* and *SV* scattered wavefields. RFs from multiple earthquakes recorded at such a linear array can be migrated in two-dimensions (2D) to generate estimates of the discontinuity structure responsible for the scattered wavefield (Bostock et al., 2001; Shragge et al., 2001; Rondenay et al., 2001). These methods correct for the effects of dipping layers and should yield accurate location and geometry estimates of discontinuities, provided they are continuous perpendicular to the array orientation.

Since the initial linear seismometer array at a subduction zone across central Oregon (e.g., Rondenay et al., 2001), the proliferation of linear arrays of seismometers has allowed high-resolution strike-perpendicular discontinuity imaging with overlapping sensitivity on subducting slab discontinuities (e.g., Rondenay et al., 2001; Ferris et al., 2003; Nicholson et al., 2005; Rondenay et al., 2008; Abers et al., 2009; Mackenzie et al., 2010; Kim et al., 2012, 2014). However, the along-strike continuity of discontinuities in subduction zones is difficult to determine without overlapping sampling at seismometers. A few previous seismometer arrays and their imaging results have aimed at determining along-strike continuity at subduction zones (e.g., Rychert et al., 2008; Pearce et al., 2012), but they simply involved multiple strike-perpendicular linear arrays.

In this dissertation, we image subduction zone discontinuity structure along-strike the Cascadia and southcentral Alaska subduction zones, where station spacing permits, using scattered wave imaging from teleseismic *P* waves. Two main aspects of subduction zones are investigated: the low-velocity zone along the plate interface (LVZ) and subducting oceanic crust orientation and metamorphism.

Water trapped in the crust and uppermost mantle lithosphere of subducting slabs is thought to control many aspects of seismicity and arc volcanism (e.g., Grove et al., 2006, 2012). Water also controls the rate at which a subducting oceanic crust eclogitizes, which involves a ~10-15% density increase (Hacker, 1996) and helps drive plate tectonics. For subduction zones with young (hot) incoming plates, the subducting crust reaches P-T conditions for eclogitization at shallower depths than at subduction zones with old (cold) incoming plates (e.g., Bostock et al., 2002; Kawakatsu et al., 2007).

Near the trench at depths <10 km along the plate interface, pore fluid pressures along the plate interface are estimated to be very high and result in aseismic slip by reducing the effective normal stress across the plate interface and concomitant shear stress require to slip (e.g., Peng & Gomberg, 2010; Saffer and Tobin, 2011). However, compaction and mineral dehydration occur at depths between 3-10 km which mostly dewater the material entrained along the plate interface leading to the seismogenic zone (e.g., Moore & Saffer, 2001; Bangs et al., 1999, 2004, 2009, 2015; Saffer & Tobin, 2011). Deeper, at depths <~30 km, the plate interface is locked and capable of hosting megathrust earthquakes (Lay et al., 2012). Down-dip of that locked zone, the plate interface exhibits a broad spectrum of seismic and aseismic activity, in some ways similar to the shallow (<5-10 km) portion (Peng & Gomberg, 2010).

Throughout this dissertation, scattered waves from teleseismic *P* waves are used to investigate various aspects of subduction zones, from the properties of the plate interface LVZ at shallow (10-35 km) depths, through to the eclogitization and concomitant dehydration of the subducting crust at deeper depths (>35 km). A focus is placed on the continuity of structure along-strike in the Cascadia and southcentral Alaska subduction zones where there have been deployments of seismometer arrays that are dense both perpendicular and parallel to subducting slab strike. In Chapter 2, we detail the results of a scattered wave imaging study around Mount St. Helens in southwestern Washington, USA. In Chapter 3, the scattered wavefield estimation is improved upon by considering variations in surface velocity that affect amplitudes. That improved scattered wavefield estimation method is applied to multiple dense seismometer arrays across the southcentral Alaska subduction zone. The scattered wavefield estimated at those arrays is used in 2D and 3D scattered wave imaging methods that look at the along-strike continuity of the LVZ, subducting crust Moho, and continental crust Moho. Chapter 4 uses the RF data and

the improved scattered wavefield estimation method from Chapter 3 to regenerate RFs from an older dense array of seismometers across central Washington, USA. These data are used to investigate the *Vp/Vs* and thickness of the LVZ imaged in Chapter 3 across southcentral Alaska, as well as the LVZ atop the subducting JdF slab beneath central Washington.

INTRODUCTION REFERENCES

Abers, G. A., MacKenzie, L. S., Rondenay, S., Zhang, Z., Wech, A. G., & Creager, K. C. (2009). Imaging the source region of Cascadia tremor and intermediate-depth earthquakes. *Geology*, *37*(12), 1119–1122. https://doi.org/10.1130/G30143A.1

Abers, Geoffrey A. (1998). Array Measurements of Phases Used in Receiver-Function Calculations: Importance of Scattering. *Bulletin of the Seismological Society of America*, *88*, 313-318.

Bangs, N. L., Shipley, T. H., Gulick, S. P. S., Moore, G. F., Kuromoto, S., & Nakamura, Y. (2004). Evolution of the Nankai Trough décollement from the trench into the seismogenic zone: Inferences from three-dimensional seismic reflection imaging. *Geology*, *32*(4), 273. https://doi.org/10.1130/G20211.2

Bangs, N. L., McIntosh, K. D., Silver, E. A., Kluesner, J. W., & Ranero, C. R. (2015). Fluid accumulation along the Costa Rica subduction thrust and development of the seismogenic zone: The Costa Rica subduction thrust. *Journal of Geophysical Research: Solid Earth*, *120*(1), 67–86. https://doi.org/10.1002/2014JB011265

Bangs, Nathan L. B., Shipley, T. H., Moore, J. C., & Moore, G. F. (1999). Fluid accumulation and channeling along the northern Barbados Ridge decollement thrust. *Journal of Geophysical Research: Solid Earth*, *104*(B9), 20399–20414. https://doi.org/10.1029/1999JB900133

Bangs, N.L.B., Moore, G. F., Gulick, S. P. S., Pangborn, E. M., Tobin, H. J., Kuramoto, S., & Taira, A. (2009). Broad, weak regions of the Nankai Megathrust and implications for shallow coseismic slip. *Earth and Planetary Science Letters*, *284*(1–2), 44–49. https://doi.org/10.1016/j.epsl.2009.04.026

Bostock, M. G. (2004). Green's functions, source signatures, and the normalization of teleseismic wave fields. *Journal of Geophysical Research*, *109*(B3), B03303. https://doi.org/10.1029/2003JB002783

Bostock, M. G., & Rondenay, S. (1999). Migration of scattered teleseismic body waves. *Geophysical Journal International*, *137*(3), 732–746. https://doi.org/10.1046/j.1365-246x.1999.00813.x

Bostock, M. G., Rondenay, S., & Shragge, J. (2001). Multiparameter two-dimensional inversion of scattered teleseismic body waves 1. Theory for oblique incidence. *Journal of Geophysical Research: Solid Earth*, *106*(B12), 30771–30782. https://doi.org/10.1029/2001JB000330

Bostock, M. G., Hyndman, R. D., Rondenay, S., & Peacock, S. M. (2002). An inverted continental Moho and serpentinization of the forearc mantle. *Nature*, *417*(6888), 536–538. https://doi.org/10.1038/417536a

Ferris, A., Abers, G. A., Christensen, D. H., & Veenstra, E. (2003). High resolution image of the subducted Pacific (?) plate beneath central Alaska, 50–150 km depth. *Earth and Planetary Science Letters*, *214*(3–4), 575–588. https://doi.org/10.1016/S0012-821X(03)00403-5

Forsyth, D., & Uyeda, S. (1975). On the Relative Importance of the Driving Forces of Plate Motion. *Geophysical Journal International*, *43*(1), 163–200. https://doi.org/10.1111/j.1365-246X.1975.tb00631.x

French, S. W., & Romanowicz, B. (2015). Broad plumes rooted at the base of the Earth's mantle beneath major hotspots. *Nature*, *525*(7567), 95–99. https://doi.org/10.1038/nature14876

Grove, T., Chatterjee, N., Parman, S., & Medard, E. (2006). The influence of H2O on mantle wedge melting. *Earth and Planetary Science Letters*, *249*(1–2), 74–89. https://doi.org/10.1016/j.epsl.2006.06.043

Grove, T. L., Till, C. B., & Krawczynski, M. J. (2012). The Role of H $_2$ O in Subduction Zone Magmatism. *Annual Review of Earth and Planetary Sciences*, *40*(1), 413–439. https://doi.org/10.1146/annurev-earth-042711-105310

Hacker, B. R. (2013). Eclogite formation and the Rheology, Buoyancy, Seismicity, and H $_2$ O Content of Oceanic Crust. In G. E. Bebout, D. W. Scholl, S. H. Kirby, & J. P. Platt (Eds.), *Geophysical Monograph Series* (pp. 337–346). Washington, D. C.: American Geophysical Union. https://doi.org/10.1029/GM096p0337

Jiang, C., Schmandt, B., Ward, K. M., Lin, F., & Worthington, L. L. (2018). Upper Mantle Seismic Structure of Alaska From Rayleigh and *S* Wave Tomography. *Geophysical Research Letters*, *45*(19). https://doi.org/10.1029/2018GL079406

Kawakatsu, H., & Watada, S. (2007). Seismic Evidence for Deep-Water Transportation in the Mantle. *Science*, *316*(5830), 1468–1471. https://doi.org/10.1126/science.1140855

Langston, C. A. (2001). The Vertical Component P-Wave Receiver Function. *Bulletin of the Seismological Society of America*, *91*(6), 1805–1819. https://doi.org/10.1785/0120000225

Langston, Charles A. (1979). Structure under Mount Rainier, Washington, inferred from teleseismic body waves. *Journal of Geophysical Research*, *84*(B9), 4749. https://doi.org/10.1029/JB084iB09p04749

Lay, T., Kanamori, H., Ammon, C. J., Koper, K. D., Hutko, A. R., Ye, L., et al. (2012). Depth-varying rupture properties of subduction zone megathrust faults. *Journal of Geophysical Research: Solid Earth*, *117*(B4). https://doi.org/10.1029/2011JB009133

Lin, C., Shih, M., & Lai, Y. (2020). A Strong Seismic Reflector within the Mantle Wedge above the Ryukyu Subduction of Northern Taiwan. *Seismological Research Letters*, *91*(1), 310–316. https://doi.org/10.1785/0220190174

Lin, C.-H. (2021). Mantle wedge diapirs detected by a dense seismic array in Northern Taiwan. *Scientific Reports*, *11*, 1-12.

Moore, J. C., & Saffer, D. (2001). Updip limit of the seismogenic zone beneath the accretionary prism of southwest Japan: An effect of diagenetic to low-grade metamorphic processes and increasing effective stress, 4.

Nicholson, T., Bostock, M., & Cassidy, J. F. (2005). New constraints on subduction zone structure in northern Cascadia. *Geophysical Journal International*, *161*(3), 849–859. https://doi.org/10.1111/j.1365-246X.2005.02605.x

Pearce, F. D., Rondenay, S., Sachpazi, M., Charalampakis, M., & Royden, L. H. (2012). Seismic investigation of the transition from continental to oceanic subduction along the western Hellenic Subduction Zone. *Journal of Geophysical Research: Solid Earth*, *117*(B7). https://doi.org/10.1029/2011JB009023

Peng, Z., & Gomberg, J. (2010). An integrated perspective of the continuum between earthquakes and slow-slip phenomena. *Nature Geoscience*, *3*(9), 599–607. https://doi.org/10.1038/ngeo940

Plafker, G. (1965). Tectonic deformation associated with the 1964 Alaska earthquake. *Science*, *148*, 1675-1687.

Roecker, S. W. (1982). Velocity structure of the Pamir-Hindu Kush Region: Possible evidence of subducted crust. *Journal of Geophysical Research: Solid Earth*, *87*(B2), 945–959. https://doi.org/10.1029/JB087iB02p00945

Rondenay, S., Bostock, M. G., & Shragge, J. (2001). Multiparameter two-dimensional inversion of scattered teleseismic body waves 3. Application to the Cascadia 1993 data set. *Journal of Geophysical Research: Solid Earth*, *106*(B12), 30795–30807. https://doi.org/10.1029/2000JB000039

Rondenay, Stéphane. (2009). Upper Mantle Imaging with Array Recordings of Converted and Scattered Teleseismic Waves. *Surveys in Geophysics*, *30*(4–5), 377–405. https://doi.org/10.1007/s10712-009-9071-5

Rondenay, Stéphane, Abers, G. A., & van Keken, P. E. (2008). Seismic imaging of subduction zone metamorphism. *Geology*, *36*(4), 275. https://doi.org/10.1130/G24112A.1

Rychert, C. A., Fischer, K. M., Abers, G. A., Plank, T., Syracuse, E., Protti, J. M., et al. (2008). Strong along-arc variations in attenuation in the mantle wedge beneath Costa Rica and Nicaragua. *Geochemistry, Geophysics, Geosystems*, *9*(10). https://doi.org/10.1029/2008GC002040

Saffer, D. M., & Tobin, H. J. (2011). Hydrogeology and Mechanics of Subduction Zone Forearcs: Fluid Flow and Pore Pressure. *Annual Review of Earth and Planetary Sciences*, *39*(1), 157–186. https://doi.org/10.1146/annurev-earth-040610-133408

Schmandt, B., Jacobsen, S. D., Becker, T. W., Liu, Z., & Dueker, K. G. (2014). Dehydration melting at the top of the lower mantle. *Science, 344,* 1265-1268.

Shragge, J., Bostock, M. G., & Rondenay, S. (2001). Multiparameter two-dimensional inversion of scattered teleseismic body waves 2. Numerical examples. *Journal of Geophysical Research: Solid Earth*, *106*(B12), 30783–30793. https://doi.org/10.1029/2001JB000326

Vinnik, L. P. (1977). Detection of waves converted from P to SV in the mantle. *Physics of the Earth and Planetary Interiors*, *15*(1), 39–45. https://doi.org/10.1016/0031-9201(77)90008-5

Zheng, T., Zhao, L., & Chen, L. (2005). A detailed receiver function image of the sedimentary structure in the Bohai Bay Basin. *Physics of the Earth and Planetary Interiors*, *152*(3), 129–143. https://doi.org/10.1016/j.pepi.2005.06.011

Note on publication status:

Chapter 2 and Appendix A have already been published in peer-reviewed journals. Chapter 3 has been returned to the authors with revisions that were due shortly after the defense of this dissertation. These portions are reproduced here without modification – Chapter 3 is reproduced after applying corrections from the first round of peer review at *Journal of Geophysical Research: Solid Earth*. Chapter 4 has not been submitted yet for publication.

Note on authorship:

Michael Everett Mann did the bulk of the work for all parts of this dissertation and the bulk of the writing for all chapters. Even though the work for **Appendix A** was conducted by Michael Everett Mann, the first draft of the text was originally written by Geoffrey A. Abers and submitted as the Final Technical Report for the USGS National Earthquake Hazard Research Program award that funded the research. As a result, we deemed it inappropriate to include that section as a chapter of this dissertation.

CHAPTER 2

IMAGING SUBDUCTION BENEATH MOUNT ST. HELENS: IMPLICATIONS FOR SLAB DEHYDRATION AND MAGMA TRANSPORT

Co-authors: G. A. Abers, K. J. Crosbie, K. Creager, C. Ulberg, S. Moran, S. Rondenay

Abstract

Mount St. Helens (MSH) is anomalously 35–50 km trenchward of the main Cascade arc. To elucidate the source of this anomalous forearc volcanism, the teleseismic-scattered wavefield is used to image beneath MSH with a dense broadband seismic array. Two-dimensional migration shows the subducting Juan de Fuca crust to at least 80-km depth, with its surface only 68 ± 2 km deep beneath MSH. Migration and three-dimensional stacking reveal a clear upper-plate Moho east of MSH that disappears west of it. This disappearance is a result of both hydration of the mantle wedge and a westward change in overlying crust. Migration images also show that the subducting plate continues without break along strike. Combined with low temperatures inferred for the mantle wedge, this geometry greatly limits possible source regions for mantle melts that contribute to MSH magmas and requires lateral migration over large distances.

2.1. Introduction

Subduction zone volcanoes form arcs parallel to slab strike where the subducting plate reaches depths of ~100 km, with this characteristic depth varying from region to region (e.g., England et al., 2004; Syracuse & Abers, 2006). At these depths, the slab has passed beneath a cold forearc and into a mantle wedge environment hot enough to produce arc basalts (e.g., Syracuse et al., 2010). Within this hot subarc region, fluids and melt ascend from the slab to arc volcanoes on paths that are often assumed to be vertical (e.g., Grove et al., 2012) but are likely

deflected downward by solid flow (Cagnioncle et al., 2007) and channeled updip in compaction-mediated permeability pathways (Wilson et al., 2014). Overall, it is often assumed that the volcanic front location reflects the trenchward extent of high temperatures in the wedge (England & Wilkins, 2004).

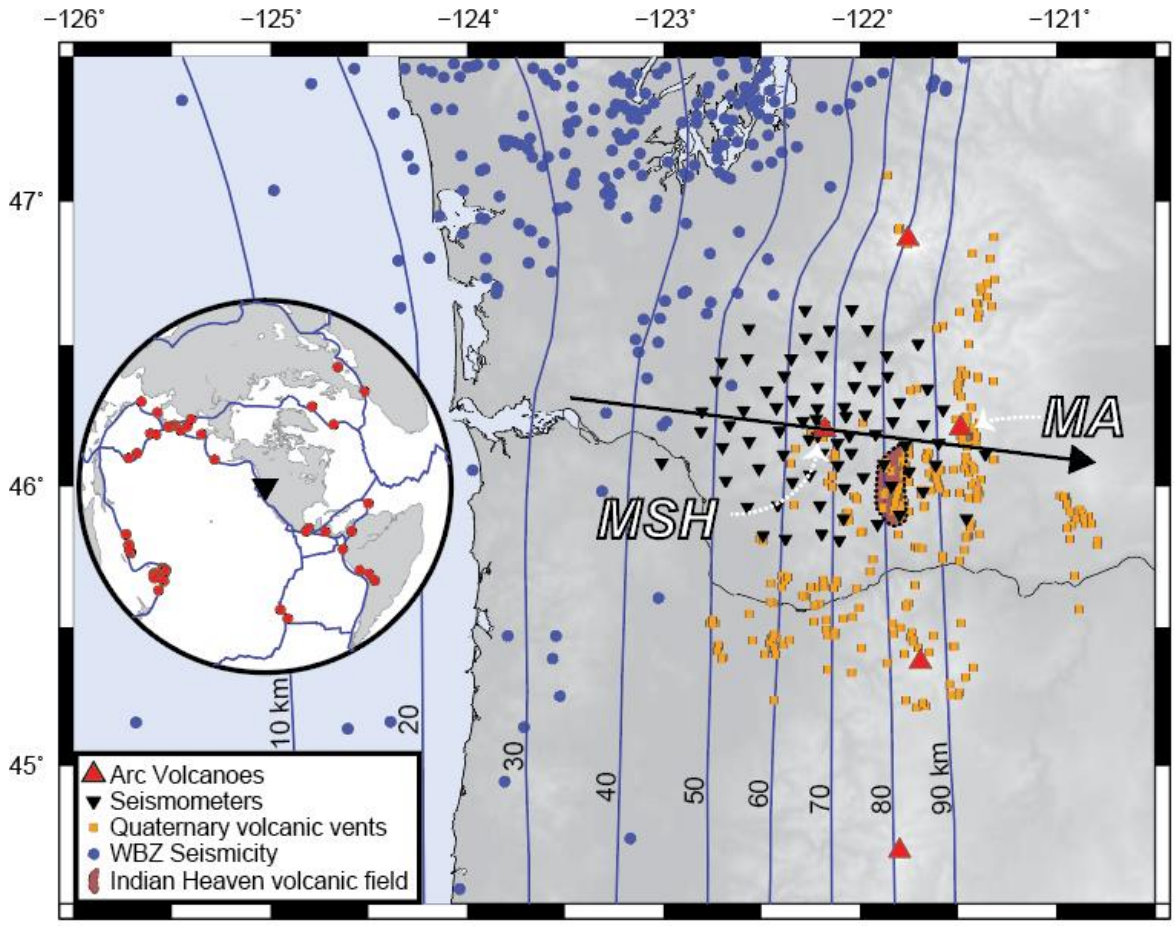

Figure 2.1. Cascadia subduction zone and seismic network. Slab contours from McCrory et al. (2012). MSH: Mount St. Helens; MA: Mount Adams; maroon: Indian Heaven volcanic field (Hildreth, 2007); black arrow: dip direction of Juan de Fuca plate. Inset: distribution of earthquakes analyzed.

The Mount St. Helens (MSH) volcano is located 35-50-km west of the main Cascade arc defined locally by Mount Adams (Figure 2.1; Hansen et al., 2016). In addition to its main edifice, nearly 150 Quaternary basaltic volcanic vents extend east and south from MSH to the Columbia

River, with a few vents lying even further west (Evarts et al., 2009; Hildreth, 2007). Regional slab models extrapolate geometry for hundreds of kilometers due to the absence of Wadati-Benioff zone (WBZ) seismicity between 41°N and 47°N and suggest slab depths of 65–70 km under MSH (McCrory et al., 2012). These depths are unusually shallow compared with other arc volcanoes globally (Syracuse & Abers, 2006) and are shallower than for all other Cascade arc volcanoes. This unusual geometry may be due to an error in the slab geometry models, or it may be a consequence of a nearby hole or tear in the subducting Juan de Fuca (JdF) slab that allows melt in the shallow mantle wedge, an idea supported by teleseismic arrival time tomography (e.g., Darold & Humphreys, 2013; Michaelson & Weaver, 1986). By contrast, the forearc Moho is absent in much of the region, leading to interpretations of widespread serpentinization of the shallow forearc that require mantle temperatures too cold to allow melting (Bostock et al., 2002; Brocher et al., 2003), extending to the edifice at MSH. To explain this contradiction, Hansen et al. (2016) proposed that melt migrates laterally from the backarc.

To distinguish between these possibilities for arc geometry, we image the subduction system beneath MSH using receiver function (RF) methods from a dense array of broadband seismometers. Strong signals show that the subducting JdF crust is continuous without holes or tears and is anomalously shallow beneath MSH. We also delineate the sharp change in the upper-plate Moho from east to west of MSH. While lateral melt transport remains the most likely explanation for the forearc volcanism, it remains unclear where these pathways are or why this phenomenon occurs in part of the Cascade arc and not elsewhere either in the Cascades or globally.

2.2. Data and Preprocessing

The imaging Magma Under MSH (iMUSH) broadband experiment deployed 70 seismometers at ~10-km spacing within 50 km of MSH (Figure 2.1), from June 2014 to August 2016. Unlike most previous linear broadband arrays in subduction zones (e.g., see review in Bostock, 2013), the iMUSH array was distributed to allow three-dimensional (3-D) imaging, with crossing rays to at least 100-km depth. We analyze the P coda for teleseismic arrivals, initially for all 269 earthquakes with visible signals between 30° and 90° distance with Mw > 5.5 recorded by the iMUSH array, supplemented with six nearby broadband stations (Figure 2.1). Each three-component seismogram is decimated to 10 samples per second and band-pass filtered between 0.03 and 1 Hz using a zero-phase second-order Butterworth filter. The first 90 s of the P wavetrain is used to estimate the teleseismic-scattered P wavefield using an array-based deconvolution procedure (Bostock & Rondenay, 1999; Pearce et al., 2012). We refer to the resulting time series as RFs despite some differences with traditional RFs, most notably the lack of a zero-lag peak due to transformation into P-SV polarization prior to deconvolution (Rondenay, 2009).

We generate array-based RFs for each of the 269 earthquakes and examine them for coherency (Figures 2.2a and 2.2b). First, data are low-pass filtered at 0.2 Hz to better isolate coherent phases such as slab conversions. These event gathers are visually inspected, retaining only signals where coherent phases could be visually identified. To better visualize the structures responsible for those phases, we plot them with depth in a reference 1-D velocity model (e.g., Figures 2.2a and 2.2b), assuming that dominant conversions are the Ppxs phase (free-surface-reflected P converting to S at the scatterer; Figure 2.2b) due to its high-depth resolution (Rondenay, 2009) and low noise (Pearce et al., 2012). The back-projections use a reference 1-D

S velocity model derived from an inversion of surface waves from ambient noise and earthquakes (supporting information Figure B1; Crosbie, 2018), estimating crustal Vp/Vs and density in the upper 40 km from Brocher (2005) and mantle Vp/Vs of 1.75. These analyses result in 61 earthquakes after eliminating earthquakes producing ringy or inconsistent RFs. Of the 71 stations with usable data, we retain an average of 43 RFs per event and 2,652 RFs in total after removing individual RFs that show anomalous amplitudes, long-period drift, or near-monochromatic ringing.

Five stations had measured orientation problems; four stations were misoriented by 15–17° and one by 180°. Inspection of transverse-component RFs confirmed these corrections; however, these stations did not produce usable RFs.

2.3. Methods

2.3.1 Back-Projection

The 61 RF sets are analyzed by means of two back-projection analyses. First, we select peaks in the RFs we believe are associated with the subducting JdF plate and back-project them to depth while explicitly accounting for 3-D ray bending from a planar dipping interface (Supporting Information S1; Richards et al., 1991). Rays are traced through a uniform-velocity mantle wedge with an identical average slowness as in the 1-D velocity model used in the migration (Figure 2.2b), while an underlying dipping interface generates conversion-point locations (Figure 2.2b). This analysis allows for areal mapping of the slab interface, correcting for the dip artifacts that are present in simpler back-projections (e.g., Figure 2.2a). In the second analysis, the RF signals form the basis of 3-D Common-Conversion-Point (CCP) stacking (e.g., Dueker & Sheehan, 1997) to image the upper-plate Moho, discussed below.

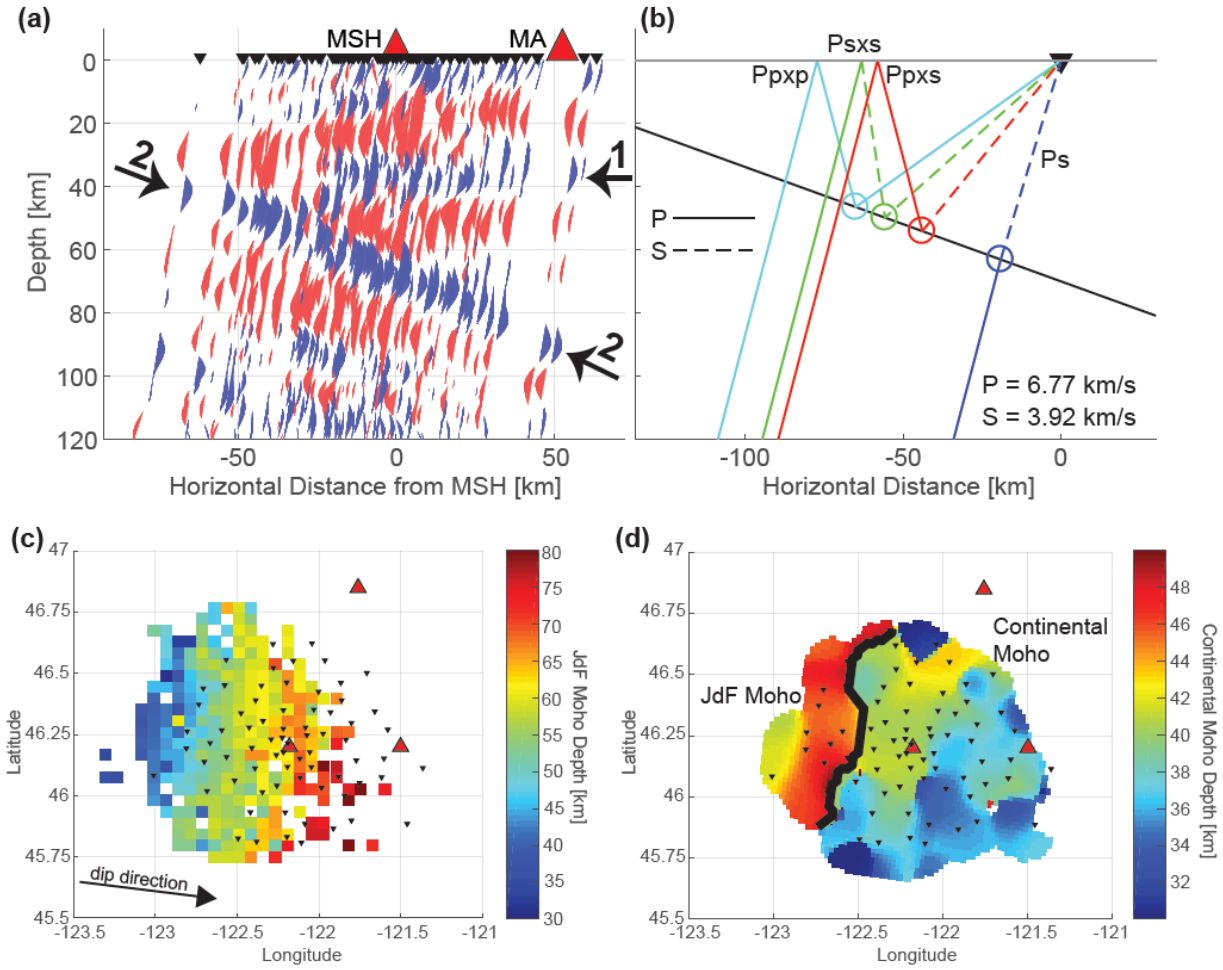

Figure 2.2. (a) RF back-projection from one earthquake at 244° back azimuth. Blue peaks are positive, red are negative. Each trace is normalized to peak amplitude. 1: subhorizontal continental Moho signals. 2: dipping JdF Moho signals. (b) Ray nomenclature and paths calculated for different phases. Circles along dipping interface represent conversion/reflection points. (c) Averaged conversion points from picked Ppxs peaks after back projection; see text. (d) Depth of continental Moho from CCP stack of both the Ppxs and Psxs phases. Red triangles: arc volcanoes; inverted black triangles: seismometers.

2.3.2 Migration

The scattered wavefield is migrated with a 2-D generalized Radon transform method that utilizes ray theory and assumes single scattering (Figure 2.3), using a process fully described elsewhere (Bostock et al., 2001; Rondenay, 2009). We invert the scattered wavefield for 2-D P

and S wave velocity perturbations necessary to produce the scattering in the plane normal to slab strike. The migration method is best at constraining gradients in these velocity perturbations. The same 61 earthquakes used in our back-projection analyses are used in the migration, after band-pass filtering 0.03 to 0.6 Hz. The P wave velocity perturbations are generated from the surface-reflected P scattered wavefield (Ppxp; Figure 2.3c), and the S wave velocity perturbations are generated from several forward-scattered and primary surface-reflected conversions (Figures 2.2b and 2.3a–2.3f). Because the surface-reflected conversions have superior depth resolution relative to the forward-scattered conversions, they are weighted higher than Ps (Pearce et al., 2012), with weights of 0.1 for Ps, 1 for Ppxs, 0.5 for Psxs-SH, and 0.25 for Psxs-SV.

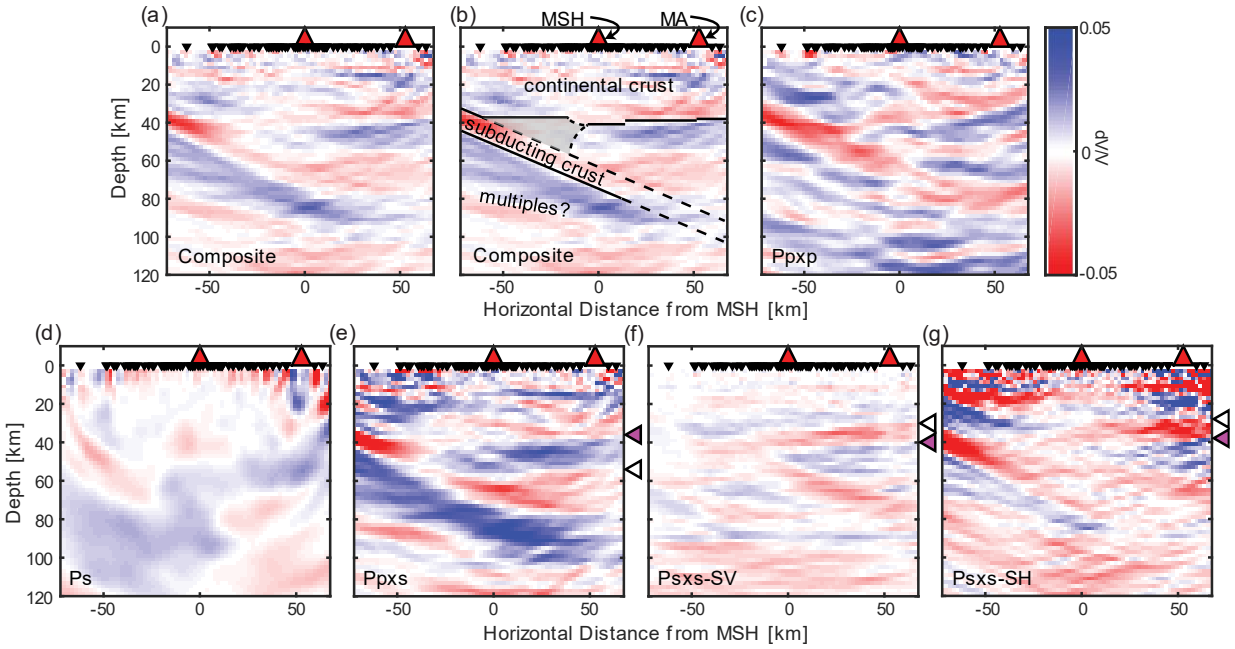

Figure 2.3. (a) Composite S migration image. (b) Interpreted S migration image, boundaries dashed where inferred. Grey polygon: potentially hydrated mantle wedge. (c)-(g) Individual-phase S migration images, as labeled. Black inverted triangle: seismometers; red triangle: Cascade Arc volcanoes; MA: Mount Adams; MSH: Mount St. Helens; purple triangles: interpreted continental Moho; white triangles: ghost Mohos.

2.4. Results

2.4.1 Slab Discontinuity Geometry

The RFs show a strong converter dipping eastward, related to the subducting JdF plate (Figure B3a). It resembles features seen in similar data sets (Abers et al., 2009; Nicholson et al., 2005; Rondenay et al., 2001), and its polarity indicates increasing velocity with depth. We infer that this is the Moho in the JdF plate. The RFs also reveal a subhorizontal interface near 35–40-km depth in several phases, which appears to be the upper-plate Moho. Because of the consistency and resolution of the JdF Ppxs phase, we use it to map the subducting plate throughout the area. Specifically, we pick lag times from 1,514 positive-polarity peaks identified by hand on back-projections of individual earthquakes. Peaks are picked as the highest positive amplitude within a 20-km vertically thick window manually defined around these projected peaks (e.g., Figure 2.2a). This method generates some artifacts, particularly in the western region where it is difficult to separate the subducting JdF Moho from the upper-plate Moho or from complexities sometimes seen in the nose of the mantle wedge. However, this procedure captures the slab interface sufficiently to determine its geometry.

The conversion points inferred from the individual RF peaks are then fit to a 2-D polynomial describing the converter depth, after the dip-corrected back-projection described above, iteratively adjusting the strike and dip used in the back-projection to fit observed lag times. We iterate the fitting process until strike and dip converge at <0.01° change. An F test shows that a plane fits the data as well as any higher-order surface. The resulting strike, dip, and depth of the JdF Moho are 7.0 ± 2.6° clockwise from North, 19.8 ± 0.6°, and 70.0 ± 0.6 km directly beneath MSH, respectively (uncertainties represent 95% confidence interval).

Once the strike and dip are established, all rays are retraced to the converter. The converting interface is then mapped by averaging the back-projected conversion points in horizontal 5 km × 5 km bins (Figure 2.2c). This 3-D imaging procedure yields two important results. First, it shows that the mapped interface is continuous along-strike beneath this array. Second, this map illustrates that the coverage of the subducting slab is complete in the along-strike span of the array but displaced updip from the stations.

2.4.2 CCP Stacking for Upper Plate Moho

To better image the upper-plate Moho in 3-D, we use a CCP stacking method that back-projects RFs to depth in three dimensions in the 1-D reference velocity model. CCP volumes are stacked separately for Ps, Ppxs, and Psxs phases (Figure B4), and the reverberated phases are stacked together (Figure B5). Details regarding the CCP stacking method are described in Supporting Information S1. Because CCP stacking assumes flat-lying layers, conversions from the dipping JdF Moho decorrelate and are not interpreted here.

The continental Moho is mapped as the maximum amplitude between 30- and 50-km depth within nodes that include more than six measurements. These amplitudes are identified and mapped in each individual-phase CCP stack (Figure B7), as well as in the reverberated-phase CCP stack. Peak amplitudes and depths of the continental Moho are determined by fitting a Gaussian function to each vertical column of the stacked CCP volume in this depth range. The peaks appear more consistent in the reverberated phases than in the direct Ps phase (Figure B7), as with 2-D migration (Figure 2.3d). Consequently, we interpret the continental Moho in the Ppxs phase.

The continental Moho signal disappears 15-km west of MSH in our CCP stacking image, and farther west, this procedure picks up the JdF Moho (Figure 2.2d). We define the westward extent

of the continental Moho as the point at which our procedure begins to pick the JdF Moho and has reduced amplitude (Figure 2.2d). The continental crust is thicker to the north of MSH (40–44 km) than to the south, with the thinnest crust (34 km) found 15-km south-southeast of MSH beneath the Indian Heaven volcanic field.

2.4.3 Two-Dimensional Migration Images

Unlike the back-projection method, the migration method makes no assumptions concerning conversion geometry other than two-dimensionality of structure, a simple 1-D background velocity model, and single scattering (Rondenay, 2009). We migrate the RF waveforms as described above, assuming the strike of 2-D structure determined from back-projection (7.0°). The P migration image (Figure 2.3c) has lower resolution than the composite S migration image (Figures 2.3a and 2.3b) but shows a similar overall structure.

Robust features in the composite S image ideally appear in each individual phase, but some potential artifacts appear. A subhorizontal velocity inversion (i.e., a fast layer over a slow layer) at 55-km depth appears in the mantle wedge of the Ppxs image (Figure 2.3e), which is the only individual-phase image in which this boundary occurs. This velocity inversion exhibits the exact timing as the upper-plate Moho in Psxs, which for flat interfaces can appear in the Ppxs image due to similarity of moveout and small ray parameter range. It is likely a ghost image of that Psxs Moho, with reversed polarity due to the differing behavior of these two signals. This likely ghost signal persists as a subhorizontal velocity inversion in the composite S image. It could be incorrectly interpreted as, for example, the base of the lithosphere. Similarly, the velocity inversion seen at 30-km depth in the Psxs images is most likely a ghost generated by the Moho in Ppxs (Figures 2.3f and 2.3g). For these reasons, interpretation focuses on features that appear consistently in multiple phases.

The composite S image (Figures 2.3a and 2.3b) shows a low-velocity layer between 32- and 43-km depth at the west edge of the image dipping eastward; we interpret this as the subducting JdF crust. It resembles that seen elsewhere along strike (e.g., Abers et al., 2009; Audet et al., 2010; Bostock et al., 2002). It is difficult to determine if the top of the JdF crust disappears below 40-km depth or simply decreases in S velocity contrast with the overlying mantle to noise levels. A dipping positive discontinuity (slow over fast), interpreted as the JdF Moho, persists to at least 80-km depth, beyond which resolution degrades (Figure 2.2c). The resulting depth of the JdF Moho beneath MSH is 74 km, placing the slab surface at 68 km beneath MSH assuming a JdF crustal thickness of 6 kmas seen offshore (Han et al., 2016). The 4-km-depth discrepancy between the migration and the 70-km Moho depth determined from back-projection (Figure 2.2c) is due to several factors, primarily the use of a constant velocity model in the back-projection. The depth of 74 km from the migration is preferred for these reasons. The continental Moho is well defined as a positive interface near MSH at 40 ± 1-km depth and near Mount Adams at 37 ± 1-km depth.

The main feature of the P wave migration image is the eastward-dipping low-velocity JdF crust (Figure 2.3c) that continues to at least 60-km depth. It provides independent confirmation of the JdF Moho mapped from S wave conversions. Other features of the P migration image are not interpreted here because it has a lower resolution than the S migration images.

Although a full 3-D migration of this data set is beyond the scope of this study, the data are divided into three independent station groups at different across-strike corridors and migrated separately within each group (Figures 2.4a–c). Each migration shows a dipping JdF Moho at approximately the same location and a well-defined continental Moho east of MSH, with slightly shallower continental Moho depths to the south (Figure 2.4e) consistent with our CCP stacking

(Figure 2.2d). These results indicate a planar slab surface with no obvious variation along-strike, whereas there is an 8–10-km variation in topography of the upperplate Moho.

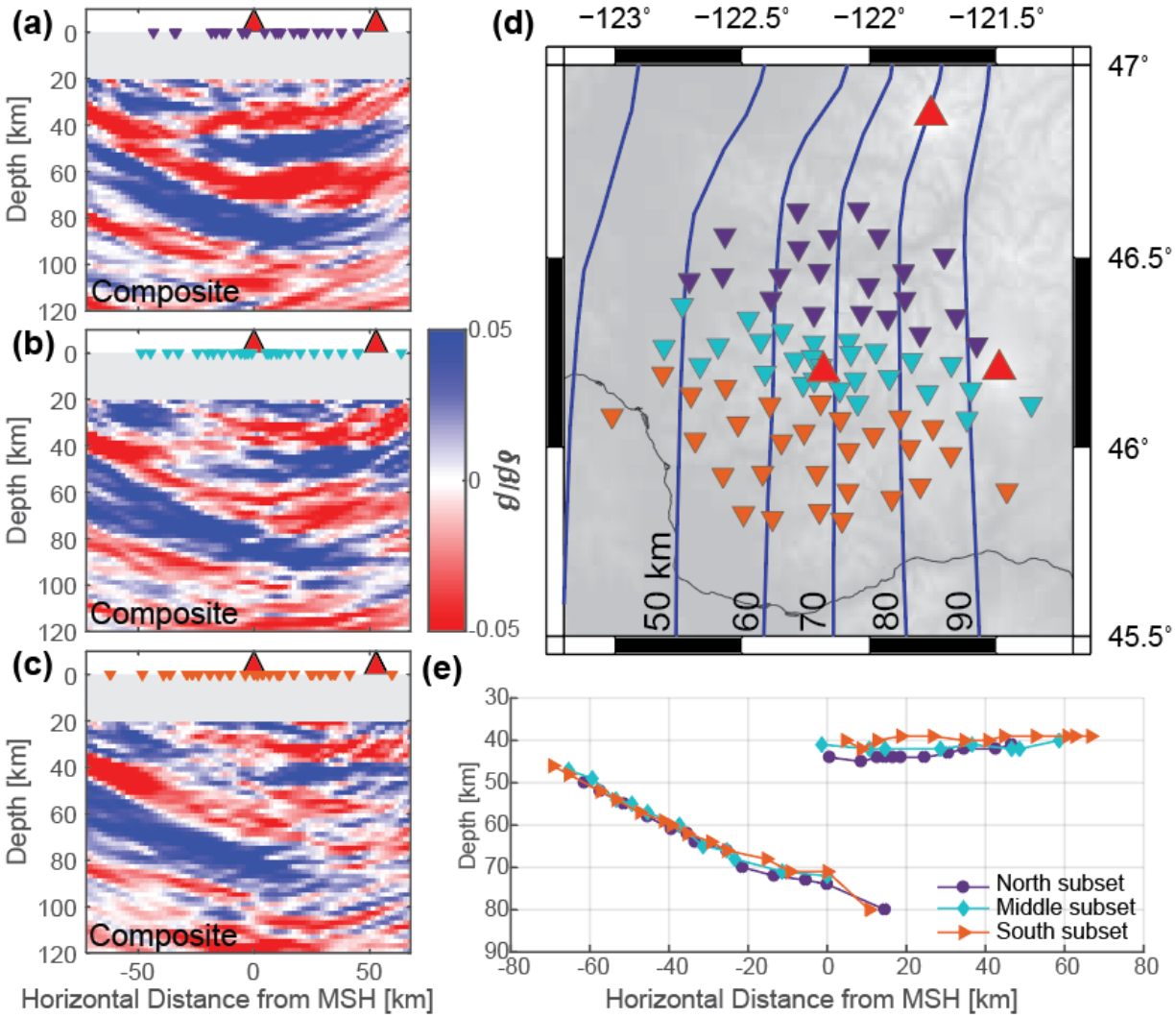

Figure 2.4. (a) Migration for northern subset of the array, (b) middle subset, and (c) southern subset. All migration images are composite S images as Figure 2.3a. (d) Subset station locations, denoted by color. Blue lines: slab contours (McCrory et al., 2012). (e) Continental and JdF Moho locations for the three migration subsets, picked where Vs perturbations cross from negative above to positive below.

The small variability in JdF Moho location between the three independent migrations (Figure 2.4) provides an indication of uncertainty in slab depth due to noise in the migration

procedure and to the assumption of twodimensionality. The root-mean-square (RMS) variation in depth between the three sections is ≤1 km (Figure 2.4e) between 49- and 72-km depth. We estimate an additional 2-km uncertainty due to the assumed velocity model, taken here as the RMS variation in travel time through the 3-D model of Crosbie (2018). This gives an aggregate uncertainty in slab depth of 2 km.

2.5. Discussion and Conclusions

2.5.1 Slab Geometry and JdF Moho

The top of the subducting JdF crust is inferred to be 68 ± 2 km beneath MSH (Figure 2.3a), making this the shallowest directly imaged subducting crust beneath an arc volcano to date; arc volcanoes with shallower subducting slabs either lie at the edges of slabs where geometry is poorly resolved or in regions without imaging that have poor slab depth constraints (Syracuse & Abers, 2006). The depth determined from our migration results is within 2–3 km of the hand-contoured subduction model of McCrory et al. (2012; Figure 2.1). Although our ray coverage is weak directly beneath Mount Adams due to ray bending, the JdF Moho extrapolates to a depth of 100 km beneath it, consistent with 94-km depth for the top of the JdF crust, which is slightly deeper than beneath other Cascade arc volcanoes (McCrory et al., 2012) but consistent with global averages (England et al., 2004; Syracuse & Abers, 2006).

The persistence of the JdF Moho to depths greater than 60 km is difficult to reconcile with petrologic models that predict the velocity contrast at the JdF Moho should disappear once the subducting crust eclogitizes by 60-km depth (Rondenay et al., 2008; van Keken et al., 2011, 2018). Similar seismic analyses in Cascadia show a noticeably weaker putative JdF Moho than what we find beneath MSH (Abers et al., 2009; Bostock et al., 2002; Nicholson et al., 2005). Potential explanations for the persistence of the boundary to greater depths include the JdF crust

persisting metastably as gabbro or the boundary being produced by the base of a hydrated peridotite layer below the Moho rather than the Moho (Rondenay et al., 2008). The latter interpretation implies that a significant amount ofH2O is being subducted to subarc depths, consistent with evidence for elevated H2O in Cascade arc magmas (Ruscitto et al., 2010). It is not clear if the stronger Moho here is due to a large iMUSH data set or a peculiarity of the MSH region.

2.5.2 The North American Plate

Absence of the continental Moho in the forearc has been seen in other migration images in Cascadia and is typically attributed to serpentinization of the cold mantle forearc wedge (e.g., Bostock et al., 2002). A sharp decrease in Moho P wave reflectivity immediately to the west of MSH has also been attributed to hydration of the mantle wedge (Brocher et al., 2003; Hansen et al., 2016). However, it is difficult to reconcile the abrupt disappearance of the continental Moho within 10–20 km of MSH with the notion that it is entirely controlled by mantle hydration. Antigorite, the likely serpentine species, lowers the velocity of peridotite much less than older lizardite-based calculations so cannot account for the Moho's complete disappearance (Reynard, 2013). Hydrous phases such as serpentine and chlorite should be stable in the mantle wedge only at <800 °C (reviewed in Abers et al., 2017), whereas MSH dacites equilibrated at 925–940 °C in the lower crust (Blatter et al., 2017). In addition, the presence of Quaternary mantle-sourced basalts at MSH and proximal vents (Hildreth, 2007) indicates temperatures potentially approaching 1,460 °C (Leeman et al., 2005), although H2O may reduce this estimate by 100–200 °C (Lee et al., 2009).

Observations from ambient-noise tomography (Crosbie, 2018) and regional P wave tomography (Parsons et al., 1999) suggest an alternative effect—lower-crustal velocities are 10–

15% higher west of MSH than east of it, reducing the Moho velocity contrast. Anomalously high velocities likely result from the gabbroic Siletz terrane forming the basement west of MSH (Wells et al., 2014). Hence, in contrast to previous interpretations, we infer that lower crustal composition contributes to the change in Moho character in the Cascadia forearc, perhaps equally to mantle hydration.

2.5.3 Slab Continuity and the Search for Magma Origins

These observations further complicate the search for the origin of MSH and nearby magmas. One possibility is that high-temperature basalts originate from below the young JdF plate through a hole or tear in the slab (Leeman et al., 2005; Weaver & Michaelson, 1985). The continuous signals from the JdF Moho preclude any such hole or tear in the area of the array, and similar observations immediately north (Abers et al., 2009; McGary et al., 2014) indicate this continuity extends northward along-strike. Back-projection supports this assertion (Figure 2.2c), as do the three migrations using independent data sets (Figures 2.4a–c), all of which show a coherent JdF slab along-strike. It is possible that a hole exists south of the array, for example, beneath the Boring volcanics 50 km to the south (Hildreth, 2007), in which case magmas would be required to migrate northward more than 50 km.

Features smaller than the Fresnel-zone diameter cannot be imaged using our techniques, but that diameter is small. For reflected phases like Psxs, the Fresnel-zone diameter is approximately $\sqrt{(2z\beta T + T^2\beta^2/4}$, where z is the depth to the interface, β is the S wave velocity, and T is the shortest period (Ryberg & Weber, 2000). For β = 4.0 km/s and T = 1 s, this diameter is 25 km at 75-km depth, limiting possible holes to smaller than 25 km. Although we have not modeled processes creating slab holes, it seems reasonable that holes smaller in diameter than

~40 km (the thermal boundary layer thickness for a 10-Ma plate) are geodynamically implausible.

Alternatively, the forearc magma may originate farther into the backarc (Bedrosian et al., 2018). The Quaternary basaltic vents occur at the latitude of the ~17-Ma Columbia River flood basalts (Camp & Ross, 2004), which, although originating much farther east, represent a significant thermal perturbation to the subduction system that could still be disrupting the slab at greater depth (Obrebski et al., 2010). Numerous Quaternary vents form a 150-km-long cross-arc trend at this latitude (Leeman et al., 2005), indicating unusual magma generation and transport. A substantial and unusual amount of lateral magmatic transport must occur to explain the location of MSH; it is difficult to identify another major volcanic center worldwide that is displaced this far from the arc.

REFERENCES

Abers, G. A., Keken, P. E. van, and Hacker, B. R. (2017). The cold and relatively dry nature of mantle forearcs in subduction zones. *Nature Geoscience*, 10(5), 333–337. https://doi.org/10.1038/ngeo2922

Abers, G.A., MacKenzie, L. S., Rondenay, S., Zhang, Z., Wech, A. G., and Creager, K. C. (2009). Imaging the source region of Cascadia tremor and intermediate-depth earthquakes. *Geology*, 37(12), 1119–1122. https://doi.org/10.1130/G30143A.1

Audet, P., Bostock, M. G., Boyarko, D. C., Brudzinski, M. R., and Allen, R. M. (2010). Slab morphology in the Cascadia fore arc and its relation to episodic tremor and slip. Journal of *Geophysical Research: Solid Earth*, 115(B4).

Bedrosian, P. A., Peacock, J. R., Bowles-Martinez, E., Schultz, A., & Hill, G. J. (2018). Crustal inheritance and a top-down control on arc magmatism at Mount St Helens. Nature Geoscience, 11(11), 865. https://doi.org/10.1038/s41561-018-0217-2

Blatter, D. L., Sisson, T. W., and Hankins, W. B. (2017). Voluminous arc dacites as amphibole reaction-boundary liquids. *Contributions to Mineralogy and Petrology*, 172(5), 27. https://doi.org/10.1007/s00410-017-1340-6

Bostock, M. G., and Rondenay, S. (1999). Migration of scattered teleseismic body waves. *Geophysical Journal International*, 137(3), 732–746. https://doi.org/10.1046/j.1365-246x.1999.00813.x

Bostock, M. G., Rondenay, S., and Shragge, J. (2001). Multiparameter two-dimensional inversion of scattered teleseismic body waves 1. Theory for oblique incidence. *Journal of Geophysical Research: Solid Earth*, 106(B12), 30771–30782.

Bostock, M. G., Hyndman, R. D., Rondenay, S., and Peacock, S. M. (2002). An inverted continental Moho and serpentinization of the forearc mantle. *Nature*, 417(6888), 536–538. https://doi.org/10.1038/417536a

Brocher, T. M., Parsons, T., Tréhu, A. M., Snelson, C. M., and Fisher, M. A. (2003). Seismic evidence for widespread serpentinized forearc upper mantle along the Cascadia margin. *Geology*, 31(3), 267–270. https://doi.org/10.1130/0091-7613(2003)031<0267:SEFWSF>2.0.CO;2

Brocher, T. M. (2005). Empirical relations between elastic wavespeeds and density in the Earth's crust. *Bulletin of the Seismological Society of America*, 95(6), 2081–2092.

Cagnioncle, A.-M., Parmentier, E. M., and Elkins-Tanton, L. T. (2007). Effect of solid flow above a subducting slab on water distribution and melting at convergent plate boundaries. *Journal of Geophysical Research: Solid Earth*, 112(B9).

Camp, V. E., and Ross, M. E. (2004). Mantle dynamics and genesis of mafic magmatism in the intermontane Pacific Northwest. *Journal of Geophysical Research: Solid Earth*, 109(B8), art. no. B08204.

Crosbie, K.J. (2018), Shear velocity structure from ambient noise and teleseismic surface wave tomography in the Cascades around Mount St. Helens, MS Thesis, Cornell Univ.

Darold, A., and Humphreys, E. (2013). Upper mantle seismic structure beneath the Pacific Northwest: A plume-triggered delamination origin for the Columbia River flood basalt eruptions. *Earth and Planetary Science Letters*, 365, 232–242. https://doi.org/10.1016/j.epsl.2013.01.024

Dueker, K. G., and Sheehan, A. F. (1997). Mantle discontinuity structure from midpoint stacks of converted P to S waves across the Yellowstone hotspot track. *Journal of Geophysical Research: Solid Earth*, 102(B4), 8313–8327.

England, P., Engdahl, R., and Thatcher, W. (2004). Systematic variation in the depths of slabs beneath arc volcanoes. *Geophysical Journal International*, 156(2), 377–408. https://doi.org/10.1111/j.1365-246X.2003.02132.x

Evarts, R. C., Conrey, R. M., Fleck, R. J., Hagstrum, J. T. (2009). The Boring Volcanic Field of the Portland-Vancouver area, Oregon and Washington: Tectonically anomalous forearc volcanism in an urban setting. *The Geological Society of America Field Guide #15*, 253-270. https://doi.org/10.1130/2009.fld015(13).

Grove, T. L., Till, C. B., and Krawczynski, M. J. (2012). The Role of H2O in Subduction Zone Magmatism. *Annual Review of Earth and Planetary Sciences*, 40(1), 413–439. https://doi.org/10.1146/annurev-earth-042711-105310

Han, S., Carbotte, S. M., Canales, J. P., Nedimović, M. R., Carton, H., Gibson, J. C., and Horning, G. W. (2016). Seismic reflection imaging of the Juan de Fuca plate from ridge to trench: New constraints on the distribution of faulting and evolution of the crust prior to subduction. *Journal of Geophysical Research: Solid Earth*, 121(3), 1849–1872. https://doi.org/10.1002/2015JB012416

Hansen, S. M., Schmandt, B., Levander, A., Kiser, E., Vidale, J. E., Abers, G. A., and Creager, K. C. (2016). Seismic evidence for a cold serpentinized mantle wedge beneath Mount St Helens. *Nature Communications*, 7, 13242. https://doi.org/10.1038/ncomms13242

Hildreth, W. (2007). *Quaternary Magmatism in the Cascades: Geologic Perspectives*. U.S. Geological Survey.

Kiser, E., Palomeras, I., Levander, A., Zelt, C., Harder, S., Schmandt, B., et al. (2016). Magma reservoirs from the upper crust to the Moho inferred from high-resolution Vp and Vs models beneath Mount St. Helens, Washington State, USA. *Geology*, 44(6), 411–414. https://doi.org/10.1130/G37591.1

Lee, C.-T. A., Luffi, P., Plank, T., Dalton, H., and Leeman, W. P. (2009). Constraints on the depths and temperatures of basaltic magma generation on Earth and other terrestrial planets using new thermobarometers for mafic magmas. *Earth and Planetary Science Letters*, 279, 20–33.

Leeman, W. P., Lewis, J. F., Evarts, R. C., Conrey, R. M., and Streck, M. J. (2005). Petrologic constraints on the thermal structure of the Cascades arc. *Journal of Volcanology and Geothermal Research*, 140(1), 67–105. https://doi.org/10.1016/j.jvolgeores.2004.07.016

McCrory, P. A., Blair, J. L., Waldhauser, F., and Oppenheimer, D. H. (2012). Juan de Fuca slab geometry and its relation to Wadati-Benioff zone seismicity. *Journal of Geophysical Research: Solid Earth*, 117(B9).

McGary, R. S., Evans, R. L., Wannamaker, P. E., Elsenbeck, J., and Rondenay, S. (2014). Pathway from subducting slab to surface for melt and fluids beneath Mount Rainier. *Nature*, 511(7509), 338–340. https://doi.org/10.1038/nature13493

Michaelson, C. A., and Weaver, C. S. (1986). Upper mantle structure from teleseismic P wave arrivals in Washington and northern Oregon. *Journal of Geophysical Research: Solid Earth*, 91(B2), 2077–2094.

Nicholson, T., Bostock, M., and Cassidy, J. F. (2005). New constraints on subduction zone structure in northern Cascadia. *Geophysical Journal International*, 161(3), 849–859. https://doi.org/10.1111/j.1365-246X.2005.02605.x

Obrebski, M., Allen, R. M., Xue, M., and Hung, S.-H. (2010). Slab-plume interaction beneath the Pacific Northwest. *Geophysical Research Letters*, 37, art. no. L14305.

Parsons, T., Wells, R. E., Fisher, M. A., Flueh, E., and Ten Brink, U. S. (1999). Three-dimensional velocity structure of Siletzia and other accreted terranes in the Cascadia forearc of Washington. *Journal of Geophysical Research: Solid Earth*, 104(B8), 18015–18039.

Pearce, F. D., Rondenay, S., Sachpazi, M., Charalampakis, M., and Royden, L. H. (2012). Seismic investigation of the transition from continental to oceanic subduction along the western Hellenic Subduction Zone. *Journal of Geophysical Research: Solid Earth*, 117(B7).

Reynard, B. (2013). Serpentine in active subduction zones. Lithos, 178, 171–185. https://doi.org/10.1016/j.lithos.2012.10.01

Richards, P. G., Witte, D. C., and Ekström, G. (1991). Generalized ray theory for seismic waves in structures with planar nonparallel interfaces. *Bulletin of the Seismological Society of America*, 81(4), 1309–1331.

Rondenay, S. (2009). Upper Mantle Imaging with Array Recordings of Converted and Scattered Teleseismic Waves. *Surveys in Geophysics*, 30(4–5), 377–405. https://doi.org/10.1007/s10712-009-9071-5

Rondenay, S., Abers, G. A., and Keken, P. E. van. (2008). Seismic imaging of subduction zone metamorphism. *Geology*, 36(4), 275–278. https://doi.org/10.1130/G24112A.1

Ruscitto, D. M., Wallace, P. J., Johnson, E. R., Kent, A. J. R., and Bindeman, I. N. (2010). Volatile contents of mafic magmas from cinder cones in the Central Oregon High Cascades: Implications for magma formation and mantle conditions in a hot arc. *Earth*

and Planetary Science Letters, 298(1), 153–161. https://doi.org/10.1016/j.epsl.2010.07.037

T. Ryberg, M. Weber; Receiver function arrays: a reflection seismic approach, *Geophysical Journal International*, Volume 141, Issue 1, 1 April 2000, Pages 1–11, https://doi.org/10.1046/j.1365-246X.2000.00077.x

Shen, W., and Ritzwoller, M. H. (2016). Crustal and uppermost mantle structure beneath the United States. *Journal of Geophysical Research: Solid Earth*, 121(6), 4306–4342. https://doi.org/10.1002/2016JB012887

Syracuse, E. M., and Abers, G. A. (2006). Global compilation of variations in slab depth beneath arc volcanoes and implications. *Geochemistry, Geophysics, Geosystems*, 7(5). https://doi.org/10.1029/2005GC001045

Syracuse, E. M., van Keken, P. E., and Abers, G. A. (2010). The global range of subduction zone thermal models. *Physics of the Earth and Planetary Interiors*, 183(1), 73–90. https://doi.org/10.1016/j.pepi.2010.02.004

van Keken, P. E., Hacker, B. R., Syracuse, E. M., and Abers, G. A. (2011). Subduction factory: 4. Depth-dependent flux of H2O from subducting slabs worldwide. *Journal of Geophysical Research: Solid Earth*, 116(B1).

Weaver, C. S., and Michaelson, C. A. (1985). Seismicity and volcanism in the Pacific Northwest: Evidence for the segmentation of the Juan De Fuca Plate. *Geophysical Research Letters*, 12(4), 215–218. https://doi.org/10.1029/GL012i004p00215

Wells, R., Bukry, D., Friedman, R., Pyle, D., Duncan, R., Haeussler, P., and Wooden, J. (2014). Geologic history of Siletzia, a large igneous province in the Oregon and Washington Coast Range: Correlation to the geomagnetic polarity time scale and implications for a

long-lived Yellowstone hotspot. *Geosphere*, 10(4), 692–719. https://doi.org/10.1130/GES01018.1

Wilson, C. R., Spiegelman, M., van Keken, P. E., and Hacker, B. R. (2014). Fluid flow in subduction zones: The role of solid rheology and compaction pressure. *Earth and Planetary Science Letters*, 401, 261–274. https://doi.org/10.1016/j.epsl.2014.05.052

CHAPTER 3

SUBDUCTION OF AN OCEANIC PLATEAU ACROSS SOUTHCENTRAL ALASKA: SCATTERED-WAVE IMAGING

Co-authors: G. A. Abers, K. Daly, D. H. Christensen

Abstract

An oceanic plateau, the Yakutat terrane, has entered the subduction system across southcentral Alaska. Its down-dip fate and relationship to overlying volcanism is still debated. Broadband seismometers from the Wrangell Volcanism and Lithospheric Fate (WVLF) temporary experiment were deployed with <20 km spacing across southcentral Alaska to study this region. An array-based deconvolution procedure is used to isolate the scattered *P* and *S* coda of teleseismic *P* waves for imaging discontinuity structure. This procedure is applied to WVLF and other dense seismic arrays across southcentral Alaska in a manner that accounts for near-surface wavespeed variations. Two imaging techniques are employed: two-dimensional migration and three-dimensional common-conversion-point (CCP) stacking. Migrating the scattered phases along WVLF stations shows the ~18±4 km thick Yakutat crust subducting beneath the Wrangell Volcanic field to the NNE. It is offset from the Alaska seismic zone laterally by 250 km to the southeast at 100 km depth, and dips more steeply (45°). At depths <45 km, CCP stacking reveals that the Yakutat crust is continuous for over 450 km along strike. This shallow continuity and deeper offset suggest a tear in the subducting Yakutat slab at depths >45 km, around 146°W. CCP stacking also reveals a continuous thin low-velocity layer atop the underthrust Yakutat crust for >450 km along strike, at all depths <35 km. The uniform low-velocity thrust zone indicates consistent megathrust properties through multiple rupture-zone segments.

3.1 Introduction

Subduction is driven by the negative buoyancy of down-going lithosphere (Forsyth and Uyeda, 1975). The primary factors governing that buoyancy are the thickness of subducting crust and age of the mantle lithosphere (Molnar and Grey, 1979; Cloos, 1993; Mason et al., 2010). The negative buoyancy of the subducting crust is thought to influence the geometry of subducting slabs, until eclogitization of its crust drastically increases its density (e.g., van Hunen et al., 2002; Abers, 2008; Arrial and Billen, 2013). The basaltic crust atop typical subducting oceanic lithosphere is typically 6-7 km thick and usually subducts completely. However, when a thick oceanic plateau enters a subduction zone the dynamics change (e.g., McGeary et al., 1985; Mason et al., 2010). Subduction of buoyant oceanic plateaus is associated with collision (e.g., Elliott et al., 2013), tearing and window formation in the subducting slab (e.g., Mason et al., 2010), and drives for upper-plate processes (e.g., Tetreault and Buiter, 2012, 2014; Tao et al., 2020).

The subduction and collision of the Yakutat terrane across southcentral Alaska provides a clear example of a buoyant oceanic plateau entering a subduction zone. Offshore, the Yakutat terrane crust exhibits an eastward thickening wedge shape, with crustal thicknesses ranging from <15 km to >30 km (Worthington et al., 2012). Between about 150°W and 146°W, the Yakutat plateau crust is 11-22 km thick and is underthrust beneath Alaska, before subducting to 130 km depth (Rondenay et al., 2008; Kim et al., 2014). At its eastern end ~141°W the Yakutat plateau crust is ≥30 km thick and is apparently colliding with Alaska (Elliott et al., 2013; Marechal et al., 2014). The fate of the Yakutat plateau in the intervening region is unknown.

This study generates images of the seismic discontinuity structure beneath southcentral Alaska to elucidate the subducting Yakutat oceanic plateau across the entire region, from the plate interface to the mantle. Subduction of the 18-km thick Yakutat crust is confirmed to 110-km depth

between about 145.5°W and 143.5°W beneath the Wrangell Volcanic Field (WVF) and is accompanied by nearby intermediate-depth seismicity. Three-dimensional (3D) imaging reveals a thin low-velocity layer (LVL) that is ubiquitous along the plate interface for at least 450 km along strike atop the subducting Yakutat terrane. This shows that the underthrust Yakutat crust, as well as the megathrust interface, is continuous across southcentral Alaska, at depths of about 35 km. Deeper, clear RF phases from the subducting Yakutat Moho provide evidence for a N-S tear in the subducting lithosphere ~100-200 km west of the WVF. The 3D imaging also reveals an eastward-thickening Yakutat terrane crust, with crustal thicknesses ranging from 12 km at the western end where it meets the Pacific plate and 32 km at the eastern end.

3.2 Regional Tectonic Setting

The eastern end of the Alaska subduction zone is characterized by an eastward transition from Pacific slab subduction to Yakutat terrane collision (Figure 3.1). We focus on two segments: the Denali segment in the west and the Wrangell segment in the east (Figure 3.1). The Denali segment includes most of the Denali volcanic gap between about 152°W and 147°W, where there is clear ongoing subduction and its associated Wadati-Benioff Zone (WBZ) seismicity without any arc volcanism (e.g., Eberhart-Phillips et al., 2006; Rondenay et al., 2010; Chuang et al., 2017). The Wrangell segment is the portion of southcentral Alaska east of 147°W that has very little WBZ seismicity and contains the WVF.

The WVF is one of the most voluminous calc-alkaline volcanic fields in the world, with individual edifices reaching 900 km^3 and eruption rates that may be higher than any other convergent margin (Nye, 1983). The WVF has eleven major volcanic centers in Alaska that show a northwesterly age progression, most of which has occurred in the Quaternary (Richter et al., 1990). Mount Drum, at the western end of the WVF, and Mount Churchill, the southeasternmost

Alaskan WVF volcano (Figure 3.1), have both erupted in the last 0.2 Ma. Both show an adakitic signature that has been used as evidence for edge-melting of the subducting crust (Preece and Hart, 2004; Brueseke et al., 2018).

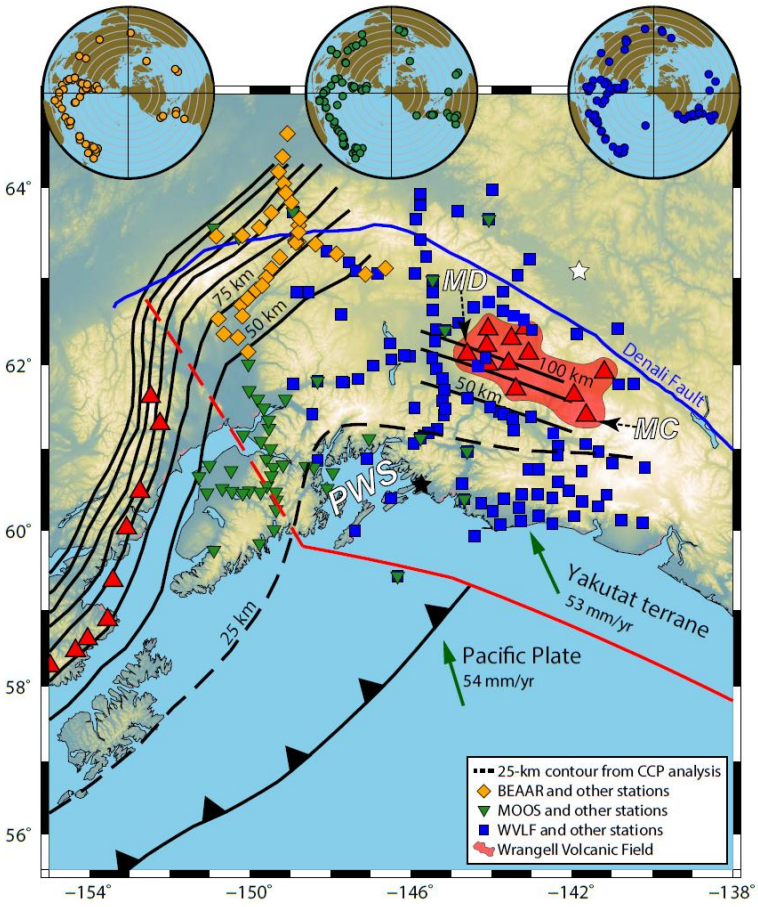

Figure 3.1: Map of the study region. Inset maps show location of teleseismic earthquakes during each temporary array deployment: left inset map – BEAAR array 6/2000-7/2001 (Ferris et al., 2003), middle inset map – MOOS array 6/2007-10/2008 (Li et al., 2013), right inset map – WVLF array 6/2016-5/2018 (Soto Castañeda et al., 2021). Color of earthquakes in inset maps match corresponding station arrays: orange – BEAAR, green – MOOS, blue – WVLF. PWS – Prince William Sound, MD – Mount Drum, MC – Mount Churchill, solid red line – slope magnetic anomaly (Naugler and Wageman, 1973) and Transition fault (e.g., Christeson et al., 2010), dashed red line – inferred southwestern boundary of subducted Yakutat terrane. Slab-depth contours beneath Denali segment (Section 2) at 25-km intervals (thin black lines) after Ratchkovski and Hansen (2002). Slab-depth contours beneath Wrangell segment at 25-km intervals from this RF migration analysis and Daly et al. (*subm.*). Black and white stars are the forearc and backarc stations, respectively, used for Figure 3.3. Green arrows show Pacific plate and Yakutat motion relative to North America. Dashed black line is 25-km contour of the plate interface from CCP analysis (see Appendix C).

The Yakutat terrane is a 50-55 Ma oceanic plateau that has been colliding with and subducting beneath southcentral Alaska for the last 10-30 Ma, with approximately the same direction and velocity as the Pacific plate (Bruns et al., 1983; Rondenay et al., 2008; Rondenay et al., 2010; Elliott et al., 2010; Brueseke et al., 2018; Elliott et al., 2020). Beneath the Denali segment, the 11-22 km thick Yakutat crust subducts beneath southcentral Alaska, extending down-dip in the thrust zone for over 200 km at dips <5° before steepening and subducting to a depth of 130 km or more beneath the Denali segment (Ferris et al., 2003; Rossi et al., 2006; Rondenay et al., 2008; Rondenay et al., 2010; Kim et al., 2014). At the eastern end, the Yakutat crust is thicker, perhaps >30 km, and collides with North America near Mount St. Elias (Koons et al., 2010; Marechal et al., 2014; Chapman et al., 2012), potentially generating deformation up to 800 km inland (e.g., Mazzotti et al., 2008).

The eastern extent of subduction across southcentral Alaska is unclear. Offshore, the Yakutat terrane extends from (e.g., Christeson et al., 2010; Worthington et al., 2012; Figure 3.1). Low-frequency earthquakes and tremor suggest that the plate interface extends east to ~146°W (Wech, 2016). Dense Wadati-Benioff zone (WBZ) seismicity ends abruptly around 146°W, although a distinct sparse WBZ has been observed beneath the Wrangell segment (Stephens et al., 1984; Page et al., 1989; Daly et al., *subm*.). Some tomographic studies of the region show a faint high-velocity anomaly at mantle depths in the Wrangell segment that has been interpreted as subducting material as far east as 140°W (e.g., Jiang et al., 2018; Gou et al., 2019; Feng and Ritzwoller., 2019), but other studies see no such anomaly (e.g., Eberhart-Phillips et al., 2006; Martin-Short et al., 2016, 2018; Nayak et al., 2020). Teleseismic attenuation indicates an attenuating arc/backarc and low-attenuation forearc, consistent with subduction (Soto Castañeda et al., 2021). Overall, the accommodation of convergence east of 146°W is poorly defined and the

nature of subduction of the Yakutat terrane across southcentral Alaska is poorly documented (Eberhart-Phillips et al., 2006; Elliott et al., 2013, 2020).

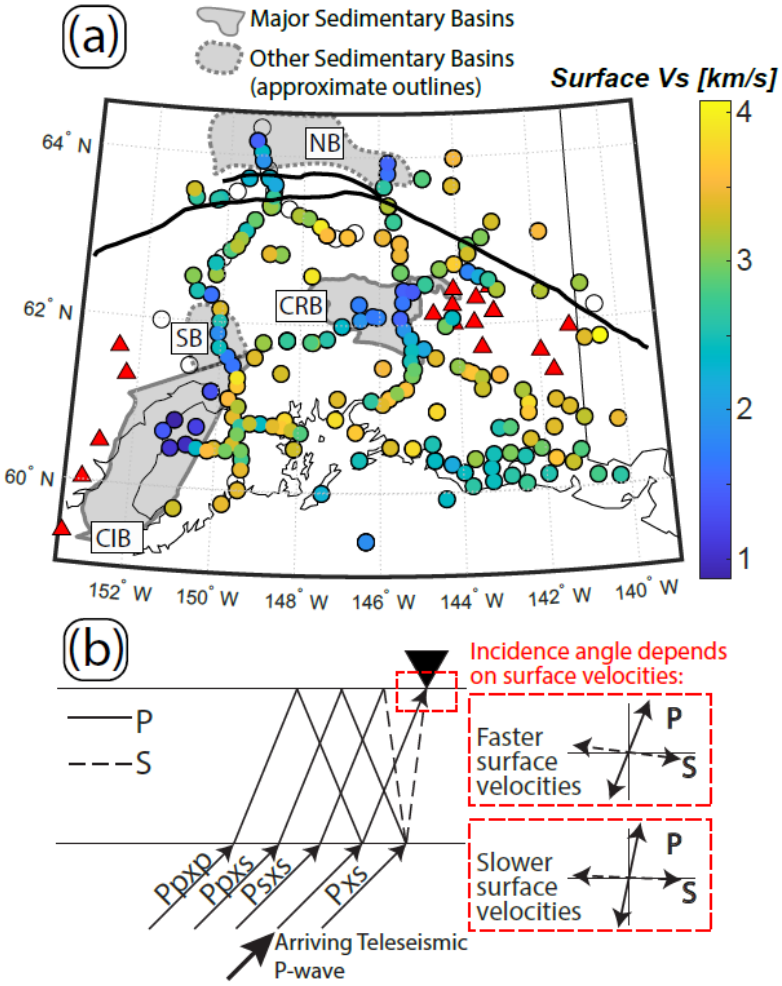

Figure 3.2: (a) Surface *Vs* estimates from free-surface transform analysis. Circles: stations, colored by surface Vs. CRB – Copper River Basin, CIB – Cook Inlet Basin, SB – Susitna Basin, NB – Nenana Basin. Stations without usable measurements shown as open circles. (b) Schematic receiver function mode ray paths showing nomenclature used, with cartoon showing incidence angle difference for P- and converted S-wave motions from increasing/decreasing surface *Vs*. Red triangles – arc volcanoes

3.3 Data and Preprocessing

This study uses data from the Wrangell Volcanism and Lithospheric Fate (WVLF) experiment (https://doi.org/10.7914/SN/YG_2016; Soto Castañeda et al., 2021), which deployed

36 broadband seismometers across the eastern half of southcentral Alaska from June 2016 to July 2018 (Figure 3.1). In addition, this study uses data from previous temporary deployments, namely the Broadband Experiment Across the Alaska Range (BEAAR; Ferris et al., 2003) and Multidisciplinary Observations of Onshore Subduction (MOOS; Li et al., 2013), along with Transportable Array (TA; Ruppert & West, 2020), the Alaska Earthquake Center Network, and other local network stations. Collectively, these experiments yield an array of 218 broadband seismometers at stations spaced 10-20 km along the road system and at greater distances between roads, across most of southcentral Alaska (Figure 3.1).

P waves from teleseismic earthquakes (M_w > 5.5, 30° > distance > 95° from the center of the array) were used to generate Receiver Functions (RFs) using an array-based deconvolution procedure (Bostock and Rondenay, 1999). We use the term "receiver function" to refer to the output of the array-based deconvolution but recognize that it differs from traditional RFs (e.g., Langston et al., 1977), most notably by the lack of a peak at zero lag time associated with the direct *P* arrival, and by the generation of the backscattered *P* wavefield (i.e., Ppxp in Figure 3.2b). For the WVLF array, we analyzed the *P* coda from 571 teleseismic earthquakes, selecting 92 events that generated visibly coherent RFs across the array that were not dominated by monochromatic ringing or anomalously high amplitudes (right inset map in Figure 3.1). For the BEAAR array, we reanalyzed the *P* coda from 513 teleseismic earthquakes, selecting 78 events that generated RFs that follow the same criteria as above (left inset map in Figure 3.1). For the MOOS array, we reanalyzed the 78 events used by Kim et al. (2014) and retained 77 of them for further analysis (center inset map in Figure 3.1).

The methodology for generating RFs is described in detail by Rondenay (2009) and summarized here. The incident *P* wavefield is extracted from the principal component of the

isolated *P* wavefields at all the recording seismometers, after free-surface corrections to isolate *P* from *S*, discussed in detail below. This requires several seismographs with equalized instrument responses, so we deconvolve responses from the various instrument types from all stations in the WVLF array. This incident *P* wavefield is then deconvolved from the *S* and residual *P* wavefield to generate array-based RFs. After generating RFs for all of the selected earthquakes, we applied a Gaussian low-pass filter with a characteristic frequency of 0.5 Hz that is represented by the equation:

$$G(f) = \exp\left(-\frac{1}{2}f^2/f_c^2\right) \qquad (1)$$

where f represents the frequency, and f_c is the characteristic frequency. We then examine the suite of RFs at each station and remove individual waveforms that are incoherent with the suite, show monochromatic ringing or exhibit anomalous amplitudes. This process results in a total of 11066 usable RFs, with an average of 65 at each of the 218 stations.

3.4 Methods and Results

The subsurface discontinuity structure is analyzed using the RFs in two ways. First, we migrate the RFs to generate a two-dimensional (2D) image of the scattered wavefield assuming Born scattering (Bostock et al., 2001). Provided that structure can be treated as 2D, this approach should properly image dipping structure. Second, under the assumption that discontinuities are essentially horizontal, we back-project the RFs through a three-dimensional (3D) velocity model to their common-conversion-point (CCP) locations. This procedure provides a 3D image of the subhorizontal discontinuity structure across the study area. Together, these methods allow for regional mapping of major seismic discontinuities such as the top of the down-going plate and the Moho of both the subducting crust and the upper plate crust.

3.4.1 Surface Vs Measurements and the Deconvolution Procedure

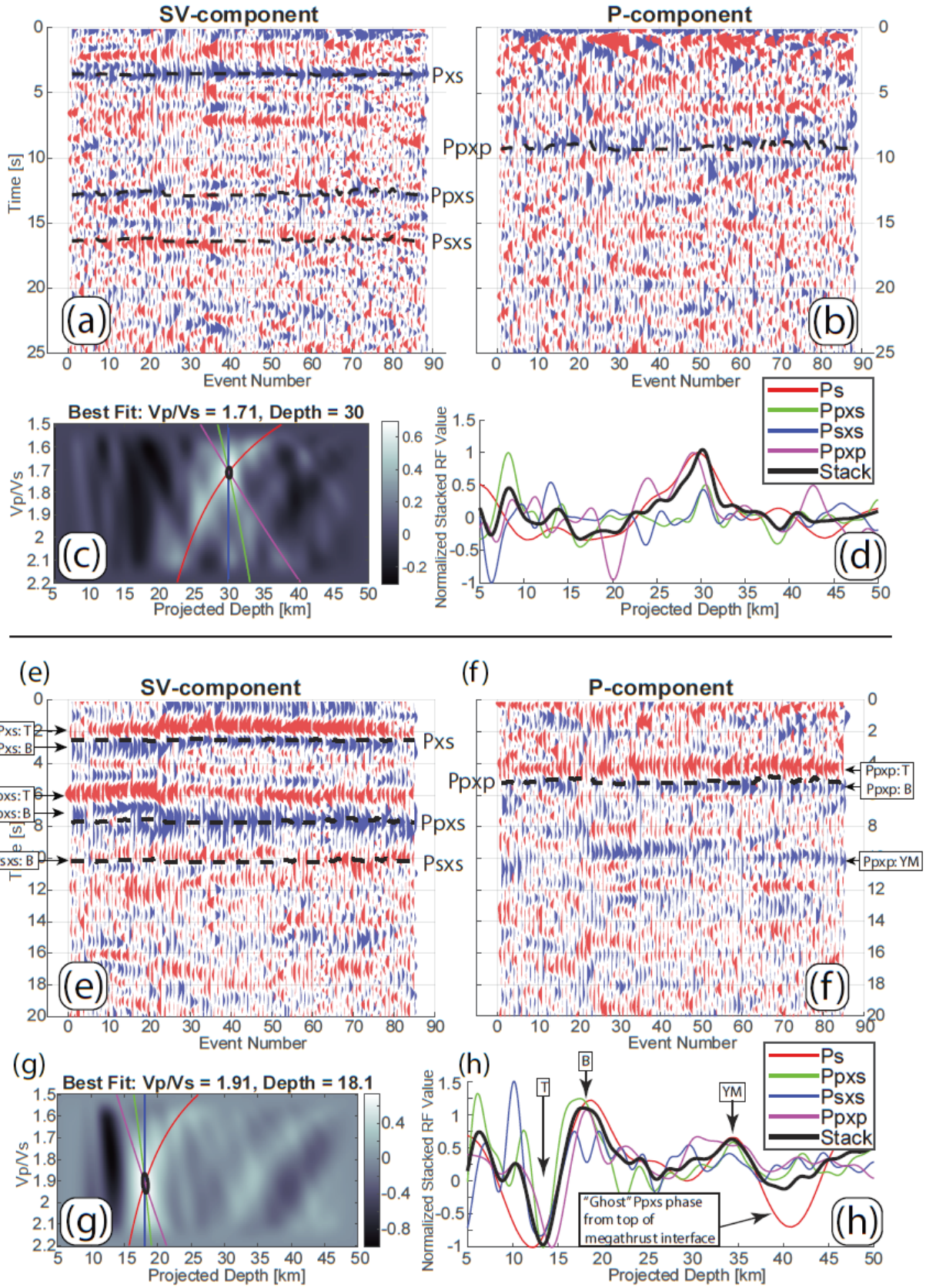
SV-component
P-component
Pxs
Ppxp
Ppxs
Psxs
Time [s]
Event Number
(a)
(b)
Best Fit: Vp/Vs = 1.71, Depth = 30
Vp/Vs
Projected Depth [km]
(c)
Normalized Stacked RF Value
Ps
Ppxs
Psxs
Ppxp
Stack
(d)
(e)
SV-component
Pxs: T
Pxs: B
Ppxs: T
Ppxs: B
Psxs: B
(e)
(f)
P-component
Ppxp: T
Ppxp: B
Ppxp: YM
(f)
(g)
Best Fit: Vp/Vs = 1.91, Depth = 18.1
(g)
(h)
T
B
YM
"Ghost" Ppxs phase from top of megathrust interface
(h)

Figure 3.3 Example RFs from stations depicted with the stars in Figure 1. (a) SV-component RFs from station L27K in backarc. Note that Psxs has reversed polarity. (b) P-component RF after source removal (Ppxp), with flipped polarity so that it matches that of Pxs and Ppxs. Dashed lines are estimated arrival times for each RF mode as indicated, after accounting for the ray parameter for each event. Events arranged by order of increasing back-azimuth. (c) Phase stacking analysis grid search surface; gray shade shows stacked amplitude. Lines correspond to each RF mode's moveout, colored as indicated in legend in (d). (d) Stack of all four RF modes for best-fit Vp/Vs = 1.71, showing agreement among all four RF modes at depth = 30 km. (e) – (h) same analysis for station EYAK near coast. Format same as panels (a)-(d). (e) SV-component RFs. Note that Psxs has reversed polarity. (f) P-component RF (Ppxp), with flipped polarity so that it matches that of Pxs and Ppxs. (g) Phase stacking result. (h) Stack of all four RF modes for Vp/Vs = 1.91. T – top of plate interface LVL, B – bottom of plate interface LVL, YM – Yakutat Moho.

The array-based deconvolution procedure requires an estimate of near-surface velocities to isolate the *P* and *SV* components of the incident wavefield from the measured ground motion (Kennett, 1991). Typically, one *S*- and *P*-wave velocity value (*Vs* and *Vp*) is used as the surface velocity estimates for an entire array of seismometers (e.g., Rondenay et al., 2001). This approach is not valid when arrays span varying surficial geology, such as low-velocity basins, which can deleteriously affect RF imaging (e.g., Sheehan et al., 1995; Cunningham and Lekic, 2019). One way that RFs are affected is that conservation of energy increases the amplitude at stations on low-velocity sediments compared to those on basement. Additionally, strong reverberated energy within the basin can cause monochromatic ringing. The Copper River and Cook Inlet basins in southcentral Alaska are at least 1 km and 7 km thick, respectively, with various other smaller sedimentary basins throughout our study region (Shellenbaum et al., 2010; USGS Sedimentary Basin Map of Alaska, 1994).

Measurements of surface *Vs* are made at each station from the initial incidence angle of teleseismic *P* waves, filtered between 0.03 Hz and 1 Hz, using the polarization method of Abt et al. (2010). This method searches for the surface *Vs* value used in a free-surface transform (Kennett,

1991) that minimizes the correlation between the *P* and *SV* components derived from measured vertical and radial ground motion, within a time window from 1 s before to 2 s after the arrival of the *P* wave. The grid search is conducted over surface *Vs* values between 0.3 km/s and 5 km/s in increments of 0.1 km/s and *Vp/Vs* between 1.55 and 2.15. At each station, a weighted sum of the accepted surface *Vs* measurements from various earthquakes determines the final surface *Vs* value for that station. The free surface transform for P waves is relatively insensitive to *Vp*, so we fix *Vp* from the surface *Vs* assuming *Vp/Vs* = 1.75. After estimating the scattered wavefield from the array, we apply an inverse free-surface transform assuming a uniform surface *Vs* and *Vp* for all stations and use that modified scattered wavefield as the basis for further analysis. This process minimizes amplification due to low surface *Vs*.

The mean and median surface *Vs* from our analysis are 2.83 km/s and 3.0 km/s, respectively, varying between 0.8 km/s and 4.1 km/s (Figure 3.2). Comparison of *P* wave polarity with synthetic local earthquake waveforms has revealed that they are sensitive to depths equal to about 20% of the relevant shear wavelength (Park and Ishii, 2018; Park et al., 2019). Given the average dominant frequency is ~0.6 Hz, that scaling indicates that these signals are sampling depths ranging from 0.3 km to 1.4 km depth. Notable surface *Vs* features include the reduced surface *Vs* values at stations within the Cook Inlet and Copper River basins (Figure 3.2a), with lesser reductions within the Nenana and Susitna Basins, and the region of thick accreting Yakutat Terrane sediments.

3.4.2 RF Characteristics

We use the first 90 seconds of the *P* wavetrain from teleseismic *P* waves to estimate the scattered wavefield after correcting for interstation variations in near-surface velocities as describe above. Prominent positive (velocity increase with depth) *P*-to-*S* mode conversions exist across the

array between 2 and 7 s lag. In the northern half of the region, typified by Figure 3.3a-d, a clear positive RF phase is seen at almost all stations, probably the Pxs conversion from the upper plate

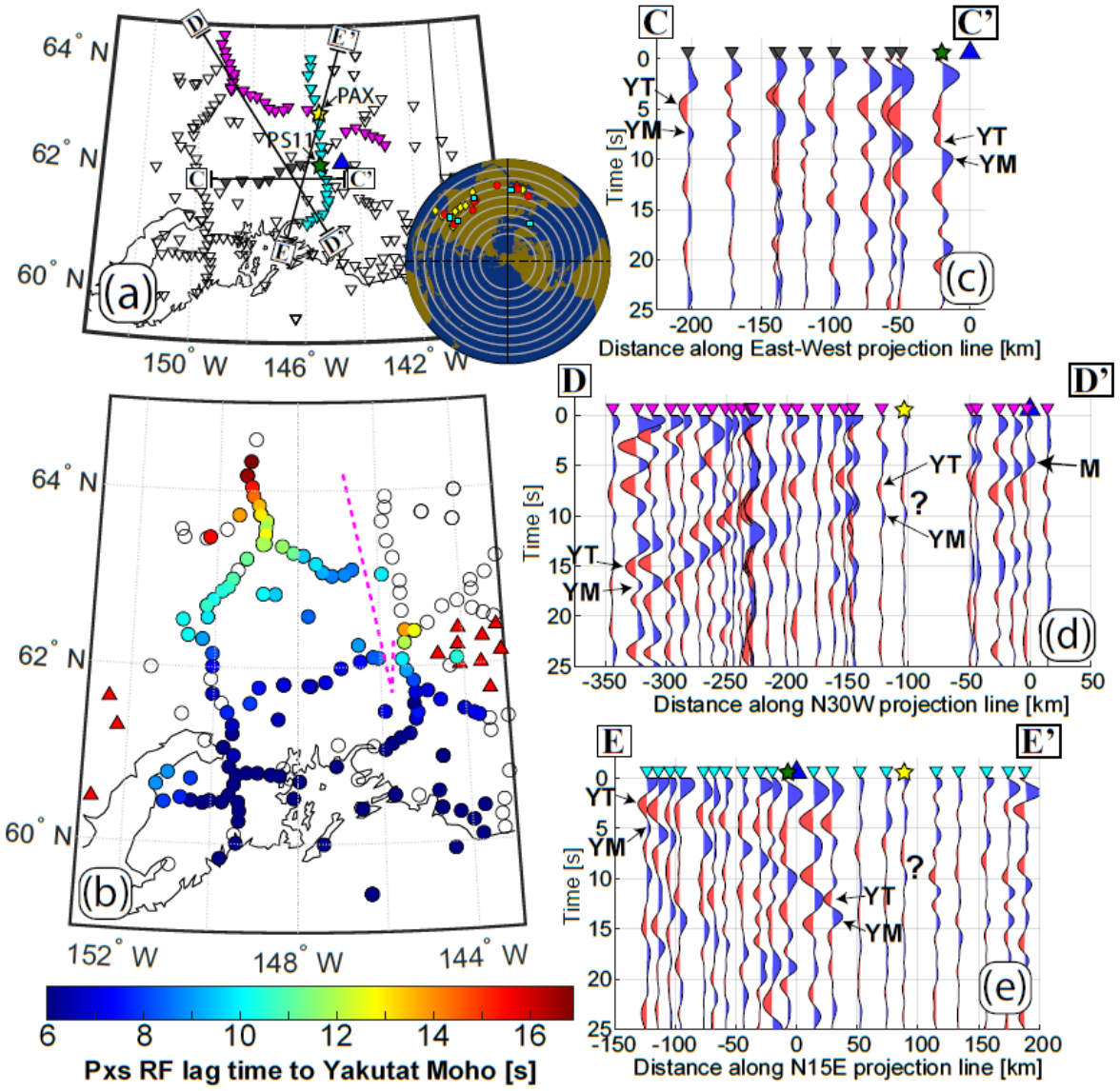

Figure 3.4: Stacked time-domain RFs for events from northern back-azimuths, along three transects. (a) Map showing selected lines of stations used, along with orientation of each projection line shown as boxed letters. Inset map – earthquakes used, colored by array (Figure 1): red circles – BEAAR, yellow diamonds – MOOS, cyan squares – WVLF. (b) RF lag time for Pxs to Yakutat Moho in individual-station RF stacks, plotted at the station. Red triangles – arc volcanoes. Open circles: subducting crust not seen. Dashed lines indicate inferred edges of the slab tear region. Note actual conversion points at slab surface are offset. (c) Individual-station RF stacks along E-W line C-C' in forearc. (d) Individual-station RF stacks along oblique NW-SE line D-D' in backarc. (e) Individual-station RF stacks along N-S line E-E' near WVF. YT – top of Yakutat crust, YM – Yakutat Moho, M – upper plate Moho. Blue triangle – Mount Drum. Positive RF phases are shaded blue, negative RF phases shaded red. Question mark in (d) highlights low-amplitude apparent doublet phases that are continuous with the Yakutat crust on D-D' but are not associated with any other doublet phases along E-E', possibly a diffraction tail.

Moho. In the southern half of the region, typified by Figure 3.3e-h, the subducting slab produces two positive RF phases. The shallower positive phase has a consistent negative phase directly preceding, indicating a low-velocity layer; these phases correspond with the plate interface (Kim et al., 2014). The deeper positive phase is consistent with the subducting Yakutat terrane Moho (Figure 3.3e-h).

The RFs are first examined in the time domain, Gaussian low-pass filtered at a characteristic frequency of 0.2 Hz (Equation 1) to ensure coherent stacking between events. We select RFs from events with back-azimuths clockwise from North from -80° to +30° to highlight and examine north-dipping structure (Figure 3.4). The strongest and most coherent RF phases at southern stations consist of positive phases that have increasing lag times with increasing distance from the coast, indicating a northward-dipping boundary. Negative phases of nearly equal amplitude precede the positive phases across the array by about 1.5 – 3 s.

Along the W-E C-C', which spans the eastern end of the Denali segment forearc and WBZ, the doublet feature is continuous with RF lag times of 3 – 8 s west of station PS11 (green star;

Figure 3.4c). Along the oblique WNW-ESE D-D' (projected to match the subducting slab direction in the Denali segment; Rondenay et al., 2010), which also spans the eastern end of the Denali segment WBZ, a doublet feature is continuous between RF lag times of 6 – 9 s at the eastern end increasing to 15 – 17 s at the northwestern end (Figure 3.4d). The shorter lag times for the doublet just to the west of station PAX (yellow star) in D-D' are almost the same as those just to the west of station PS11 of C-C', even though D-D' is ≥100 km to the north. This indicates the slab is relatively flat between these points. At the western end of D'-D' the doublet feature was previously imaged and interpreted as low-velocity Yakutat crust subducting to the northwest (Ferris et al., 2003; Rossi et al., 2006). Along the N-S E-E' adjacent to the WVF, the doublet is a continuous feature at 2.5 – 5 s lag at southern stations, increasing northward to 12 –14 s before disappearing just beyond the WVF.

The feature does not appear to be continuous between D-D' and E-E'. Picks of the RF lag times for the Yakutat Moho across the region highlights the offset that occurs along or just to the west of the stations used in E-E' (Figure 3.4b). The conversion points associated with these lag times should be offset from the stations, in a manner that depends on local dip of structure. Nonetheless, the offset of the Yakutat Moho RF lag times to the west of the E-E' stations indicates an offset in the subducting crust in the intervening region west and/or northwest of the WVF.

3.4.3 RF Migration

We generate images of the seismic discontinuity structure using a 2D generalized Radon transform-based multi-channel inversion of the scattered wavefield (Figure 3.5; Bostock and Rondenay, 1999; Bostock et al., 2001). We refer to this analysis as "RF migration". The one-dimensional (1D) velocity model used in the RF migration derives from an inversion of direct *P* and *S* wave arrivals from local earthquakes beneath the WVLF array (Daly et al., *subm*.). A subset

of 80 teleseismic earthquakes that occurred during the WVLF array deployment are used in the migration (see Appendix C). We migrate the RFs for a line of stations that transects the WVF, to complement previous results that used a similar technique to image the Denali segment (Kim et al., 2014; Rondenay et al., 2010). The RF migration strike direction is chosen as 15° to approximately follow the 20° down-dip direction of Wadati-Benioff Zone (WBZ) seismicity beneath the entire WVF (Figure 3.1). For the 15° orientation, WBZ epicenters within 30 km of the stations project within the dipping LVL (Figure 3.5a), consistent with the earthquakes located in the nearby Denali segment (Abers et al., 2013).

We generate five individual-mode RF migration images, each corresponding to a different RF mode (Pxs, Ppxs, Psxs-SV, Psxs-SH, and Ppxp; Figure 3.5 and S5). The Ppxp migration constrains *Vp* perturbations, while the other modes are stacked to generate a composite scattered-*Vs* image. Steeply dipping (>35-40°) boundaries are imaged only by Pxs, so the migration weights of each mode vary with depth (MacKenzie et al., 2010). The weights at depths <40 km are 0 for Pxs, 0.15 for Ppxs, 0.1 for Psxs-SV, and 0.1 for Psxs-SH. The Pxs weight increases from 0 to 1 between 40 and 60 km depth. In this way, the image deeper than 60 km relies almost completely on Pxs, while the other modes provide greater resolution at shallow depths.

In the composite *Vs* migration image (Figure 3.5a-b), a continuous ~18-km thick LVL enters the southern edge of the image dipping 10° between 24 km and 50 km depth and steepens northward to 43° dip beneath the WVF. The southern part of this feature is also apparent in the Ppxp migration image where the dip is shallow. The LVL extends 140 km inland from the coast and resembles the crust of the Yakutat terrane imaged farther west (Kim et al., 2014). The top of this layer is 80 km deep beneath Mount Drum, the westernmost Wrangell volcano, and reaches a maximum depth of ~110 km beneath the WVF. In the Ppxs migration image, the bottom of the

~18-km thick LVL that is seen in the Pxs migration image is not as clear, but the top of the LVL is split instead into the boundaries of a thin LVL that appears to be ~6-7 km thick (Figure S5d). This thin LVL dips northward from 20 km depth at the southern boundary of the image to ~32 km

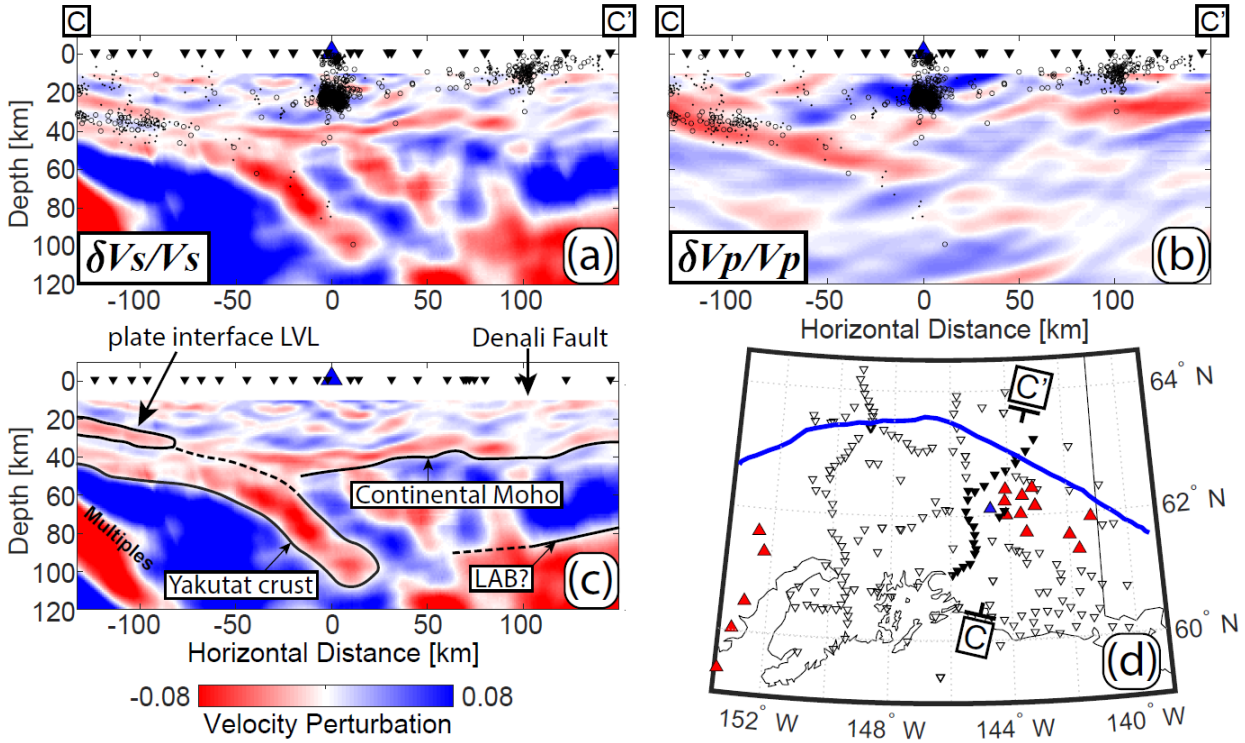

Figure 3.5 (a) Composite Vs migration. **(b)** P migration image, showing thin LVL along plate interface and Yakutat Moho. Steeply dipping features such as subducted Yakutat crust cannot be resolved in surface-reflected phases such as Ppxp (Mackenzie et al., 2010). **(c)** Composite Vs migration with interpreted boundaries. Circles are earthquakes within 15 km of stations used in migration from Daly et al. (subm.), dots are earthquakes between 15 km and 30 km of the stations. **(d)** Map showing stations used in the migration and approximate projection angle. Blue triangle – Mount Drum. Blue line – Denali Fault.

depth, disappearing where it meets other upper-plate phases, and begins to steepen (between horizontal distance of -75 km and -45 km in Figure 3.5a). The feature strongly resembles that seen at similar depths beneath the Kenai Peninsula (Kim et al., 2014), so presumably results from a similar plate boundary structure.

The composite migration image (Figure 3.5a-b) shows continuity of the thin LVL at the plate interface and the deeper ~18-km thick dipping LVL beneath the WVF. It also shows what

appears to be the upper-plate Moho beneath northern stations, with depths between 25-32 km north of the Denali fault, to 36-45 km south of the Denali fault, and up to 49 km at the center of the WVLF array. Well-located nearby earthquakes (Figure 3.5) with epicenters within 15 km of the stations used in the migration mostly do not occur within the plate interface LVL.

The composite *Vs* migration image also shows a sharp velocity decrease with depth at around 80-85 km depth in the backarc of the WVF (starting at horizontal distance = 105 km in Figure 3.5a-b). This boundary only exists north of the Denali fault and extends to the northern end of the migration image.

3.4.4 Common-Conversion-Point Stacking

A CCP stacking method (e.g., Dueker & Sheehan, 1997) complements the two 2D migration sections. The CCP volume is constructed by back projecting both direct and surface-reflected modes to depth. We back-project the 11066 RFs as follows: (1) generate a ray path using a 1D reference velocity model (Daly et al., *subm*.) according to the ray parameter of the incident signal, (2) extract *Vp* and *Vs* along that ray path from the three-dimensional (3D) velocity model, (3) convert time to depth for each of four assumptions about which RF mode generates the signal (Pxs, Ppxs, Psxs, Ppxp; Figure 3.2b), and (4) stack all RFs for each mode. The 3D model derives from a surface-wave based *Vs* model (Feng & Ritzwoller, 2019). The *Vp* model is determined from a phase-stacking method similar to that of Rossi et al. (2006) and Zhu and Kanamori (2000), described in Appendix C.

We filter each RF differently for each RF mode, using Gaussian low-pass filters with characteristic frequencies (Equation 1) that equalize the wavenumber content for signals in the spatial (depth) domain: 0.6 Hz for Pxs, 0.2 Hz for Ppxs, 0.15 Hz for Psxs, and 0.3 Hz for Ppxp. For each RF mode (i.e., for each unique characteristic frequency), we calculate the average RMS

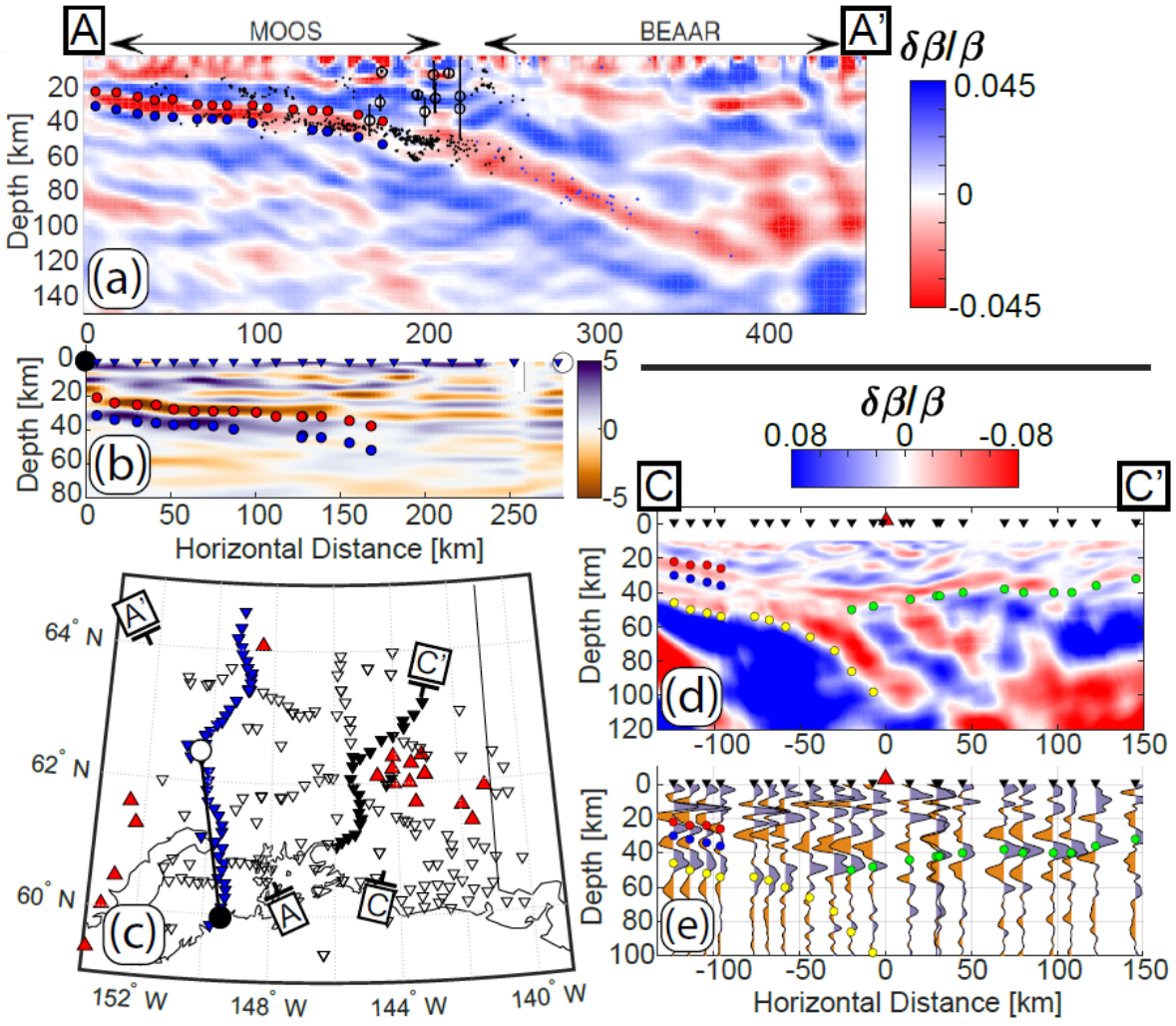

Figure 3.6: Comparisons of composite Vs migration with CCP results and surface picks (Section 4.5). (a) BEAAR and MOOS composite Vs migration results figure using a similar analysis to Figure 3.5, modified from Kim et al. (2014). Red and blue circles show picked top and bottom of LVL in the migration, respectively. Circles with vertical lines are tremor locations and depth uncertainties (1-σ) (Peterson & Christensen, 2009). Horizontal scale is the same as in (b). (b) CCP volume cross section along comparable line to (a). Red and blue circles from the top and bottom of plate interface LVL in (a). (c) 2D migration profile locations for (a) and (c), and cross section of CCP volume for (b). (d) WVLF composite Vs migration with picked boundaries beneath station locations. Symbols are colored to indicate different boundaries, red: top of plate interface LVL; blue: bottom of plate interface LVL; yellow: Yakutat Moho; green: North America Moho. (e) Vertical profiles of the CCP volume beneath stations used in the migration analysis. Vertical profiles are used instead of cross sections because of the contorted line of stations (Figure 3.5d). (d) and (e) have different orientations and locations because (d) uses data from the stations projected onto a 2D profile whereas (e) is a cross section through a 3D CCP volume beneath the stations themselves.

of the first three seconds of all RFs at a given station and use that value to normalize each RF amplitude. This rescaling tends to de-emphasize stations that show high-amplitude basin reverberations. The signals are back projected in the 3D velocity model, stacked in nodes spaced 2 km x 2 km horizontally and 1 km vertically, and then smoothed horizontally using a weighting function that scales to twice the Fresnel zone half width (Lekic and Fischer, 2017). The horizontal smoothing wavelength is determined by the frequency of each filter and the velocity at depth to account for the increased resolution of the reverberated phases. In the upper 15 km of the CCP volumes, we maintain the horizontal smoothing operator appropriate for a depth of 15 km to enhance continuity of structures at depths less than the station spacing.

We generate a composite CCP volume as a weighted sum of the Pxs, Ppxs, and Psxs, where the weights are 0.75 for Pxs, 1 for Ppxs, and -0.5 for Psxs. The Ppxp CCP is not stacked with the others because it samples *Vp* structure, while the other modes sample predominantly *Vs* structure. However, Ppxp does provide complementary images because *Vp* is typically correlated with *Vs*.

In the southern half of the study area, the most prominent feature in the CCP volume is a ~7-km thick negative-positive doublet, which is consistent with the LVL in the composite RF migration image (Figure 3.5) and that of Kim et al. (2014). A positive phase follows the doublet with increasing separation to the east, consistent with the subducting Yakutat Moho seen in the migration image. The northern half is typically dominated by a single, positive conversion from the upper plate Moho. CCP stacking does not correctly image steeply dipping discontinuities, so we interpret the discontinuities that only dip <~15°.

3.4.5 Depth Picks from CCP Images

Figure 3.6 compares slices of the CCP volume to the migration images in the two corridors where they overlap. We hand-pick co-located phases associated with the top and bottom of the

plate interface LVL, the Yakutat Moho, and the upper plate Moho along these corridors and then follow them throughout the CCP volume in East-West and North-South cross sections at 10-km increments. We pick these boundaries following two criteria: (1) in each cross-section, our picks had to be at least 20 km apart horizontally, and (2) these boundaries match similarly-picked boundaries in the RF migration images. We then fit a Gaussian-shape pulse in depth to the picked peaks in vertical columns through the CCP volume at each hand-picked points to determine the final depth for that boundary location (Figures 3.7-3.8).

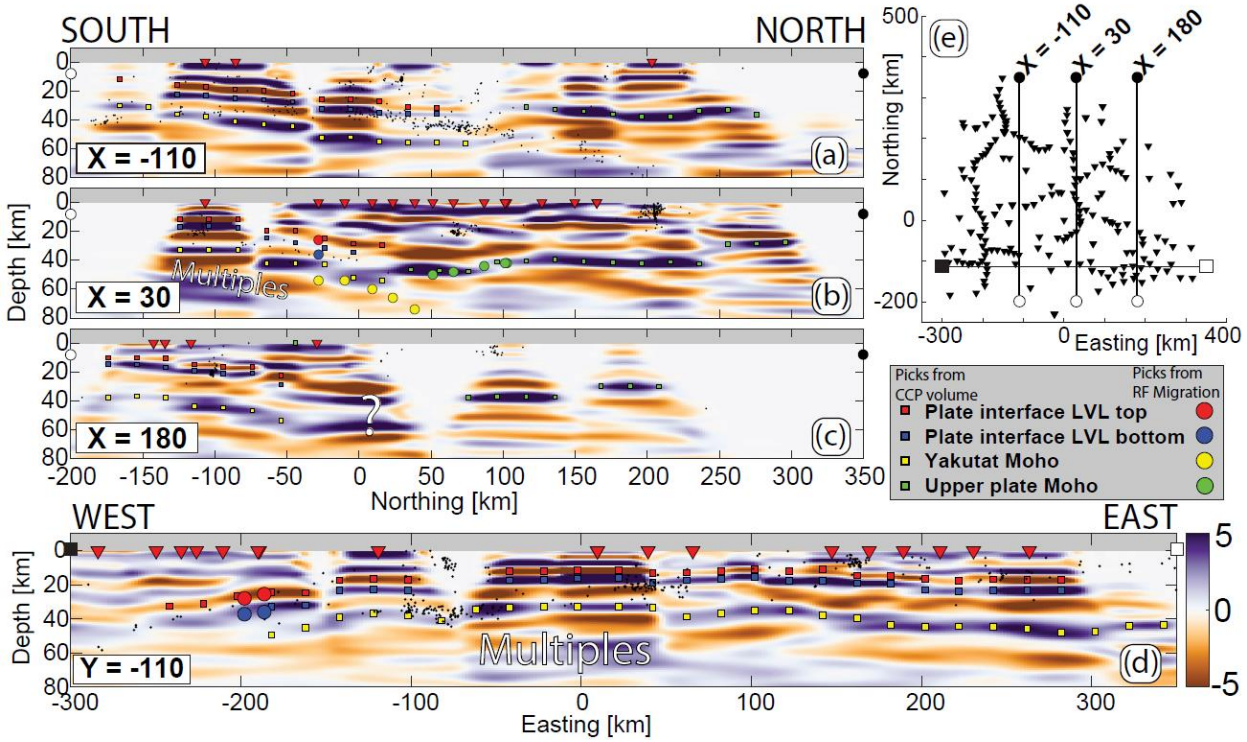

Figure 3.7: Cross sections through the CCP volume with picked boundaries. (a) N-S cross section through Denali segment showing underthrust Yakutat crust. (b) N-S cross section through center of WVLF array (Figure 1) showing underthrust Yakutat crust disappearing where it starts to steeply dip. (c) N-S cross section through Wrangell segment showing underthrust Yakutat crust. Question mark shows phases that are probably artifacts of dipping layers due to the assumption of horizontality in the CCP method. (d) E-W cross section near the coast showing continuity of plate interface LVL. (e) Map showing cross sections.

We interpret only those phases that appear on multiple RF modes to minimize the risk of picking reverberations. Figures C3 and C4 show cross-sections of each individual-mode CCP volume, highlighting that all four of the picked boundaries (i.e., top and bottom of thin plate interface LVL, Yakutat Moho, and continental Moho) show up in all three typical RF modes (Pxs, Ppxs, and Psxs). The Ppxp CCP volume also shows the same major features, providing additional independent confirmation of their validity (Figures C3 and C4).

The final depths for the Yakutat terrane Moho, the continental Moho, and the top of the plate interface LVL are shown in Figure 3.8. The thin plate interface LVL can be followed across southcentral Alaska for over 450 km along strike, showing that the same surface lies along the plate boundary between the Yakutat terrane and North America, beneath both the Wrangell segment and the Denali segment at depths < 35 km. The northern extent of the plate interface LVL in the Wrangell segment could extend further north based on our picking criteria (see Figures 3.7c and 3.8b), but we stop picking at the last line of stations south of the WVF due to data coverage. The plate interface beneath the Yakutat collision is continuous with the Alaska plate interface. East of ~150°W, it is underlain by the Yakutat terrane Moho. This shallow continuity contrasts with the clear offset in the deeper slab surface, as discussed below.

The thickness of the Yakutat crust in the shallow section can be estimated from the spatial separation between the top of the plate interface LVL and the Yakutat Moho (Figure 3.7). Because interference effects and variation in *Vp* and *Vs* can bias the apparent thickness of layers, further analysis of the RFs would be necessary to accurately determine the thickness of the plate interface LVL. That reanalysis for layer thickness is part of a follow-on study. Given that caveat, the average thickness of the plate interface LVL from the final CCP depths is 7±2 km (1σ), using the *Vs* from the 3D volume; biases are discussed below. The décollement is probably somewhere within this

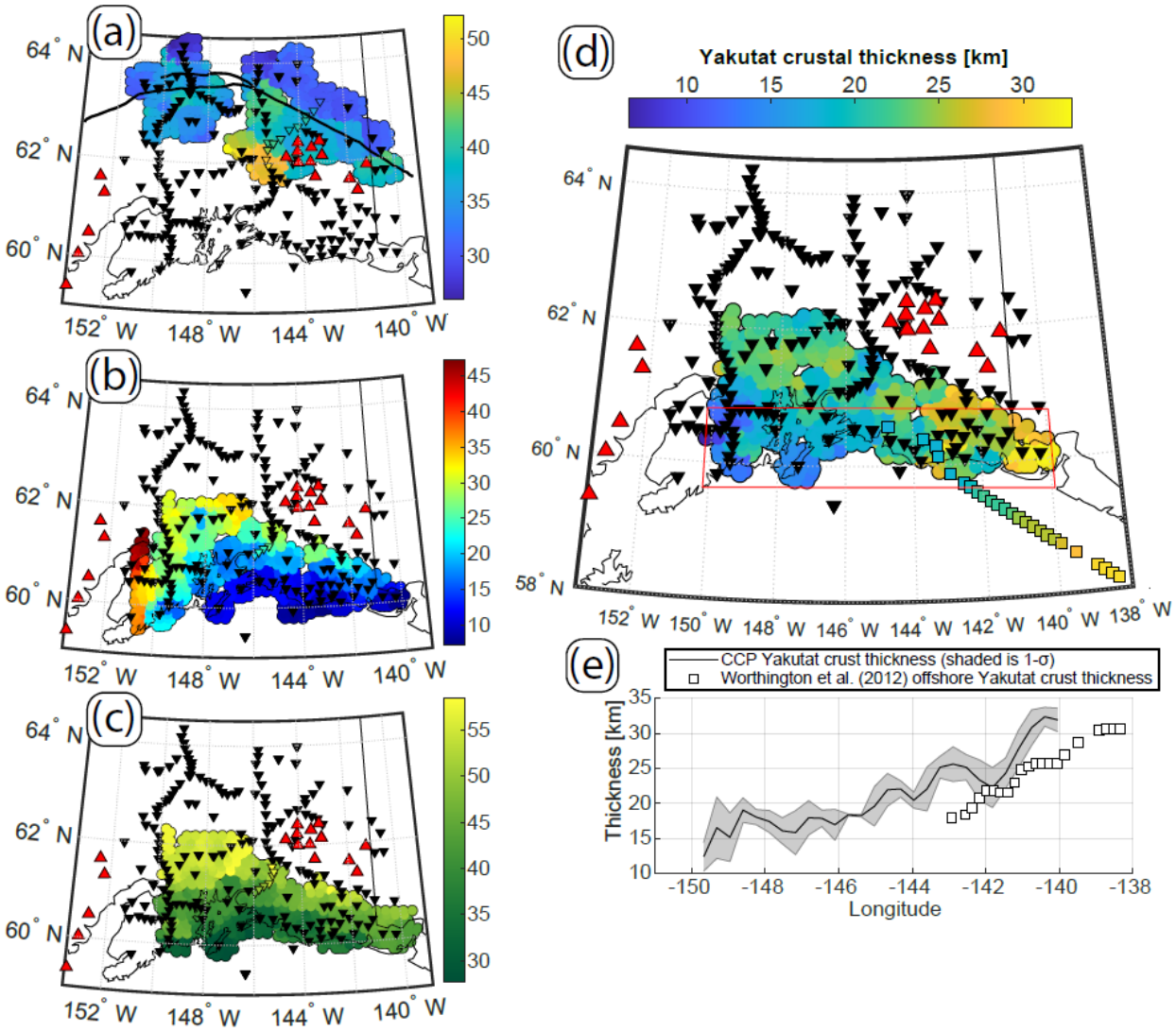

Figure 3.8: Interface depths and layer thicknesses from CCP volume. (a) Continental Moho depth. Black lines – Denali fault system; red triangles – volcanoes; black inverted triangles – seismometers. (b) Top of plate interface LVL. (c) Yakutat Moho depth. The depths to the continental Moho (a), LVL top (b), and Yakutat Moho (c) from the RF migration (Figure 3.6) are also shown by the color of their corresponding stations in the respective figure parts. (d) Yakutat crustal thicknesses. Circles are measurements from the CCP analysis based on difference between (b) and (c). Squares are measurements from active-source image (Worthington et al., 2012). Red boxes are longitudinal bins used in (e). For (a)-(d), all depths are in kilometers and indicated by adjacent color scale. (e) Yakutat crustal thickness vs longitude. Gray area – average thicknesses of Yakutat crust from red bin in (d), with gray shading that indicates one standard deviation from the mean at each value of longitude. Open squares – offshore Yakutat crustal thickness from Worthington et al. (2012). All depths are relative to overlying station elevation

layer (e.g., Bangs et al., 2009), so we add about half of the plate interface LVL thickness (3 km) to the depth of the top of the plate interface LVL to estimate the top of the Yakutat crust. That depth is subtracted from the Yakutat Moho depth determined from the CCP picks to estimate Yakutat crustal thicknesses (Figure 3.8d). The Yakutat crust thickens from 10 km at 150°W to 32 km at 140°W (Figure 3.8e).

The upper-plate Moho can be observed farther north, where the subducting crust is at mantle depths (Figure 3.8a). Its depth appears to vary across major terrane boundaries, with the most prominent change corresponding to a decrease in thickness of 5-10 km northward across the Denali fault. South of the Denali fault, crustal thickness increases from about 42 km northwest of the WVF to 50 km beneath the southern portion of the Copper River Basin.

3.5 Discussion

3.5.1 LVL Thickness Resolution

The resolution of layer thickness for these imaging methods is dependent on the wavelength of the signal, which is itself dependent on the frequency of the signal and the seismic velocity (Rondenay, 2009). To quantify vertical resolution, we generate synthetic seismograms for an LVL embedded in a half-space and vary the LVL thickness to determine the range of resolvable layer thicknesses. This analysis is repeated for both a horizontal and dipping LVL. The source pulse for these RFs has a Gaussian shape with a duration of 1 s, defined by the equation:

$$G(t) = \frac{4}{d\sqrt{2\pi}} \exp\left(-\frac{8(t-\mu)^2}{d^2}\right) \qquad (2)$$

where t is the time, μ is the time at the center of the pulse, and d is the "duration" of the pulse (i.e., the time from -2σ to +2σ around the center of the Gaussian). All thicknesses described in these models are the layer-perpendicular thicknesses.

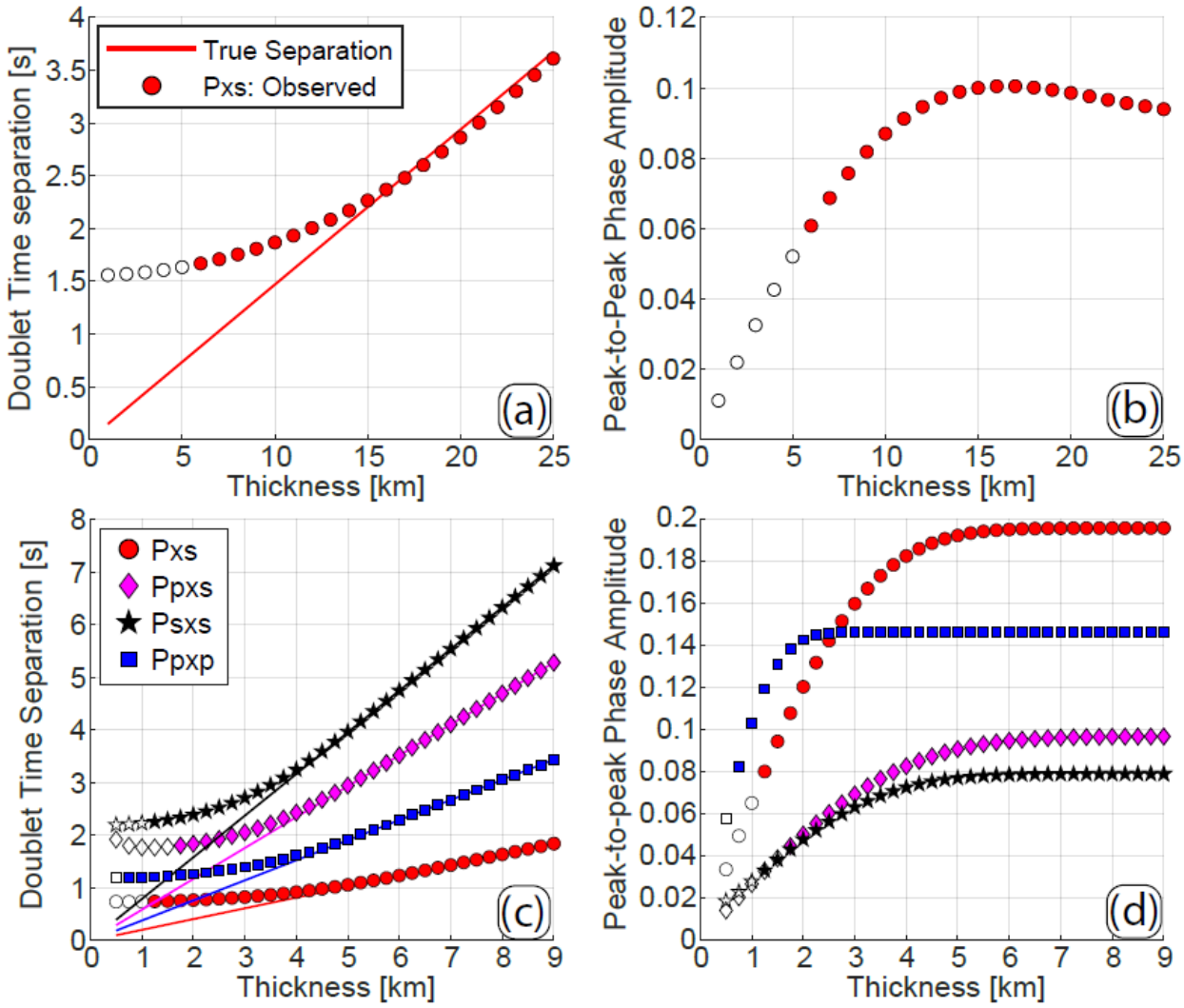

Figure 3.9: LVL thickness resolution analysis results. (a) Time separation for the positive-negative doublet in Ps for a 43° dipping LVL that is 80 km deep for an incident plane wave with back-azimuth = 15° and ray parameter = 0.06 s/km, filtered at 0.03-0.3 Hz using a second order Butterworth filter. Solid line shows prediction at ray-theoretical limit. (b) Peak-to-peak SV component amplitude of LVL signal for dipping layer in (a). (c) Time separation for a horizontal layer resembling the plate-interface LVL, for all major RF phases as labeled. Incident Gaussian pulse is filtered differently for each phase using a Gaussian low-pass filter (Equation 1; characteristic frequency used in each: 0.6 Hz for Pxs, 0.2 Hz for Ppxs, 0.15 Hz for Psxs, and 0.3 Hz for Ppxp). (d) Peak-to-peak SV component amplitude for signals and RF phases corresponding to (c). Open circles have peak-to-peak amplitudes less than twice the average standard deviation of the pre-incident noise from the RFs.

This test shows two thickness limits, a minimum observable thickness below which the layer cannot be seen, and a larger minimum resolvable thickness below which the LVL produces

signals but the thickness is biased upward (Figure 3.9). As the thickness of a LVL decreases past the minimum resolvable thickness, the phases from the top and bottom of the layer destructively interfere resulting in decreasing amplitudes, while the apparent peak-to-peak time remains roughly constant and limited by the duration of the source pulse. At the minimum observable thickness, the amplitudes of the LVL doublet phases have decreased to background noise levels, (defined here as twice the average standard deviation of pre-incident noise standard deviation) – thinner layers cannot be reliably observed.

To assess the thickness resolution of the subducted crust in the RF migration, we use a velocity model that involves a LVL with the same geometry as the Yakutat crust dipping beneath the WVF in the migration (Figure 3.9a-b). The top boundary of the subducted crust is set at 80 km depth and its thickness is varied from 1 km to 25 km. Velocities within the dipping crust (dip = 43°) are Vp = 7 km/s and Vs = 3.9 km/s to mimic Yakutat terrane crustal velocities (Worthington et al., 2012), and the surrounding half space has typical upper-mantle velocities (Vp = 8.15 km/s and Vs = 4.5 km/s). The only RF mode with non-negligible weights at these depths in the composite migration image is Pxs, so we test only that mode, for a ray parameter of 0.06 s/km and a back-azimuth in the down-dip direction (15°). The synthetic tests are conducted using the Gaussian source pulse described earlier but filtered as the RFs used in the migration (band-pass filtered, 0.03-0.3 Hz). For these parameters, the minimum resolvable subducted crustal thickness is ~14 km and the minimum observable thickness is ~5 km (Figure 3.9a-b). After correcting the dipping Yakutat crust to the more realistic velocities used in the synthetic tests, the true thickness is probably closer to ~15 km. This result confirms that the Yakutat crust is resolved to be subducting beneath the WVF in the RF migration. Even though its thickness is close to where it would begin to become spatially aliased (Figure 3.9a), it is clearly thicker than ~6-7 km of typical oceanic crust.

To assess the thickness resolution of the plate interface LVL, we use a horizontal LVL embedded in a half-space. The top boundary of the LVL is set at 20 km depth and its thickness is varied from 0.25 km to 9 km. Velocities within the LVL are Vp = 5.0 km/s and Vs = 2.5 km/s (following Kim et al., 2014), and the surrounding half-space has Vp = 6.5 km/s and Vs = 3.7 km/s. The CCP analysis is conducted using a different frequency for each RF mode (Section 3.4), so we filter each mode of the synthetic seismograms in the same way. For simplicity we measure the amplitudes of each model phase without accounting for interference among the different RF modes, which can occur for LVLs at such shallow depths (e.g., interference between Pxs and Ppxs for the Yakutat Moho in Figure 3.3h). Using a ray parameter of 0.06 s/km, this test shows that the minimum resolvable plate interface LVL thickness in RFs is ~5 km, and the minimum observable thickness is ~1 km. For actual data, the measured plate interface LVL is 7±2 km (1σ) thick in the composite CCP volume. After correcting the CCP analysis measurements to the more realistic LVL velocities used in the synthetic model, the measured thickness would be ~5 km or equal to the minimum resolvable thickness. Hence the observations are at the resolution limit, and the true average thickness of the plate interface LVL is ≤5 km and ≥~1 km.

3.5.2 The Yakutat Megathrust

At shallow depths, the plate interface is continuous along strike beneath the entire region, showing an antiformal shape at the western end (e.g., Figure 3.7b). The hinge line lies in Prince William Sound (PWS) at the eastern limit of rupture for the M9.2 1964 earthquake and trends in the direction of plate convergence (-30°) (Figure 3.10). The 1964 earthquake rupture zone extended from the epicenter at the eastern end of PWS to west of Kodiak Island and had two main regions of moment release, the larger of which occurred around the epicenter and PWS (Ruff and Kanamori, 1983; Christensen and Beck, 1994; Ichinose et al., 2007). The antiformal shape of the

plate interface is probably related to the subduction of the relatively buoyant Yakutat lithosphere as well as the convex, oceanward shape of the subduction zone in southcentral Alaska, resulting in the Yakutat plate bowing upwards (e.g., Chiao and Creager, 2002). Interestingly, a region of repeating slow-slip events lies down-dip of PWS along the hinge line and may be related to the antiformal shape (e.g., Kanamori et al., 1970; Ohta et al., 2006; Fu and Freymueller, 2013). We speculate that this antiformal structural arch limited the eastward rupture of the 1964 earthquake. The along-strike continuity of the plate interface could allow a megathrust earthquake to rupture farther east, as was the case for at least two prehistoric great earthquakes (Shennan et al., 2009). Perhaps the antiform in the subduction zone here acts as an occasional barrier to rupture further eastward (e.g., Das and Aki, 1977; Aki, 1979; Klinger et al., 2006).

3.5.3 LVL Along Plate Interface

The CCP analysis documents along-strike and down-dip continuity of the plate interface LVL across the imaged volume (Figure 3.7). The thin LVL between 7 and 35 km depth is a ubiquitous feature along the shallow plate boundary above the subducted Yakutat crust, which exhibits similar properties for over 450 km along strike. The plate-interface LVL is resolved in each individual-mode CCP volume, including Ppxp, which is sensitive to sharp gradients in *Vp* and indicates that this layer has both low *Vs* and low *Vp* (Figures C3 and C4). Thin LVLs are difficult to image at RF wavelengths when their thickness is less than 5-7 km, as discussed above. Analysis is further complicated because they may overlie or include part of thin oceanic crust and require forward modeling to constrain their seismic properties (e.g., Kim et al., 2012; Hansen et al., 2012). The thick crust of the Yakutat terrane simplifies the problem, because conversions from the subducting Moho do not interfere with those from the plate interface.

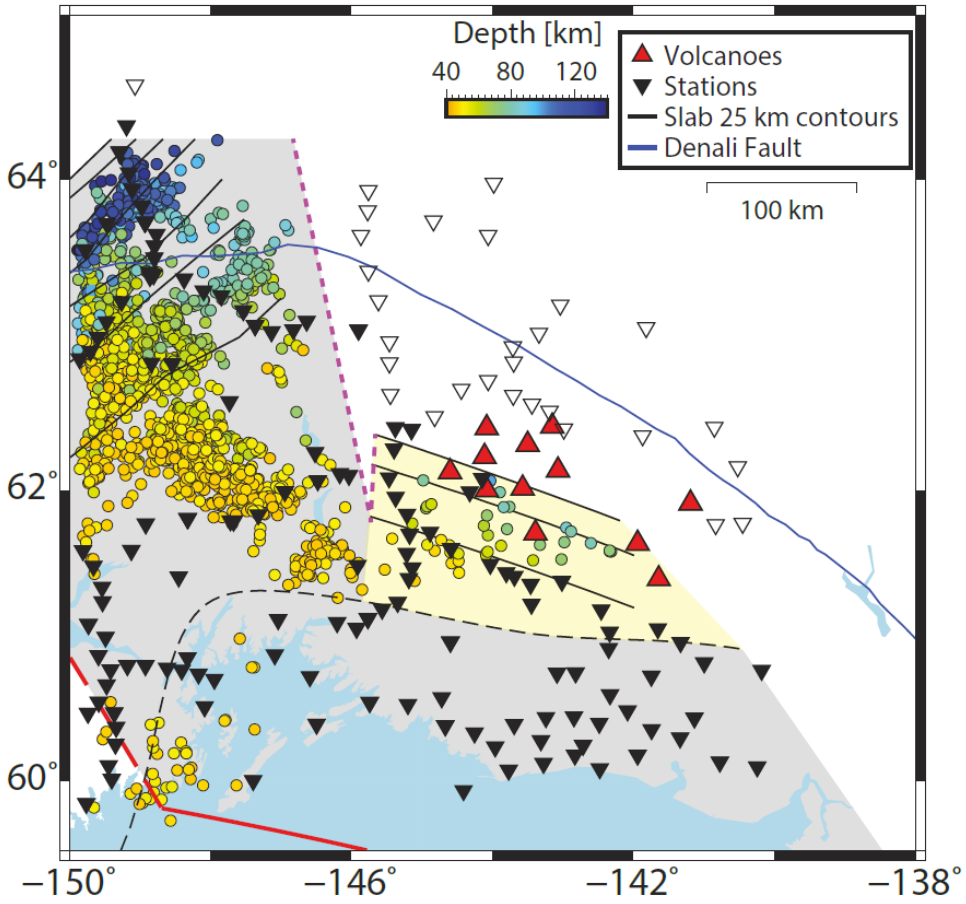

Figure 3.10: Outline of subducting Yakutat crust and tear location. Colored circles are WBZ earthquakes at depths >45 km (Daly et al., *subm.*). Filled inverted triangles are stations that have a clear doublet associated with the subducting crust, and unfilled inverted triangles are stations that do not (Figure 4). Grey region is inferred outline of subducted Yakutat crust from previous studies, yellow region is outline of additional piece of subducted Yakutat crust beneath WVF from RFs and WBZ seismicity. Purple dashed lines indicate inferred edges of the slab tear region. All other symbols as in Figure 3.1.

Similar LVLs have been seen in many other subduction zones (e.g., Clowes et al., 1987; Hansen et al., 2012; Kim et al., 2012), where stations have similarly dense spacing for RFs (<~20 km) along trench-normal profiles (e.g., Abers et al., 2009; Audet et al., 2009; Kim et al., 2014; Schaeffer and Audet, 2018). In Cascadia, studies of the plate interface LVL along strike are limited to sparse station spacing (e.g., Hansen et al., 2012). Imaging the plate interface in 3D has been limited to active source seismic imaging of small areas beneath the accretionary prism, with results

showing a patchy reflective interface (e.g., Bangs et al., 1999; Bangs et al., 2009; Bangs et al., 2015). These active-source studies interpret the patchy amplitudes as reflections from a layer of a variably hydrated fault zone. In Alaska (Figures 3.7 and 3.8), the RF images are the first direct imaging of the plate interface LVL spanning a 450-km wide region along strike and between 7-35 km depth using RFs (7 km is the up-dip limit of station coverage).

Plate interface LVLs are reported to have high *Vp/Vs* ratios (>2), low *Vs* (<3 km/s), and thicknesses ranging between 1-7 km (e.g., Kodaira et al., 2004; Abers et al., 2009; Hansen et al., 2012; Kim et al., 2012; Kim et al., 2014). LVLs along plate interfaces have been interpreted as resulting from high pore-fluid pressures within the uppermost oceanic crust and/or whatever subducted sediment and subcrustally eroded material is entrained beneath an impermeable megathrust interface (e.g., Audet et al., 2009; Peacock et al., 2011; Hansen et al., 2012). However, plate interface LVLs could also result from other processes. For instance, metamorphosed sediment should have lower velocities and higher *Vp/Vs* ratios than basalt or gabbro and could instead make up the bulk of the plate interface LVL, along with any eroded material from the upper plate (e.g., Calvert et al., 2004; Abers et al., 2009; Kim et al., 2014; Kim et al., 2019). Additionally, highly fractured basalt can manifest high *Vp/Vs* ratios without the need for high pore-fluid pressures (Nishimura et al., 2019). We interpret low velocities along the plate interface as largely due to metamorphosed sediment and tectonically eroded and fractured material, with free fluid playing a secondary role. *Vp/Vs* estimates of this layer in Alaska are part of a follow-on study.

3.5.4 Subducting Yakutat Crust

The eastward thickening wedge shape of the Yakutat crust offshore (Worthington et al., 2012) is observed in the CCP stack image onshore, with Yakutat crust thicknesses ranging from 10 km at 150°W to 32 km at 140°W (Figure 3.8d). The ~18-km thick LVL that steeply dips beneath

the WVF in our RF migration images is continuous with the subducting Yakutat terrane crust near the coast, so appears to be the same crust (Figure 3.6d-e). The thickness and continuity of the layer from the coast to beneath the WVF are consistent with RF migration images of the subducting Yakutat terrane in the Denali segment (Ferris et al., 2003; Kim et al., 2014) (Figure 3.6d-e). Below 90-km depth, the velocity contrasts weaken (Figure 3.5). At 110-km depth beneath the WVF, the Yakutat crust velocity contrasts disappear, either because the deeper subducting crust has broken off (e.g., Nye, 1983) or because progressive metamorphic reactions change the subducting basaltic crust to eclogite and eliminate its velocity contrast with the surrounding mantle. The latter explanation is consistent with interpretations for the Denali segment (e.g., Rondenay et al., 2008).

3.5.5 Potential Tear in Subducting Yakutat Lithosphere

RFs from the BEAAR array show a LVL in the upper mantle in the Denali segment (Ferris et al., 2003), similar to that observed beneath the WVF (Figure 3.4e). RF migration of these signals from both segments show clear subducting crust 11 – 22 km thick that contain nearby intermediate-depth earthquakes (IDEs; earthquakes ~40-300 km depth) (Figure 3.5; cf. Kim et al., 2014). The similarity of the signals at >60 km depth, and their connection up-dip with the continuous subducting Yakutat plate at shallow (<35 km) depths, suggests that they show the same feature: subducting Yakutat terrane crust. Still, at ~100 km depth the subducting crust shows a ~250-km offset between the two segments in the direction of plate convergence, with differences in strike and dip of 45° and 20°, respectively. The eastern limit of Denali segment WBZ seismicity and tremor lies <50 km west of the stations that image the much steeper WVF slab (e.g., Wech, 2016), leaving very little room for a continuous slab, a geometry that strongly suggests a tear (Figures 3.4 and 3.10). Up dip, the two slabs converge in depth somewhere beneath the Copper River Basin or just south of it (Figure 3.10).

A slab tear would create a window in the subducting Yakutat lithosphere and allow lateral flow of asthenospheric mantle material into the mantle wedge beneath the WVF, perhaps leading to hotter slab-surface temperatures, as argued near other slab edges globally (e.g., Thorkelson, 1996; Zandt & Humphreys, 2008). From Rayleigh waves, Feng et al. (2020) measure upper mantle anisotropy fast directions and show a toroidal pattern around the subducting Yakutat slab in the Denali segment. This toroidal pattern was interpreted as clockwise flow around the Denali segment subducting slab, as predicted by geodynamic models (e.g., Jadamec and Billen, 2010). Near the location of the possible slab tear (Figure 3.10), azimuthal anisotropy is significantly reduced, with complex shear-wave splitting patterns (e.g., Hanna & Long, 2012; Feng et al., 2020; McPherson et al., 2020; Venereau et al., 2019). Additionally, the Yakutat slab beneath the WVF is subducting obliquely (Figure 3.1), which retards vertical velocity and may increase the temperature of the shallow subducting slab (Daly et al., *subm*.). Anomalous wedge and slab heating could explain the adakitic signature at Mount Drum, closest to the tear corner, and the generally large melt volumes required to generate the WVF (Thorkelson and Breitsprecher, 2005; Moyen, 2009; Jadamec and Billen, 2010).

3.5.6 Alaskan Moho and Lithosphere-Asthenosphere Boundary

Our upper plate crustal thickness results agree with previous studies across Alaska (e.g., O'Driscoll and Miller, 2015; Miller and Moresi, 2018; Ward and Lin, 2018; Feng and Ritzwoller, 2019; Berg et al., 2020; Haney et al., 2020). Upper plate crustal thickness seen in the composite RF migration images of this region match the CCP volume (Figure 3.6). The decrease in crustal thickness of around 5-10 km northward across the Denali Fault throughout the imaged region (Figure 3.8a) has been seen previously (e.g., Rossi et al., 2006; Veenstra et al., 2006; Allam et al., 2017; Miller et al., 2018).

We observe the largest crustal thickness (up to 51 km) at the center of the WVLF array (Figure 3.7). The deeper Moho is accompanied by an overlying negative conversion (velocity decrease with depth), suggesting a layer of low-velocity material. This observation of a potential low-velocity region is corroborated by the low velocities seen in the same location by Ward and Lin (2018). However, there is some uncertainty as to whether the velocity increase with depth seen up to 51 km beneath the Copper River Basin is the Moho or the base of a LVL below the continental crust. Additionally, sedimentary basins, such as the overlying Copper River Basin, can cause significant artifacts in the Moho Pxs conversion, but they have only a small effect on the later reverberated phases (Rossi et al., 2006). The low-velocity region at the base of the continental crust is best imaged in the reverberated phases and does not exist beneath all stations within the Copper River Basin, which suggest this feature is unlikely to be the result of basin reverberations.

The *Vs* decrease with depth around 80 km in the WVF backarc of the RF migration image (Figure 3.5) is similar to that seen beneath the Denali region at 60 km depth (Rondenay et al., 2010). Joint inversions of *S*-to-*P* RFs and Rayleigh wave phase velocities reveal shear velocity reductions typically associated with the lithosphere-asthenosphere boundary (LAB) at depths beneath stations in the Denali segment of 60 km and beneath the WVF backarc of 80 km (Gama et al., 2021). *S*-to-*P* RF CCP stacking across Alaska shows a negative velocity gradient at 80-km depth north of the Denali fault that extends to the north and is also continuous across both the Wrangell and Denali segments of the subduction zone (O'Driscoll and Miller, 2015). We interpret this feature to be the seismic signature of the LAB of the Yukon-Tanana terrane north of the Denali fault. The RF migration image provides increased resolution of the LAB and shows that the LAB abruptly disappears southward across location of the Denali fault (Figure 3.5). Hence, the sharp LAB beneath the Yukon-Tanana terrane in the Denali segment is unlikely to be a result of peculiar

dynamics there (Rondenay et al., 2010). These observations support the hypothesis of O'Driscoll and Miller (2015) that the Denali fault, much like other major strike-slip fault systems (e.g., Lekic et al., 2011), is a lithosphere-scale feature.

3.6 Conclusions

RF migration in 2D using the WVLF seismic array and a 3D CCP stacking method using multiple dense seismic arrays image the subduction zone across southcentral Alaska. These methods are refined here to account for and remove the effects of varying surface velocities. The 2D RF migration imaging reveals the subduction of the ~18-km thick Yakutat terrane crust up to 110 km depth beneath the WVF, dipping at 43° and striking at 285°. The plate interface in the migration appears as a thin low-velocity layer at depths <35. The 3D CCP stacking shows that both the Yakutat terrane crust and the plate interface low-velocity layer extend for over 450 km along strike, spanning the entire image volume. The Yakutat terrane subducts continuously as a single unit throughout southcentral Alaska at depths <45 km, where it dips < 10°. Near the coast the Yakutat crust thickens to the east, with thicknesses ranging from 12 km at 150°W to 32 km at 140°W. The along-strike continuity of a thin (≤5 km thick) low-velocity layer along the plate interface at depths <35 km in the CCP and RF migration images suggests that the region has the potential to rupture much further to the east than in the great 1964 earthquake.

The upper plate Moho is imaged across the array. Notable features include a 5-10 km shallowing northward across the Denali fault and a deepening beneath the southern half of the Copper River Basin. The RF migration also images a velocity decrease with depth at ~80 km depth that only exists North of the Denali fault. This could potentially be the base of the lithosphere beneath the Yukon-Tanana terrane and suggests the Denali fault is a lithospheric-scale feature.

Combined with previous RF imaging, our results show that there is likely a tear in the subducting slab beneath southcentral Alaska near 146°W. The tear splits the subducting Yakutat slab into two segments below 45 km depth, with a 45° difference in strike, 20° difference in dip, and vastly different overlying volcanism. The tear is located to the west of the WVF, probably somewhere beneath the Copper River basin. Either or both oblique subduction and asthenospheric flow through the slab tear is heating the subducting slab beneath the WVF on its west side.

REFERENCES

Abers, G. A., MacKenzie, L. S., Rondenay, S., Zhang, Z., Wech, A. G., & Creager, K. C. (2009). Imaging the source region of Cascadia tremor and intermediate-depth earthquakes. *Geology*, *37*(12), 1119–1122. https://doi.org/10.1130/G30143A.1

Abers, G. A. (2008), Orogenesis from Subducting Thick Crust and Evidence from Alaska, in *Active Tectonics and Seismic Potential of Alaska, Geophys. Mohogr. Ser.*, vol. 179, edited by J. T. Freymueller et al., pp. 337-349, AGU, Washington, D. C. https://doi.org/10.1029/179GM19

Abers, Geoffrey A., Nakajima, J., van Keken, P. E., Kita, S., & Hacker, B. R. (2013). Thermal–petrological controls on the location of earthquakes within subducting plates. *Earth and Planetary Science Letters*, *369–370*, 178–187. https://doi.org/10.1016/j.epsl.2013.03.022

Abt, D. L., Fischer, K. M., French, S. W., Ford, H. A., Yuan, H., & Romanowicz, B. (2010). North American lithospheric discontinuity structure imaged by Ps and Sp receiver functions. *Journal of Geophysical Research*, *115*(B9), B09301. https://doi.org/10.1029/2009JB006914

Aki, K. (1979). Characterization of barriers on an earthquake fault. *Journal of Geophysical Research*, *84*(B11), 6140. https://doi.org/10.1029/JB084iB11p06140

Allam, A. A., Schulte-Pelkum, V., Ben-Zion, Y., Tape, C., Ruppert, N., & Ross, Z. E. (2017). Ten kilometer vertical Moho offset and shallow velocity contrast along the Denali fault zone from double-difference tomography, receiver functions, and fault zone head waves. *Tectonophysics*, *721*, 56–69. https://doi.org/10.1016/j.tecto.2017.09.003

Arrial, P.-A., & Billen, M. I. (2013). Influence of geometry and eclogitization on oceanic plateau subduction. *Earth and Planetary Science Letters, 363*, 34–43. https://doi.org/10.1016/j.epsl.2012.12.011

Audet, P., & Schaeffer, A. J. (2018). Fluid pressure and shear zone development over the locked to slow slip region in Cascadia. *Science Advances*, *4*(3), eaar2982. https://doi.org/10.1126/sciadv.aar2982

Audet, P., Bostock, M. G., Christensen, N. I., & Peacock, S. M. (2009). Seismic evidence for overpressured subducted oceanic crust and megathrust fault sealing. *Nature*, *457*(7225), 76–78. https://doi.org/10.1038/nature07650

Bangs, N. L., McIntosh, K. D., Silver, E. A., Kluesner, J. W., & Ranero, C. R. (2015). Fluid accumulation along the Costa Rica subduction thrust and development of the seismogenic zone: The Costa Rica subduction thrust. *Journal of Geophysical Research: Solid Earth*, *120*(1), 67–86. https://doi.org/10.1002/2014JB011265

Bangs, Nathan L. B., Shipley, T. H., Moore, J. C., & Moore, G. F. (1999). Fluid accumulation and channeling along the northern Barbados Ridge decollement thrust. *Journal of Geophysical Research: Solid Earth*, *104*(B9), 20399–20414. https://doi.org/10.1029/1999JB900133

Bangs, N.L.B., Moore, G. F., Gulick, S. P. S., Pangborn, E. M., Tobin, H. J., Kuramoto, S., & Taira, A. (2009). Broad, weak regions of the Nankai Megathrust and implications for shallow coseismic slip. *Earth and Planetary Science Letters*, *284*(1–2), 44–49. https://doi.org/10.1016/j.epsl.2009.04.026

Berg, E. M., Lin, F., Allam, A., Schulte-Pelkum, V., Ward, K. M., & Shen, W. (2020). Shear Velocity Model of Alaska Via Joint Inversion of Rayleigh Wave Ellipticity, Phase

Velocities, and Receiver Functions Across the Alaska Transportable Array. *Journal of Geophysical Research: Solid Earth*, *125*(2). https://doi.org/10.1029/2019JB018582

Bostock, M. G., & Rondenay, S. (1999). Migration of scattered teleseismic body waves. *Geophysical Journal International*, *137*(3), 732–746. https://doi.org/10.1046/j.1365-246x.1999.00813.x

Bostock, M. G., Rondenay, S., & Shragge, J. (2001). Multiparameter two-dimensional inversion of scattered teleseismic body waves 1. Theory for oblique incidence. *Journal of Geophysical Research: Solid Earth*, *106*(B12), 30771–30782. https://doi.org/10.1029/2001JB000330

Brueseke, M. E., Benowitz, J. A., Trop, J. M., Davis, K. N., Berkelhammer, S. E., Layer, P. W., & Morter, B. K. (2018). The Alaska Wrangell Arc: ~30 million years of subduction-related magmatism along a still active arc-transform junction. *Terra Nova*, ter.12369. https://doi.org/10.1111/ter.12369

Bruns, T. R. (1983). Model for the origin of the Yakutat block, an accreting terrane in the northern Gulf of Alaska. *Geology*, *11*, 718-721. https://doi.org/10.1130/0091-7613

Calvert, A. J. (2004). Seismic reflection imaging of two megathrust shear zones in the northern Cascadia subduction zone. *Nature*, *428*(6979), 163–167. https://doi.org/10.1038/nature02372

Chapman, J. B., Pavlis, T. L., Bruhn, R. L., Worthington, L. L., Gulick, S. P. S., & Berger, A. L. (2012). Structural relationships in the eastern syntaxis of the St. Elias orogen, Alaska. *Geosphere*, *8*(1), 105–126. https://doi.org/10.1130/GES00677.1

Chiao, L.-Y., & Creager, K. C. (2002). Geometry and membrane deformation rate of the subducting Cascadia slab. *The Cascadia subduction zone and related subduction*

system—Seismic structure, intraslab earthquakes and processes, and earthquake hazards, 02–328 https://doi.org/10.4095/222496

Christensen, D. H., & Beck, S. L. (1994). The rupture process and tectonic implications of the great 1964 Prince William Sound earthquake, *Pure Appl. Geophys., 142*, 29-53.

Chuang, L., Bostock, M., Wech, A., & Plourde, A. (2017). Plateau subduction, intraslab seismicity, and the Denali (Alaska) volcanic gap. *Geology*, *45*(7), 647–650. https://doi.org/10.1130/G38867.1

Cloos, M. (1993), Lithospheric buoyancy and collisional orogenesis: Subduction of oceanic plateaus, continental margins, island arcs, spreading ridges and seamounts, *Geol. Soc. Am. Bull., 105*, 715-737.

Clowes, R. M., Brandon, M. T., Green, A. G., Yorath, C. J., Brown, A. S., Kanasewich, E. R., & Spencer, C. (1987). LITHOPROBE—southern Vancouver Island: Cenozoic subduction complex imaged by deep seismic reflections. *Canadian Journal of Earth Sciences, 24*(1), 31–51. https://doi.org/10.1139/e87-004

Cunningham, E., & Lekic, V. (2019). Constraining crustal structure in the presence of sediment: a multiple converted wave approach. *Geophysical Journal International, 219*(1), 313–327. https://doi.org/10.1093/gji/ggz298

Daly, K.A., Abers, G.A., Mann, M.E., Roecker, S.W., & Christensen, D.H. (2019), A Wadati-Benioff Zone Beneath the Wrangell Volcanic Field Revealed By The WVLF Broadband Array, Abstr. T41F-0298, Amer. Geophys. Un. 2019 Fall Meeting, San Francisco, 9-13 Dec.

Daly, K.A., Abers, G.A., Mann, M.E., Roecker, S.W., & Christensen, D.H. (2021), Subduction of an Oceanic Plateau Across Southcentral Alaska: High-resolution seismicity. *Journal of Geophysical Research: Solid Earth*, submitted.

Das, S., & Aki, K. (1977). Fault plane with barriers: A versatile earthquake model. *Journal of Geophysical Research, 82*(36), 5658–5670. https://doi.org/10.1029/JB082i036p05658

Dueker, K. G., & Sheehan, A. F. (1997). Mantle discontinuity structure from midpoint stacks of converted P to S waves across the Yellowstone hotspot track. *Journal of Geophysical Research: Solid Earth*, *102*(B4), 8313–8327. https://doi.org/10.1029/96JB03857

Eberhart-Phillips, D., Christensen, D. H., Brocher, T. M., Hansen, R., Ruppert, N. A., Haeussler, P. J., & Abers, G. A. (2006). Imaging the transition from Aleutian subduction to Yakutat collision in central Alaska, with local earthquakes and active source data. *Journal of Geophysical Research: Solid Earth*, *111*(B11), n/a-n/a. https://doi.org/10.1029/2005JB004240

Elliott, J., & Freymueller, J. T. (2020). A Block Model of Present-Day Kinematics of Alaska and Western Canada. *Journal of Geophysical Research: Solid Earth*, *125*(7). https://doi.org/10.1029/2019JB018378

Elliott, J., Freymueller, J. T., & Larsen, C. F. (2013). Active tectonics of the St. Elias orogen, Alaska, observed with GPS measurements. *Journal of Geophysical Research: Solid Earth*, *118*(10), 5625–5642. https://doi.org/10.1002/jgrb.50341

Elliott, J. L., Larsen, C. F., Freymueller, J. T., & Motyka, R. J. (2010). Tectonic block motion and glacial isostatic adjustment in southeast Alaska and adjacent Canada constrained by GPS measurements. *Journal of Geophysical Research*, *115*(B9), B09407. https://doi.org/10.1029/2009JB007139

Feng, L., Liu, C., & Ritzwoller, M. H. (2020). Azimuthal Anisotropy of the Crust and Uppermost Mantle Beneath Alaska. *Journal of Geophysical Research: Solid Earth*, *125*(12). https://doi.org/10.1029/2020JB020076

Feng, Lili, & Ritzwoller, M. H. (2019). A 3-D Shear Velocity Model of the Crust and Uppermost Mantle Beneath Alaska Including Apparent Radial Anisotropy. *Journal of Geophysical Research: Solid Earth*, *124*(10), 10468–10497. https://doi.org/10.1029/2019JB018122

Ferris, A., Abers, G. A., Christensen, D. H., & Veenstra, E. (2003). High resolution image of the subducted Pacific (?) plate beneath central Alaska, 50–150 km depth. *Earth and Planetary Science Letters*, *214*(3–4), 575–588. https://doi.org/10.1016/S0012-821X(03)00403-5

Forsyth, D., & Uyeda, S. (1975). On the Relative Importance of the Driving Forces of Plate Motion. *Geophysical Journal International*, *43*(1), 163–200. https://doi.org/10.1111/j.1365-246X.1975.tb00631.x

Fu, Y., & Freymueller, J. T. (2013). Repeated large Slow Slip Events at the southcentral Alaska subduction zone. *Earth and Planetary Science Letters*, *375*, 303–311. https://doi.org/10.1016/j.epsl.2013.05.049

Gama, I., Fischer, K. M., Eilon, Z., Krueger, H. E., Dalton, C. A., & Flesch, L. M. (2021). Shear-wave velocity structure beneath Alaska from a Bayesian joint inversion of Sp receiver functions and Rayleigh wave phase velocities. *Earth and Planetary Science Letters*, *560*, 116785. https://doi.org/10.1016/j.epsl.2021.116785

Gou, T., Zhao, D., Huang, Z., & Wang, L. (2019). Aseismic Deep Slab and Mantle Flow Beneath Alaska: Insight From Anisotropic Tomography. *Journal of Geophysical Research: Solid Earth*, *124*(2), 1700–1724. https://doi.org/10.1029/2018JB016639

Haney, M. M., Ward, K. M., Tsai, V. C., & Schmandt, B. (2020). Bulk Structure of the Crust and Upper Mantle beneath Alaska from an Approximate Rayleigh-Wave Dispersion Formula. *Seismological Research Letters*, *91*(6), 3064–3075. https://doi.org/10.1785/0220200162

Hanna, J., & Long, M. D. (2012). SKS splitting beneath Alaska: Regional variability and implications for subduction processes at a slab edge. *Tectonophysics*, *530–531*, 272–285. https://doi.org/10.1016/j.tecto.2012.01.003

Hansen, R. T. J., Bostock, M. G., & Christensen, N. I. (2012). Nature of the low velocity zone in Cascadia from receiver function waveform inversion. *Earth and Planetary Science Letters*, *337–338*, 25–38. https://doi.org/10.1016/j.epsl.2012.05.031

van Hunen, J., van den Berg, A. P., & Vlaar, N. J. (2002). On the role of subducting oceanic plateaus in the development of shallow flat subduction. *Tectonophysics*, *352*(3–4), 317–333. https://doi.org/10.1016/S0040-1951(02)00263-9

Ichinose, G., Somerville, P., Thio, H. K., Graves, R., & O'Connell, D. (2007). Rupture process of the 1964 Prince William Sound, Alaska, earthquake from the combined inversion of seismic, tsunami, and geodetic data. *Journal of Geophysical Research*, *112*(B7), B07306. https://doi.org/10.1029/2006JB004728

Jadamec, M. A., & Billen, M. I. (2010). Reconciling surface plate motions with rapid three-dimensional mantle flow around a slab edge. *Nature*, *465*(7296), 338–341. https://doi.org/10.1038/nature09053

Jiang, C., Schmandt, B., Ward, K. M., Lin, F., & Worthington, L. L. (2018). Upper Mantle Seismic Structure of Alaska From Rayleigh and S Wave Tomography. *Geophysical Research Letters*, *45*(19), 10,350-10,359. https://doi.org/10.1029/2018GL079406

Kanamori, H. (1970). The Alaska Earthquake of 1964: Radiation of long-period surface waves and source mechanism. *Journal of Geophysical Research, 75*(26), 5029–5040. https://doi.org/10.1029/JB075i026p05029

Kennett, B. L. N. (1991). The Removal of Free Surface Interactions From Three-Component Seismograms. *Geophysical Journal International, 104*(1), 153–154. https://doi.org/10.1111/j.1365-246X.1991.tb02501.x

Kim, D., Keranen, K. M., Abers, G. A., & Brown, L. D. (2019). Enhanced resolution of the subducting plate interface in Central Alaska from autocorrelation of local earthquake coda. *Journal of Geophysical Research: Solid Earth, 124*. https://doi.org/10.1029/2018JB016167

Kim, Y., Miller, M. S., Pearce, F., & Clayton, R. W. (2012). Seismic imaging of the Cocos plate subduction zone system in central Mexico. *Geochemistry, Geophysics, Geosystems, 13*(7), n/a-n/a. https://doi.org/10.1029/2012GC004033

Kim, Y., Abers, G. A., Li, J., Christensen, D., Calkins, J., & Rondenay, S. (2014). Alaska Megathrust 2: Imaging the megathrust zone and Yakutat/Pacific plate interface in the Alaska subduction zone. *Journal of Geophysical Research: Solid Earth, 119*(3), 1924–1941. https://doi.org/10.1002/2013JB010581

Kirschner, C.E., 1994, Sedimentary basins in Alaska, in Plafker, G., & Berg, H.C., eds., The Geology of Alaska: Geological Society of America, 1 sheet, scale 1:2,500,000.

Klinger, Y., Michel, R., & King, G. (2006). Evidence for an earthquake barrier model from Mw~7.8 Kokoxili (Tibet) earthquake slip-distribution. *Earth and Planetary Science Letters, 242*(3–4), 354–364. https://doi.org/10.1016/j.epsl.2005.12.003

Kodaira, S. (2004). High Pore Fluid Pressure May Cause Silent Slip in the Nankai Trough. *Science, 304(*5675), 1295–1298. https://doi.org/10.1126/science.1096535

Koons, P. O., Hooks, B. P., Pavlis, T., Upton, P., & Barker, A. D. (2010). Three-dimensional mechanics of Yakutat convergence in the southern Alaskan plate corner. *Tectonics, 29*(4), n/a-n/a. https://doi.org/10.1029/2009TC002463

Langston, C. A. (1977). Corvallis, Oregon, crustal and upper mantle receiver structure from teleseismic P and S waves. *Bulletin of the Seismological Society of America 67*(3), 713-724.

Lekić, V., & Fischer, K. M. (2017). Interpreting spatially stacked Sp receiver functions. *Geophysical Journal International, 210(*2), 874–886. https://doi.org/10.1093/gji/ggx206

Lekic, V., French, S. W., & Fischer, K. M. (2011). Lithospheric Thinning Beneath Rifted Regions of Southern California. *Science, 334*(6057), 783–787. https://doi.org/10.1126/science.1208898

Li, J., Abers, G. A., Kim, Y., & Christensen, D. (2013). Alaska megathrust 1: Seismicity 43 years after the great 1964 Alaska megathrust earthquake. *Journal of Geophysical Research: Solid Earth*, *118*(9), 4861–4871. https://doi.org/10.1002/jgrb.50358

MacKenzie, L. S., Abers, G. A., Rondenay, S., & Fischer, K. M. (2010). Imaging a steeply dipping subducting slab in Southern Central America. *Earth and Planetary Science Letters*, *296*(3–4), 459–468. https://doi.org/10.1016/j.epsl.2010.05.033

Marechal, A., Mazzotti, S., Elliott, J. L., Freymueller, J. T., & Schmidt, M. (2015). Indentor-corner tectonics in the Yakutat-St. Elias collision constrained by GPS. *Journal of Geophysical Research: Solid Earth*, *120*(5), 3897–3908. https://doi.org/10.1002/2014JB011842

Martin-Short, R., Allen, R. M., & Bastow, I. D. (2016). Subduction geometry beneath south central Alaska and its relationship to volcanism: Imaging Mantle Structure Beneath Alaska. *Geophysical Research Letters*, *43*(18), 9509–9517. https://doi.org/10.1002/2016GL070580

Martin-Short, R., Allen, R., Bastow, I. D., Porritt, R. W., & Miller, M. S. (2018). Seismic Imaging of the Alaska Subduction Zone: Implications for Slab Geometry and Volcanism. *Geochemistry, Geophysics, Geosystems*, *19*(11), 4541–4560. https://doi.org/10.1029/2018GC007962

Mason, W. G., Moresi, L., Betts, P. G., & Miller, M. S. (2010). Three-dimensional numerical models of the influence of a buoyant oceanic plateau on subduction zones. *Tectonophysics*, *483*(1–2), 71–79. https://doi.org/10.1016/j.tecto.2009.08.021

Mazzotti, S., Leonard, L. J., Hyndman, R. D., & Cassidy, J. F. (2008). Tectonics, Dynamics, and Seismic Hazard in *Active Tectonics and Seismic Potential of Alaska, Geophys. Mohogr. Ser.*, vol. 179, edited by J. T. Freymueller et al., pp. 297-319, AGU, Washington, D. C. https://doi.org/10.1029/179GM17

McGeary, S., Nur, A., & Ben-Avraham, Z. (1985). Spatial gaps in arc volcanism: The effect of collision or subduction of oceanic plateaus. *Tectonophysics*, *119*(1–4), 195–221. https://doi.org/10.1016/0040-1951(85)90039-3

McPherson, A. M., Christensen, D. H., Abers, G. A., & Tape, C. (2020). Shear Wave Splitting and Mantle Flow Beneath Alaska. *Journal of Geophysical Research: Solid Earth*, *125*(4). https://doi.org/10.1029/2019JB018329

Miller, M. S., O'Driscoll, L. J., Porritt, R. W., & Roeske, S. M. (2018). Multiscale crustal architecture of Alaska inferred from P receiver functions. *Lithosphere*, *10*(2), 267–278. https://doi.org/10.1130/L701.1

Miller, M. S., & Moresi, L. (2018). Mapping the Alaskan Moho. *Seismological Research Letters*, *89*(6), 2430–2436. https://doi.org/10.1785/0220180222

Moyen, J.-F. (2009). High Sr/Y and La/Yb ratios: The meaning of the "adakitic signature." *Lithos*, *112*(3–4), 556–574. https://doi.org/10.1016/j.lithos.2009.04.001

Nayak, A., Eberhart-Phillips, D., Ruppert, N. A., Fang, H., Moore, M. M., Tape, C., et al. (2020). 3D Seismic Velocity Models for Alaska from Joint Tomographic Inversion of Body-Wave and Surface-Wave Data. *Seismological Research Letters*, *91*(6), 3106–3119. https://doi.org/10.1785/0220200214

Nishimura, K., Uehara, S., & Mizoguchi, K. (2019). An Alternative Origin of High Vp/Vs Anomalies in Slow Slip Regions: Experimental Constraints From the Elastic Wave Velocity Evolution of Highly Fractured Rock. *Journal of Geophysical Research: Solid Earth*, *124*(5), 5045–5059. https://doi.org/10.1029/2018JB016929

Nye, C. J. (1983). Petrology and geochemistry of Okmok and Wrangell volcanoes, Alaska. Ph.D., dissertation, University of California Santa Cruz.

O'Driscoll, L. J., & Miller, M. S. (2015). Lithospheric discontinuity structure in Alaska, thickness variations determined by Sp receiver functions. *Tectonics*, *34*(4), 694–714. https://doi.org/10.1002/2014TC003669

Ohta, Y., Freymueller, J., Hreinsdottir, S., & Suito, H. (2006). A large slow slip event and the depth of the seismogenic zone in the south central Alaska subduction zone. *Earth and Planetary Science Letters*, *247*(1–2), 108–116. https://doi.org/10.1016/j.epsl.2006.05.013

Page, R. A., Stephens, C. D., & Lahr, J. C. (1989). Seismicity of the Wrangell and Aleutian Wadati-Benioff Zones and the North American Plate along the Trans-Alaska Crustal Transect, Chugach Mountains and Copper River Basin, southern Alaska. *Journal of Geophysical Research: Solid Earth*, *94*(B11), 16059–16082. https://doi.org/10.1029/JB094iB11p16059

Park, S., & Ishii, M. (2018). Near-surface compressional and shear wave speeds constrained by body-wave polarization analysis. *Geophysical Journal International*, *213*(3), 1559–1571. https://doi.org/10.1093/gji/ggy072

Park, S., Tsai, V. C., & Ishii, M. (2019). Frequency-Dependent P Wave Polarization and Its Subwavelength Near-Surface Depth Sensitivity. *Geophysical Research Letters*, *46*(24), 14377–14384. https://doi.org/10.1029/2019GL084892

Peacock, S. M., Christensen, N. I., Bostock, M. G., & Audet, P. (2011). High pore pressures and porosity at 35 km depth in the Cascadia subduction zone. *Geology*, *39*(5), 471–474. https://doi.org/10.1130/G31649.1

Pearce, F. D., Rondenay, S., Sachpazi, M., Charalampakis, M., & Royden, L. H. (2012). Seismic investigation of the transition from continental to oceanic subduction along the western Hellenic Subduction Zone. *Journal of Geophysical Research: Solid Earth*, *117*(B7), n/a-n/a. https://doi.org/10.1029/2011JB009023

Peterson, C. L., & Christensen, D. H. (2009). Possible relationship between nonvolcanic tremor and the 1998-2001 slow slip event, south central Alaska, *Journal of Geophysical Research: Solid Earth, 114,* B06302, https://doi.org/10.1029/2008JB006096

Preece, S. J., & Hart, W. K. (2004). Geochemical variations in the <5 Ma Wrangell Volcanic Field, Alaska: implications for the magmatic and tectonic development of a complex continental arc system. *Tectonophysics*, *392*(1–4), 165–191. https://doi.org/10.1016/j.tecto.2004.04.011

Ratchkovski, N.A. & Hansen, R.A. (2002). New Evidence for Segmentation of the Alaska Subduction Zone. *Bulletin of the Seismological Society of America 92*, 1754–1765. https://doi.org/10.1785/0120000269

Richter, D. H., Smith, J. G., Lanphere, M. A., Dalrymple, G. B., Reed, B. L., & Shew, N. (1990). Age and progression of volcanism, Wrangell volcanic field, Alaska. *Bulletin of Volcanology*, *53*(1), 29–44. https://doi.org/10.1007/BF00680318

Rondenay, S., Bostock, M. G., & Shragge, J. (2001). Multiparameter two-dimensional inversion of scattered teleseismic body waves 3. Application to the Cascadia 1993 data set. *Journal of Geophysical Research: Solid Earth*, *106*(B12), 30795–30807. https://doi.org/10.1029/2000JB000039

Rondenay, Stéphane. (2009). Upper Mantle Imaging with Array Recordings of Converted and Scattered Teleseismic Waves. *Surveys in Geophysics*, *30*(4–5), 377–405. https://doi.org/10.1007/s10712-009-9071-5

Rondenay, Stéphane, Abers, G. A., & van Keken, P. E. (2008). Seismic imaging of subduction zone metamorphism. *Geology*, *36*(4), 275. https://doi.org/10.1130/G24112A.1

Rondenay, Stéphane, Montési, L. G. J., & Abers, G. A. (2010). New geophysical insight into the origin of the Denali volcanic gap: Denali volcanic gap. *Geophysical Journal International*, *182*(2), 613–630. https://doi.org/10.1111/j.1365-246X.2010.04659.x

Rossi, G., Abers, G. A., Rondenay, S., & Christensen, D. H. (2006). Unusual mantle Poisson's ratio, subduction, and crustal structure in central Alaska. *Journal of Geophysical Research*, *111*(B9), B09311. https://doi.org/10.1029/2005JB003956

Ruff, L., & Kanamori, H. (1983). The rupture process and asperity distribution of three great earthquakes from long-period diffracted P-waves, *Phys. Earth Planet. Inter.*, *31*, 202–230

Ruppert, N. A., & West, M. E. (2020). The Impact of USArray on Earthquake Monitoring in Alaska. *Seismological Research Letters*, *91*(2A), 601–610. https://doi.org/10.1785/0220190227

Sheehan, A. F., Abers, G. A., Jones, C. H., & Lerner-Lam, A. L. (1995). Crustal thickness variations across the Colorado Rocky Mountains from teleseismic receiver functions. *Journal of Geophysical Research: Solid Earth*, *100*(B10), 20391–20404. https://doi.org/10.1029/95JB01966

Shellenbaum, D. P., L. S. Gregersen, and P. R. Delaney (2010). Top Mesozoic unconformity depth map of the Cook Inlet basin, Alaska, Rept. Investig. 2010-2, Alaska Division of Geological and Geophysical Surveys, Fairbanks, Alaska.

Shennan, I., Bruhn, R., & Plafker, G. (2009). Multi-segment earthquakes and tsunami potential of the Aleutian megathrust. *Quaternary Science Reviews*, *28*(1–2), 7–13. https://doi.org/10.1016/j.quascirev.2008.09.016

Soto Castaneda, R.A., G.A. Abers, Z. Eilon and D.H. Christensen (2021), Teleseismic attenuation, temperature, and melt of the upper mantle in the Alaska subduction zone, *J. Geophys. Res.126*, https://doi.org/10.1029/2021JB021653

Stephens, C. D., Fogelman, K. A., Lahr, J. C., & Page, R. A. (1984). Wrangell Benioff zone southern Alaska, *Geology*, *12*, 373–376.

Tao, J., Dai, L., Lou, D., Li, Z.-H., Zhou, S., Liu, Z., et al. (2020). Accretion of oceanic plateaus at continental margins: Numerical modeling. *Gondwana Research, 81*, 390–402. https://doi.org/10.1016/j.gr.2019.11.015

Tetreault, J. L., & Buiter, S. J. H. (2012). Geodynamic models of terrane accretion: Testing the fate of island arcs, oceanic plateaus, and continental fragments in subduction zones. *Journal of Geophysical Research: Solid Earth*, *117*(B8), n/a-n/a. https://doi.org/10.1029/2012JB009316

Thorkelson, D. J. (1996). Subduction of diverging plates and the principles of slab window formation. *Tectonophysics*, *255*(1–2), 47–63. https://doi.org/10.1016/0040-1951(95)00106-9

Thorkelson, D. J., & Breitsprecher, K. (2005). Partial melting of slab window margins: genesis of adakitic and non-adakitic magmas. *Lithos*, *79*(1–2), 25–41. https://doi.org/10.1016/j.lithos.2004.04.049

van Hunen, J., van den Berg, A. P., & Vlaar, N. J. (2002). On the role of subducting oceanic plateaus in the development of shallow flat subduction, *Tectonophysics*, *352*, 317–333.

Veenstra, E., Christensen, D. H., Abers, G. A., & Ferris, A. (2006). Crustal thickness variation in south-central Alaska. *Geology*, *34*(9), 781. https://doi.org/10.1130/G22615.1

Venereau, C. M. A., Martin-Short, R., Bastow, I. D., Allen, R. M., & Kounoudis, R. (2019). The Role of Variable Slab Dip in Driving Mantle Flow at the Eastern Edge of the Alaskan Subduction Margin: Insights From Shear-Wave Splitting. *Geochemistry, Geophysics, Geosystems*, *20*, 2433–2448. https://doi.org/10.1029/2018GC008170

Ward, K. M., & Lin, F. (2018). Lithospheric Structure Across the Alaskan Cordillera From the Joint Inversion of Surface Waves and Receiver Functions. *Journal of Geophysical Research: Solid Earth*, *123*(10), 8780–8797. https://doi.org/10.1029/2018JB015967

Wech, A. G. (2016). Extending Alaska's plate boundary: Tectonic tremor generated by Yakutat subduction. *Geology*, *44*(7), 587–590. https://doi.org/10.1130/G37817.1

Worthington, L. L., Van Avendonk, H. J. A., Gulick, S. P. S., Christeson, G. L., & Pavlis, T. L. (2012). Crustal structure of the Yakutat terrane and the evolution of subduction and collision in southern Alaska. *Journal of Geophysical Research: Solid Earth*, *117*(B1), n/a-n/a. https://doi.org/10.1029/2011JB008493

Zandt, G., & Humphreys, E. (2008). Toroidal mantle flow through the western U.S. slab window. *Geology*, *36*(4), 295. https://doi.org/10.1130/G24611A.1

Zhu, L., & Kanamori, H. (2000). Moho depth variation in southern California from teleseismic receiver functions. *Journal of Geophysical Research: Solid Earth*, *105*(B2), 2969–2980. https://doi.org/10.1029/1999JB900322

CHAPTER 4

PLATE INTERFACE LOW-VELOCITY ZONE Vp/Vs AND THICKNESS FROM RECEIVER FUNCTIONS: A TEST OF THE HIGH PORE-FLUID PRESSURE HYPOTHESIS

Co-authors: G. A. Abers

4.1 Abstract

The interface between subducting and overriding plates sometimes exhibits low seismic velocities within a thin layer. Many analyses of this interface low-velocity zone (LVZ) utilize receiver functions (RFs) which sample sharp seismic velocity gradients or discontinuities. Estimates of thickness and *Vp*/*Vs* within the layer depend primarily on the time separation between RF phases from the top and bottom of the layer. Some of these analyses estimate that the *Vp/Vs* exceeds 2.5, corresponding to Poisson's ratios exceeding 0.4. Such high *Vp*/*Vs* does not match common lithologies so is interpreted to require high pore-fluid pressures within the LVZ. Other estimates of *Vp*/*Vs*, e.g., from tomography or from RF waveform fitting, are lower (≤2) and allow the possibility that the plate interface LVL is dominantly metasediment with much less porosity. The low-frequency nature of teleseisms may bias typical RF analyses of the LVZ that utilize the upgoing *P*-to-*S* scattered wavefield. Using array-based deconvolution, we measure the receiver-side, surface-reflected and back-scattered *P*-to-*P* wavefield and apply it in a new inversion method for LVZ *Vp*/*Vs* with its *P*-to-*S* surface-reflected and back-scattered analog. Using the differential timing of surface-reflected RF phases in southcentral Alaska, our investigation shows that the average LVZ thickness is 3.6 km and the majority of *Vp/Vs* estimates are <2 with our new method. When the traditional method with the upgoing *P*-to-*S* scattered

phases is applied, the estimate of thickness increases by an average of 1 km, and *Vp*/*Vs* >2.5 in most cases. These results indicate that evidence for high pore-fluid pressures may instead be an artifact of using band-limited signals or RF phase interference. These results suggest that the entrained metasediment and tectonically eroded material along plate interface control megathrust earthquake and slow-slip physics, with free fluid playing a secondary role.

4.2 Introduction

A spectrum of fault slip behavior has been detected at the subduction zone plate interface, with an aseismic, creeping up-dip region near the trench, an intervening locked zone where megathrust earthquakes occur, and a down-dip region where slow slip and tremor occurs (e.g., Ide et al., 2007; Beroza and Ide, 2009; Gomberg et al., 2010; Peng and Gomberg, 2014). Elevated pore fluid pressure has been hypothesized as a main control on fault slip behavior across the spectrum of fault slip behaviors (e.g., Bangs et al., 1999, 2004, 2009, 2015; Audet et al., 2009; Saffer & Tobin, 2011; Peacock et al., 2011; Moreno et al., 2014). Seismic imaging of subduction zones shows a landward-dipping low-velocity zone (LVZ) at the top of subducting slabs (e.g., Rondenay et al., 2001; Nicholson et al., 2005; Abers et al., 2009; Kim et al., 2014; Guo et al., 2021; Mann et al., *subm.*). It has been interpreted as a fluid-rich shear zone with near-lithostatic pore-fluid pressure that incorporates the upper oceanic crust and whatever material is entrained along the plate interface (e.g., Audet et al., 2009; Peacock et al., 2011; Audet and Schwartz, 2013; Audet and Bürgmann, 2014; Gosselin et al., 2018). However, the fault slip behavior down-dip of the locked zone has also been interpreted to result from distributed weak interface shear zones composed of mixed lithologies, including metasediment (e.g., Abers et al., 2009; Delph et al., 2018; Tewksbury-Christle & Behr, 2021; Miller et al., *in press*) or creep in hydrous metabasalts of the oceanic crust (e.g., Tulley et al., 2020). Additionally, experimental results show that slow-

slip events can be generated under dry conditions and that result from common frictional mechanics (e.g., Carpenter et al., 2016; Leeman et al., 2016, 2018; Wu & McLaskey, 2019).

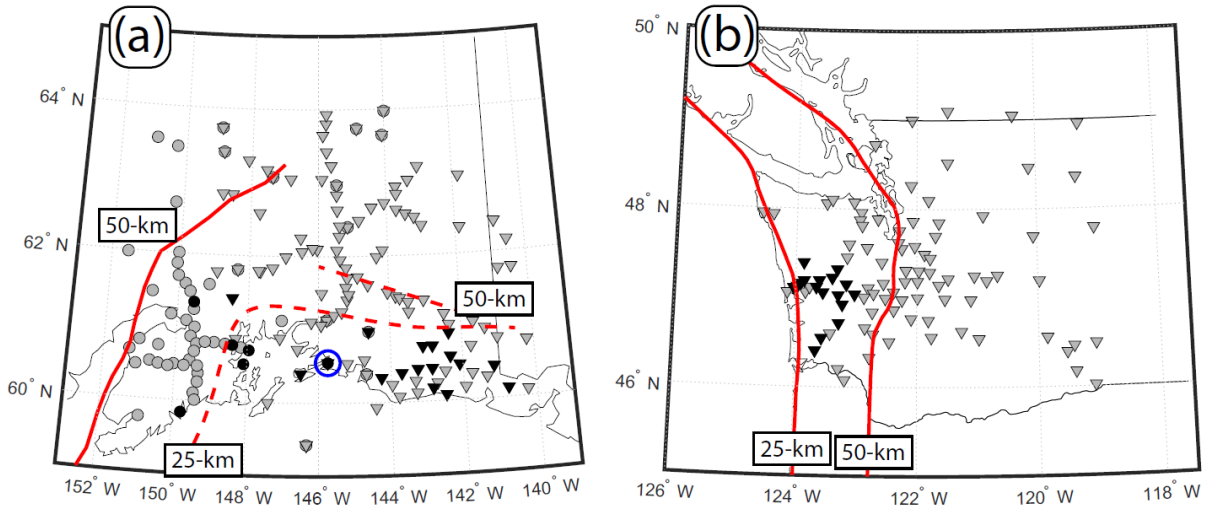

Figure 4.1. Location of seismometers. (**a**) Alaska stations for both arrays (WVLF and MOOS). Circles are stations deployed during MOOS experiment (2006-2009) and inverted triangles are stations deployed during WVLF deployment (2016-2018). Blue circle is station EYAK. Dashed red lines are plate interface contours from Chapter 3. Red line is Wadati-Benioff Zone contour from Ratchkovski and Hansen, 2002). (**b**) Cascadia stations that were deployed during the CAFE experiment (2006-2008). All stations shown were used in the array-based deconvolution procedure to generate the RFs. Black symbols denote stations with RFs that were used in the LVZ analysis here. Red lines are 25-km and 50-km Wadati-Benioff Zone contours (McCrory et al., 2012).

The key observation supporting high pore-fluid pressure down-dip of the locked region in subduction zones are estimates of high Poisson's ratios (derived from *Vp*/*Vs*, the ratio of *P*- to *S*-wave velocities) for the LVZ from teleseismic *P* wave receiver function (RF) inversions (e.g., Audet et al., 2009; Peacock et al., 2011; Hansen et al., 2012; Audet and Schwartz, 2013; Audet and Bürgmann, 2014). These observations were made by jointly analyzing the signals from the top and bottom of the LVZ from upgoing and surface-reflected *P*-to-*S* mode conversions in RFs (from earthquakes with Mw > 5.5, at 30°-95° great circle distances). Such high Poisson's ratios of >0.37 correspond to Vp/Vs > 2.2, values higher than any found in naturally occurring dry rocks from lithology alone (Christensen, 1996; Abers & Hacker, 2016). The common explanation

is that they result from high porosities due to near-lithostatic pore-fluid pressures, which drastically reduces Vs compared to Vp (Peacock et al., 2011).

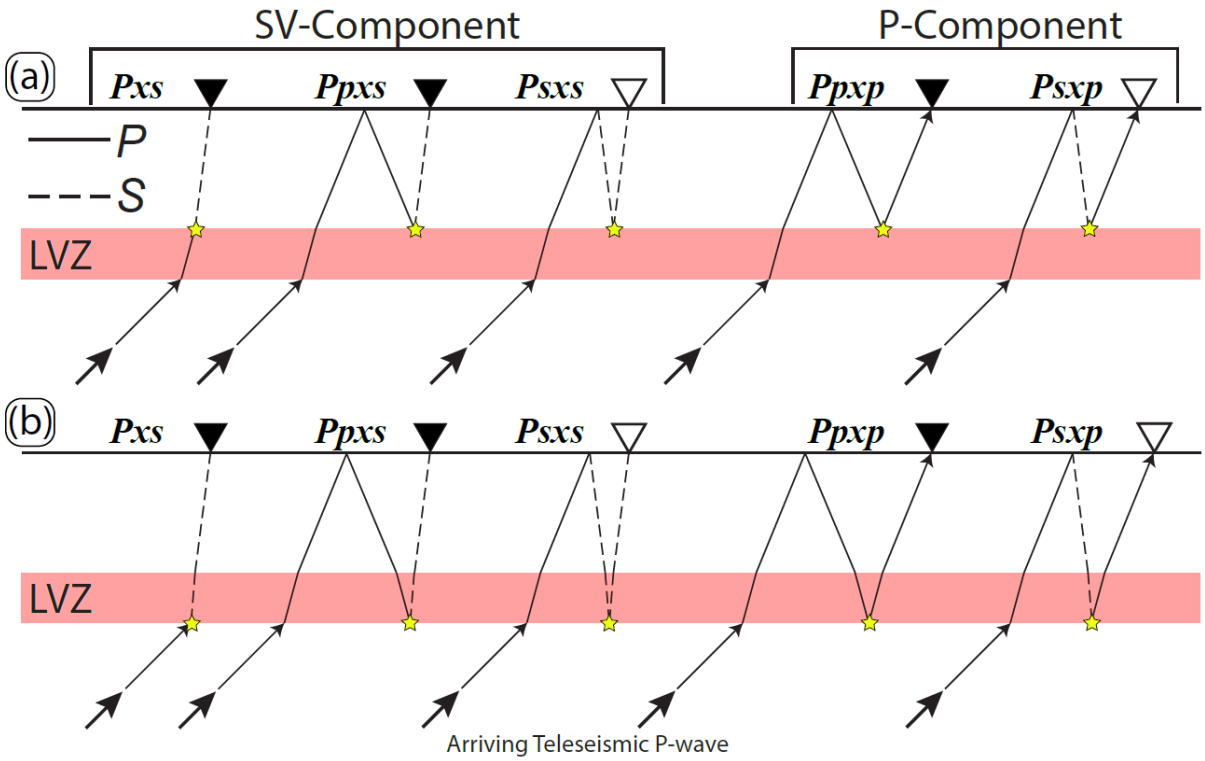

Figure 4.2: Depiction of RF modes discussed in this study. (a) Ray paths for phases from the top of the LVZ. (b) Ray paths for phases from the bottom of the LVZ. Yellow stars emphasize conversion or reflection points associated with the RF phase time. Filled inverted triangles at the surface denote RF modes that were used in the analysis here.

This study uses a new method to test the high pore-fluid pressure hypothesis using RF waveforms from both southcentral Alaska and northern Cascadia (Figure 4.1). The advantage of analyzing the LVZ in southcentral Alaska is that the subducting crust is >11-km thick (e.g., Christeson et al., 2010; Worthington et al., 2012; Chapter 3), and the RF phases from the bottom of the LVZ are separated from the subducting crust Moho. Investigations using RFs from *P* waves typically involve an analysis of *P*-to-*S* scattered phases with amplitudes that have a first order effect on the RFs (RF "modes") (Figure 4.2). Most other RF energy is from multiply surface-reflected phases and peg-leg multiples with relatively small amplitude. The upgoing *P*-to-*S* RF

mode arrives earliest, while surface-reflected RF modes arrive later and have greater volume resolution (e.g., Rondenay, 2009). We utilized an additional RF mode – the surface-reflected (back-scattered) teleseismic *P*-wave phase. An analysis of the time separation between RF phases from the top and bottom of the LVZ using only higher resolution surface-reflected *P*-to-*S* and *P*-to-*P* modes show that the Vp/Vs of the LVZ is <~2. These measurements are biased to high Vp/Vs (>2.2) with the inclusion of the upgoing *P*-to-*S* mode because in many cases the frequency content is too low to resolve the true LVZ thickness. The Vp/Vs results from our analysis do not require high porosity and the existence of near-lithostatic pore-fluid pressures within the LVZ down-dip of the locked region. We suggest instead that the fault slip behavior down-dip of the locked region is controlled primarily by the frictional properties of material entrained along the plate interface, with pore fluid pressure playing a secondary role.

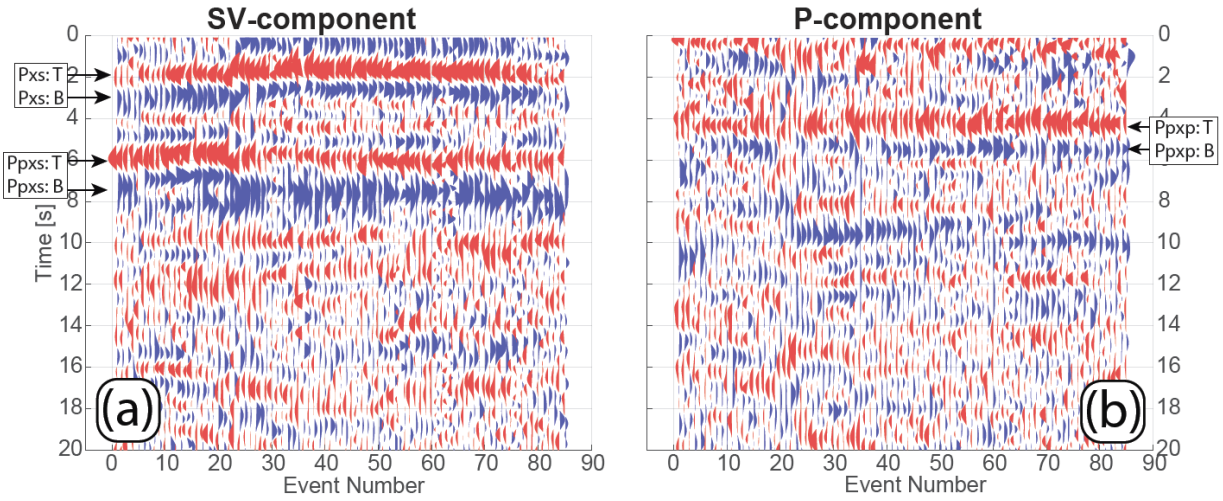

Figure 4.3: RFs from station EYAK in Alaska. (a) SV-component RFs (b) P-component RFs. T - top of LVZ, B - bottom of LVZ.

4.3 Data and Preprocessing

P waves from teleseismic earthquakes were used to generate RFs using an array-based deconvolution procedure (Bostock & Rondenay, 1999), as implemented in Chapter 3 (e.g., Figure

4.3). In Alaska, this study used the RFs from the Multidisciplinary Observations of Onshore Subduction (MOOS) experiment (Li et al., 2013) and the Wrangell Volcanism and Lithospheric Fate (WVLF) experiment (https://doi.org/10.7914/SN/YG_2016; Soto Castañeda et al., 2021) from Chapter 3 (Figure 4.1a). In Cascadia, we focused on teleseismic earthquakes around the period that the Cascadia Arrays For Earthscope (CAFE) experiment was deployed across central Washington, USA (Abers et al., 2009). The preprocessing steps for the data are described elsewhere (Chapter 3). The site-specific near-surface velocity was estimated and used to separate the *P* and *SV* wavefields, as described in Chapter 3. We re-analyzed the P coda from 513 teleseismic earthquakes on the CAFE array stations, along with 51 additional broadband stations in the region (Figure 4.1b). We selected 197 events that generated visibly coherent RFs across the array that were not dominated by monochromatic ringing or anomalously high amplitudes, following the same quality control criteria used on the Alaska data (Chapter 3).

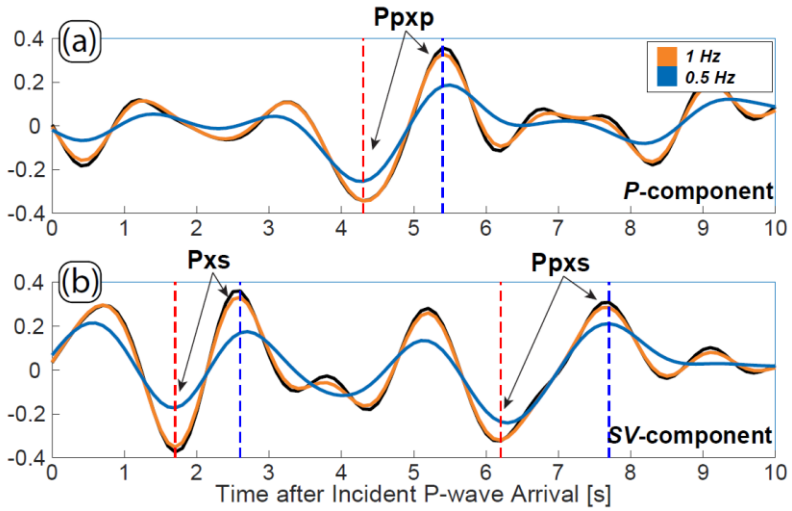

Figure 4.4: Example RF from EYAK for one event with back-azimuth of 270 degrees and ray parameter of 0.0461 s/km. (a) P-component RF. Ppxp phases from the top and bottom of the LVZ are referred to by the arrows. (b) SV-component RF. Red and blue dashed lines are timing of LVZ top and bottom, respectively, in unfiltered RF for each RF mode. Colors correspond to low-pass cutoff frequency used in second order Butterworth filter. Black lines are RFs without additional filtering after deconvolution (**Section 4.4**).

For the Cascadia stations, the inversion was applied separately on RFs from events within back-azimuthal bins of 75°-175°, 200°-260°, and 270°-340°, resulting in an average of 45, 32, and 60 RFs per station, respectively. For the Alaska stations, the only back-azimuthal range that had >20 RFs at most stations was between 200°-300°, resulting in an average of 38 RFs per station for both time periods.

4.4 Frequency Content of RFs

The *P* wave arrival data was filtered between 0.03 Hz and 3 Hz before deconvolution. Using a higher low-pass cutoff frequency may not significantly affect the RFs because teleseismic *P* waves are effectively low-pass filtered by mantle attenuation (e.g., Cormier, 1982). The deconvolution procedure estimates a "water level" to fill in spectral holes in the source before deconvolution, which effectively applies an additional filter to each waveform (e.g., Clayton & Wiggins, 1976). Even though each incident *P* wave has a slightly different frequency content that depends on its source properties and depth, the deconvolution procedure should equalize these effects among events. All RFs were analyzed after bandpass filtering between 0.05 Hz and 1 Hz using a second order Butterworth filter. When filtering these signals, care must be taken to not filter at periods less than twice the time separation of the desired RF phases (Audet et al., 2009). For example, a low-pass cutoff of 1 Hz would bias RF phases separated by less than 0.5 seconds. The effective frequency content of these signals after deconvolution is demonstrated by one RF example from station EYAK in Alaska (red circle in Figure 4.1). Filtering using a low-pass cutoff frequency of 1 Hz does not significantly affect the RF waveforms (Figure 4.4). However, filtering using low-pass cutoff frequencies <1 Hz begins to affect the spacing of signals from Pxs but not from the other phases (Figure 4.4). So, a low-pass cutoff frequency of 1 Hz was used for the inversions.

4.5 Inversion for Plate Interface LVZ Properties

The differential arrival times of RF phases from delimiting boundaries of a layer in the Earth are dependent on the thickness of that layer and the *Vp* and *Vs* of the material within it (Zhu & Kanamori, 2000; Audet et al., 2009). The differential arrival times in each RF mode for a flat-lying LVZ can be calculated as follows:

$$\delta t_{Pxs} = \frac{Z}{V_P}[Rcos(j_S) - \cos(i_P)] \quad (1)$$

$$\delta t_{Ppxs} = \frac{Z}{V_P}[Rcos(j_S) + \cos(i_P)] \quad (2)$$

$$\delta t_{Ppxp} = \frac{2Z}{V_P}\cos(i_P) \quad (3)$$

where Z is the thickness of the layer, V_P is the *P*-wave velocity within the layer, R is *Vp*/*Vs* within the layer, and j_S and i_P are the incidence angles (measured from vertical) of the traveling *S* or *P* wave, respectively. The angles are determined using Snell's law and the ray parameter of the incident *P* wave. These equations show that the RF modes are all dependent on H/V_P, and that Pxs and Ppxs are also dependent on *Vp*/*Vs* but in different ways. Consequently, a combination of these RF modes together at a given station would yield an estimated H/V_P for a layer and the average *Vp/Vs*, or R within that layer (e.g., Zhu & Kanamori, 2000; Audet et al., 2009). This is possible because the travel times for rays above the LVZ are approximately identical for phases from the top and bottom of the LVZ in each RF mode (Figure 4.2) – the time separation of the LVZ phases in a given RF mode does not depend on velocities above or below the LVZ. Some peg-leg multiples occur, but their amplitudes are typically small compared to the first order converted phases (Figure 4.4). Additionally, RF phases from the Moho of the subducting plate may interfere with LVZ phases (see **Section 4.7.3**), but this is not a significant issue in Alaska where the subducting crust is >11 km thick and the LVZ RF phases are sufficiently separated

from the subducting crust Moho. Overall, analyzing the time separation of the phases that correspond to the top and bottom of the LVZ in multiple RF modes, at a range of LVZ depths, eliminates the need to constrain the velocity model above the LVZ (e.g., Audet et al., 2009).

We focused our analysis on three combinations of RF modes: Ppxs and Ppxp ("Case 1"), Pxs and Ppxs ("Case 2"), and Pxs, Ppxs, and Ppxp ("Case 3"). It is clear that δt_{Ppxs} and δt_{Ppxp} have different sensitivity to both R and Z (Equations 2 and 3). In the limiting case of vertical incidence (ignoring the fact that no mode conversions occur in this case), the sensitivity of R to the time separation of LVZ phases for Case 1 and Case 2 are given by the following equations:

$$\text{Case 1: } R \approx 2\frac{\delta t_{Ppxs}}{\delta t_{Ppxp}} - 1 \qquad (4)$$

$$\text{Case 2: } R \approx \frac{\delta t_{Ppxs} + \delta t_{Pxs}}{\delta t_{Ppxs} - \delta t_{Pxs}} \qquad (5)$$

The dependence on RF phase time separation for R in Case 3 is more complicated because it depends on a combination of three RF modes and depends on their relative weighting. In any case, analyzing the time separation of LVZ phases in multiple RF modes could yield estimates of R.

In each RF mode, the LVZ manifests as one negative phase and one positive phase from sharp gradients in velocity at the top and bottom of the layer (Figures 4.3-4.5). LVZ phases are not clear for every RF mode, at every station. This is due to interference between RF modes for LVZ phases (see **Section 4.6.1**) and/or from other sharp velocity gradients and discontinuities, such as the subducting crust Moho (see **Section 4.7.3**), reverberations within sedimentary basins, and/or intracrustal discontinuities. The RF phases may have additional complications due to surface topography and/or surface geology variations at the bounce point for surface-reflected phases (e.g., Rondenay et al., 2005). Previous RF imaging using 3D CCP stacking in Alaska

(Chapter 3), as well as 2D GRT migration in both Alaska (e.g., Kim et al., 2014; Chapter 3) and Cascadia (e.g., Rondenay et al., 2001; Nicholson et al., 2005; Abers et al., 2009; McGary et al., 2012), have shown low velocities along the plate interface and determined the depth and orientation of the top of the plate interface LVZ.

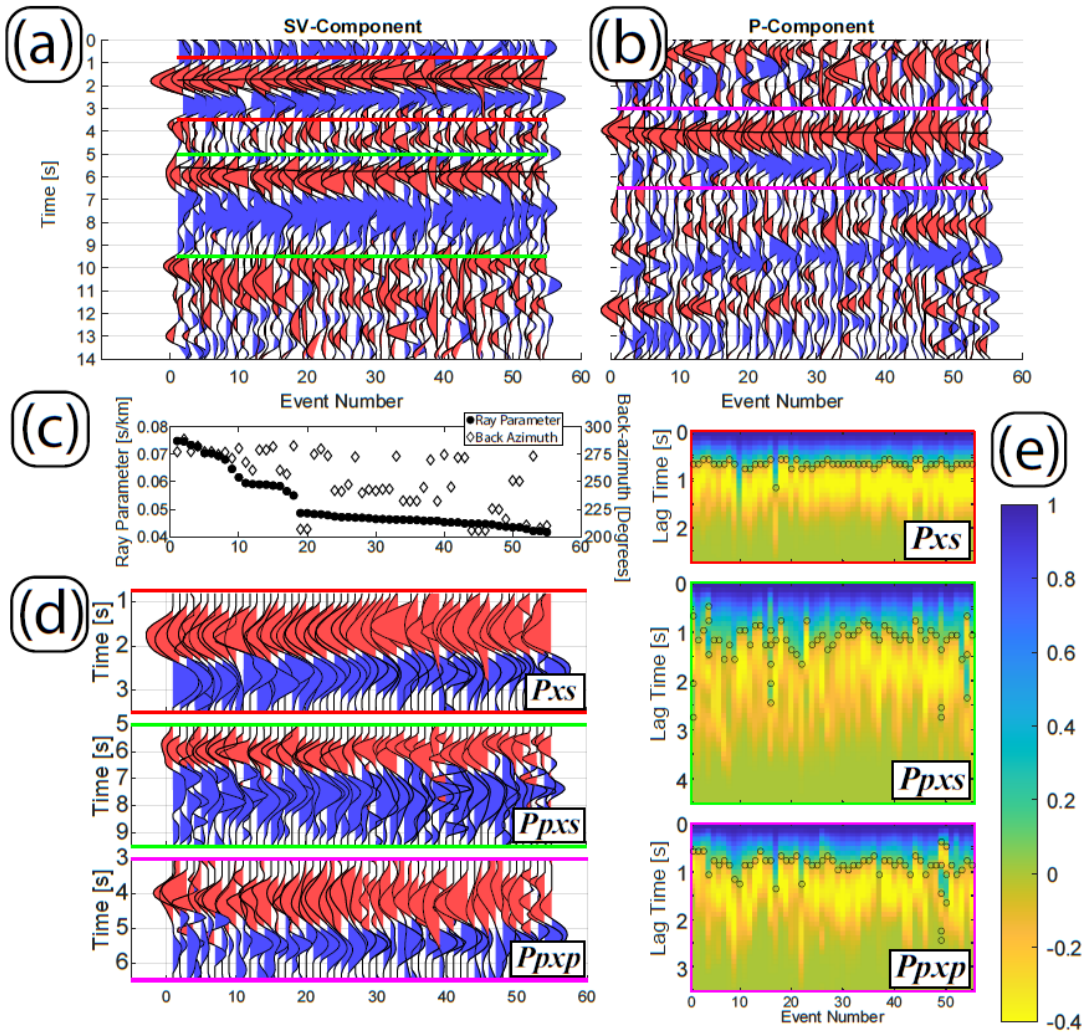

Figure 4.5: Extraction steps for each RF mode at station EYAK in Alaska. (a) SV-component RFs. Red lines delineate selection of Pxs phases. Green lines delineate selection of Ppxs phases. (b) P-component RFs. Magenta lines delineate Ppxp phases. (c) Back-azimuth and ray parameter of RFs. (d) Extracted waveforms from between phase delineating lines in (a) and (b). Note that all blue (positive) phases in the first 1/4 and red (negative) phases in the last 1/4 of the extracted waveform have been zeroed out. (e) Autocorrelation waveforms of extracted waveforms in (d). Circles are all zero-crossing for each waveform.

These previous imaging studies are used to estimate arrival times for the LVZ top in each RF mode (black lines in Figure 4.5a-b). Using these estimated LVZ top arrival times, the nearest consistent (i.e., across all RFs at the station) negative phase is selected as the LVZ top and the next proceeding consistent positive phase is selected as the LVZ bottom (Figure 4.5). The LVZ inversion begins by identifying and fixing analysis windows around the LVZ phases for the Ppxs and Ppxp LVZ phases (Figure 4.5a-b). If all four Ppxs and Ppxp LVZ phases are not visible, the station is skipped. Additionally, if the RFs exhibit broad phases (>~1 s in width for each individual phase), the station is skipped.

To reduce the influence of phases immediately before the LVZ top and after the LVZ bottom that are included in the analysis windows, all oppositely polarized phases (relative to the LVZ top and bottom phases) in the first and final ¼ of the extracted waveforms were set to zero (Figure 4.5d). In doing so, the extracted RF waveforms for each RF mode ideally start at the beginning of the corresponding LVL top RF phase and end after the corresponding LVL bottom RF phase.

Psxs (Figure 4.2) was not analyzed because it is usually less clear in real data, and its greater time separation (e.g., 4.6 s for a LVZ with $R = 2$ and $Z = 3$, compared to 1.4 s for Pxs, 1.8 s for Ppxp, or 3.2 s for Ppxs) encompasses multiple phase cycles in the RFs and makes LVZ bottom phase identification in Psxs ambiguous.

For each RF mode in the analysis, the extracted waveform is autocorrelated to represent the time separation between the top and bottom of the LVZ, following Audet et al. (2009) (Figure 4.5e). These autocorrelation waveforms have a positive peak at zero lag time, and a negative peak at the time separation between the RF phases from the top and bottom of the LVZ. The autocorrelation waveform is the basis for the LVZ inversion.

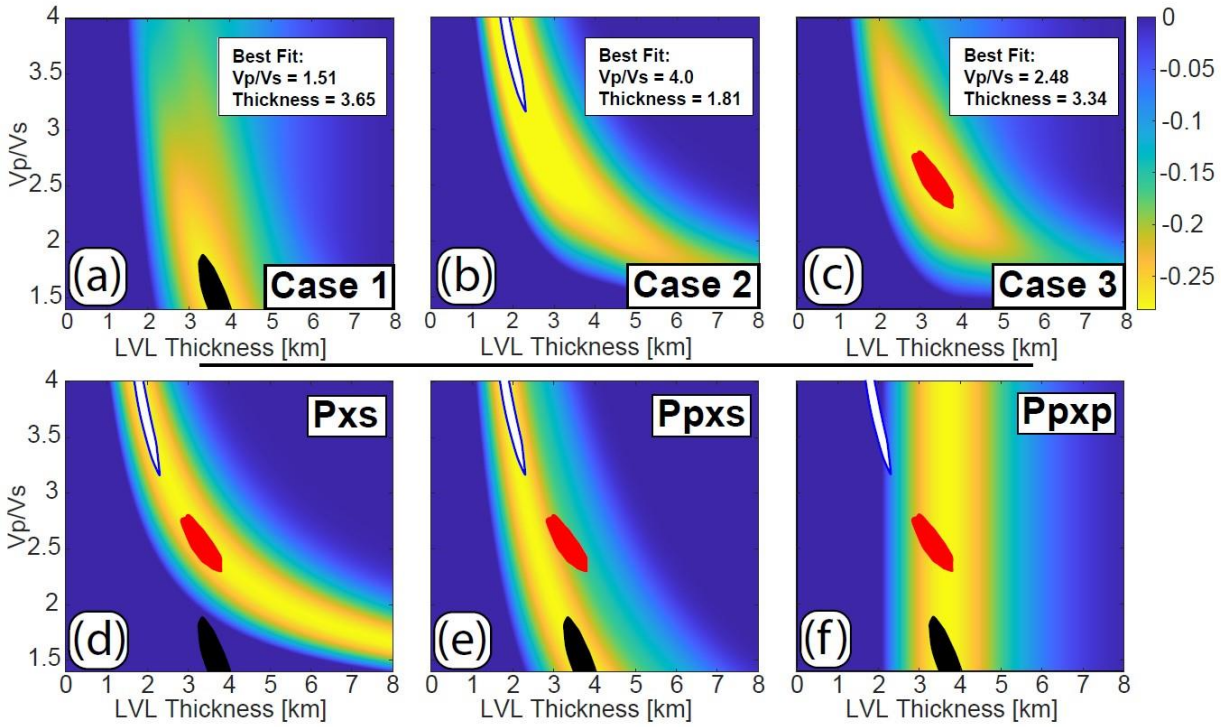

Figure 4.6: Inversion results for station EYAK in Alaska (blue circle in Figure 1a). (a) Case 1 inversion result uncertainty range, black shape. (b) Case 2 inversion result uncertainty range, white with blue line. (c) Case 3 inversion result uncertainty range, red shape. (d) Inversion result for only Pxs autocorrelation waveforms. (e) Inversion result for only Ppxs autocorrelation waveforms. (f) Inversion result for only Ppxp autocorrelation waveforms. All three Cases' uncertainty ranges are shown on each individual-mode inversion result (d)-(e). Tradeoff curves for individual-mode inversion results are clearly shown by yellow swath of background color.

For the inversion, a range of R is searched from 1.4 (Poisson's ratio of ~0) to 4 (Poisson's ratio of 0.47). For each value of R, the autocorrelation waveforms are stacked from Z = 0 km to 8 km after converting δt to Z and correcting for RF mode and ray parameter using Equations (1)-(3) (Figure 4.6a-c). *Vp* for the LVZ in the inversion is set at 5 km/s, a reasonable value for subducted metasediment (e.g., Kim et al., 2014; Miller et al., *in press*) and *Vs* is allowed to vary. However, the estimated R is only weakly dependent on the chosen *Vp* (Equations 1-3; Zandt and Ammon, 1995; Audet et al., 2009). The resulting stack from the grid search should have a minimum amplitude at the parameters corresponding to the best fit R and Z. Uncertainties for the

best fit R and Z are determined at the 95% confidence level using a Student's t-test (Rossi et al., 2006) applied to that minimum (Figure 4.6a-c). This inversion method was applied to both cases.

In each inversion Case, the autocorrelated waveforms are weighted in the inversion based on the standard deviation at the minimum of the stacked autocorrelated waveforms, following Rossi et al. (2006). If the entire range of R and Z in the grid is dominated by only one RF mode as the result of this weighting, meaning that the range of uncertainty followed only one RF mode's tradeoff curve (Figure 4.6d-e), the station is skipped.

4.6 Results

4.6.1 LVZ Synthetic Tests: RF Frequency, Volume Resolution, and Bias

The ability of RF modes to detect an LVZ without bias depends on the volume resolution of the signal, i.e., the minimum distance necessary to resolve two separate scatterers or discontinuities (e.g., Rondenay, 2009; Mackenzie et al., 2010). That distance is usually approximated as ½ the signal's wavelength for Pxs phases (e.g., Bostock, 1999) and ¼ wavelength for surface-reflected phases (e.g., Benz & Vidale, 1993; Levin et al., 2016). To show the range of LVZ models that are capable of being resolved using this method, synthetic seismograms using a ray parameter of 0.06 s/km and a velocity model of a LVZ (Vp = 5 km/s, Vs = 2.5 km/s) embedded in a half space (Vp = 6.5 km/s, Vs = 3.7 km/s) were generated using the Thomson-Haskell layer transform for both vertical and radial components (Haskell, 1962). This frequency-domain approach generates synthetic seismograms that incorporate all combinations of conversions and reverberations. The source pulse for these synthetic seismograms has a Gaussian shape, defined by the equation:

$$G(t) = \frac{4}{d\sqrt{2\pi}} \exp\left(-\frac{8(t-\mu)^2}{d^2}\right) \qquad (6)$$

where t is the time, μ is the time at the center of the pulse, and d is the "duration" of the pulse in seconds (i.e., the time from -2σ to +2σ around the center of the Gaussian). For d = 1 s, this pulse produces a signal with energy primarily at or below 1 Hz, like most teleseismic P-wave signals (see **Section 4.4**). The resulting radial and vertical components were transformed into *P* and *SV* components using the free surface transformation (Kennett, 1991).

These synthetic seismograms are directly comparable to RFs, even though they do not involve deconvolution, because the synthetic seismograms mimic the shape, frequency content, and timing of RF phases by using a single Gaussian source pulse (Equation 6) (Figure 4.7). Hence the synthetic seismograms are hereafter referred to as synthetic RFs. Once the *P* component is isolated, the source pulse at t = 0 s that represented the incident *P*-wave was removed to mimic the source-removal of the array-based deconvolution procedure (e.g., Bostock & Rondenay, 1999). This step ensures the synthetics are directly comparable with the real RFs.

In the case of a 2 km thick LVZ, synthetic RFs with energy at frequencies up to 5 Hz (d= 0.2 s, which is unrealistic but used here simply as a visual example) show clear separation in the phases from the top and bottom of the LVZ (Figure 4.7). However, band-pass filtering the same seismogram between 0.05 Hz and 0.5 Hz using the same second order Butterworth filter used in the analysis causes bias in the Pxs phases from the top and bottom of the LVZ that act to artificially increase their time separation by 0.3 s (Figure 4.7b). Each RF mode is sensitive to R in different ways (Equations 1-3), and interference of the RF phases from the top and bottom of the LVZ generates a different bias in R estimation for each RF mode (Equations 4-5). As the thickness of the LVZ or the low-pass frequency cutoff decreases, Pxs, with the worst volume resolution of the RF modes, is the first mode whose LVZ phases would interfere. This

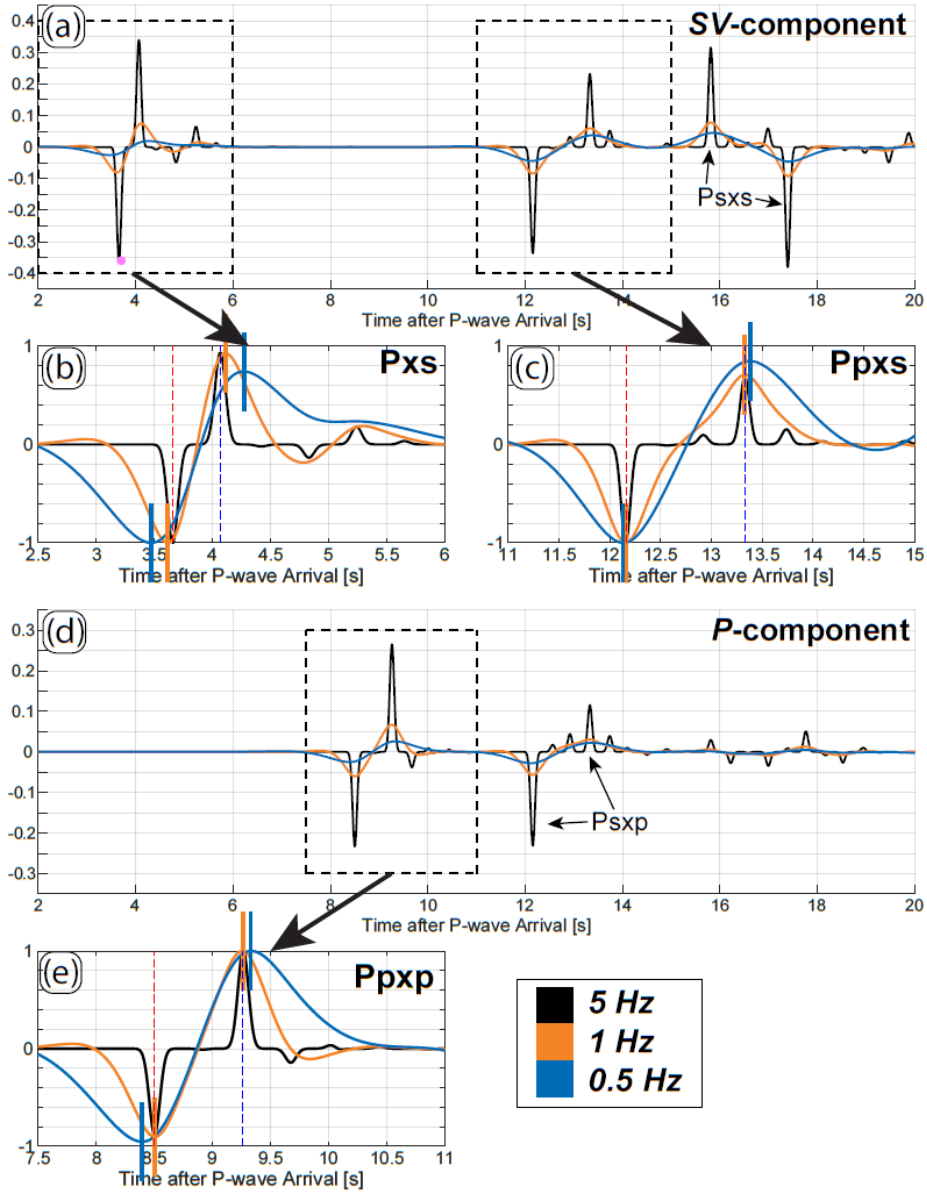

Figure 4.7: Synthetic RFs generated for a low-velocity layer embedded in a half space. Different filter frequencies highlight the influence of frequency content on bias in RF phases from the top and bottom of the LVZ. Thick black line is synthetic RF generated with a source pulse that has energy at frequencies <~5 Hz (d = 0.2, Equation 6). Other colored lines are different filtered versions of the black synthetic RF; orange line is low-pass filtered at 1 Hz, blue line is low-pass filtered at 0.5 Hz. (a) SV-component of synthetic RF. (b) SV-component extracted around Pxs LVZ phases. (c) same as (b) but for Ppxs LVZ phases. (d) P-component of synthetic RF. (e) P-component extracted around Ppxp LVZ phases. Dashed red and blue vertical lines correspond to the arrival times of RF phases from the top and bottom of the LVZ, respectively, in the ray theoretic limit. Solid vertical lines correspond to the peak or trough of the LVZ bottom or top phases, respectively, after filtering; colors correspond with their synthetic RF. Psxs and Psxp (Figure 4.2) are noted but not analyzed here.

interference increases the apparent time separation and decreases the amplitude of the phases (Figure 4.7a-b).

This interference and subsequent drop in amplitude could make the LVZ phases drop below some threshold of visibility and even disappear for a sufficiently thin layer. Additionally, if the LVZ phases in a given RF mode are comparable in amplitude to phases from other interfaces or RF modes, then interference with these other phases could erase one or more of the LVZ phases. The threshold of visibility is called the "noise level" here and is defined as the peak-to-peak amplitude required to detect these LVZ phases without erasure from interference with one another or from other RF phases. Therefore, we measure the noise level of the real RFs as twice times the mean standard deviation (1-σ) of the signal in a 70 s window *after* the arrival of

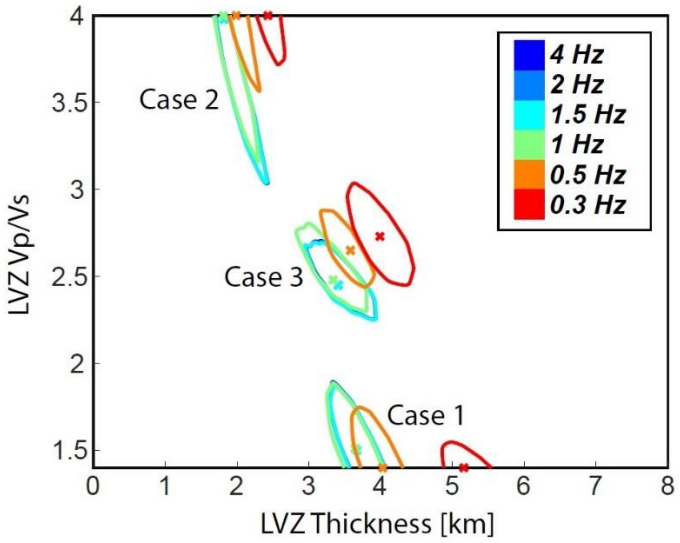

Figure 4.8: Uncertainty ranges and best results from grid search at station EYAK at different low-pass cutoff frequencies. Note that the uncertainty ranges overlap for all low-pass cutoff frequencies tested above 0.5 Hz and deviate at or below 0.5 Hz.

the incident *P* wave in all Alaska and Cascadia RFs used in the analysis, which is 0.13. Twice the standard deviation is used for the noise level to compare with the peak-to-peak amplitude of the LVZ phases. The deconvolution procedure normalizes the RFs to the deconvolved *P*

component source pulse, so 0.13 is the *SV*-component RF value relative to the peak amplitude of the *P* component source pulse. At the low-pass cutoff frequency used in the LVZ inversions here (i.e., 1 Hz), the synthetic LVZ phases (e.g., Figure 4.7) in all RF modes have peak-to-peak amplitudes greater than the noise level at $Z \geq 1$ km. At values of Z below 1 km, the peak-to-peak phase amplitudes for the top and bottom of the LVZ fall below the noise level. This result suggests that the LVZ phases should be visible for Z values down to at least 1 km.

4.6.2 Effect of Filter Frequency on RF Inversion

The volume resolution of the RF phases is dependent on the frequency content of the signals (Rondenay, 2009). We examined LVZ inversion results from one station varying low-pass cutoff frequencies to determine at which frequency the filtering begins to affect the results. At one representative station in Alaska, decreasing the low-pass cutoff frequency does not affect the results until it is <1 Hz (Figure 4.8). Compared with the 1 Hz result, filtering with low-pass cutoff frequencies greater than 1 Hz did not significantly change the inversion results where the LVZ phases are dominant and clear.

4.6.3 Synthetic Tests: Autocorrelation Inversion

Synthetic RFs using the same LVZ parameters as in **Section 4.6.1** were generated with the top of the LVZ at depths between 10 km and 30 km, in 5-km increments. This approach used a duration of 1 s for the Gaussian source pulse (d = 1 s, Equation 6). For each RF mode, the RF phases from the top and bottom of the LVZ were extracted, from 0.5 s before the arrival of the

top phase to 0.5 s after the arrival of the bottom phase. The extracted waveforms were then autocorrelated and stacked after moveout, as described in **Section 4.5**.

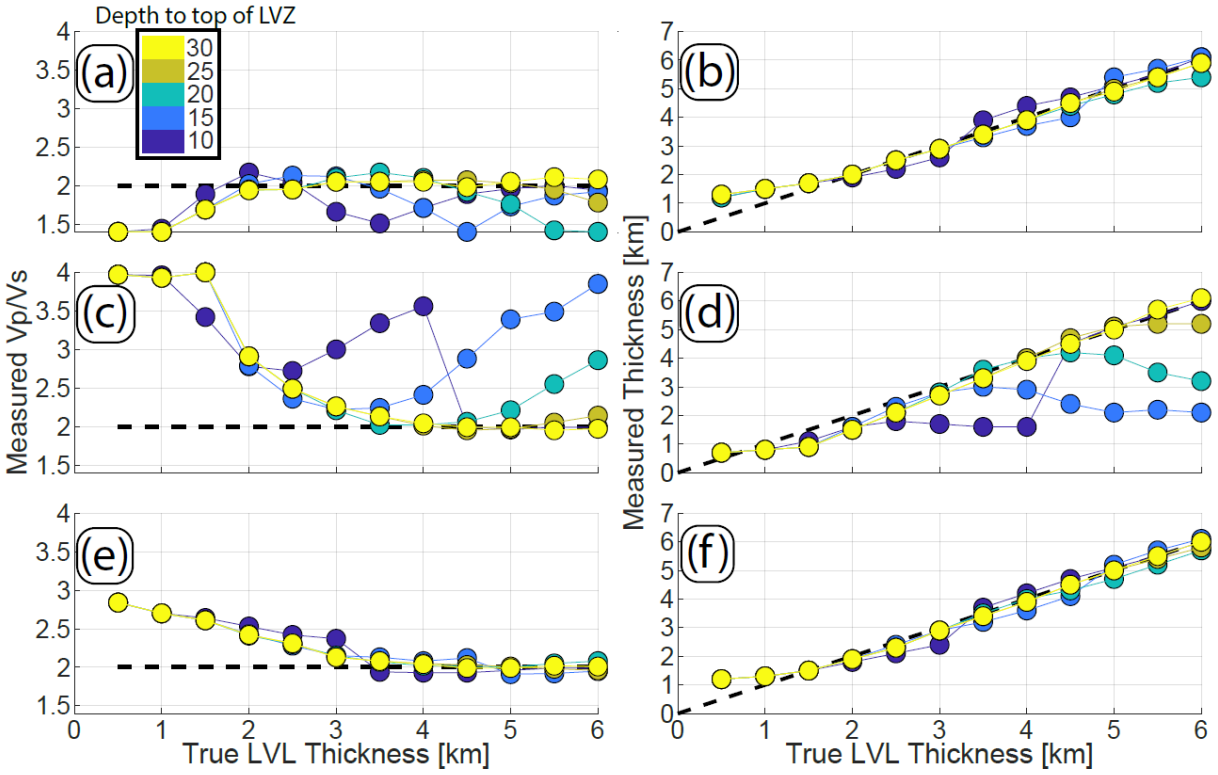

Figure 4.9: Autocorrelation inversion results from synthetic RFs for a LVZ (Vp/Vs = 2) embedded in a half space at different depths and LVZ thicknesses. Color denotes depth to top of LVZ. (a)-(b) Case 1 (Ppxs and Ppxp) inversion Vp/Vs and thickness results, respectively. (c)-(d) Case 2 (Pxs and Ppxs) inversion Vp/Vs and thickness results, respectively. (e)-(f) Case 3 (Pxs, Ppxs, and Ppxp) inversion Vp/Vs and thickness results, respectively).

Overall, the synthetic tests show that the inversion recovers LVZ properties (Figure 4.9). In these synthetic tests for a LVZ with R = 2, the maximum estimated R for Case 1 is ~2.2 and the minimum is 1.4. There is some variation in measured R at certain LVZ depths for Case 1 as the result of interference between Ppxs and Psxs. This interference occurs for thinner layers at shallower depths and for thicker layers at greater depths. When the LVZ is $\leq$ 2.5 km thick, estimated R is biased down, eventually reaching 1.4 at Z = ~1 km. This is because the Ppxp phases interfere and are biased to a greater time separation. This effect can be shown by

examining the sensitivity of R to changes in δt_{Ppxs} and δt_{Ppxp} (Equation 4): if δt_{Ppxp} is biased to greater time separation then R will be underestimated.

There is more variation in measured R for Case 2 when compared with Case 1 (Figure 4.9). This is because of interference between the Ppxs and Psxs LVZ phases at different depths, a phenomenon that occurs at shallower depths for thicker layers. For this case, if the LVZ is < 3.5 km thick it will be biased to higher values of R due to its sensitivity to changes in δt_{Pxs} and δt_{Ppxs} (Equation 5). The inclusion of three RF modes in Case 3 decreases the variation of estimated R and Z among the tests at different LVZ depths (Figure 4.9c). However, if the LVZ is < ~3 km thick, the inclusion of Pxs in Cases 2 and 3 artificially increases estimates of R to >2.3. This increase is due to interference in the Pxs phases from the top and bottom of a thin LVZ biasing to greater time separation.

4.6.4 Alaska

Previous analyses of RFs in Alaska in both 3D and 2D have revealed a LVZ along the plate interface that extends for at least 450 km along strike at all imaged depths <35 km (e.g., Kim et al., 2014; Mann et al., *subm.*). Depths to the plate interface in Alaska were determined in a previous analysis of a 3D CCP stacking volume generated using the same RFs (Mann et al., *subm.*) and converted to time for each RF mode here. These estimated arrival times for each RF mode were used to guide LVZ phase selection.

The >11-km thick subducting Yakutat crust in Alaska allows for better separation of phases from the LVZ and the subducting crust Moho than in other subduction zones with typical oceanic crustal thicknesses of ~6 km. We limited the analysis of the LVZ along-strike in Alaska to only stations that overlie the subducting Yakutat terrane (Kim et al., 2014; Chapter 3; Figure 4.1), to ensure sufficient separation of LVZ and Yakutat Moho phases. Additionally, the analysis

was limited down-dip to where the LVZ is away from potential contamination by RF phases from the upper plate Moho.

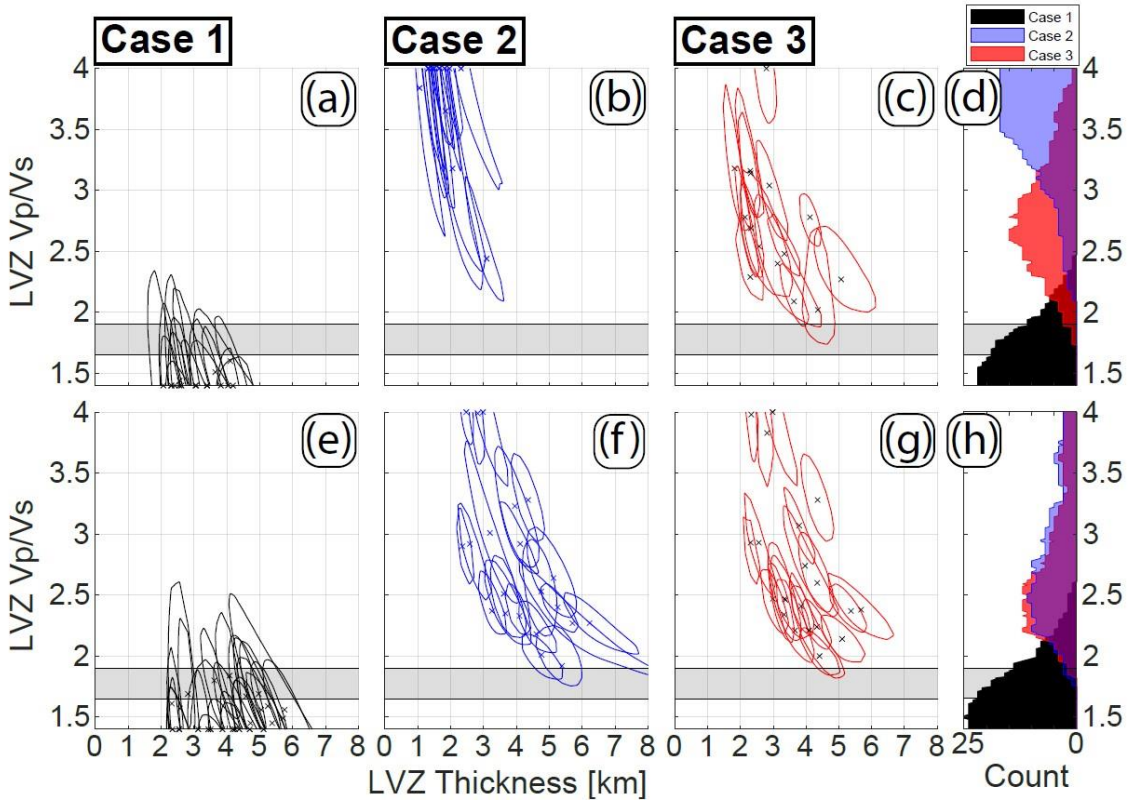

Figure 4.10: LVZ inversion results for southcentral Alaska (top row) and Cascadia (bottom row). (a) and (e) Case 1 (Ppxs and Ppxp) inversions. (b) and (f) Case 2 (Pxs andPpxs) inversion results. (c) and (g) Case 3 (Pxs, Ppxs, and Ppxp) inversion results. (d) and (h) Histograms of uncertainty ranges from results in (a)-(c) and (e)-(g), respectively. Gray bar shows range of dry rock Vp/Vs values (Christensen, 1996; Reynard, 2013)..

Inversion results of the LVZ atop the subducting Yakutat terrane in Alaska in Case 1 show a 3.0±0.7-km (all uncertainty ranges on results are 1-σ) thick layer with R = 1.4±0.1 (Figure 4.10a). The best fit R values at a majority of the 17 stations is 1.4, but uncertainty ranges for nearly all values extend up to 2, with only one station with an uncertainty range that exceeds R = 2.2. Of the 17 stations used in the Case 1 inversion, 15 of those had Pxs LVZ phases that were identifiable and aligned with the estimated arrival times. For Case 2, the results show a 1.7±0.5-km thick LVZ with R = 3.8±0.4 (Figure 3.10b). Such a high value of R makes sense for Case 2

given the variability shown in the synthetic results (Figure 4.9c-d). For Case 3, the average of R estimates increased to 2.7±0.5, and the estimated thickness remains roughly the same (2.9±0.9 km) (Figure 4.10c). The 95% confidence intervals for the Case 1 and the Case 2 or 3 inversion measurements do not overlap (Figure 4.10a-b), and only a few measurements have overlapping R uncertainty ranges with (Case 1) and without (Cases 2 and 3) the use of Pxs (Figure 4.10). This could suggest either that the confidence intervals selected are too small to accommodate these different inversions, or that there is bias in the time separation of LVZ phases in one or more RF mode.

4.6.5 Cascadia

Cascadia is the site of the original dense (<15 km spacing) seismometer deployments that determined the down-dip continuity of low velocities along the plate interface using RFs (e.g., Rondenay et al., 2001). Since then, multiple dense seismometer deployments have been conducted across Cascadia and the LVZ RF phases have been analyzed extensively (e.g., Nicholson et al., 2005; Audet et al., 2009; Abers et al., 2009; Hansen et al., 2012; Mann et al., 2018).

The depths to the plate interface were determined based on the 2D GRT migration images from the CAFE array (Abers et al., 2009; McGary et al., 2012; McGary, 2014), which were converted to time for each RF mode. As in Alaska, we limited our analysis down-dip to where the LVZ is away from potential contamination by RF phases from the upper-plate Moho.

The inversion results for the three back-azimuthal bins in Cascadia were combined. Back-azimuthal bins were used to ensure the RFs sample the same region of the LVZ beneath a station. In Case 1, the average Z is 4.0±1.1 km and R is 1.5±0.1 (Figure 4.10e). Like the measurements from Alaska, while the majority of "best fit" R values from the 17 stations with clear LVZ RF

phases are at 1.4, the average maximum *R* from the uncertainty ranges for those stations is 2 (Figure 4.10h). Additionally, 95% of estimated *R* values fall below *R* = 2 (Figure 4.10h).

R results from the LVZ in Cascadia also show a clear separation between inversions that use Pxs and those that do not (Figure 4.10d-e). Of the 17 stations used in the Case 1 inversions, 14 of those had Pxs phases that were identifiable and aligned with the estimated arrival times (e.g., Figure 4.5a-b). For Case 2, the average *Z* is 3.8±1.0 km and *R* is 2.7±0.7 (Figure 4.8d). For Case 3, the average *RZ* is 4.5±1.0 km and *R* is 2.4±0.2.

4.7 Discussion

4.7.1 *R*

Measuring Ppxp is possible only with RFs generated using array-based deconvolution methods, where surface reflections can be isolated from the incident P wave (e.g., Bostock & Rondenay, 1999; Langston and Hammer, 2001). This *P*-to-*P* scattered mode is recorded on the *P* component and has greater volume resolution than the upgoing *P*-to-*S* mode, but less than the surface-reflected *P*-to-*S* modes. The *P*-to-*P* scattered mode arrival time is dependent on the *P* wave velocity above the reflecting boundary and its amplitude is dependent on both *Vp* and *Vs* on either sides of the boundary. The use of Ppxp instead of Pxs improves the resolution of RF inversions for LVZ properties.

Using the higher-resolution surface-reflected modes, the *R* measurements in Cascadia and Alaska (based on the uncertainty ranges in Figure 4.10d,h) are almost all less than 2.0. The inclusion of Pxs influences the inversion results such that the *R* uncertainty bounds for Case 1 and Case 2 or 3 do not overlap (Figure 4.10), offering near complete separation of solutions for *R* for inversion with and without Pxs. While these estimates are dependent on the weights for each RF mode, in practice most of the weights are equal or slightly biased toward Pxs. This is

probably why the inversion results for Case 2 and 3 (Figure 4.10) follow the tradeoff curve for Pxs (cf. Figure 4.6d).

Many previous RF phase inversions for LVZ properties in Cascadia and elsewhere, which rely on Pxs, have yielded R between 2 and 4 (e.g., Audet et al., 2009; Peacock et al., 2011; Hansen et al., 2012; Audet and Schwartz, 2013; Audet and Bürgmann, 2014). We can reproduce those values when we include Pxs, but as shown in the synthetic tests, those results become biased when the thickness of the layer decreases past the shortest wavelength resolvable by Pxs. Hence, we suspect that many measurements of R that incorporate Pxs may be biased to high values, especially when low-pass filtering at cutoff frequencies below ~1 Hz.

4.7.2 Implications of observed *R*

Typical values of R for relevant dry lithologies are between 1.65 and 1.9 (e.g., Christensen, 1996; Reynard, 2013). The addition of water, porosity, and/or pore fluid pressure reduces velocities overall, but the reduction in Vs is greater than the reduction in Vp (e.g., Christensen, 1989). Because $R > 2.2$ is not observed in dry rocks, previous measurements that show $R > 2.2$ for the LVZ have been interpreted as resulting from high pore-fluid pressures within the uppermost oceanic crust, maintaining high porosities that primarily reduce shear moduli beneath an impermeable megathrust interface (e.g., Audet et al., 2009; Peacock et al., 2011; Hansen et al., 2012). However, plate interface LVZs with elevated R could result from other processes. Highly fractured basalt can manifest high R ratios without the need for high pore-fluid pressures (Nishimura et al., 2019). Exhumed subduction complexes from the plate interface down-dip of the seismogenic zone show predominantly metasedimentary rocks (e.g., Rowe et al., 2013; Behr & Bürgmann, 2020; Tewksbury-Christle et al., 2021). Metamorphosed sediment has lower velocities and higher values of R than basalt or gabbro expected away from the

interface (e.g., Calvert et al., 2004; Abers et al., 2009; Calvert et al., 2011; Kim et al., 2014; Kim et al., 2019; Delph et al., 2021). Experimental measurements of seismic velocity for exposed fossil LVZs show a high degree of anisotropy in both *Vp* and *Vs*, with $R \leq 2$ (e.g., Tewksbury-Christle & Behr, 2021; Miller et al., *in press*). Given that the values of R determined in our analysis (Case 1) fits the values for normal dry rocks (Figure 4.10), we interpret the thin (< 5 km in Cascadia and < 3 km in Alaska) layer of low velocities with $R < 2$ along the plate interface as largely due to metamorphosed sediment and tectonically eroded and fractured material, with free fluid playing a secondary role.

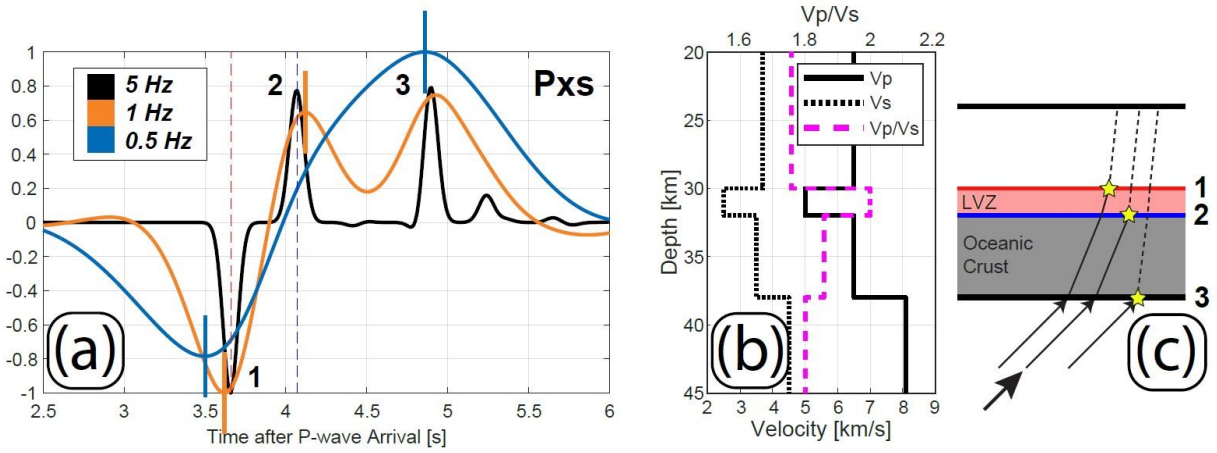

Figure 4.11: (a) Zoom-in of Pxs mode of synthetic RF for case of a LVZ atop typical oceanic crust, as in Cascadia. 1, 2, 3 highlight peaks associated with the LVZ top, LVZ bottom, and oceanic crust Moho at high frequency. All other symbols as in Figure X. Peaks have been normalized after filtering to emphasize offset. (b) Velocity model. From top (surface) down, the layers represent the upper crust (Vp = 6.5 km/s, Vs = 3.7 km/s), a 2-km thick LVZ (Vp = 5 km/s, Vs = 2.5 km/s), a 6-km thick oceanic crust (Vp = 6 km/s, Vs = 3.3 km/s), and the underlying mantle lithosphere (Vp = 8.1 km/s, Vs = 4.4 km/s). (c) Cartoon depicting raypaths for each Pxs phase in this model. Each discontinuity number corresponds with (a): 1 - LVZ top, 2 - LVZ bottom, 3 - Oceanic Crust Moho. Arrows represent incident P-wave. Solid lines are P-waves, dashed lines are S-waves.

4.7.3 Influence of Subducting Crust Thickness

The bias from Pxs could be the result of misidentification of Pxs RF phases. Interpretations of the LVZ are varied but typically include some portion of a sedimentary

sequence along the plate interface, tectonically eroded material from the upper plate, and/or part of the subducting crust (e.g., Audet et al., 2009; Abers et al., 2009; Calvert et al., 2011; Bostock, 2013). In any case, for typical oceanic crustal thicknesses there will be an oceanic Moho phase that immediately follows the RF phase from the LVZ bottom, unless the LVZ incorporates the entire oceanic crust. As can be seen from our inversion results (Figure 3.10), and those of many others (e.g., Abers et al., 2009; Audet et al., 2009; Kim et al., 2014): the LVZ is too thin to represent the entire oceanic crust. The presence of a crustal Moho phase after the LVZ could have a significant impact on Pxs RF phases in subduction zones because low-pass filtering may cause Pxs to have only two phases: one negative from the top of the LVZ and one positive from either the Moho of the subducting crust or as the result of constructive interference between the Moho of the subducting crust and the bottom of the LVZ. If these two oppositely polarized phases are misidentified as the top and bottom of the LVZ, it could lead to additional bias in R and thickness estimates for the LVZ.

To illustrate this issue, we generated synthetic RFs (with source duration d = 0.2 s, Equation 6) using a ray parameter of 0.06 s/km and a four-layer velocity model (Figure 4.11). The high frequency synthetics show three Pxs RF phases from the LVZ boundaries and the oceanic Moho. The synthetics filtered between 0.05 Hz and 1 Hz still show the same three phases, with barely any variation in arrival times for the phases. However, filtering the synthetics between 0.05 Hz and 0.5 Hz causes constructive interference between the LVZ bottom and oceanic Moho phases, resulting in only two phases from the top of the LVZ and the oceanic Moho.

We filter between 0.05 Hz and 1 Hz in our analysis to avoid these potential issues with Pxs. Analyzing the LVZ in Alaska where the subducting crust is >11 km thick avoids potential

interference between the Moho and LVZ bottom phases, because the Pxs phases from the subducting crust Moho are sufficiently separated from the LVZ. However, this did not change the fact that the incorporation of Pxs in Alaska biased the estimates of R (Figure 4.10a-d), suggesting that the LVZ in Alaska is very thin.

4.8 Conclusion

Inversions of RF phases for the Vp/Vs and thickness of the plate interface LVZ in southcentral Alaska and Cascadia were conducted using only surface-reflected RF modes, which have greater resolution than the direct (up-going) *P*-to-*S* scattered phases that are typically used in RF analyses. The LVZ in Alaska atop the subducting >11 km-thick crust of the Yakutat terrane is < 5 km thick, with $Vp/Vs < 2$. In Cascadia, the LVZ atop the subducting JdF crust is < 5 km thick, with $R < 2.2$, though a majority of uncertainty ranges span R between 1.4 and 2. Invoking high pore fluid pressures for these estimates of R are unnecessary. By contrast, the inclusion of the direct (i.e., Pxs) scatter RF mode in the inversion resulted in a significant (>1-2) increase in Vp/Vs from the initial inversion results in almost every case. From this we conclude that previous analyses, which rely on Pxs and result in consistent $R > 2$ for the LVZ, are erroneous due to bias in Pxs for such a thin layer, misidentification and/or interference of RF phases from the LVZ and the subducting plate Moho, or a combination of the two. The inferred low friction down dip of the locked megathrust region is therefore most likely the result of weak metasediment, along with any other tectonically eroded material, entrained along the plate interface. In this model, any pore-fluid pressure would play a secondary role in weaking the plate interface.

REFERENCE

Abers, G. A., MacKenzie, L. S., Rondenay, S., Zhang, Z., Wech, A. G., & Creager, K. C. (2009). Imaging the source region of Cascadia tremor and intermediate-depth earthquakes. *Geology*, *37*(12), 1119–1122. https://doi.org/10.1130/G30143A.1

Abers, Geoffrey A., & Hacker, B. R. (2016). A MATLAB toolbox and E xcel workbook for calculating the densities, seismic wave speeds, and major element composition of minerals and rocks at pressure and temperature. *Geochemistry, Geophysics, Geosystems*, *17*(2), 616–624. https://doi.org/10.1002/2015GC006171

Audet, P., & Bürgmann, R. (2014). Possible control of subduction zone slow-earthquake periodicity by silica enrichment. *Nature*, *510*(7505), 389–392. https://doi.org/10.1038/nature13391

Audet, P., & Schwartz, S. Y. (2013). Hydrologic control of forearc strength and seismicity in the Costa Rican subduction zone. *Nature Geoscience*, *6*(10), 852–855. https://doi.org/10.1038/ngeo1927

Audet, P., Bostock, M. G., Christensen, N. I., & Peacock, S. M. (2009). Seismic evidence for overpressured subducted oceanic crust and megathrust fault sealing. *Nature*, *457*(7225), 76–78. https://doi.org/10.1038/nature07650

Bangs, N. L., Shipley, T. H., Gulick, S. P. S., Moore, G. F., Kuromoto, S., & Nakamura, Y. (2004). Evolution of the Nankai Trough décollement from the trench into the seismogenic zone: Inferences from three-dimensional seismic reflection imaging. *Geology*, *32*(4), 273. https://doi.org/10.1130/G20211.2

Bangs, N. L., McIntosh, K. D., Silver, E. A., Kluesner, J. W., & Ranero, C. R. (2015). Fluid accumulation along the Costa Rica subduction thrust and development of the

seismogenic zone: The Costa Rica subduction thrust. *Journal of Geophysical Research: Solid Earth*, *120*(1), 67–86. https://doi.org/10.1002/2014JB011265

Bangs, Nathan L. B., Shipley, T. H., Moore, J. C., & Moore, G. F. (1999). Fluid accumulation and channeling along the northern Barbados Ridge decollement thrust. *Journal of Geophysical Research: Solid Earth*, *104*(B9), 20399–20414. https://doi.org/10.1029/1999JB900133

Bangs, N.L.B., Moore, G. F., Gulick, S. P. S., Pangborn, E. M., Tobin, H. J., Kuramoto, S., & Taira, A. (2009). Broad, weak regions of the Nankai Megathrust and implications for shallow coseismic slip. *Earth and Planetary Science Letters*, *284*(1–2), 44–49. https://doi.org/10.1016/j.epsl.2009.04.026

Behr, W. M., & Bürgmann, R. (2021). What's down there? The structures, materials and environment of deep-seated slow slip and tremor. *Philosophical Transactions of the Royal Society A: Mathematical, Physical and Engineering Sciences*, *379*(2193), 20200218. https://doi.org/10.1098/rsta.2020.0218

Benz, H. M., & Vidale, J. E. (1993). Sharpness of upper-mantle discontinuities determined from high-frequency reflections. *Nature*, *365*(6442), 147–150. https://doi.org/10.1038/365147a0

Beroza, G. C., & Ide, S. (2009). Deep Tremors and Slow Quakes. *Science*, *324*(5930), 1025–1026. https://doi.org/10.1126/science.1171231

Bostock, M. G. (1999). Seismic waves converted from velocity gradient anomalies in the Earth's upper mantle. *Geophysical Journal International*, *138*(3), 747–756. https://doi.org/10.1046/j.1365-246x.1999.00902.x

Bostock, M. G. (2013). The Moho in subduction zones. *Tectonophysics*, *609*, 547–557. https://doi.org/10.1016/j.tecto.2012.07.007

Bostock, M. G., & Rondenay, S. (1999). Migration of scattered teleseismic body waves. *Geophysical Journal International*, *137*(3), 732–746. https://doi.org/10.1046/j.1365-246x.1999.00813.x

Calvert, A. J. (2004). Seismic reflection imaging of two megathrust shear zones in the northern Cascadia subduction zone. *Nature*, *428*(6979), 163–167. https://doi.org/10.1038/nature02372

Calvert, A. J., Preston, L. A., & Farahbod, A. M. (2011). Sedimentary underplating at the Cascadia mantle-wedge corner revealed by seismic imaging. *Nature Geoscience*, *4*(8), 545–548. https://doi.org/10.1038/ngeo1195

Christensen, N. I. (1996). Poisson's ratio and crustal seismology. *Journal of Geophysical Research: Solid Earth*, *101*(B2), 3139–3156. https://doi.org/10.1029/95JB03446

Clayton, R. W., Wiggins, R. A. (1976). Source shape estimation and deconvolution of teleseismic bodywaves. *Geophysical Journal of the Royal Astronomical Society*, *47*(1), 151-177.

Cormier, V. F. (1982). The Effect of Attenuation On Seismic Body Waves. *Bulletin of the Seismological Society of America*, *72*(6), S169-S200.

Delph, J. R. (2021). Subcretionary tectonics: Linking variability in the expression of subduction along the Cascadia forearc. *Earth and Planetary Science Letters*, 556, 116724. https://doi.org/10.1016/j.epsl.2020.116724

Delph, J. R., Levander, A., & Niu, F. (2018). Fluid Controls on the Heterogeneous Seismic Characteristics of the Cascadia Margin. *Geophysical Research Letters*, *45*(20). https://doi.org/10.1029/2018GL079518

Gomberg, J. & the Cascadia 2007 and Beyond Working Group. (2010). Slow-slip phenomena in Cascadia from 2007 and beyond: A review. *Geological Society of America Bulletin*, *122*(7–8), 963–978. https://doi.org/10.1130/B30287.1

Gosselin, J. M., Audet, P., Estève, C., McLellan, M., Mosher, S. G., & Schaeffer, A. J. (2020). Seismic evidence for megathrust fault-valve behavior during episodic tremor and slip. *Science Advances*, *6*(4), eaay5174. https://doi.org/10.1126/sciadv.aay5174

Guo, H., McGuire, J. J., & Zhang, H. (2021). Correlation of porosity variations and rheological transitions on the southern Cascadia megathrust. *Nature Geoscience*, *14*(5), 341–348. https://doi.org/10.1038/s41561-021-00740-1

Hansen, R. T. J., Bostock, M. G., & Christensen, N. I. (2012). Nature of the low velocity zone in Cascadia from receiver function waveform inversion. *Earth and Planetary Science Letters*, *337–338*, 25–38. https://doi.org/10.1016/j.epsl.2012.05.031

Haskell, N. A. (1962). Crustal reflection of plane *P* and *SV* waves. *Journal of Geophysical Research*, *67*(12), 4751–4768. https://doi.org/10.1029/JZ067i012p04751

Ide, S., Beroza, G. C., Shelly, D. R., & Uchide, T. (2007). A scaling law for slow earthquakes. *Nature*, *447*(7140), 76–79. https://doi.org/10.1038/nature05780

Kennett, B. L. N. (1991). The Removal of Free Surface Interactions From Three-Component Seismograms. *Geophysical Journal International*, *104*(1), 153–154. https://doi.org/10.1111/j.1365-246X.1991.tb02501.x

Kim, D., Keranen, K. M., Abers, G. A., & Brown, L. D. (2019). Enhanced Resolution of the Subducting Plate Interface in Central Alaska From Autocorrelation of Local Earthquake Coda. *Journal of Geophysical Research: Solid Earth*, *124*(2), 1583–1600. https://doi.org/10.1029/2018JB016167

Kim, Y., Abers, G. A., Li, J., Christensen, D., Calkins, J., & Rondenay, S. (2014). Alaska Megathrust 2: Imaging the megathrust zone and Yakutat/Pacific plate interface in the Alaska subduction zone. *Journal of Geophysical Research: Solid Earth*, *119*(3), 1924–1941. https://doi.org/10.1002/2013JB010581

Langston, C. A. (1977). Corvallis, Oregon, crustal and upper mantle receiver structure from teleseismic P and S waves. *Bulletin of the Seismological Society of America* 67(3), 713-724.

Langston, C. A., & Hammer, J. K. (2001). The Vertical Component P-Wave Receiver Function. *Bulletin of the Seismological Society of America* 91(6), 1805-1819.

Levin, V., VanTongeren, J. A., & Servali, A. (2016). How sharp is the sharp Archean Moho? Example from eastern Superior Province: How Sharp is Archean Moho? *Geophysical Research Letters*, *43*(5), 1928–1933. https://doi.org/10.1002/2016GL067729

Li, J., Abers, G. A., Kim, Y., & Christensen, D. (2013). Alaska megathrust 1: Seismicity 43 years after the great 1964 Alaska megathrust earthquake. *Journal of Geophysical Research: Solid Earth*, *118*(9), 4861–4871. https://doi.org/10.1002/jgrb.50358

MacKenzie, L. S., Abers, G. A., Rondenay, S., & Fischer, K. M. (2010). Imaging a steeply dipping subducting slab in Southern Central America. *Earth and Planetary Science Letters*, *296*(3–4), 459–468. https://doi.org/10.1016/j.epsl.2010.05.033

Mann, M. E., Abers, G. A., Crosbie, K., Creager, K., Ulberg, C., Moran, S., & Rondenay, S. (2019). Imaging Subduction Beneath Mount St. Helens: Implications for Slab Dehydration and Magma Transport. *Geophysical Research Letters*, *46*(6), 3163–3171. https://doi.org/10.1029/2018GL081471

McGary, R. S., Evans, R. L., Wannamaker, P. E., Elsenbeck, J., & Rondenay, S. (2014). Pathway from subducting slab to surface for melt and fluids beneath Mount Rainier. *Nature*, *511*(7509), 338–340. https://doi.org/10.1038/nature13493

Moreno, M., Haberland, C., Oncken, O., Rietbrock, A., Angiboust, S., & Heidbach, O. (2014). Locking of the Chile subduction zone controlled by fluid pressure before the 2010 earthquake. *Nature Geoscience*, *7*(4), 292–296. https://doi.org/10.1038/ngeo2102

Nicholson, T., Bostock, M., & Cassidy, J. F. (2005). New constraints on subduction zone structure in northern Cascadia. *Geophysical Journal International*, *161*(3), 849–859. https://doi.org/10.1111/j.1365-246X.2005.02605.x

Peacock, S. M., Christensen, N. I., Bostock, M. G., & Audet, P. (2011). High pore pressures and porosity at 35 km depth in the Cascadia subduction zone. *Geology*, *39*(5), 471–474. https://doi.org/10.1130/G31649.1

Peng, Z., & Gomberg, J. (2010). An integrated perspective of the continuum between earthquakes and slow-slip phenomena. *Nature Geoscience*, *3*(9), 599–607. https://doi.org/10.1038/ngeo940

Reynard, B. (2013). Serpentine in active subduction zones. *Lithos*, *178*, 171-185.

Rondenay, S., Bostock, M. G., & Shragge, J. (2001). Multiparameter two-dimensional inversion of scattered teleseismic body waves 3. Application to the Cascadia 1993 data

set. *Journal of Geophysical Research: Solid Earth*, *106*(B12), 30795–30807. https://doi.org/10.1029/2000JB000039

Rondenay, Stéphane. (2009). Upper Mantle Imaging with Array Recordings of Converted and Scattered Teleseismic Waves. *Surveys in Geophysics*, *30*(4–5), 377–405. https://doi.org/10.1007/s10712-009-9071-5

Rondenay, Stéphane, Bostock, M. G., & Fischer, K. M. (2005). Multichannel inversion of scattered teleseismic body waves: Practical considerations and applicability. In A. Levander & G. Nolet (Eds.), *Geophysical Monograph Series* (Vol. 157, pp. 187–203). Washington, D. C.: American Geophysical Union. https://doi.org/10.1029/157GM12

Rossi, G., Abers, G. A., Rondenay, S., & Christensen, D. H. (2006). Unusual mantle Poisson's ratio, subduction, and crustal structure in central Alaska. *Journal of Geophysical Research*, *111*(B9), B09311. https://doi.org/10.1029/2005JB003956

Rowe, C. D., Moore, J. C., Remitti, F., & the IODP Expedition 343/343T Scientists. (2013). The thickness of subduction plate boundary faults from the seafloor into the seismogenic zone. *Geology*, *41*(9), 991–994. https://doi.org/10.1130/G34556.1

Ruppert, N. A., & West, M. E. (2020). The Impact of USArray on Earthquake Monitoring in Alaska. *Seismological Research Letters*. *91*(2A), 601-610.

Saffer, D. M., & Tobin, H. J. (2011). Hydrogeology and Mechanics of Subduction Zone Forearcs: Fluid Flow and Pore Pressure. *Annual Review of Earth and Planetary Sciences*, *39*(1), 157–186. https://doi.org/10.1146/annurev-earth-040610-133408

Soto Castañeda, R. A., Abers, G. A., Eilon, Z. C., & Christensen, D. H. (2021). Teleseismic Attenuation, Temperature, and Melt of the Upper Mantle in the Alaska Subduction

Zone. *Journal of Geophysical Research: Solid Earth*, *126*(7). https://doi.org/10.1029/2021JB021653

Tewksbury-Christle, C. M., & Behr, W. M. (2021). Constraints from exhumed rocks on the seismic signature of the deep subduction interface. *Geophysical Research Letters*, *48*, e2021GL093831. https://doi.org/10.1029/2021GL093831

Tewksbury-Christle, C. M., Behr, W. M., & Helper, M. A. (2021). Tracking Deep Sediment Underplating in a Fossil Subduction Margin: Implications for Interface Rheology and Mass and Volatile Recycling. *Geochemistry, Geophysics, Geosystems*, *22*(3). https://doi.org/10.1029/2020GC009463

Tulley, C. J., Fagereng, Å., & Ujiie, K. (2020). Hydrous oceanic crust hosts megathrust creep at low shear stresses. *Science Advances*, *6*(22), eaba1529. https://doi.org/10.1126/sciadv.aba1529

Worthington, L. L., Van Avendonk, H. J. A., Gulick, S. P. S., Christeson, G. L., & Pavlis, T. L. (2012). Crustal structure of the Yakutat terrane and the evolution of subduction and collision in southern Alaska. *Journal of Geophysical Research: Solid Earth*, *117*(B1), n/a-n/a. https://doi.org/10.1029/2011JB008493

Zandt, G., & Ammon, C. J. (1995). Continental crust composition constrained by measurements of crustal Poisson's ratio. *Nature*, *374*(6518), 152–154. https://doi.org/10.1038/374152a0

Zhu, L., & Kanamori, H. (2000). Moho depth variation in southern California from teleseismic receiver functions. *Journal of Geophysical Research: Solid Earth*, *105*(B2), 2969–2980. https://doi.org/10.1029/1999JB900322

CHAPTER 5

SYNTHESIS

The seismic expression of drastic compositional variations, along with the addition or lack of water, throughout the subduction system generates sharp velocity contrasts at the major boundaries that can be investigated using scattered waves from teleseismic earthquakes. This dissertation details seismic imaging efforts using scattered waves from teleseismic earthquakes at the southcentral Alaska and Cascadia subduction zones.

In Cascadia, the subducting slab beneath Mount St. Helens (MSH), a Cascades arc volcano that is 50-km trenchward of the main Cascades arc, is imaged at an anomalously shallow depth beneath MSH (68±2 km). This depth requires complicated mantle or crustal pathways to connect melt generated from down-dip dehydration of the subducting slab to the volcano. The subducting crust Moho velocity contrast disappears at a greater depth than is predicted from geodynamic modeling, indicating that the metamorphism of the subducting crust is retarded, possibly by high water content. In southcentral Alaska, the Wrangell Volcanic Field (WVF) is a field of 11 major volcanic centers and make up the largest grouping of calc-alkaline volcanoes in the world. The Yakutat terrane, an oceanic plateau that has entered the subduction system across the region, is imaged along-strike and down-dip in the subduction zone. At shallow depths, the Yakutat Moho and a low velocity zone along the plate interface (LVZ) are imaged subducting across the region. Deeper, the Yakutat terrane is imaged subducting beneath the WVF to at least 110-km depth, with a strike (285°) and dip (~45°) that are drastically different from previous scattered wave imaging immediately to the West. The shallow continuity and down-dip offset

suggest the presence of a tear in the subducting slab that is currently 50-100 km to the West of the WVF and probably plays a direct role in WVF volcanism.

Observations of relatively low shear velocity along the plate interface in subduction zones, and estimates of high Vp/Vs, have been used to suggest that the LVZ has high porosity and water content. The greater crustal thickness of the subducting Yakutat terrane (>11 km) allows for a clear separation of upgoing P-to-S scattered phases from the LVZ and the Yakutat Moho. We take advantage of this separation, which is not present in subduction zones with subducting oceanic crust of typical thicknesses (i.e., ~6-7 km), such as Cascadia, to investigate the thickness and Vp/Vs of the LVZ using the differential timing of scattered waves generated by teleseismic earthquake P-waves at the delimiting boundaries of the LVZ. Our method incorporates the surface-reflected and back-scattered P-to-P scattered wavefield, which has higher resolution than the upgoing P-to-S scattered phases and allows for more accurate estimates of LVZ thickness and Vp/Vs. Using only P-to-S and P-to-P scattered phases that have higher resolution than the upgoing P-to-S phases, we show that the LVZ has a Vp/Vs < ~2. Previous investigations, which rely heavily on the upgoing P-to-S scattered phases, showed ubiquitous Vp/Vs > 2.2. We also show that the inclusion of the upgoing P-to-S scattered phases biases our measurements to Vp/Vs > 2.2, indicating the previous estimates are the result of bias. Our LVZ Vp/Vs results are typical for a wide range of dry igneous and metamorphic rocks and do not require high porosity and water content.

The power of seismic imaging methods that utilize scattered waves from teleseismic earthquakes is displayed throughout this dissertation. Although it has been used in the past to provide complementary results to P-to-S scattered wave imaging, the application of the P-to-P scattered wavefield in Chapters 3 and 4 of this dissertation to image the along-strike continuity

and properties of the LVZ along the plate interface may mark the first time the P-to-P scattered wavefield has been used to investigate a major problem in Earth science. Hopefully these studies encourage further work in seismic imaging using scattered waves and provide evidence for the importance of seismic arrays in determining the along-strike continuity of subduction zone structure.

APPENDIX A

First-order mantle subduction zone structure effects on ground motion: the Alaska 2016 Iniskin and 2018 Anchorage Mw 7.1 earthquakes

Abstract

The 24 January 2016 Iniskin, Alaska earthquake, at Mw 7.1 and 111 km depth, is the largest intermediate-depth earthquake felt in Alaska, generating 0.2 g shaking near Anchorage. Ground motion from the Iniskin earthquake is underpredicted by at least an order of magnitude near Anchorage and the Kenai Peninsula, and similarly overpredicted in the back arc north and west of Cook Inlet. This is in strong contrast with the 30 November 2018 earthquake near Anchorage, also Mw 7.1 but only 48 km deep. For the Anchorage earthquake, signals show strong distance decay and are generally well predicted by ground motion prediction equations. Smaller intermediate-depth earthquakes (depth >70 km and 3<M<6.4) with hypocenters near the Iniskin mainshock show similar patterns in ground shaking as the Iniskin earthquake, indicating that the shaking pattern is due to path effects and not the source. The patterns indicate a first-order role for mantle attenuation in the spatial variability in strong motion. Additionally, along-slab paths appear to be amplified by waveguide effects due to subduction of crust at >1 Hz; the Anchorage and Kenai regions are particularly susceptible to this amplification due to their forearc position. Both of these effects are absent in the 2018 Anchorage shaking pattern, because that earthquake is shallower and waves largely propagate in the crust. Basin effects are also present locally, but do not explain the first-order amplitude variations. These analyses show that intermediate-depth earthquakes can pose a significant shaking hazard, and the pattern of shaking is strongly controlled by mantle structure.

Introduction

On 24 January 2016, the population centers of southern Alaska experienced the largest shaking from earthquakes in five decades. The Mw 7.1 Iniskin earthquake occurred beneath Cook Inlet within the subducting plate at 111 km depth (Figure A1), making it the largest Alaskan intermediate-depth event known (West et al., 2016). Observations show strong shaking (>0.2 g) in and east of Anchorage, 200-300 km from the epicenter, and some damage in Anchorage and the Kenai Peninsula. On 30 November 2018, another Mw 7.1 earthquake caused extensive damage in the Anchorage area, with accelerations reaching 0.8 g (Liu et al., 2019). That earthquake was likewise within the subducting plate, but was only 47 km deep, and as a result energy propagated largely within the crust. It showed a shaking pattern that correlates well with distance. The occurrence of unexpectedly strong distant shaking from the Iniskin earthquake, but not the Anchorage one, raises questions about the predictions of shaking from in-slab earthquakes, and how much of a hazard they represent.

This study evaluates the underlying causes of this unexpected shaking pattern, relative to the predictions of common ground-motion-prediction equations (GMPEs). We demonstrate that earth structure, rather than source processes, is responsible, and that earthquakes in similar environments may be expected to show similar shaking. The critical geological structures lie at mantle depths, and the high shaking reflects wave propagation through a low-attenuation slab amplified by structural focusing.

Accelerations from the 2016 Iniskin earthquake

The recent deployment of the EarthScope Transportable Array (TA) in southern Alaska (Witze, 2013) includes many strong-motion accelerometers that recorded the Iniskin mainshock on scale at free-field sites across the region. These are the fundamental data used here. For each

operating TA strong-motion station, we extract 360 s of horizontal-component waveform (240 s for smaller earthquakes; see below), correct them for gain and removed any DC trend. From the records, pseudo-spectral acceleration (PSA) for 5% damping is calculated at periods from 0 to 10 s, and the two horizontal accelerations are combined using the GMRotI50 measure (Boore et al., 2006). These are supplemented by accelerations from the Anchorage strong-motion network (Dutta et al., 2003), specifically the peak ground acceleration (PGA) and PSA reported to the CESMD database (Haddadi et al., 2012).

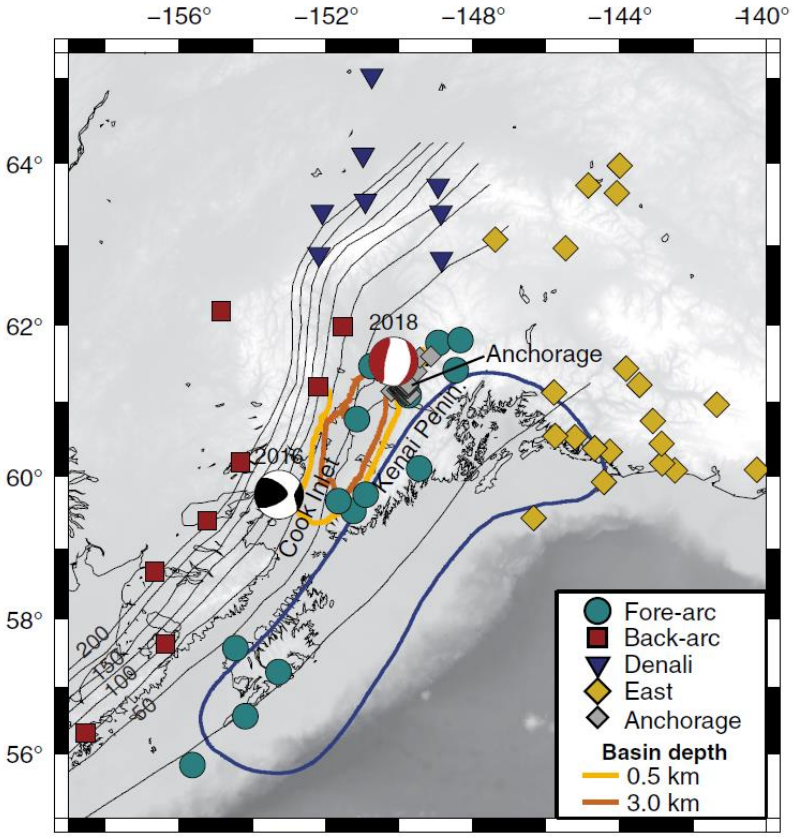

Figure A1: Location of earthquakes producing strong shaking in Anchorage, labeled by year denoted by the Global Centroid Moment Tensor (CMT) (Ekströmet al., 2012). Slab-depth contours at 25 km intervals (thin lines) after Ratchkovski and Hansen (2002). The thick yellow and orange lines show depth to basement in the Cook Inlet basin; colored symbols show accelerometers used in this study, with symbol type and color corresponding to region as shown in the legend. The thick blue line shows rupture of the 1964 M 9.2 earthquake (Davies et al., 1981).

These measurements show the spatial variability of strong shaking from the Iniskin earthquake (Figure A2). They show only weak decay in PSA with epicentral distance, but strong variations between tectonic regions. Large accelerations are observed throughout the Kenai Peninsula and greater Anchorage region, with very low accelerations observed in the backarc

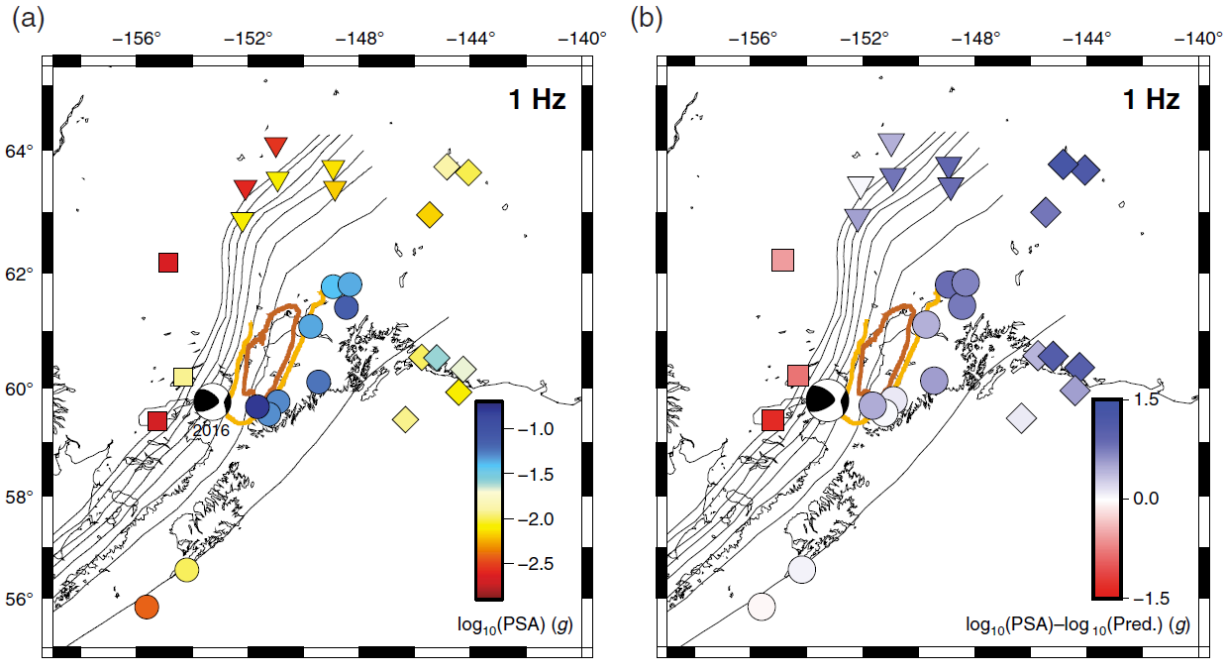

Figure A2: (a) Pseudospectral acceleration (PSA) spatial variability for the 2016 Iniskin mainshock at Alaska Transportable Array (TA) accelerometers, at 1 Hz for 5% damping. Colors show log10(PSA) relative to 1:0g. (b) Residual PSA for the Iniskin earthquake at 1 Hz. The mainshock moment tensor is shown, from the Global CMT catalog. The thin lines show slab-depth contours at 25 km intervals, whereas the thick colored lines show depths to basement beneath the Cook Inlet basin following Figure A1. The color version of this figure is available only in the electronic edition.

(defined here as the region northwest of the 75 km slab depth contour). This pattern is strongest at frequencies ≥ 1 Hz. Although basin amplification has been documented in the Cook Inlet Basin at < 0.5 Hz from this earthquake (Grapenthin et al., 2018), the pattern of acceleration seems unrelated to basin location, as discussed below.

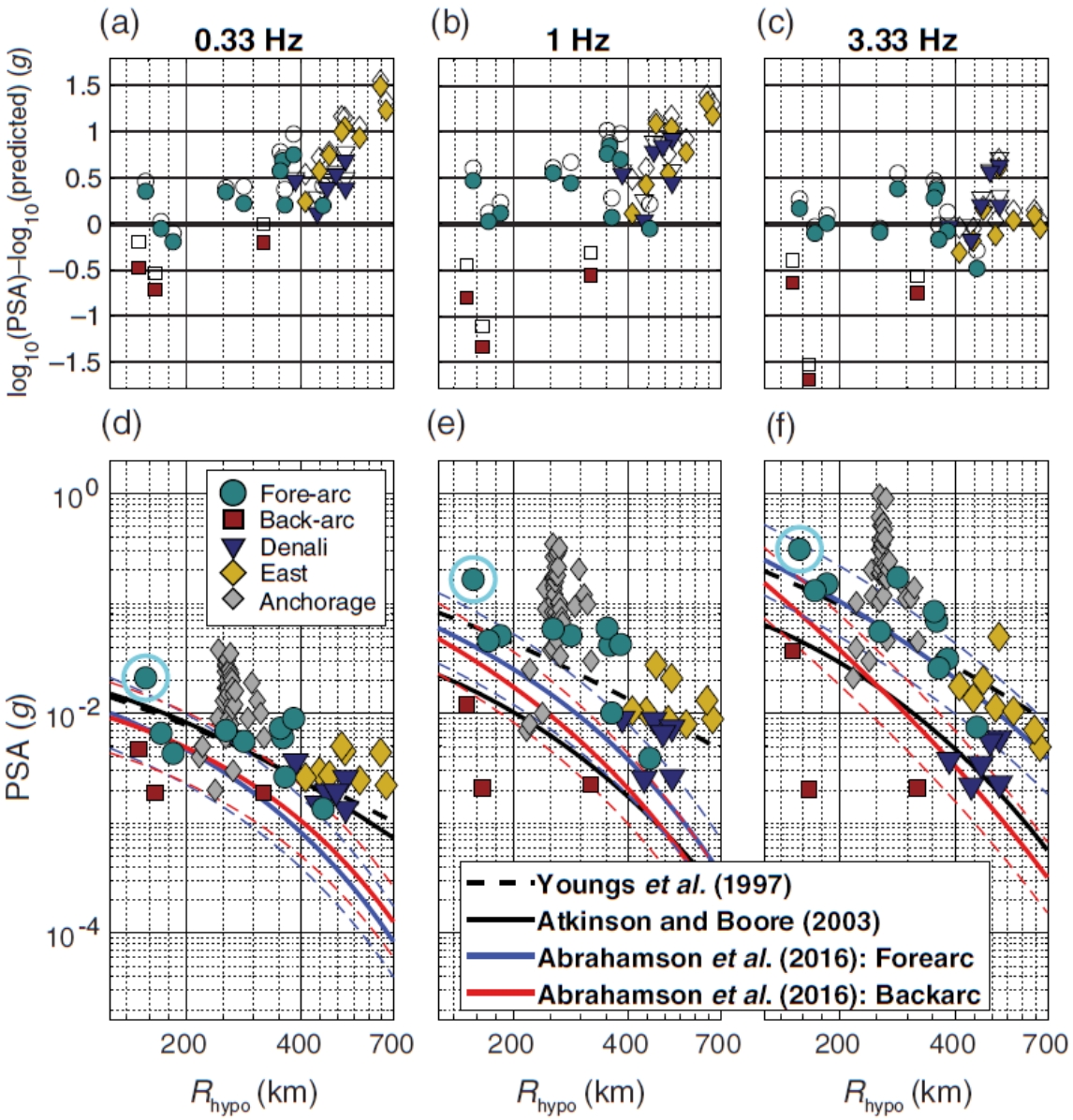

Figure A3: (a–c) Residual PSAs of the Iniskin earthquake from Abrahamson et al. (2016). The empty symbols are residuals calculated assuming hard-rock sites, that is, VS30 =1000 m/s. The solid symbols are residuals calculated assuming site-specific VS30 from Yong et al. (2016). (d–f) PSAs of the Iniskin earthquake. The lines show published ground-motion prediction equations (GMPEs) as indicated by the key; the thick dashed black line is the back-arc regression of Abrahamson et al. (2016), whereas the thinner dashed lines show 1 − σ uncertainties. All are calculated for hard-rock conditions (VS30 =1000 m/s). Horizontal axis R_{hypo} is the Cartesian distance to the hypocenter. The teal circle denotes stations on >1 km of basin sediment. Note the one- to two-order of magnitude spread in observations at most distances. The color version of this figure is available only in the electronic edition.

To understand the acceleration variations, we subdivide the stations into four geographic regions (Figure A1): Forearc – above where the slab is < 50 km deep; Backarc, behind the volcanically active arc; Denali; similar to Backarc but in the non-volcanic Denali slab segment; and East, east of the slab edge. We compare these accelerations against three GMPEs appropriate for subduction zones (Youngs et al., 1997; Atkinson and Boore, 2003; Abrahamson et al., 2016).

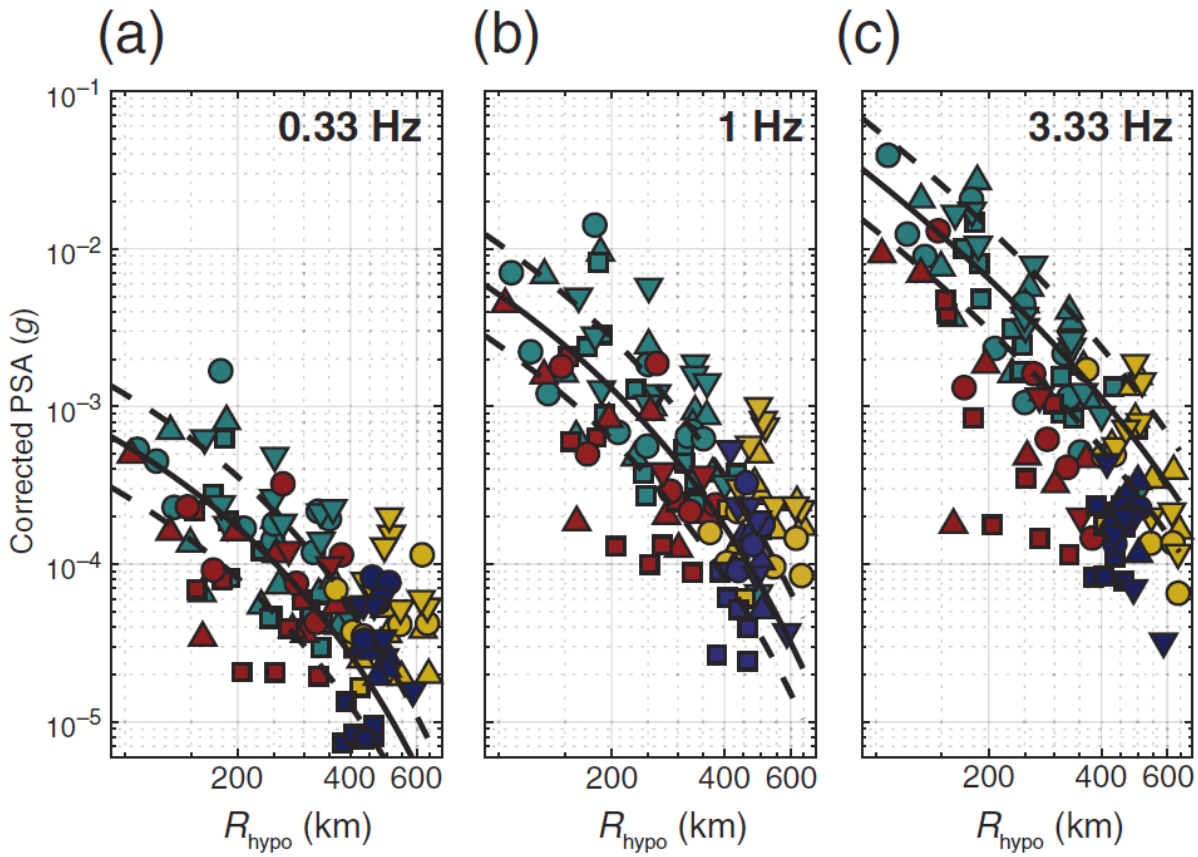

Figure A4: PSA for four M_w 5.0–6.4 earthquakes within the subducting Pacific plate near the Iniskin mainshock at (a) 0.33, (b) 1.0, and (c) 3.33 Hz as labeled. Colors correspond to regions as in Figure A1, and symbols to earthquakes in Table 1 as follows: triangles, 9 March 2018; squares, 5 November 2017; circles, 2 March 2017; and inverted triangles, 29 July 2015. PSAs are corrected to the mean magnitude (M_w 5.53) and minimum depth (78 km) for comparison. The solid line shows fore-arc GMPE at M_w 5.53 and 78 km depth (Abrahamson et al., 2016) for hard-rock sites; the dashed lines show uncertainty.

The GMPEs show up to 10x variability between models, especially at high frequencies where regional differences in attenuation should be most prominent, but all show similar relationships to the Iniskin data. Specifically, most observed accelerations exceed predictions at all frequencies (Figure A3). The pattern correlates well with geographic region – back-arc stations are significantly

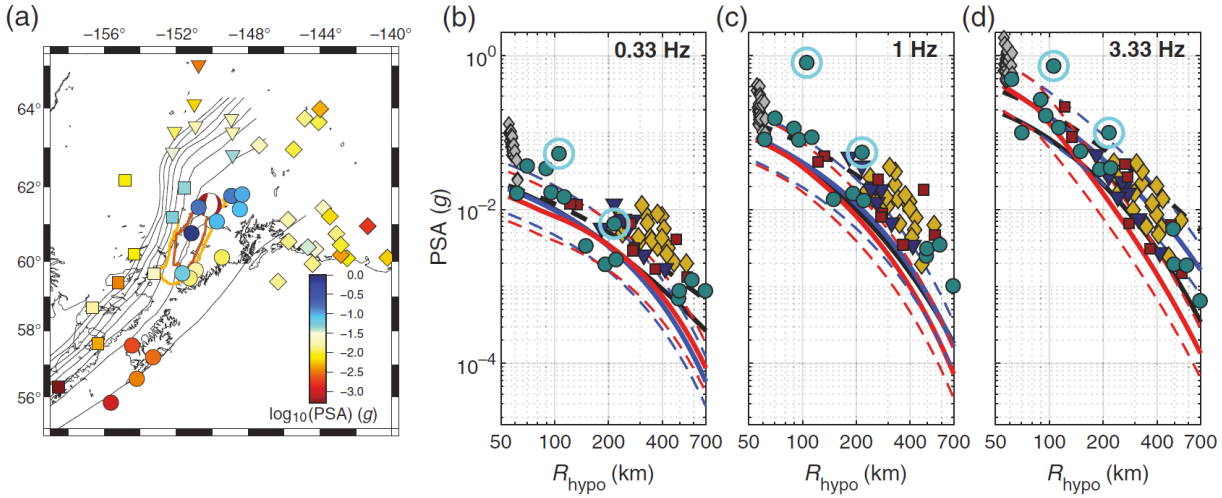

Figure A5: PSA for the 30 November 2018 Anchorage earthquake (Mw 7.1). (a) Map of 1 Hz PSA at 5% damping; format and symbols are the same as in Figure A3a. (b) PSA varying with distance at 0.33 Hz; format and reference GMPEs are the same as in Figure A3. PSAs for Anchorage stations are included from the Center for Engineering Strong Motion Data (CESMD) database. The teal circles highlight the stations over >1-km-thick Cook Inlet basin sediment. (c) Same at 1.0 Hz. (d) Same at 3.33 Hz. Note the general agreement between observations and GMPEs.

lower than the models, while forearc stations show the largest acceleration. The Denali segment accelerations behave like the Backarc. Forearc accelerations are up to two orders of magnitude larger than backarc accelerations at the same hypocentral distance. This is a remarkable variation with azimuth highlights that subduction geometry exerts a primary control. The back-arc correction of Abrahamson et al. (2016) adjusts in the right direction but is insufficient to capture this variability. The highest accelerations recorded by the TA are 2-5x larger than any prediction, and the largest in Anchorage are >10x larger, although some high Anchorage accelerations may

be partly due to structure amplification at some sites. The backarc paths show less acceleration than all models, at least at <300 km distance.

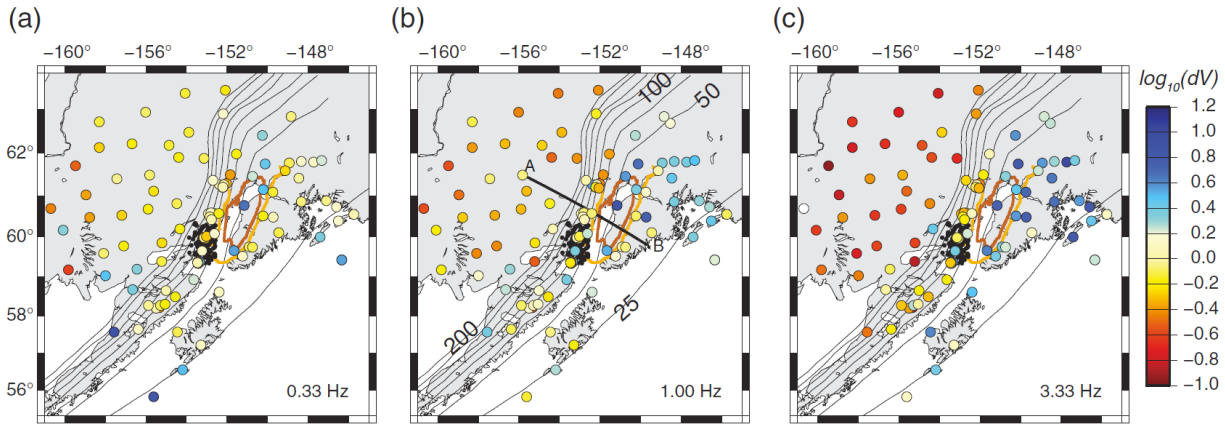

Figure A6: Weak-motion peak ground velocities (PGVs), colored as log10(dV), in which dV is PGV after removing the distance and magnitude effects as discussed in the Weak-Motion Observations section, for the root mean square (rms) horizontal motion. The black dots show the 222 earthquake hypocenters used. Panels show narrowband amplitudes at (a) 0.33, (b) 1.00, and (c) 3.33 Hz as labeled. Colors show clear variation between back-arc and forearc paths at 3.33 Hz, negligible at 0.33 Hz outside of basins. The thin lines, some labeled, show 25 km contours to the slab surface as in Figure A1. The thick black line labeled A–B shows the location of the section in Figure A7. The color version of this figure is available only in the electronic edition.

Comparison with acceleration from other Cook Inlet earthquakes, Mw≥5.0

We compare the Iniskin observations with accelerations from other nearby earthquakes (Table 1) as a test for source effects such as directivity. If other, nearby earthquakes show the same pattern in acceleration as the Iniskin main shock, then rupture effects are an unlikely explanation for the anomalous variability. These PSAs are calculated in the same manner, but then corrected to a common magnitude (Mw=5.53) and depth (78 km), by subtracting the difference in GMPE between the actual magnitude and depth and that calculated at the reference magnitude and depth from the GMPE of Abrahamson et al. (2016).

Figure A4 shows the normalized accelerations from all four moderate earthquakes. The difference between backarc and forearc stations remains, with 10-100x higher accelerations seen in the forearc near Anchorage. The range of accelerations at a given distance is similar to that observed for the mainshock (Figure A3). Again, the Denali region stations show accelerations more consistent with backarc sites. The highest accelerations only exceed the GMPE at 1 Hz by 5-10x, so are less extreme than the Iniskin mainshock, but the variability is similar. The primary conclusion is that the pattern of accelerations for the Iniskin mainshock is not unique and is almost certainly a path effect, although the absolute accelerations may be amplified by source processes.

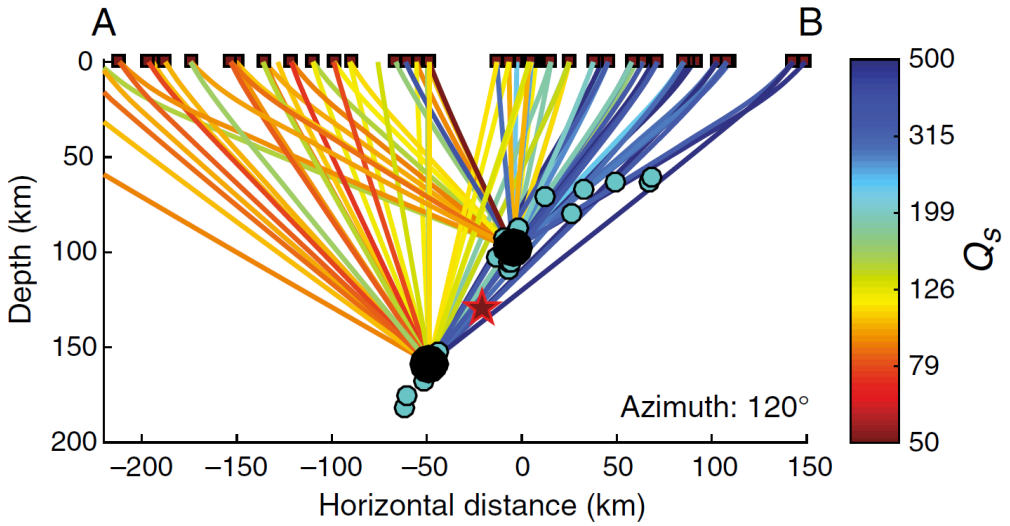

Figure A7: Cross section of path-average S-wave attenuation (1/Qs) from two earthquakes (black circles) near the Iniskin hypocenter recorded on the SALMON array (Tape et al., 2017), using methods similar to Stachnik et al. (2004). The location of profiles is shown in the right panel of Figure A6. Measurements of spectral slope in the 0.25–10 Hz band give integrated attenuation, which is divided by travel time to determine 1/Qs. The star shows the Iniskin mainshock, the black boxes show stations projected onto section, and other regional earthquakes are shown as teal circles. Note the strong contrast in Qs between back-arc and fore-arc paths; arc overlies 100 km depth of earthquakes.

The 2018 Anchorage Mw7.1 earthquake

We compare accelerations for the 30 November, 2018 earthquake (Figure A5). The moment magnitude is indistinguishable from that of the Iniskin mainshock (Mw=7.1) and it is also within the downgoing plate (Liu et al., 2019). However, the hypocenter is only 48 km deep so almost all energy recorded at these stations travels through the crust or uppermost mantle. Hence, the effects of deep structure should be different although the effects of near-surface features such as basins should be similar. The 2018 accelerations agree well with the GMPEs and show much less scatter than for any of the intermediate-depth earthquakes (Figures A3 and A4), and the distinction between backarc and forearc stations is not observed. The Anchorage network stations still show unusually high accelerations, again suggesting a site or structural effect. Also, obvious basin effects are limited. One station at R_{hypo} ~ 100 km, SW of the epicenter, sits over the thickest sediments in the Cook Inlet Basin and shows anomalously high acceleration (highlighted on Figure A5). We could not find acceleration data from this station in January 2016. Its presence shows that basin effects are obvious but limited to a small geographic region, and do not explain the overall trend.

Weak-motion observations

To better understand the nature of the deep structure effects, we examine a much more extensive broadband velocity (weak motion) dataset for earthquakes near the Iniskin mainshock. We focus on 222 earthquakes within 75 km of the Iniskin epicenter, at depths > 70 km and 3 < ML < 5. Approximately 112 stations provide on-scale recording for these earthquakes at epicentral distances up to 450 km. For each signal we filter in narrow frequency bands (±50% from the central frequency), calculate the peak ground velocity (PGV) from both horizontal-component records, and calculate the root-mean-square (RMS) of the two components. A simple

empirical geometric spreading correction is made by fitting the PGV at each frequency to a model of the functional form log10(PGV) = a1 + a2log10(R) + a3 R + a4ML, where R is the hypocentral distance. This functional form resembles the magnitude and distance variation in the GMPE of Atkinson and Boore (2003). The individual PGV measurements are weighted by signal noise during regression, calculated from pre-event ground velocities in the same way.

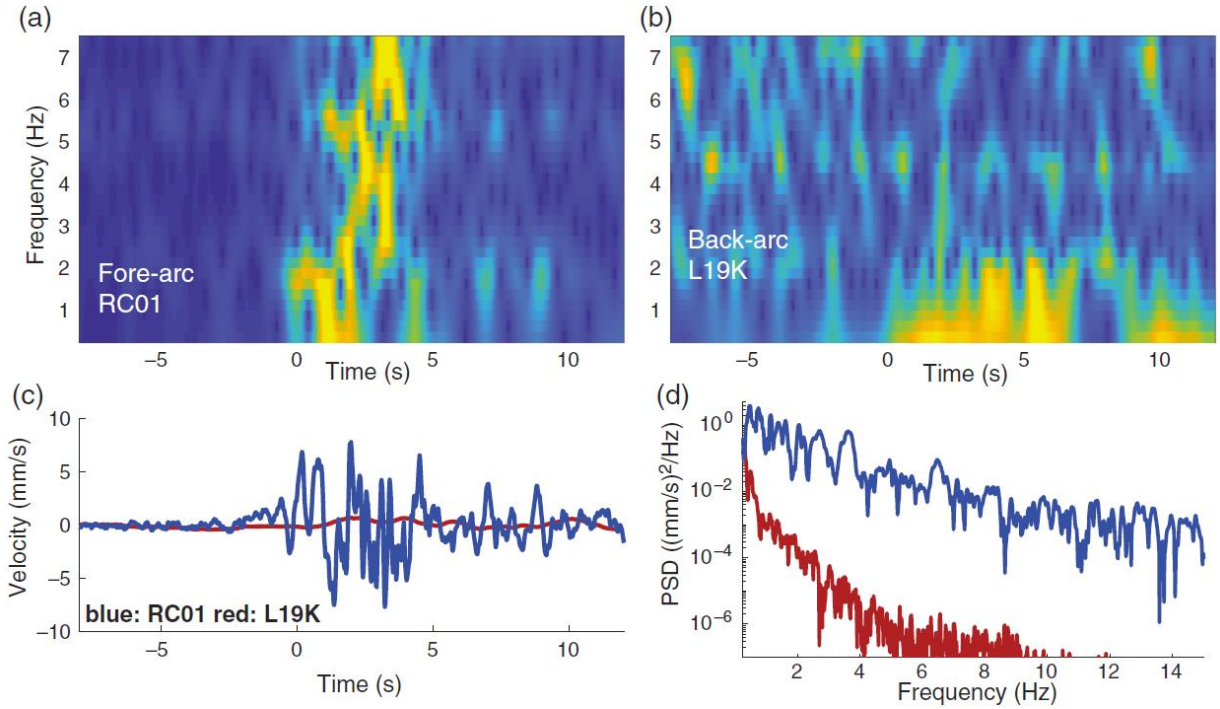

Figure A8: Spectrograms for S waves (north component) from the Iniskin earthquake for two stations at similar distance. (a) Fore-arc station near Anchorage (RC01, 257 km distance). (b) Back-arc station (L19K, 296 km distance). Spectrograms are calculated in the same manner as other body-wave dispersion studies (Abers, 2005), with brighter colors showing higher power. (c) North-component S waves integrated to velocity; time = 0 corresponds to picked S arrival. (d) Power spectra for these traces. Note the delayed high frequency (>3 Hz) relative to low-frequency energy at RC01 but not L19K, and the strong enhancement in high frequencies for RC01, both characteristic of slab waveguide effects.

Station-averaged residuals from this fit illustrate spatial variability in ground motion that cannot be explained as a simple effect of distance and source magnitude (Figure A6). Specifically, this procedure fits well the PGV at low frequencies (0.33 Hz) with most stations

lying within 0.3 log10-units of the regression. Exceptions are for stations in major basins (Cook Inlet, Bristol Bay) and near the trench, presumably due to sediment amplification. At higher frequencies the distinction between forearc and backarc paths becomes clearer, with two log10-units of variability (100x in PGV) at 3.33 Hz. This pattern strongly resembles that seen in strong-motion data for Cook Inlet intermediate-depth earthquakes (Figures A3, A4), and presumably has the same origin. These weak-motion data are available from far more earthquakes and stations so are robust and clearly delineate the spatial pattern of amplification with frequency. A sharp boundary between low and high amplitudes roughly follows the 70 km depth to slab surface.

Table 1. Earthquakes in this study with $Mw \geq 5.0$[1]

Date	Mw	Depth [km]	Latitude [°]	Longitude [°]
2016/01/24	7.1	110.7	59.64	-153.41
2018/11/30	7.1	48.2	61.35	-149.96
2018/03/09	5.0	103.2	59.78	-153.21
2017/11/05	5.1	139.6	60.23	-153.08
2017/03/02	5.6	91.9	59.58	-152.66
2015/07/29	6.4	129.8	60.02	-153.15

[1] Epicenters from Alaska Earthquake Center catalog; depth and *Mw* from GCMT

Basin effects

Deep basins of low-velocity sediment are well known to amplify ground shaking (e.g., Olsen, 2000). The Cook Inlet Basin in Alaska lies directly adjacent to both the large earthquakes studied here, and post-Mesozoic sediments reach thicknesses exceeding 7 km (Shellenbaum et al., 2010). However, two accelerometers and a handful of weak-motion stations used here lie within the basin (identified on Figures A4, A5). The station on the thickest sediments lies close to the deepest part of the basin and does show 2-5x higher accelerations than stations at similar distances, particularly near 1 Hz (Figure A5), consistent with expectation. That station only

recorded the 2018 Anchorage earthquake. However, most of the anomalous stations for the intermediate-depth Cook Inlet earthquakes here lie outside this basin and are on or near hard rock, so most of the high accelerations for the Iniskin earthquake must have another explanation.

Attenuation and waveguide focusing

The observed increasing variability at increasing frequency resembles what would be predicted from spatial variations in subcrustal attenuation. It has been long known that the sub-arc and backarc mantle is highly attenuating while signals traveling along slabs are very rich in high-frequency energy (e.g., Oliver and Isacks, 1967). In particular, very high attenuation (low Q) is observed in the mantle beneath many backarcs. In Alaska, Stachnik et al. (2004) mapped the attenuation structure along a corridor extending north from Anchorage, and saw a 10-50x decrease in Q for S waves in the mantle between the hot backarc and the cold forearc mantle – the mantle above where the slab was >75 km deep was highly attenuating. These Q estimates are based on the spectral fall-off of regional body waves from in-slab earthquakes recorded above them. For comparison, we calculate path-average Q for S waves recorded locally for two small earthquakes beneath Cook Inlet (Figure A7), using data from the TA and the SALMON temporary deployment (Tape et al., 2017) and the same technique as Stachnik et al. (2004). These show 5-10x lower Q for paths that traverse the backarc mantle compared with those that do not, similar to observations farther north (Stachnik et al., 2004). Because these path-averaged estimates include crustal portions of the raypath for which temperature variations are less, the Q differences are likely to be underestimates.

Additional effects amplify signals along forearc paths to produce high accelerations near Anchorage and the Kenai Peninsula. These signals travel distances exceeding 200 km along the top of the subducting plate, and similar paths have shown focusing of high frequency energy

caused by a waveguide due to subduction of low-velocity oceanic crust. High-frequency signals are focused by this waveguide for similar paths globally, typically at >2 Hz (e.g., Abers, 2005). In Alaska, these effects have been observed from earthquakes beneath Cook Inlet recorded to the northeast (Abers and Sarker, 1996). Signals from the Iniskin mainshock recorded near Anchorage show many characteristics of waveguides, notably enhanced high-frequency amplitudes, and delays of high-frequency energy relative to low frequency signals of 2-3 s (Figure A8). Similar effects were not observed for the 2018 Anchorage earthquake, presumably because the earthquake was too shallow – the top of the waveguide exists when fast mantle overlies low-speed material at the top of the downgoing plate, whereas the plate interface is about 40 km deep here and likely shallower than the upper-plate Moho.

A similar explanation has been proposed for anomalous accelerations recorded for the 7 September 2017 Tehuantepec Mw=8.2 in-slab earthquake, at 54 km depth, although deviations from GMPEs are less extreme than Iniskin (Sahakian et al., 2018), perhaps due to the shallower depth. Furumura and Kennett (2005) observed strong amplification for coastal Japan from intermediate-depth earthquakes in nearby subduction zones, although their physical model differs somewhat. Such waveguide focusing seems to be a common effect of subcrustal, intraslab earthquakes on forearc regions.

Summary and Recommendations

Anomalously high accelerations are observed from the 111-km-deep Iniskin (Mw 7.1) earthquake beneath Cook Inlet, but only at stations in regions above where the subducting plate is less than 50-70 km deep. That includes the greater Anchorage metropolitan area. The high amplitudes are particularly anomalous when compared with backarc sites north and northwest of the epicenter. The same pattern is observed for all intermediate-depth earthquakes in the Cook

Inlet region. The deeper path structure, and in particular the combination of a hot, high-attenuation backarc and low-attenuation and layered slab, appear to be the dominant effects responsible for these anomalous variations. These variations are not captured by standard GMPEs. The 2018 Anchorage earthquake is at a depth where the subducting plate has not yet descended beneath hot mantle, 48 km, so does not show these effects. Basin effects are also present at some frequencies at a small number of stations, but they are local and superimposed upon these much larger regional effects.

GMPEs could account for these large and first-order path effects. The most recent published subduction model we examine (Abrahamson et al., 2016) does include a flag that decreases predicted backarc amplitudes relative to other paths, but the change is significant only at frequencies > 1 Hz and produces much less of an effect than observed here (Figure A3). The datasets used for generating GMPEs from in-slab earthquakes are often dominated by back-arc and arc paths or other anomalous environments. For example, 98% of the accelerations used by Atkinson and Boore (2003) for in-slab earthquakes are from earthquakes <70 km deep, probably too shallow to encounter the mantle effects described here. Additional corrections should be added to account for increased acceleration along paths that follow subducting slabs, or that traverse attenuating backarc mantle, at least for earthquakes greater than 60-70 km deep. The comparison to the 30 November 2018 Anchorage earthquake shows that shallower earthquakes do not display these path-dependent variations. While such considerations further complicate ground motion prediction, the Iniskin experience shows that there is potential for damaging shaking from intraslab earthquakes (also demonstrated by the 2017 Mexico earthquakes), especially where population centers lie in forearcs over the shallow parts of subducting plates

APPENDIX A REFERENCES

Abers, G. A. (2005). Seismic low-velocity layer at the top of subducting slabs beneath volcanic arcs: observations, predictions, and systematics. *Phys. Earth Planet. Int.*, 149, 7–29.

Abers, G. A., & G. Sarker. (1996). Dispersion of regional body waves at 100-150 km depth beneath Alaska: In situ constraints on metamorphism of subducted crust. *Geophys. Res. Lett., 23*, 1171–1174.

Abrahamson, N., Gregor, N., & Addo, K. (2016). BC Hydro ground motion prediction equations for subduction earthquakes. *Earthquake Spectra*, *32*(1), 23–44.

Anderson, J. G., & Brune, J. N. (1999). Probabilistic seismic hazard analysis without the ergodic assumption. Seismological Research Letters, 70(1), 19-28.

Atkinson, G. M., & Boore, D. M. (2003). Empirical ground-motion relations for subduction-zone earthquakes and their application to Cascadia and other regions. *Bull. Seismol. Soc. Amer., 93*, 1703–1729.

Boore, D. M., Watson-Lamprey, J., & Abrahamson, N. (2006). Orientation-independent measures of ground motion. *Bull. Seismol. Soc. Amer., 96*, 1502-1511.

Davies, J., L. Sykes, L. House, & K. Jacob. (1981). Shumagin seismic gap, Alaska Peninsula: History of great earthquakes, tectonic setting and evidence for high seismic potential. *J. Geophys. Res., 86*, 3821–3856.

Dutta, U., Biswas, N., Martirosyan, A., Papageorgiou, A., & Kinoshita, S. (2003). Estimation of earthquake source parameters and site response in Anchorage, Alaska from strong-motion network data using generalized inversion method. *Physics of the Earth and Planetary Interiors*, *137*(1), 13–29.

Ekström, G., Nettles, M., & Dziewonski, A. M. (2012). The global CMT project 2004-2010: Centroid-moment tensors for 13,017 earthquakes. *Phys. Earth Planet. Int.*, *200–201*, 1–9.

Furumura, T., & Kennett, B. L. N. (2005). Subduction zone guided waves and the heterogeneity structure of the subducted plate: Intensity anomalies in northern Japan. *J. Geophys. Res.*, *110*, B10302.

Grapenthin, R., West, M., Tape, C., Gardine, M., & Freymueller, J. (2018). Single-Frequency Instantaneous GNSS Velocities Resolve Dynamic Ground Motion of the 2016 M w 7.1 Iniskin, Alaska, Earthquake. *Seismological Research Letters*, *89*(3), 1040–1048.

Haddadi, H., Shakal, A., Huang, M., Parrish, J., Stephens, C., Savage, W., & Leith, W. (2012). Report on progress at the center for engineering strong motion data (CESMD) (pp. 1–7). Presented at the Proc. World Conf. Earthq. Eng., Lisbon.

Liu, C., Lay, T., Xie, Z., & Xiong, X. (2019). Intraslab Deformation in the 30 November 2018 Anchorage, Alaska, M_W 7.1 Earthquake. *Geophysical Research Letters*, *46*, doi:10.1029/2018GL082041.

Martin, S., A. Rietbrock, C. Haberland, and G. Asch, Guided waves propagating in subducted oceanic crust, *J. Geophys. Res., 108(B11)*, 2536, doi:10.1029/2003JB002450, 2003.

Oliver, J., & B. Isacks (1967). Deep earthquake zones, anomalous structures in the upper mantle, and the lithosphere. *J. Geophys. Res.*, *72*, 4259–4275.

Olsen, K. (2000). Site amplification in the Los Angeles basin from three-dimensional modeling of ground motion. *Bulletin of the Seismological Society of America*, *90*(6B), S77–S94.

Ratchkovski, N. A., & Hansen, R. A. (2002), New Constraints on Tectonics of Interior Alaska: Earthquake Locations, Source Mechanisms, and Stress Regime. *Bulletin of The Seismological Society of America, 92*, 998-1014. doi:10.1785/0120010182

Sahakian, V. J., Melgar, D., Quintanar, L., Ramírez-Guzmán, L., Pérez-Campos, X., & Baltay, A. (2018). Ground Motions from the 7 and 19 September 2017 Tehuantepec and Puebla-Morelos, Mexico, Earthquakes. *Bulletin of the Seismological Society of America*, *108*(6), 3300–3312.

Shellenbaum, D. P., Gregersen, L. S., & Delaney, P. R. (2010). Top Mesozoic unconformity depth map of the Cook Inlet basin, Alaska, Report of Investigations 2010-2. Fairbanks: Alaska Division of Geological and Geophysical Surveys.

Stachnik, J. C., Abers, G. A., & Christensen, D. (2004). Seismic attenuation and mantle wedge temperatures in the Alaska subduction zone. *J. Geophys. Res., 109,* B10304, doi:10.1029/2004JB003018.

Tape, C., Christensen, D., Moore-Driskell, M. M., Sweet, J., & Smith, K. (2017). Southern Alaska Lithosphere and Mantle Observation Network (SALMON): A seismic experiment covering the active arc by road, boat, plane, and helicopter. *Seismological Research Letters*, *88*(4), 1185–1202.

West, M., M. Gardine, N. Ruppert, C. Tape, S. Holtcamp, J. Freymueller and G. Abers (2016), Perspectives on the Mw7.1 Iniskin earthquake, *Annual Meeting, Seismol. Soc. Am., Seismol. Res. Lett., 87(2B),* 470.

Witze, A. (2013). US seismic array eyes its final frontier. *Nature*, *503*(7474), 16-17. doi:10.1038/503016a

Yong, A., Thompson, E.M., Wald, D., Knudsen, K.L., Odum, J.K., Stephenson, W.J., and Haefner, S. (2015). Compilation of Vs30 Data for the United States: U.S. Geological Survey Data Series 978, 8 p.

Youngs, R. R., Chiou, S. J., Silva, W. J., & Humphrey, J. R. (1997). Strong ground motion attenuation relationships for subduction zone earthquakes. *Seismological Research Letters*, *68*(1), 58–73

APPENDIX B

SUPPLEMENTARY MATERIAL FOR CHAPTER 2

Common Conversion Point Stacking: Method Overview

A Common Conversion Point (CCP) stacking method is employed to better image subhorizontal discontinuity structure in three dimensions (Dueker and Sheehan, 1997). The CCP stacking method back-projects RFs through the 1-D reference velocity model (Fig. B1), converting time to depth for the ray parameter of the incident signal for three different assumptions about the phase generating the signal (Ps, Ppxs or Psxs; Fig. B4). The direct (Ps) phase is filtered between 0.03 Hz and 0.4 Hz and the reverberated (Ppxs and Psxs) phases are filtered between 0.03 Hz and 0.2 Hz, to approximately account for varying resolution. After filtering and converting RF lag time to conversion depth and lateral offset, the signal's amplitudes are added to those in the bin corresponded to that spatial location, averaged with all other signals passing through that common conversion point. The three resulting CCP volumes are stacked separately, corresponding to Ps, Ppxs, or Psxs conversions. Each phase's CCP volume uses the same RFs that are used in the single-phase migration images. The Ppxs and Psxs phases are treated as a plane wave reflecting off the free surface, then reflecting off the subsurface discontinuity. Projected signals are binned in nodes spaced 2 km x 2 km horizontally and 1 km vertically, after smoothing the signal horizontally with an 8-km-wide Gaussian operator to mimic Fresnel-zone averaging. The reverberated-phase CCP volumes (Ppsx and Psxs) are averaged together to make our final image (Fig. B5). The Ps CCP volume is not stacked together because it appears saturated compared to the reverberated volumes, and because the actual RFs

themselves are not coherent (e.g. Fig. B2a). Because CCP stacking assumes flat-lying layers, conversions from the dipping JdF Moho decorrelate in some places and are not interpreted here; this method optimally focuses subhorizontal interfaces (Rondenay, 2009).

Common Conversion Point Stacking: Continental Moho Selection

The continental Moho is mapped as the maximum CCP volume amplitude between 30 km and 50 km depth within nodes that include more than six measurements. Measurements are defined as the number of values added to a node, including both direct intersection of the ray path with a node as well as any value added to a node from adjacent ray paths due to horizontal smoothing. These amplitudes are identified and mapped in CCP stack (Fig. B7). To accurately measure the depth of this amplitude peak, CCP amplitudes are extracted between 26 km and 54 km depth from each vertical slice through the volume, then tapered with depth using a Tukey window such that amplitudes are unaffected between 30 and 50 km depth. Peak amplitudes and depths of the continental Moho are determined by fitting a Gaussian function to each such tapered column of the CCP volume.

Both the Ppxs and Psxs CCP Moho maps show a coherent continental Moho of appropriate depth, comparable to previous studies (see main text). The Moho picks from the average of these two CCP volumes are stacked together to generate the final stack and analysis (Fig. 1.2d; Fig. B5; Fig. B7). The continental Moho signal disappears 15 km west of MSH in our CCP stacking image, while farther west this procedure picks up the JdF Moho (Fig. 1.2d). We define the westward extent of the continental Moho as the point at which our procedure begins to pick the JdF Moho and has reduced amplitude (Fig. 1.2d). The continental crust is thicker to the north of MSH (40-44 km) than to the south and southeast, with the thinnest crust (34 km)

found 15 km south-southeast of MSH beneath the Indian Heaven volcanic field. The Ps CCP Moho picks are dissimilar to the other Moho maps, but that is to be expected given the incoherence of the Ps RFs (Fig. B2a). The time-to-depth conversion results in a factor of 2.5-3.0 decrease in resolution of this phase relative to the surface-reflected ones. As a result, the Ps Migration image (Fig. 1.3d) and Ps CCP volume (Fig. B4a) are not interpreted here.

Minimum Resolvable Moho Velocity Contrast

To estimate the uncertainty in the velocity contrast across the Moho, and hence the smallest amplitude that could be resolved, we estimate the smallest velocity contrast associated with visible boundaries in the migration images. To do this, amplitudes of the composite migration image (Fig. 1.3a) between 30 and 50 km depth are extracted (Fig. B9a). For each vertical column in this section, we find the difference between the maximum and minimum value to estimate the maximum velocity contrast imaged (Fig. B9b). At the point where we have visually determined the westward extent of the imaged continental Moho, the maximum velocity contrast imaged is ~2%, so we can say that we are able to image the Moho boundary down to at least a 2% velocity contrast. At the eastern edge of the image where ray coverage degrades, the peak-to-peak amplitudes are again 1 – 2 %. Thus, the migration method seems capable of imaging Moho contrasts greater than 2%.

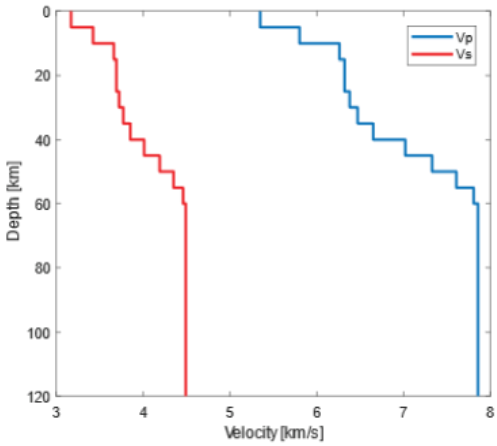

Layer Top Depth [km]	Layer Bottom Depth [km]	Vp [km/s]	Vs [km/s]	Density [g/cm^3]
0	5	5.35	3.17	2.59
5	10	5.8	3.42	2.68
10	15	6.26	3.66	2.78
15	25	6.32	3.69	2.79
25	30	6.38	3.72	2.8
30	35	6.47	3.77	2.83
35	40	6.65	3.85	2.87
40	45	7.02	4.01	3.5
45	50	7.33	4.19	3.5
50	55	7.61	4.35	3.5
55	60	7.81	4.46	3.5
60	300	7.86	4.49	3.5

Figure B1. Velocity model used in this study. The Vs model is generated from an inversion of surface wave and ambient noise phase velocities from the iMUSH array and surrounding stations (Crosbie, 2018). The Vp and density models for the upper 40 km are generated from the Vs model using the regressions from Brocher et al. (2005). The Vp values for depths below 40 km are generated from the Vs model assuming a Vp/Vs of 1.75, and the density is set to 3.5 g/cm^3.

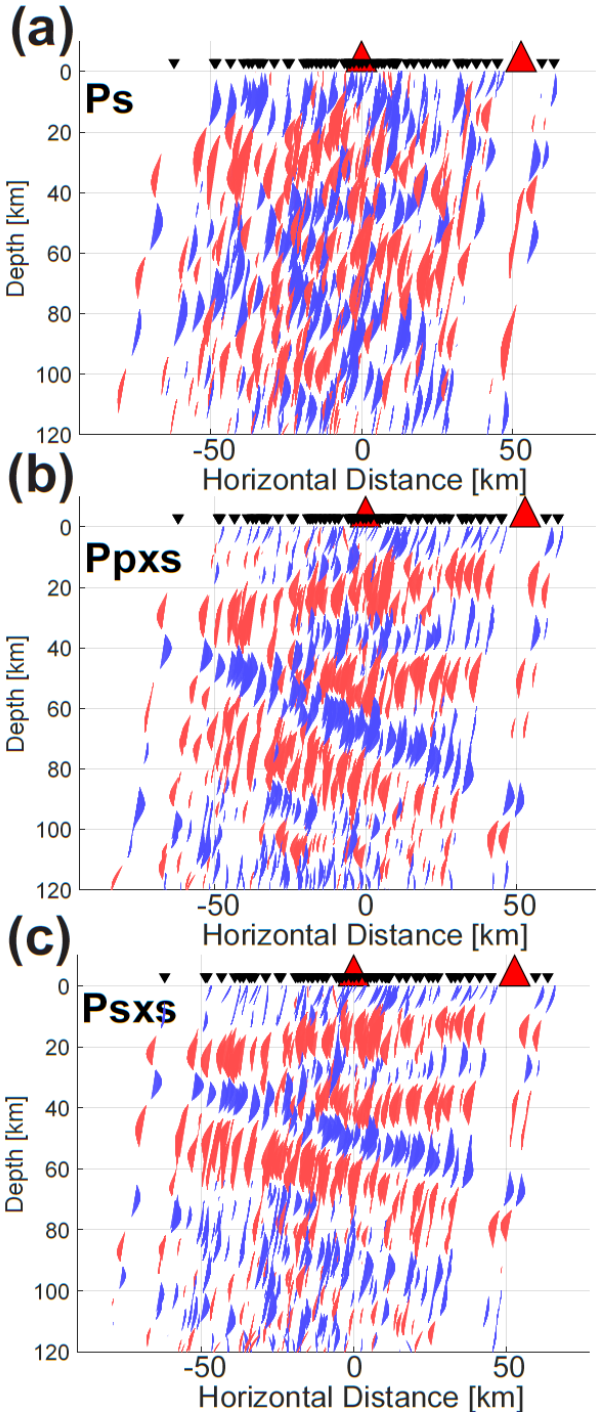

Figure B2. Example RFs back-projected in each phase for the M6.8 earthquake that occurred 231 km beneath Vanuatu on January 23, 2015, the same earthquake used to generate RFs in Figure 2.3a. RFs projected onto same projection line as migration images. Blue is positive, red is negative. Back azimuth

is 244 degrees clockwise from North. (a) Ps. (b) Ppxs. (c) Psxs-SV. Note: Psxs phase has reversed polarity, so JdF and continental Mohos are red in (c).

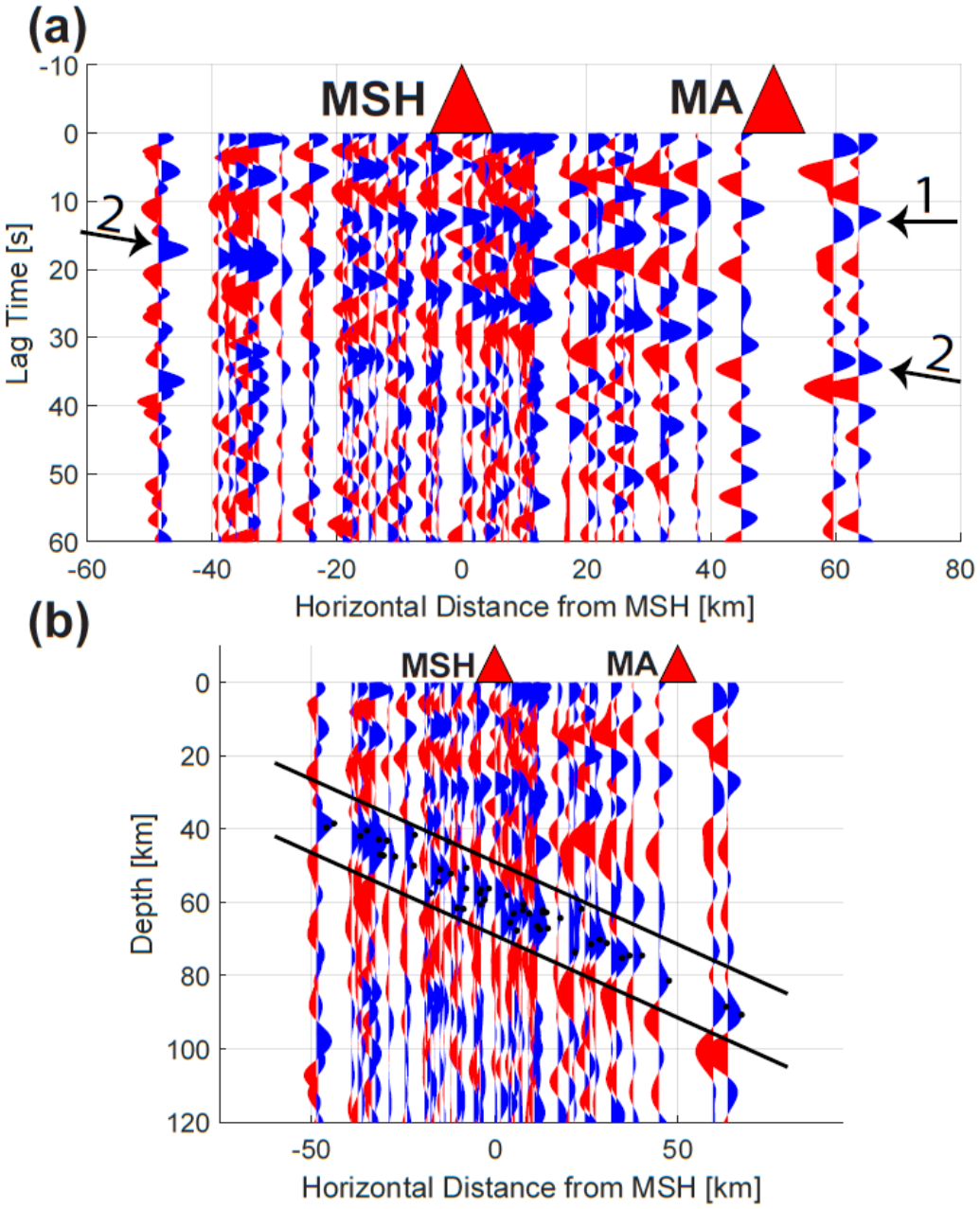

Figure B3. RFs from the same earthquake used to generate RFs in Figure 2.2a and Figure B2. Blue is positive, red is negative. RFs projected onto same projection line as migration images. (a) raw RFs. 1: points to continental Moho in Ppxs, 2: points to JdF Moho in Ppxs. (b) Example plot of Ppxs RFs used to pick positive peaks for back-projection and creation of Figure 2.2c. RFs projected to depth in same

velocity model as Figure 2.2b. Black lines outline area where peaks are selected for this event. Black dots show picked peaks for this event.

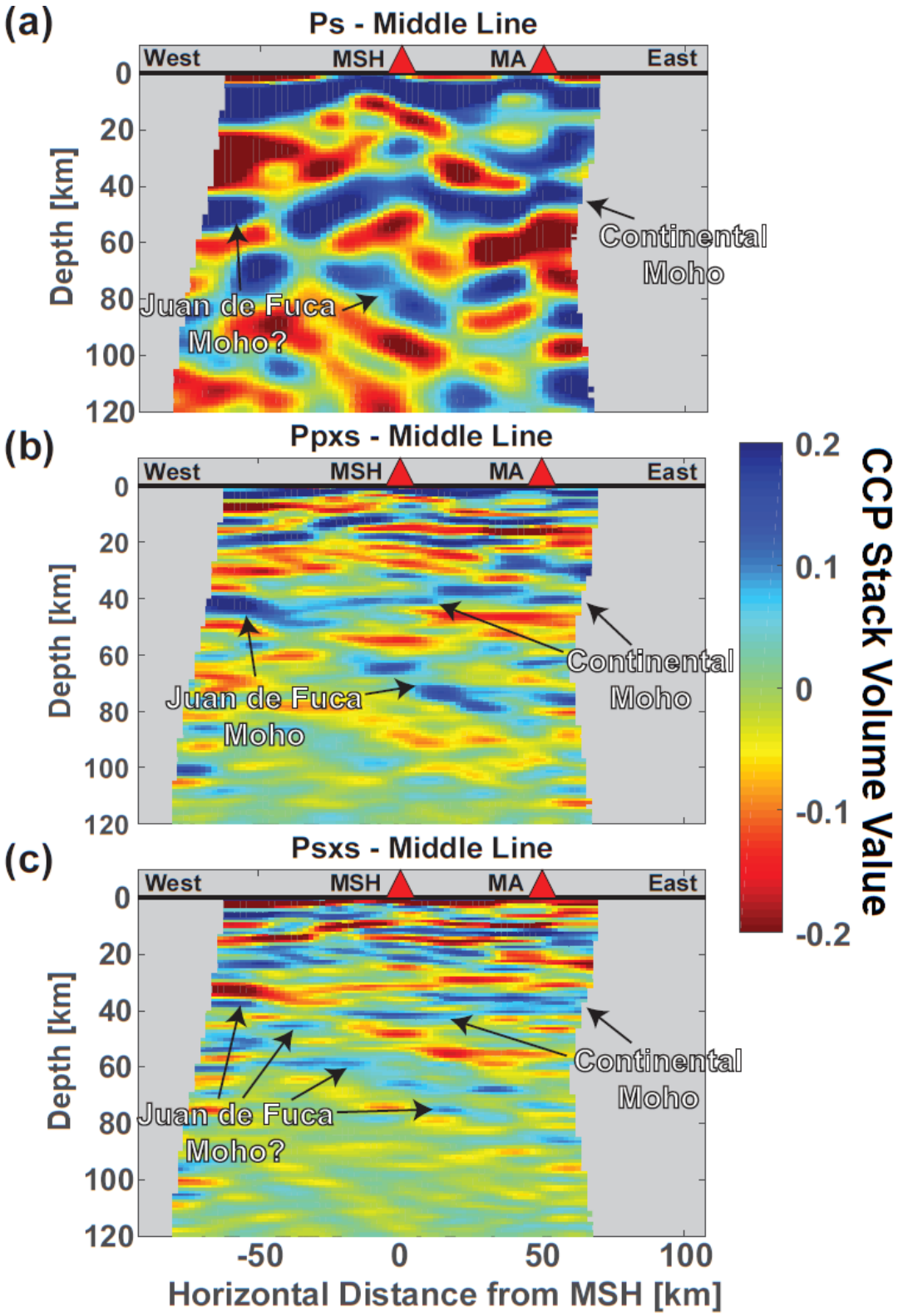
(a)
Ps - Middle Line
West
MSH
MA
East
Depth [km]
0
20
40
60
80
100
120
Continental Moho
Juan de Fuca Moho?
(b)
Ppxs - Middle Line
Continental Moho
Juan de Fuca Moho
(c)
Psxs - Middle Line
Continental Moho
Juan de Fuca Moho?
-50
0
50
100
Horizontal Distance from MSH [km]
0.2
0.1
0
-0.1
-0.2
CCP Stack Volume Value

Figure B4. Cross sections of the 3-D individual-phase CCP volumes for the (a) Ps, (b) Ppxs, and (c) Psxs RF phases along an east-west line through MSH (Middle line in Fig. B5d). Question marks denote questionable boundaries.

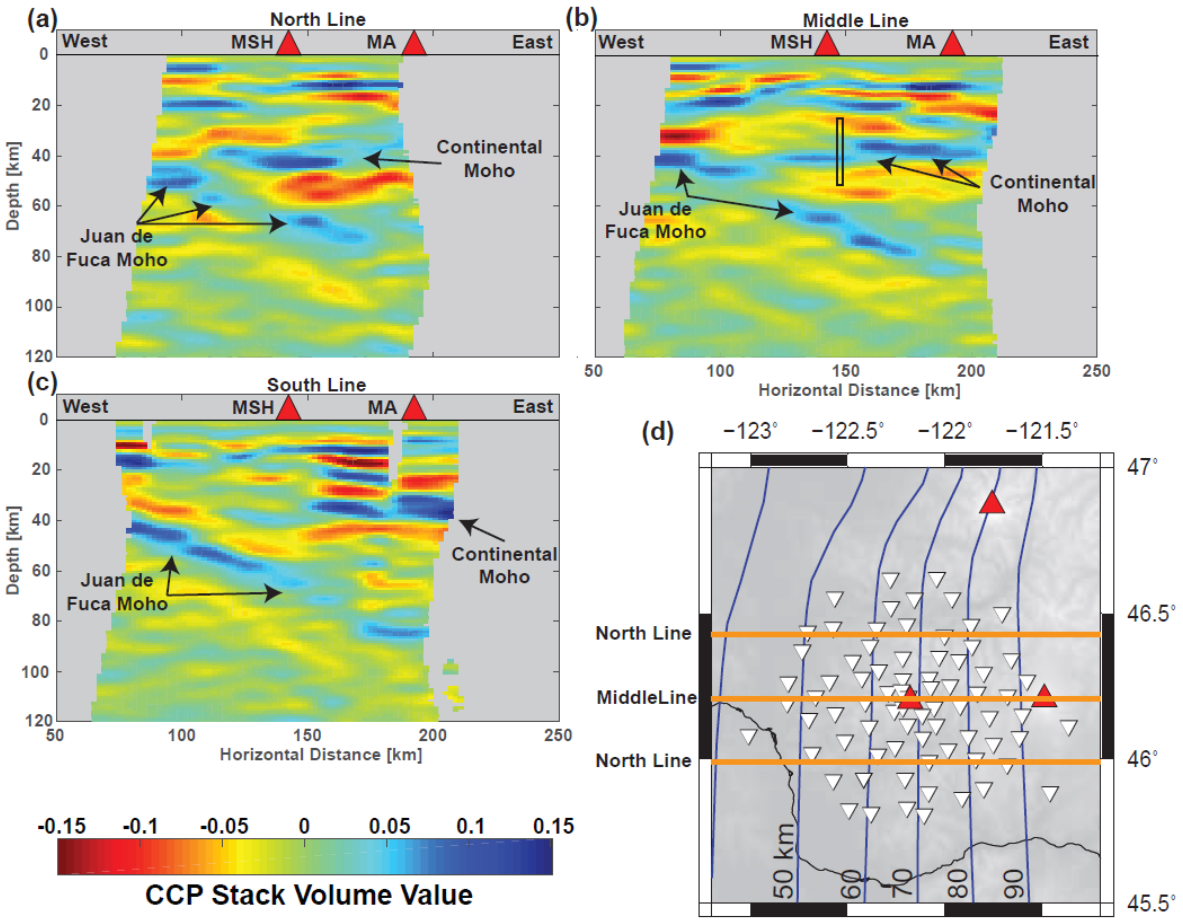

Figure B5. Three slices through our CCP stack volume generated by averaging together the CCP stack volumes from Ppxs and Psxs phases. All nodes with fewer than 6 measurements are masked out as grey. Positive (blue) on these plots represent positive values in the RFs. Black box in Part (b) is outline of values used in Figure B6. Orange lines in Part (d) are surface projections of the cross sections shown in parts (a)-(c), with each labeled on the left.

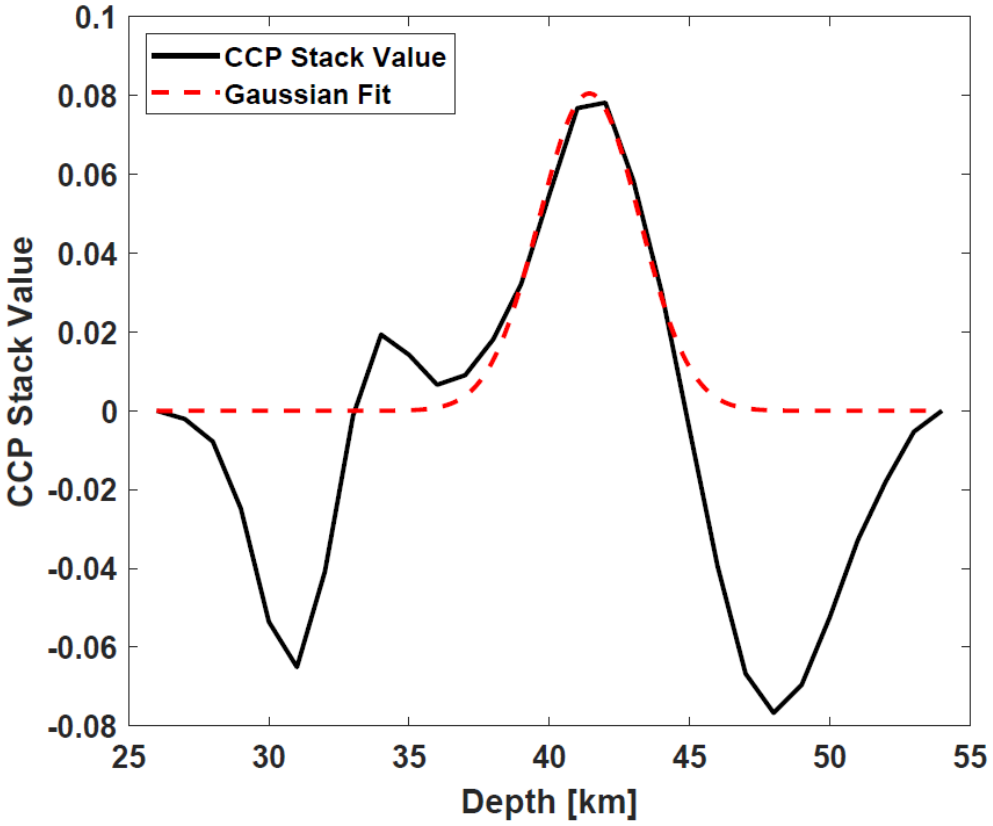

Figure B6. Example gaussian fit (described in Chapter 2 and Appendix B) of vertical slice through CCP stack volume, used to estimate Moho depth and strength. Data shown is from thin black box in Figure S5b.

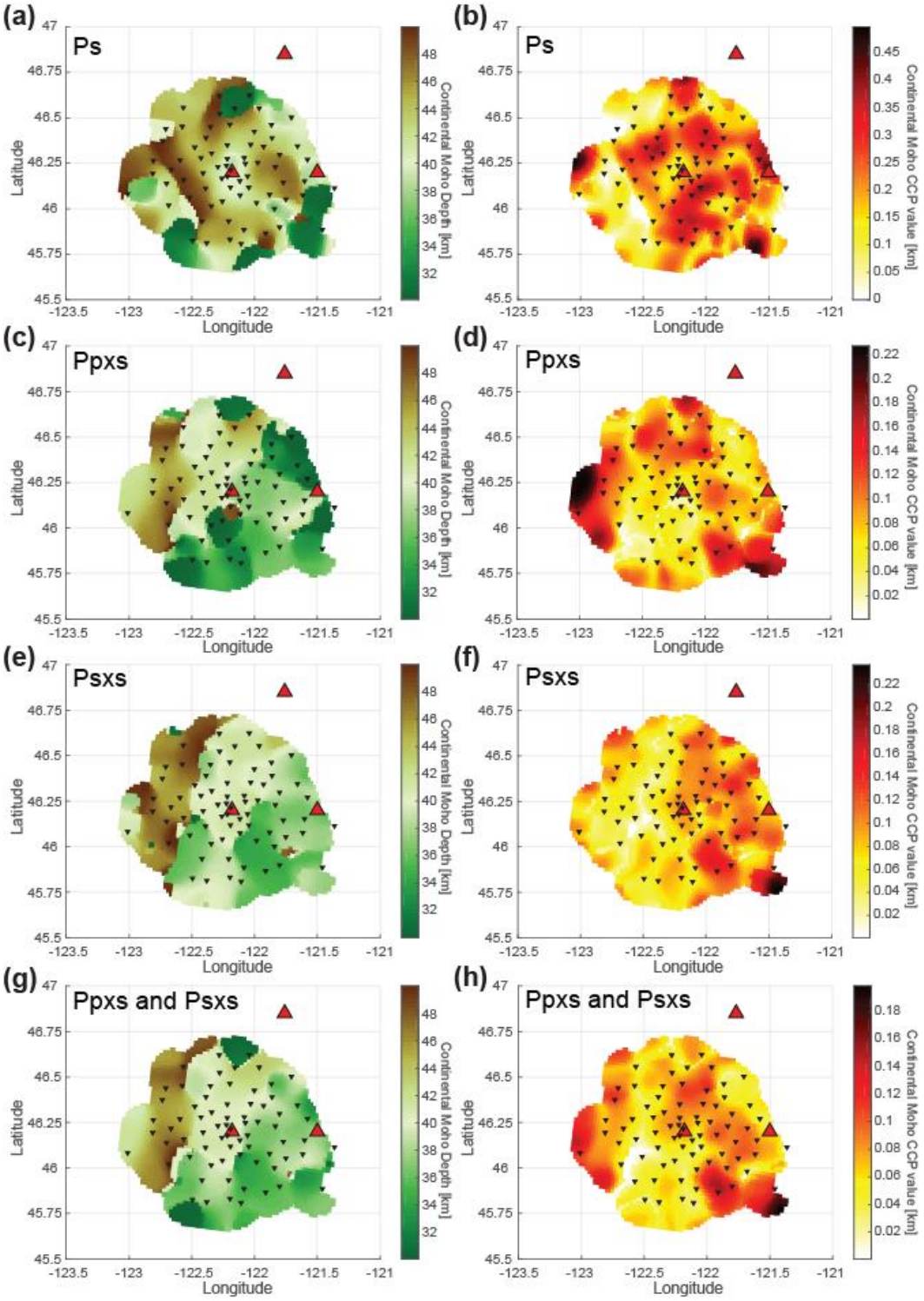
(a)
Ps
(b)
Ps
(c)
Ppxs
(d)
Ppxs
(e)
Psxs
(f)
Psxs
(g)
Ppxs and Psxs
(h)
Ppxs and Psxs
Latitude
Longitude
Continental Moho Depth [km]
Continental Moho CCP value [km]

Figure B7. (a) Ps Moho depth. (b) Ps Moho amplitude. (c) Ppxs Moho depth. (d) Ppxs Moho amplitude. (e) Psxs Moho depth. (f) Psxs Moho amplitude. (g) Average of Ppxs and Psxs CCP volume, Moho depth. (h) Average of Ppxs and Psxs CCP volume, CCP stacking maximum amplitude of Moho conversion.

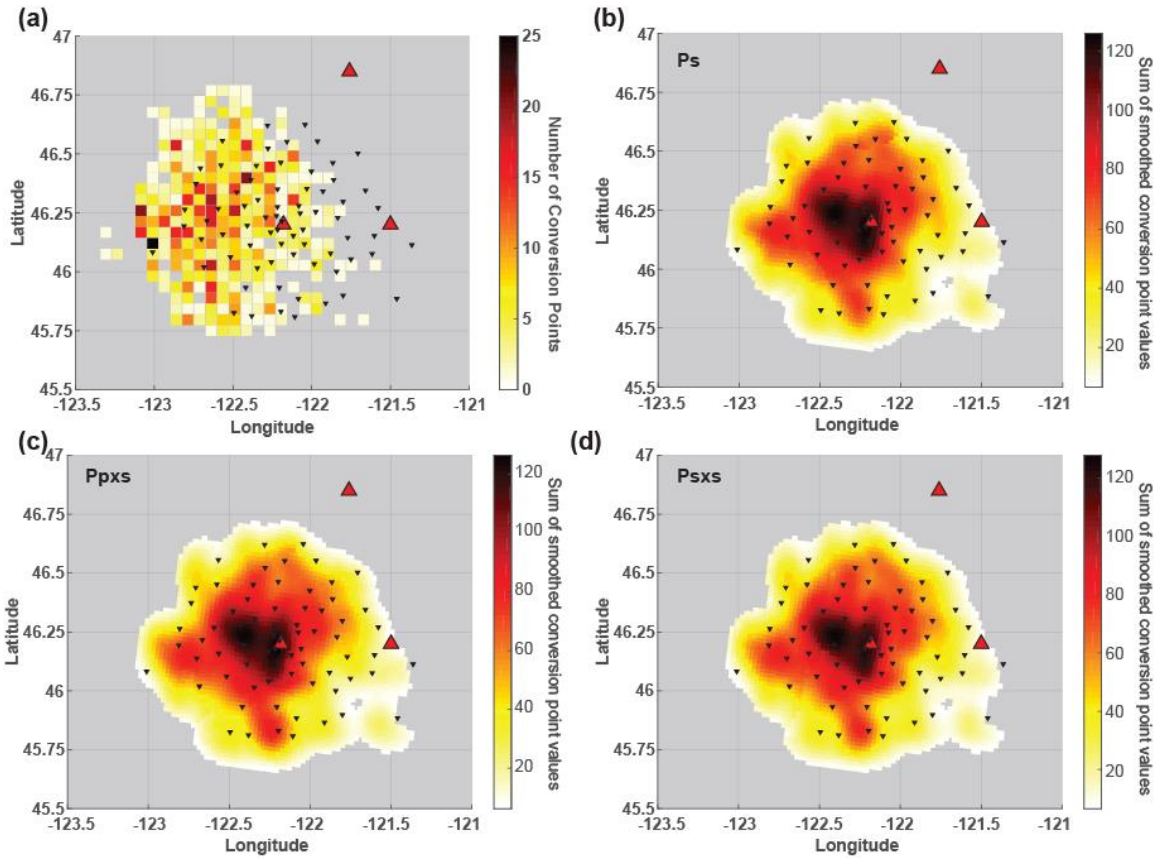

Figure B8. Ray coverage plots. (a) Bin hit count for Figure 2.2c. (b-d). Total number of measurements in nodes that were selected by Moho-picking analysis (see Section 2.4.2 of Chapter 2 and Appendix B).

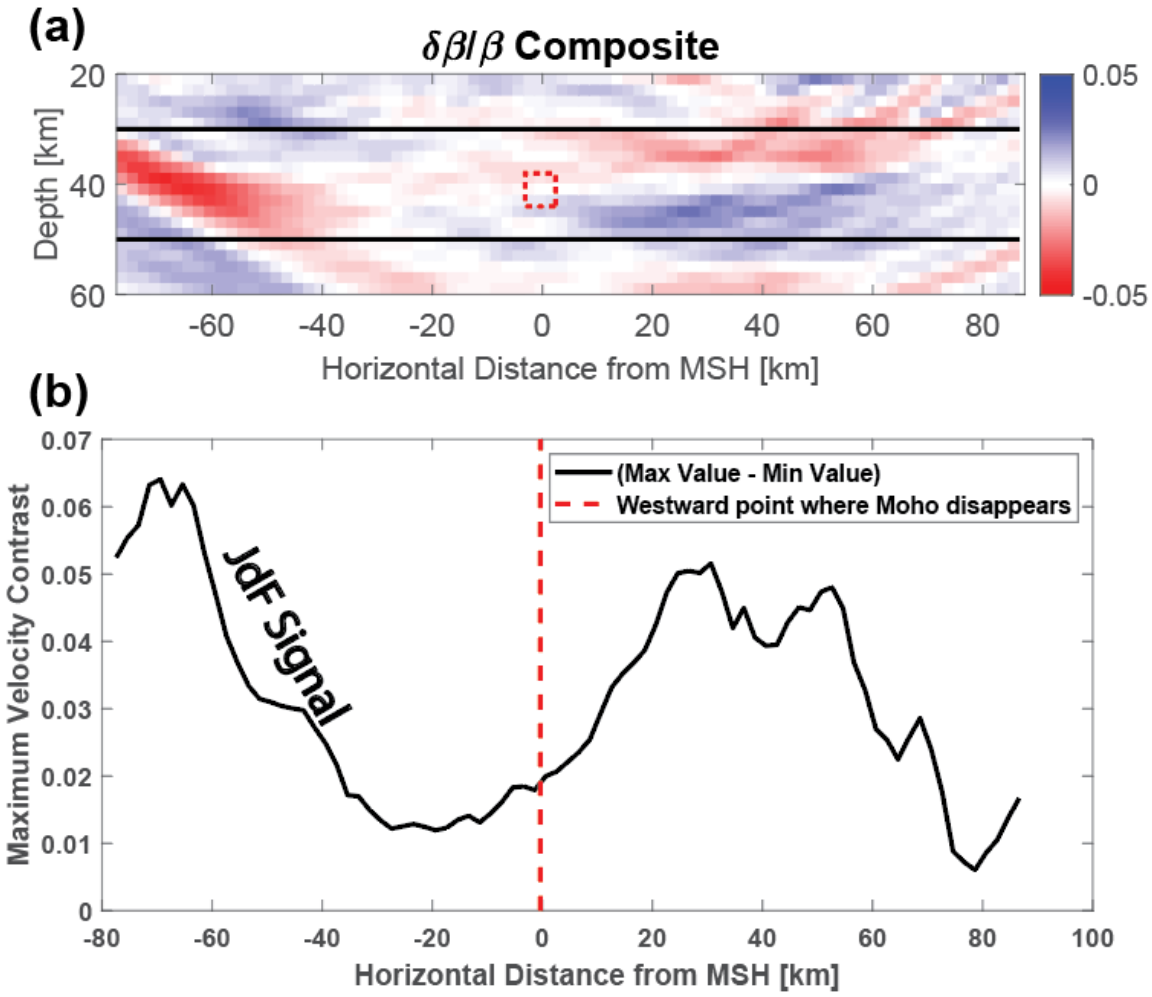

Figure B9. Part (a): zoom in on the composite S-migration image (Fig. 1.3a) between 20 and 60 km depth. Black lines denote upper and lower boundaries between which we extract values for Moho velocity contrast determination. Red dotted square outlines where we visually determine the westward extent of the continental Moho. Part (b): Maximum velocity contrast within two black lines in part (a).

Latitude	Longitude	Depth (km)	Magnitude	Distance (Δ)	Back-Azimuth	Date	PS	PPXP	PPXS	PSXS-SV	PSXS-SH
42.64	13.22	12	6.2	82.74	31.38	8/24/2016	0	1	0	1	0
50.45	142.3	12.5	5.8	59.06	312.36	8/14/2016	1	0	0	0	0
18.5	145.7	208.9	7.7	78.19	284.49	7/29/2016	0	0	1	0	0
47.68	146.91	423.2	5.8	58.25	307.66	7/23/2016	1	0	1	1	0
-28.05	-176.27	17.9	6.4	88.92	225.64	7/13/2016	1	1	1	1	0
12.92	-87.13	13.7	6.1	44.47	126.96	6/10/2016	1	0	0	0	0
-22.13	-178.17	417.5	6.9	85.02	230.42	5/28/2016	1	0	1	1	0
16.61	-97.79	23.9	5.9	35.87	137.51	5/8/2016	1	0	0	0	0
-16.05	167.26	33.5	7	88.75	245.02	4/28/2016	1	1	1	1	1
37.81	141.77	48.5	5.9	67.37	301.66	4/20/2016	1	0	1	0	0
-29.66	-111.74	21.7	5.5	76.45	170.68	4/16/2016	1	1	0	1	1
32.84	130.77	12.9	7	77.24	304.55	4/15/2016	1	0	1	1	1
-13.92	166.54	31.5	6.6	87.59	246.94	4/7/2016	0	0	1	1	0
-14.06	166.59	32.4	6.7	87.67	246.81	4/6/2016	1	1	1	1	0
-14.27	166.66	34.8	6.8	87.78	246.62	4/3/2016	0	1	1	1	1
51.4	-174.13	15.9	6	33.88	298.20	3/19/2016	0	0	0	1	0
53.86	158.73	168.1	7.2	48.69	309.56	1/30/2016	1	0	1	1	0

35.59	**-3.6**	**12**	**6.4**	**81.33**	**46.25**	**1/25/2016**	**1**	**1**	**0**	**1**	**0**
-14.88	**167.19**	**140.9**	**7.1**	**87.91**	**245.83**	**10/20/2015**	**1**	**1**	**1**	**1**	**1**
-16.14	**-172.98**	**17.8**	**6**	**77.32**	**229.73**	**10/18/2015**	**1**	**0**	**1**	**1**	**1**
-30.88	**-71.62**	**51.7**	**6.3**	**89.60**	**138.48**	**9/26/2015**	**1**	**1**	**0**	**1**	**1**
-31.13	**-72.09**	**17.4**	**8.3**	**89.60**	**138.96**	**9/16/2015**	**1**	**1**	**0**	**1**	**1**
-10.78	**163.71**	**20.6**	**6.4**	**87.07**	**251.09**	**8/15/2015**	**1**	**0**	**1**	**1**	**1**
-9.35	**158.07**	**12**	**6.6**	**89.76**	**256.16**	**8/10/2015**	**1**	**1**	**1**	**1**	**0**
-27.22	**-175.75**	**12**	**5.7**	**87.97**	**225.72**	**8/9/2015**	**1**	**1**	**1**	**1**	**1**
13.92	**-58.38**	**19.4**	**6.5**	**61.95**	**99.31**	**7/16/2015**	**1**	**0**	**0**	**0**	**0**
-9.4	**158.33**	**14.6**	**6.7**	**89.62**	**255.94**	**7/10/2015**	**1**	**0**	**1**	**1**	**1**
43.93	**148.12**	**54.4**	**6.3**	**59.78**	**303.54**	**7/7/2015**	**1**	**0**	**1**	**0**	**0**
-20.76	**-174.32**	**48.2**	**5.8**	**81.87**	**228.22**	**7/6/2015**	**1**	**1**	**1**	**1**	**1**
-15.54	**-172.69**	**51.3**	**6**	**76.66**	**229.83**	**6/12/2015**	**1**	**1**	**1**	**1**	**1**
30.8	**143**	**17.5**	**6.2**	**71.36**	**295.40**	**5/30/2015**	**0**	**0**	**1**	**1**	**0**
-15.69	**-173.19**	**70.3**	**6**	**77.05**	**230.16**	**5/30/2015**	**1**	**0**	**1**	**1**	**1**
27.94	**140.56**	**680.7**	**7.9**	**74.88**	**294.80**	**5/30/2015**	**1**	**1**	**1**	**1**	**0**
-19.4	**-176.05**	**16**	**6.3**	**81.65**	**230.35**	**5/24/2015**	**1**	**1**	**0**	**0**	**0**
-10.78	**163.91**	**19**	**6.8**	**86.94**	**250.95**	**5/20/2015**	**1**	**1**	**1**	**1**	**1**

38.89	**142.29**	**43.9**	**6.8**	**66.35**	**302.24**	**5/12/2015**	**1**	**0**	**1**	**1**	**0**
-20.79	**-178.71**	**591.4**	**6.1**	**84.22**	**231.61**	**4/28/2015**	**1**	**1**	**1**	**1**	**0**
23.96	**122.31**	**34.4**	**6.4**	**88.81**	**304.42**	**4/20/2015**	**1**	**0**	**1**	**1**	**0**
-15.25	**-173.17**	**43.2**	**6.3**	**76.67**	**230.39**	**4/7/2015**	**1**	**0**	**1**	**1**	**0**
-18.47	**-69.44**	**140.8**	**6.4**	**80.28**	**130.01**	**3/23/2015**	**1**	**1**	**0**	**1**	**1**
6.83	**-73.11**	**155.9**	**6.2**	**57.58**	**117.30**	**3/10/2015**	**1**	**1**	**0**	**1**	**1**
-16.41	**168.23**	**12**	**6.4**	**88.42**	**244.08**	**2/19/2015**	**0**	**0**	**1**	**1**	**1**
52.7	**-32.74**	**25.2**	**7.1**	**54.67**	**47.96**	**2/13/2015**	**0**	**0**	**0**	**1**	**0**
-23.14	**-66.8**	**223**	**6.7**	**85.53**	**130.62**	**2/11/2015**	**1**	**1**	**1**	**1**	**1**
-17.06	**168.36**	**231**	**6.8**	**88.83**	**243.56**	**1/23/2015**	**1**	**1**	**1**	**1**	**1**
-19.76	**-177.61**	**445.4**	**7.1**	**82.79**	**231.36**	**11/1/2014**	**1**	**1**	**1**	**1**	**1**
-15.12	**-174.58**	**13.9**	**6**	**77.32**	**231.63**	**10/28/2014**	**1**	**0**	**0**	**0**	**0**
-32.34	**-110.81**	**12**	**6.9**	**79.21**	**170.24**	**10/9/2014**	**1**	**1**	**1**	**1**	**1**
15.38	**147.66**	**13.8**	**5.6**	**79.07**	**280.89**	**10/6/2014**	**1**	**0**	**1**	**1**	**0**
13.54	**144.51**	**140.4**	**6.8**	**82.52**	**281.79**	**9/17/2014**	**1**	**0**	**1**	**1**	**0**
-26.89	**-114.56**	**12**	**6.1**	**73.42**	**172.91**	**9/6/2014**	**1**	**1**	**1**	**1**	**1**
-21.53	**-173.15**	**46.5**	**6**	**81.92**	**226.87**	**9/4/2014**	**1**	**0**	**1**	**1**	**0**
64.61	**-17.19**	**12**	**5.5**	**54.88**	**30.42**	**9/1/2014**	**1**	**0**	**1**	**1**	**1**

-14.61	**-73.72**	**84.5**	**6.8**	**74.81**	**131.36**	**8/24/2014**	**1**	**1**	**1**	**1**	**1**
41.25	**142.37**	**48.9**	**6.1**	**64.76**	**304.16**	**8/10/2014**	**1**	**1**	**1**	**1**	**0**
17.97	**-95.69**	**109.2**	**6.4**	**35.71**	**133.38**	**7/29/2014**	**1**	**0**	**1**	**1**	**1**
-19.68	**-178.32**	**627.1**	**6.9**	**83.11**	**231.96**	**7/21/2014**	**1**	**1**	**1**	**1**	**1**
44.63	**148.94**	**66.6**	**6.3**	**58.89**	**303.79**	**7/20/2014**	**1**	**0**	**1**	**0**	**0**
-15.64	**-174.18**	**233.8**	**6.2**	**77.54**	**231.00**	**7/19/2014**	**1**	**0**	**1**	**0**	**0**
36.97	**142.39**	**12**	**6.5**	**67.56**	**300.62**	**7/11/2014**	**1**	**1**	**1**	**1**	**0**
55.39	**166.94**	**12**	**5.8**	**43.71**	**309.05**	**7/3/2014**	**1**	**1**	**1**	**1**	**0**

Table B1. Composite migration earthquake information. For RF phases, 1 means it is used in the migration and 0 means it is not.

Latitude	Longitude	Depth (km)	Magnitude	Distance (Δ)	Back-Azimuth	Date	PS	PPXP	PPXS	PSXS-SV	PSXS-SH
42.64	13.22	12	6.2	82.74	31.38	8/24/2016	1	0	0	1	0
50.45	142.3	12.5	5.8	59.06	312.36	8/14/2016	1	0	0	0	0
18.5	145.7	208.9	7.7	78.19	284.49	7/29/2016	0	0	1	1	0
47.68	146.91	423.2	5.8	58.25	307.66	7/23/2016	0	1	0	1	0
-28.05	-176.27	17.9	6.4	88.92	225.64	7/13/2016	0	0	0	0	0
12.92	-87.13	13.7	6.1	44.47	126.96	6/10/2016	1	1	1	0	1
-22.13	-178.17	417.5	6.9	85.02	230.42	5/28/2016	0	1	1	1	0
16.61	-97.79	23.9	5.9	35.87	137.51	5/8/2016	1	1	0	1	1
-16.05	167.26	33.5	7	88.75	245.02	4/28/2016	1	1	1	1	1
37.81	141.77	48.5	5.9	67.37	301.66	4/20/2016	0	0	1	0	0
-29.66	-111.74	21.7	5.5	76.45	170.68	4/16/2016	1	1	1	1	1
32.84	130.77	12.9	7	77.24	304.55	4/15/2016	1	0	1	1	1
-13.92	166.54	31.5	6.6	87.59	246.94	4/7/2016	0	0	0	1	0
-14.06	166.59	32.4	6.7	87.67	246.81	4/6/2016	0	0	1	1	1
-14.27	166.66	34.8	6.8	87.78	246.62	4/3/2016	1	1	1	1	1
51.4	-174.13	15.9	6	33.88	298.20	3/19/2016	1	0	0	1	0
53.86	158.73	168.1	7.2	48.69	309.56	1/30/2016	0	0	0	0	0

35.59	**-3.6**	**12**	**6.4**	**81.33**	**46.25**	**1/25/2016**	**1**	**1**	**0**	**0**	**1**
-14.88	**167.19**	**140.9**	**7.1**	**87.91**	**245.83**	**10/20/2015**	**0**	**1**	**1**	**1**	**1**
-16.14	**-172.98**	**17.8**	**6**	**77.32**	**229.73**	**10/18/2015**	**1**	**0**	**1**	**1**	**0**
-30.88	**-71.62**	**51.7**	**6.3**	**89.60**	**138.48**	**9/26/2015**	**0**	**0**	**0**	**0**	**0**
-31.13	**-72.09**	**17.4**	**8.3**	**89.60**	**138.96**	**9/16/2015**	**0**	**0**	**0**	**0**	**0**
-10.78	**163.71**	**20.6**	**6.4**	**87.07**	**251.09**	**8/15/2015**	**0**	**0**	**1**	**1**	**1**
-9.35	**158.07**	**12**	**6.6**	**89.76**	**256.16**	**8/10/2015**	**0**	**0**	**0**	**0**	**0**
-27.22	**-175.75**	**12**	**5.7**	**87.97**	**225.72**	**8/9/2015**	**1**	**0**	**1**	**1**	**0**
13.92	**-58.38**	**19.4**	**6.5**	**61.95**	**99.31**	**7/16/2015**	**1**	**0**	**0**	**0**	**0**
-9.4	**158.33**	**14.6**	**6.7**	**89.62**	**255.94**	**7/10/2015**	**0**	**0**	**0**	**0**	**0**
43.93	**148.12**	**54.4**	**6.3**	**59.78**	**303.54**	**7/7/2015**	**0**	**0**	**0**	**0**	**0**
-20.76	**-174.32**	**48.2**	**5.8**	**81.87**	**228.22**	**7/6/2015**	**1**	**0**	**1**	**1**	**0**
-15.54	**-172.69**	**51.3**	**6**	**76.66**	**229.83**	**6/12/2015**	**1**	**0**	**1**	**1**	**0**
30.8	**143**	**17.5**	**6.2**	**71.36**	**295.40**	**5/30/2015**	**0**	**0**	**1**	**1**	**0**
-15.69	**-173.19**	**70.3**	**6**	**77.05**	**230.16**	**5/30/2015**	**0**	**0**	**1**	**1**	**0**
27.94	**140.56**	**680.7**	**7.9**	**74.88**	**294.80**	**5/30/2015**	**0**	**1**	**1**	**1**	**0**
-19.4	**-176.05**	**16**	**6.3**	**81.65**	**230.35**	**5/24/2015**	**0**	**0**	**0**	**0**	**1**
-10.78	**163.91**	**19**	**6.8**	**86.94**	**250.95**	**5/20/2015**	**0**	**0**	**1**	**1**	**1**

38.89	**142.29**	**43.9**	**6.8**	**66.35**	**302.24**	**5/12/2015**	**0**	**0**	**1**	**1**	**0**
-20.79	**-178.71**	**591.4**	**6.1**	**84.22**	**231.61**	**4/28/2015**	**0**	**0**	**1**	**0**	**0**
23.96	**122.31**	**34.4**	**6.4**	**88.81**	**304.42**	**4/20/2015**	**1**	**0**	**1**	**1**	**0**
-15.25	**-173.17**	**43.2**	**6.3**	**76.67**	**230.39**	**4/7/2015**	**1**	**0**	**1**	**1**	**0**
-18.47	**-69.44**	**140.8**	**6.4**	**80.28**	**130.01**	**3/23/2015**	**1**	**1**	**1**	**1**	**1**
6.83	**-73.11**	**155.9**	**6.2**	**57.58**	**117.30**	**3/10/2015**	**1**	**1**	**0**	**1**	**1**
-16.41	**168.23**	**12**	**6.4**	**88.42**	**244.08**	**2/19/2015**	**1**	**0**	**1**	**1**	**0**
52.7	**-32.74**	**25.2**	**7.1**	**54.67**	**47.96**	**2/13/2015**	**1**	**1**	**1**	**1**	**1**
-23.14	**-66.8**	**223**	**6.7**	**85.53**	**130.62**	**2/11/2015**	**1**	**1**	**1**	**1**	**1**
-17.06	**168.36**	**231**	**6.8**	**88.83**	**243.56**	**1/23/2015**	**1**	**1**	**1**	**1**	**1**
-19.76	**-177.61**	**445.4**	**7.1**	**82.79**	**231.36**	**11/1/2014**	**0**	**1**	**1**	**1**	**0**
-15.12	**-174.58**	**13.9**	**6**	**77.32**	**231.63**	**10/28/2014**	**1**	**0**	**1**	**0**	**0**
-32.34	**-110.81**	**12**	**6.9**	**79.21**	**170.24**	**10/9/2014**	**1**	**1**	**1**	**1**	**1**
15.38	**147.66**	**13.8**	**5.6**	**79.07**	**280.89**	**10/6/2014**	**0**	**0**	**0**	**0**	**0**
13.54	**144.51**	**140.4**	**6.8**	**82.52**	**281.79**	**9/17/2014**	**1**	**0**	**1**	**1**	**0**
-26.89	**-114.56**	**12**	**6.1**	**73.42**	**172.91**	**9/6/2014**	**1**	**1**	**1**	**1**	**1**
-21.53	**-173.15**	**46.5**	**6**	**81.92**	**226.87**	**9/4/2014**	**1**	**0**	**1**	**1**	**0**
64.61	**-17.19**	**12**	**5.5**	**54.88**	**30.42**	**9/1/2014**	**1**	**0**	**0**	**1**	**1**

-14.61	**-73.72**	**84.5**	**6.8**	**74.81**	**131.36**	**8/24/2014**	**1**	**1**	**1**	**1**	**1**
41.25	**142.37**	**48.9**	**6.1**	**64.76**	**304.16**	**8/10/2014**	**0**	**1**	**1**	**1**	**0**
17.97	**-95.69**	**109.2**	**6.4**	**35.71**	**133.38**	**7/29/2014**	**1**	**1**	**0**	**1**	**1**
-19.68	**-178.32**	**627.1**	**6.9**	**83.11**	**231.96**	**7/21/2014**	**1**	**1**	**1**	**1**	**1**
44.63	**148.94**	**66.6**	**6.3**	**58.89**	**303.79**	**7/20/2014**	**0**	**0**	**0**	**0**	**0**
-15.64	**-174.18**	**233.8**	**6.2**	**77.54**	**231.00**	**7/19/2014**	**0**	**0**	**0**	**0**	**0**
36.97	**142.39**	**12**	**6.5**	**67.56**	**300.62**	**7/11/2014**	**0**	**0**	**0**	**0**	**0**
55.39	**166.94**	**12**	**5.8**	**43.71**	**309.05**	**7/3/2014**	**0**	**0**	**0**	**0**	**0**

Table B2. North section migration earthquake information (from Fig. 1.4). For RF phases, 1 means it is used in the migration and 0 means it is not.

Latitude	Longitude	Depth (km)	Magnitude	Distance (Δ)	Back-Azimuth	Date	PS	PPXP	PPXS	PSXS-SV	PSXS-SH
42.64	13.22	12	6.2	82.74	31.38	8/24/2016	1	0	0	1	0
50.45	142.3	12.5	5.8	59.06	312.36	8/14/2016	1	0	0	0	0
18.5	145.7	208.9	7.7	78.19	284.49	7/29/2016	0	0	1	1	0
47.68	146.91	423.2	5.8	58.25	307.66	7/23/2016	0	1	0	1	0
-28.05	-176.27	17.9	6.4	88.92	225.64	7/13/2016	0	0	0	0	0
12.92	-87.13	13.7	6.1	44.47	126.96	6/10/2016	1	1	1	0	1
-22.13	-178.17	417.5	6.9	85.02	230.42	5/28/2016	0	1	1	1	0
16.61	-97.79	23.9	5.9	35.87	137.51	5/8/2016	1	1	0	1	1
-16.05	167.26	33.5	7	88.75	245.02	4/28/2016	1	1	1	1	1
37.81	141.77	48.5	5.9	67.37	301.66	4/20/2016	0	0	1	0	0
-29.66	-111.74	21.7	5.5	76.45	170.68	4/16/2016	1	1	1	1	1
32.84	130.77	12.9	7	77.24	304.55	4/15/2016	1	0	1	1	1
-13.92	166.54	31.5	6.6	87.59	246.94	4/7/2016	0	0	0	1	0
-14.06	166.59	32.4	6.7	87.67	246.81	4/6/2016	0	0	1	1	1
-14.27	166.66	34.8	6.8	87.78	246.62	4/3/2016	1	1	1	1	1
51.4	-174.13	15.9	6	33.88	298.20	3/19/2016	1	0	0	1	0
53.86	158.73	168.1	7.2	48.69	309.56	1/30/2016	0	0	0	0	0

35.59	**-3.6**	**12**	**6.4**	**81.33**	**46.25**	**1/25/2016**	**1**	**1**	**0**	**0**	**1**
-14.88	**167.19**	**140.9**	**7.1**	**87.91**	**245.83**	**10/20/2015**	**0**	**1**	**1**	**1**	**1**
-16.14	**-172.98**	**17.8**	**6**	**77.32**	**229.73**	**10/18/2015**	**1**	**0**	**1**	**1**	**0**
-30.88	**-71.62**	**51.7**	**6.3**	**89.60**	**138.48**	**9/26/2015**	**0**	**0**	**0**	**0**	**0**
-31.13	**-72.09**	**17.4**	**8.3**	**89.60**	**138.96**	**9/16/2015**	**0**	**0**	**0**	**0**	**0**
-10.78	**163.71**	**20.6**	**6.4**	**87.07**	**251.09**	**8/15/2015**	**0**	**0**	**1**	**1**	**1**
-9.35	**158.07**	**12**	**6.6**	**89.76**	**256.16**	**8/10/2015**	**0**	**0**	**0**	**0**	**0**
-27.22	**-175.75**	**12**	**5.7**	**87.97**	**225.72**	**8/9/2015**	**1**	**0**	**1**	**1**	**0**
13.92	**-58.38**	**19.4**	**6.5**	**61.95**	**99.31**	**7/16/2015**	**1**	**0**	**0**	**0**	**0**
-9.4	**158.33**	**14.6**	**6.7**	**89.62**	**255.94**	**7/10/2015**	**0**	**0**	**0**	**0**	**0**
43.93	**148.12**	**54.4**	**6.3**	**59.78**	**303.54**	**7/7/2015**	**0**	**0**	**0**	**0**	**0**
-20.76	**-174.32**	**48.2**	**5.8**	**81.87**	**228.22**	**7/6/2015**	**1**	**0**	**1**	**1**	**0**
-15.54	**-172.69**	**51.3**	**6**	**76.66**	**229.83**	**6/12/2015**	**1**	**0**	**1**	**1**	**0**
30.8	**143**	**17.5**	**6.2**	**71.36**	**295.40**	**5/30/2015**	**0**	**0**	**1**	**1**	**0**
-15.69	**-173.19**	**70.3**	**6**	**77.05**	**230.16**	**5/30/2015**	**0**	**0**	**1**	**1**	**0**
27.94	**140.56**	**680.7**	**7.9**	**74.88**	**294.80**	**5/30/2015**	**0**	**1**	**1**	**1**	**0**
-19.4	**-176.05**	**16**	**6.3**	**81.65**	**230.35**	**5/24/2015**	**0**	**0**	**0**	**0**	**1**
-10.78	**163.91**	**19**	**6.8**	**86.94**	**250.95**	**5/20/2015**	**0**	**0**	**1**	**1**	**1**

38.89	**142.29**	**43.9**	**6.8**	**66.35**	**302.24**	**5/12/2015**	**0**	**0**	**1**	**1**	**0**
-20.79	**-178.71**	**591.4**	**6.1**	**84.22**	**231.61**	**4/28/2015**	**0**	**0**	**1**	**0**	**0**
23.96	**122.31**	**34.4**	**6.4**	**88.81**	**304.42**	**4/20/2015**	**1**	**0**	**1**	**1**	**0**
-15.25	**-173.17**	**43.2**	**6.3**	**76.67**	**230.39**	**4/7/2015**	**1**	**0**	**1**	**1**	**0**
-18.47	**-69.44**	**140.8**	**6.4**	**80.28**	**130.01**	**3/23/2015**	**1**	**1**	**1**	**1**	**1**
6.83	**-73.11**	**155.9**	**6.2**	**57.58**	**117.30**	**3/10/2015**	**1**	**1**	**0**	**1**	**1**
-16.41	**168.23**	**12**	**6.4**	**88.42**	**244.08**	**2/19/2015**	**1**	**0**	**1**	**1**	**0**
52.7	**-32.74**	**25.2**	**7.1**	**54.67**	**47.96**	**2/13/2015**	**1**	**1**	**1**	**1**	**1**
-23.14	**-66.8**	**223**	**6.7**	**85.53**	**130.62**	**2/11/2015**	**1**	**1**	**1**	**1**	**1**
-17.06	**168.36**	**231**	**6.8**	**88.83**	**243.56**	**1/23/2015**	**1**	**1**	**1**	**1**	**1**
-19.76	**-177.61**	**445.4**	**7.1**	**82.79**	**231.36**	**11/1/2014**	**0**	**1**	**1**	**1**	**0**
-15.12	**-174.58**	**13.9**	**6**	**77.32**	**231.63**	**10/28/2014**	**1**	**0**	**1**	**0**	**0**
-32.34	**-110.81**	**12**	**6.9**	**79.21**	**170.24**	**10/9/2014**	**1**	**1**	**1**	**1**	**1**
15.38	**147.66**	**13.8**	**5.6**	**79.07**	**280.89**	**10/6/2014**	**0**	**0**	**0**	**0**	**0**
13.54	**144.51**	**140.4**	**6.8**	**82.52**	**281.79**	**9/17/2014**	**1**	**0**	**1**	**1**	**0**
-26.89	**-114.56**	**12**	**6.1**	**73.42**	**172.91**	**9/6/2014**	**1**	**1**	**1**	**1**	**1**
-21.53	**-173.15**	**46.5**	**6**	**81.92**	**226.87**	**9/4/2014**	**1**	**0**	**1**	**1**	**0**
64.61	**-17.19**	**12**	**5.5**	**54.88**	**30.42**	**9/1/2014**	**1**	**0**	**0**	**1**	**1**

-14.61	**-73.72**	**84.5**	**6.8**	**74.81**	**131.36**	**8/24/2014**	**1**	**1**	**1**	**1**	**1**
41.25	**142.37**	**48.9**	**6.1**	**64.76**	**304.16**	**8/10/2014**	**0**	**1**	**1**	**1**	**0**
17.97	**-95.69**	**109.2**	**6.4**	**35.71**	**133.38**	**7/29/2014**	**1**	**1**	**0**	**1**	**1**
-19.68	**-178.32**	**627.1**	**6.9**	**83.11**	**231.96**	**7/21/2014**	**1**	**1**	**1**	**1**	**1**
44.63	**148.94**	**66.6**	**6.3**	**58.89**	**303.79**	**7/20/2014**	**0**	**0**	**0**	**0**	**0**
-15.64	**-174.18**	**233.8**	**6.2**	**77.54**	**231.00**	**7/19/2014**	**0**	**0**	**0**	**0**	**0**
36.97	**142.39**	**12**	**6.5**	**67.56**	**300.62**	**7/11/2014**	**0**	**0**	**0**	**0**	**0**
55.39	**166.94**	**12**	**5.8**	**43.71**	**309.05**	**7/3/2014**	**0**	**0**	**0**	**0**	**0**

Table B3. Middle section migration earthquake information (from Fig. 1.4). For RF phases, 1 means it is used in the migration and 0 means it is not.

Latitude	Longitude	Depth (km)	Magnitude	Distance (Δ)	Back-Azimuth	Date	PS	PPXP	PPXS	PSXS-SV	PSXS-SH
42.64	13.22	12	6.2	82.74	31.38	8/24/2016	1	1	1	1	1
50.45	142.3	12.5	5.8	59.06	312.36	8/14/2016	0	0	0	0	0
18.5	145.7	208.9	7.7	78.19	284.49	7/29/2016	0	1	1	1	0
47.68	146.91	423.2	5.8	58.25	307.66	7/23/2016	0	0	1	1	0
-28.05	-176.27	17.9	6.4	88.92	225.64	7/13/2016	0	0	0	0	0
12.92	-87.13	13.7	6.1	44.47	126.96	6/10/2016	1	0	0	0	0
-22.13	-178.17	417.5	6.9	85.02	230.42	5/28/2016	0	0	1	1	1
16.61	-97.79	23.9	5.9	35.87	137.51	5/8/2016	1	0	0	0	1
-16.05	167.26	33.5	7	88.75	245.02	4/28/2016	0	1	1	0	1
37.81	141.77	48.5	5.9	67.37	301.66	4/20/2016	0	0	0	0	0
-29.66	-111.74	21.7	5.5	76.45	170.68	4/16/2016	1	1	0	1	1
32.84	130.77	12.9	7	77.24	304.55	4/15/2016	1	1	1	1	0
-13.92	166.54	31.5	6.6	87.59	246.94	4/7/2016	0	1	1	1	0
-14.06	166.59	32.4	6.7	87.67	246.81	4/6/2016	0	1	1	0	1
-14.27	166.66	34.8	6.8	87.78	246.62	4/3/2016	0	1	1	1	1
51.4	-174.13	15.9	6	33.88	298.20	3/19/2016	0	0	0	0	0
53.86	158.73	168.1	7.2	48.69	309.56	1/30/2016	1	0	1	0	0

35.59	**-3.6**	**12**	**6.4**	**81.33**	**46.25**	**1/25/2016**	**1**	**1**	**0**	**1**	**1**
-14.88	**167.19**	**140.9**	**7.1**	**87.91**	**245.83**	**10/20/2015**	**0**	**1**	**1**	**1**	**1**
-16.14	**-172.98**	**17.8**	**6**	**77.32**	**229.73**	**10/18/2015**	**0**	**0**	**1**	**1**	**1**
-30.88	**-71.62**	**51.7**	**6.3**	**89.60**	**138.48**	**9/26/2015**	**0**	**0**	**0**	**0**	**0**
-31.13	**-72.09**	**17.4**	**8.3**	**89.60**	**138.96**	**9/16/2015**	**0**	**0**	**0**	**0**	**0**
-10.78	**163.71**	**20.6**	**6.4**	**87.07**	**251.09**	**8/15/2015**	**1**	**0**	**1**	**1**	**1**
-9.35	**158.07**	**12**	**6.6**	**89.76**	**256.16**	**8/10/2015**	**0**	**0**	**0**	**0**	**0**
-27.22	**-175.75**	**12**	**5.7**	**87.97**	**225.72**	**8/9/2015**	**0**	**0**	**1**	**1**	**1**
13.92	**-58.38**	**19.4**	**6.5**	**61.95**	**99.31**	**7/16/2015**	**1**	**1**	**1**	**0**	**0**
-9.4	**158.33**	**14.6**	**6.7**	**89.62**	**255.94**	**7/10/2015**	**0**	**0**	**0**	**0**	**0**
43.93	**148.12**	**54.4**	**6.3**	**59.78**	**303.54**	**7/7/2015**	**1**	**0**	**1**	**0**	**0**
-20.76	**-174.32**	**48.2**	**5.8**	**81.87**	**228.22**	**7/6/2015**	**0**	**0**	**0**	**0**	**0**
-15.54	**-172.69**	**51.3**	**6**	**76.66**	**229.83**	**6/12/2015**	**0**	**1**	**1**	**1**	**1**
30.8	**143**	**17.5**	**6.2**	**71.36**	**295.40**	**5/30/2015**	**0**	**0**	**1**	**1**	**1**
-15.69	**-173.19**	**70.3**	**6**	**77.05**	**230.16**	**5/30/2015**	**0**	**0**	**1**	**1**	**1**
27.94	**140.56**	**680.7**	**7.9**	**74.88**	**294.80**	**5/30/2015**	**0**	**0**	**1**	**0**	**0**
-19.4	**-176.05**	**16**	**6.3**	**81.65**	**230.35**	**5/24/2015**	**1**	**0**	**1**	**0**	**0**
-10.78	**163.91**	**19**	**6.8**	**86.94**	**250.95**	**5/20/2015**	**0**	**1**	**1**	**1**	**1**

38.89	**142.29**	**43.9**	**6.8**	**66.35**	**302.24**	**5/12/2015**	**0**	**1**	**1**	**0**	**0**
-20.79	**-178.71**	**591.4**	**6.1**	**84.22**	**231.61**	**4/28/2015**	**0**	**1**	**1**	**0**	**0**
23.96	**122.31**	**34.4**	**6.4**	**88.81**	**304.42**	**4/20/2015**	**0**	**1**	**1**	**1**	**0**
-15.25	**-173.17**	**43.2**	**6.3**	**76.67**	**230.39**	**4/7/2015**	**1**	**0**	**1**	**1**	**1**
-18.47	**-69.44**	**140.8**	**6.4**	**80.28**	**130.01**	**3/23/2015**	**1**	**1**	**0**	**1**	**1**
6.83	**-73.11**	**155.9**	**6.2**	**57.58**	**117.30**	**3/10/2015**	**1**	**1**	**1**	**1**	**1**
-16.41	**168.23**	**12**	**6.4**	**88.42**	**244.08**	**2/19/2015**	**1**	**0**	**1**	**0**	**0**
52.7	**-32.74**	**25.2**	**7.1**	**54.67**	**47.96**	**2/13/2015**	**0**	**1**	**1**	**1**	**0**
-23.14	**-66.8**	**223**	**6.7**	**85.53**	**130.62**	**2/11/2015**	**1**	**1**	**1**	**1**	**1**
-17.06	**168.36**	**231**	**6.8**	**88.83**	**243.56**	**1/23/2015**	**1**	**1**	**1**	**1**	**1**
-19.76	**-177.61**	**445.4**	**7.1**	**82.79**	**231.36**	**11/1/2014**	**1**	**1**	**1**	**1**	**1**
-15.12	**-174.58**	**13.9**	**6**	**77.32**	**231.63**	**10/28/2014**	**0**	**0**	**0**	**0**	**0**
-32.34	**-110.81**	**12**	**6.9**	**79.21**	**170.24**	**10/9/2014**	**1**	**1**	**1**	**1**	**1**
15.38	**147.66**	**13.8**	**5.6**	**79.07**	**280.89**	**10/6/2014**	**0**	**0**	**0**	**0**	**0**
13.54	**144.51**	**140.4**	**6.8**	**82.52**	**281.79**	**9/17/2014**	**0**	**1**	**1**	**1**	**0**
-26.89	**-114.56**	**12**	**6.1**	**73.42**	**172.91**	**9/6/2014**	**1**	**0**	**1**	**1**	**0**
-21.53	**-173.15**	**46.5**	**6**	**81.92**	**226.87**	**9/4/2014**	**1**	**0**	**1**	**1**	**1**
64.61	**-17.19**	**12**	**5.5**	**54.88**	**30.42**	**9/1/2014**	**1**	**0**	**1**	**1**	**0**

-14.61	**-73.72**	**84.5**	**6.8**	**74.81**	**131.36**	**8/24/2014**	**1**	**1**	**1**	**1**	**1**
41.25	**142.37**	**48.9**	**6.1**	**64.76**	**304.16**	**8/10/2014**	**0**	**0**	**1**	**1**	**0**
17.97	**-95.69**	**109.2**	**6.4**	**35.71**	**133.38**	**7/29/2014**	**1**	**0**	**0**	**1**	**1**
-19.68	**-178.32**	**627.1**	**6.9**	**83.11**	**231.96**	**7/21/2014**	**1**	**1**	**1**	**1**	**1**
44.63	**148.94**	**66.6**	**6.3**	**58.89**	**303.79**	**7/20/2014**	**0**	**0**	**0**	**0**	**0**
-15.64	**-174.18**	**233.8**	**6.2**	**77.54**	**231.00**	**7/19/2014**	**0**	**0**	**0**	**0**	**0**
36.97	**142.39**	**12**	**6.5**	**67.56**	**300.62**	**7/11/2014**	**0**	**0**	**0**	**0**	**0**
55.39	**166.94**	**12**	**5.8**	**43.71**	**309.05**	**7/3/2014**	**0**	**0**	**0**	**0**	**0**

Table B4. South section migration earthquake information (from Fig. 1.4). For RF phases, 1 means it is used in the migration and 0 means it is not.

APPENDIX C

SUPPLEMENTARY MATERIAL FOR CHAPTER 3

Overview of phase stacking and 3D Vp model in main text

The inclusion of spatial variations in crustal velocity improves mapping of RF phase delay times to depth. Surface-wave tomography provides estimates of Vs for crust and uppermost mantle across the array (e.g., Feng and Ritzwoller, 2019). The Vs at each station is determined by averaging the slowness of the upper 36 km of the Vs model from Feng and Ritzwoller (2019) beneath each station. To estimate crustal Vp, we derive Vp/Vs ratios beneath each station using a variant of H-K stacking (Zhu and Kanamori, 2000) and select the Vp that provides the most coherent stacks between direct (Pxs) and reflected (Ppxs, Psxs, Ppxp) mode conversions from prominent interfaces (Figures 3.3c-d, 3.3g-h).

The *Vp/Vs* was allowed to vary between 1.5 and 2.2, and interface depth between 20 and 70 km (Figure 3.3). Near the coast, the depth range was extended to between 10 and 70 km. Also, unlike Rossi et al. we included the free-surface *P* reflection RF mode, Ppxp, which is sensitive only to *Vp* and depth (Figure 3.2b and Figure 3.3b,f). These modifications helped resolve velocity-depth ambiguities common to previous phase-stacking studies in the region (e.g., Veenstra et al., 2006; Miller and Moresi, 2018). Because the slab is dipping throughout the southern portion of region, phase stacking seems to pick the positive RF phase associated with the bottom of the megathrust interface near the coast. The positive RF phase associated with Yakutat Moho was picked at a few stations further inland (Figure C1). Individual measurements of Vp/Vs vary between 1.61 and 2.08 with an average of 1.82, which is slightly higher than the

global average of 1.77 for continental crust (Christensen, 1996) and agrees with intermediate-to-mafic crustal composition for the regional accreted terranes (Brocher, 2005; Rossi et al., 2006).

Nearby stations often have overlapping Fresnel zones with respect to Moho mode conversions, so variations in interstation Vp/Vs and depth should be smooth. To smooth the *Vp/Vs* estimates, we fit a 2D thin-plate spline surface across the entire array using 40 knots whose locations were determined using MATLAB's k-means clustering algorithm (Figure C3). We refer to the resulting spline surface as the "*Vp/Vs* Surface". We fit another 2D thin-plate spline surface, with the same knot locations, to the boundary depths to generate the corresponding "Depth Surface". In the spline fitting procedure, each boundary depth and *Vp/Vs* measurement is weighted by its uncertainty from the phase stacking analysis. The *Vp/Vs* Surface and Depth Surface were used to generate the 3D model of *Vp* above the Depth Surface interface to parallel the *Vs* model of Feng and Ritzwoller (2019). Below the Depth Surface the AK135 *Vp/Vs* model was used (Kennett and Engdahl, 1991), with a 15-km thick linear transition. Note that this Depth Surface is only used to convert time to depth in CCP stacking and is different from the picked surfaces described in the text.

Starting from the Feng and Ritzwoller (2019) Vs model, we test three methods for incorporating these spatially varying Vp/Vs measurements to generate the Vp model. The first method set Vp/Vs for the entire velocity model to the regional average of 1.82. The second method fit a 2D thin-plate spline surface to the Vp/Vs values to spatially smooth them and apply the resulting 2D Vp/Vs surface to all depths in the velocity model. The third method fit a 2D thin-plate spline surface to the Vp/Vs and depth values to spatially smooth both of them and apply the resulting 2D Vp/Vs surface to the Vs model from the surface down to the fitted depth surface, with a 10-km transition to the Vp/Vs from AK135 below. The variations for most of the

resulting boundary depths among the three velocity models are < 3 km. However, variations in the resulting Vp model that are not captured by the tomographic Vs models will defocus Ppxp phases, so we use the velocity model generated from Method 3 in our 3D CCP stacking procedure to allow a direct comparison with Ppxp.

Text S2. Making the 25-km contour

As a proxy for the megathrust interface, we map a horizon roughly in the center of the thin LVL atop the subducting Yakutat crust, 3-km deeper than the top. Three kilometers are added to this depth in an attempt to account for the 2-5 km thickness of the thin LVL inferred from modeling (Kim et al., 2014) or the <6 km constrained by the LVL resolution analyses here. A 2D thin-plate spline surface is fit to the 914 megathrust interface picks (Figure 3.8b) with 20 knot locations generated using MATLAB's k-means clustering algorithm on our megathrust interface pick locations. This approach smoothed out the step-like shape of the picks that resulted from uneven station spacing and assumptions of horizontality in CCP stacking (see Section 2.4.5). A 25-km contour is extracted from the 2D thin-plate spline surface between 140.5°W and 148.5°W. Farther west, we smoothly joined that contour with the 25-km contour from Ratchkovski and Hansen (2002) between 148.5°W and 151°W to generate our final 25-km contour (Figure 3.1). That contour is within 2 km of the plate interface in our RF migration image (Figure 3.5) as well as in the RF migration image from Kim et al. (2014). The deeper subduction contours in the Wrangell segment are from a combined consideration of the RF migration locations and the along-strike variations of IDEs (Daly et al., *subm.*). This new contour highlights the bend in the shallow subducting slab (Figure 3.1).

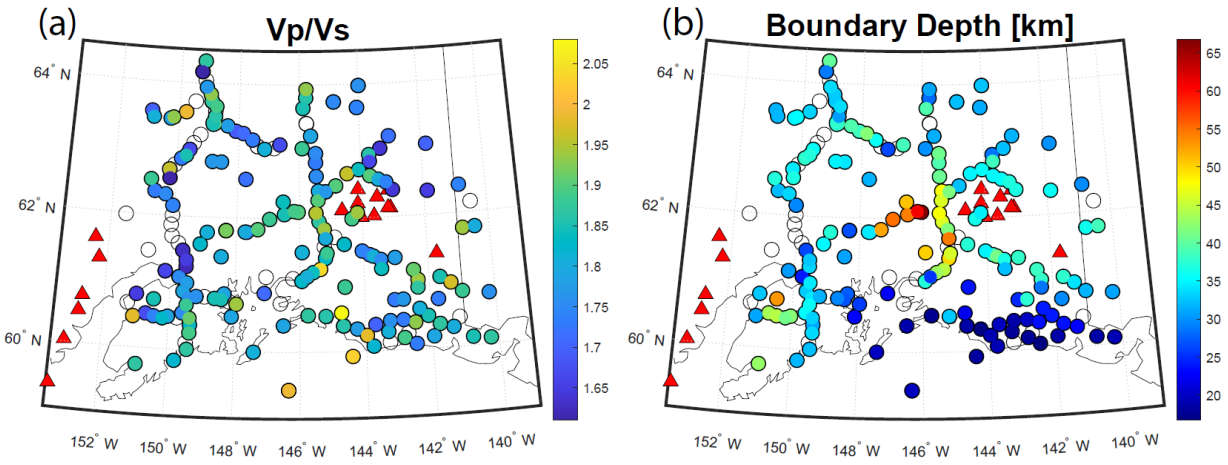

Figure C1. Single-station results from phase stacking. (a) *Vp/Vs* above boundary (b) depth to boundary. The shallow southern phases are probably the base of the megathrust interface low-velocity layer, while the more northern phases are the continental Moho.

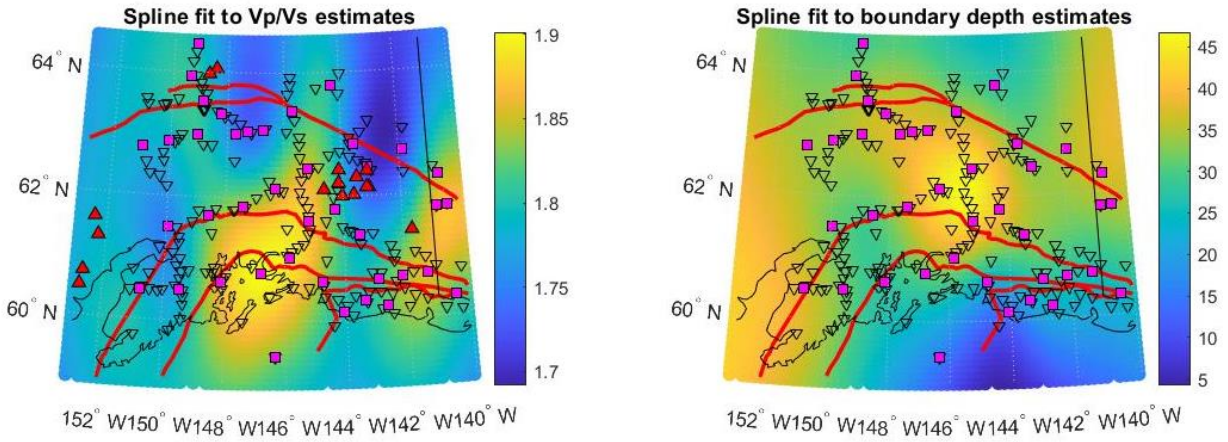

Figure C2. Left: spline fit to *Vp/Vs* estimates from Figure C1. Right: spline fit to boundary depth estimates from Figure C1. Red triangles = arc volcanoes, inverted triangles = stations, magenta squares = k-means knot locations

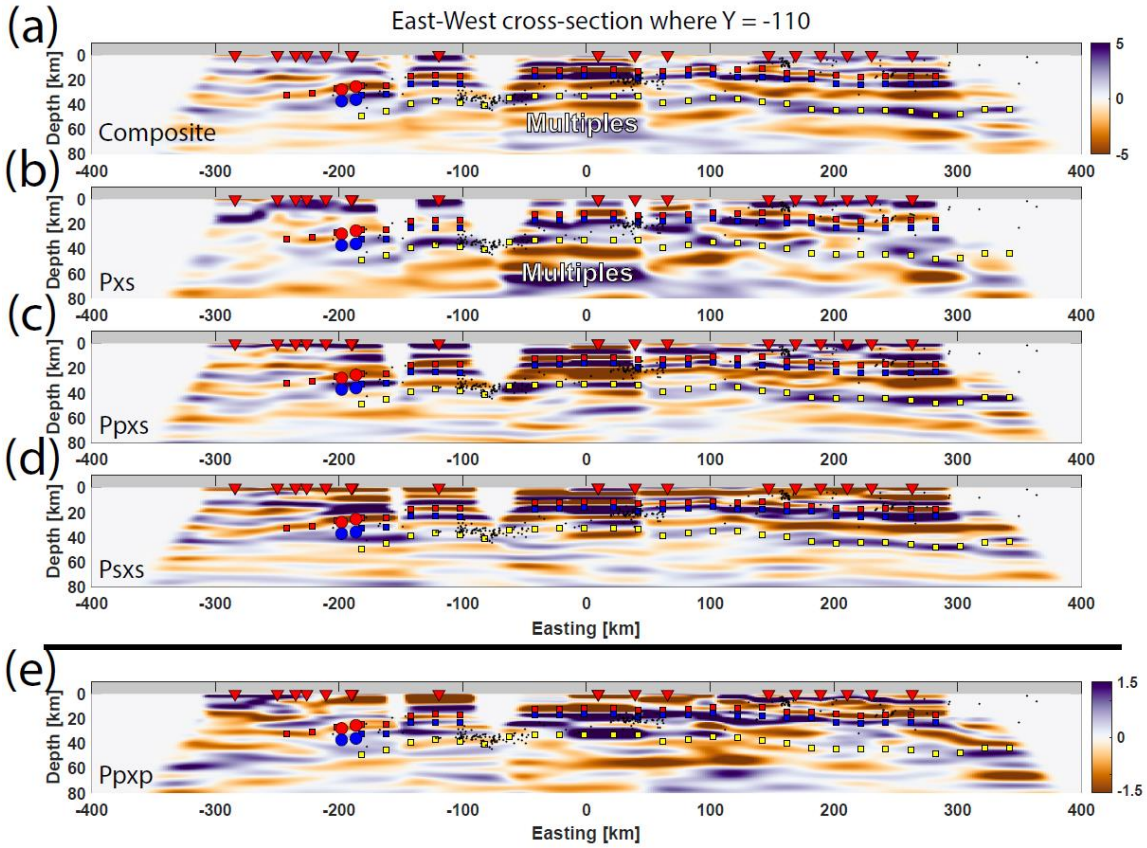

Figure C3. East-West cross sections from the composite and individual-mode CCP volumes where Y = -110 km (Figure 3.8) highlighting the consistency of the plate interface LVL along-strike. (b) CCP volume cross section only assuming energy is from Pxs (Figure 3.2b). (c) CCP volume cross section only assuming energy is from Ppxs. (d) CCP volume cross section only assuming energy is from Psxs. (e) CCP volume cross section through Ppxp CCP volume. All picked points are made on the composite CCP volume and plotted on each cross section (see **Section 3.4.5**).

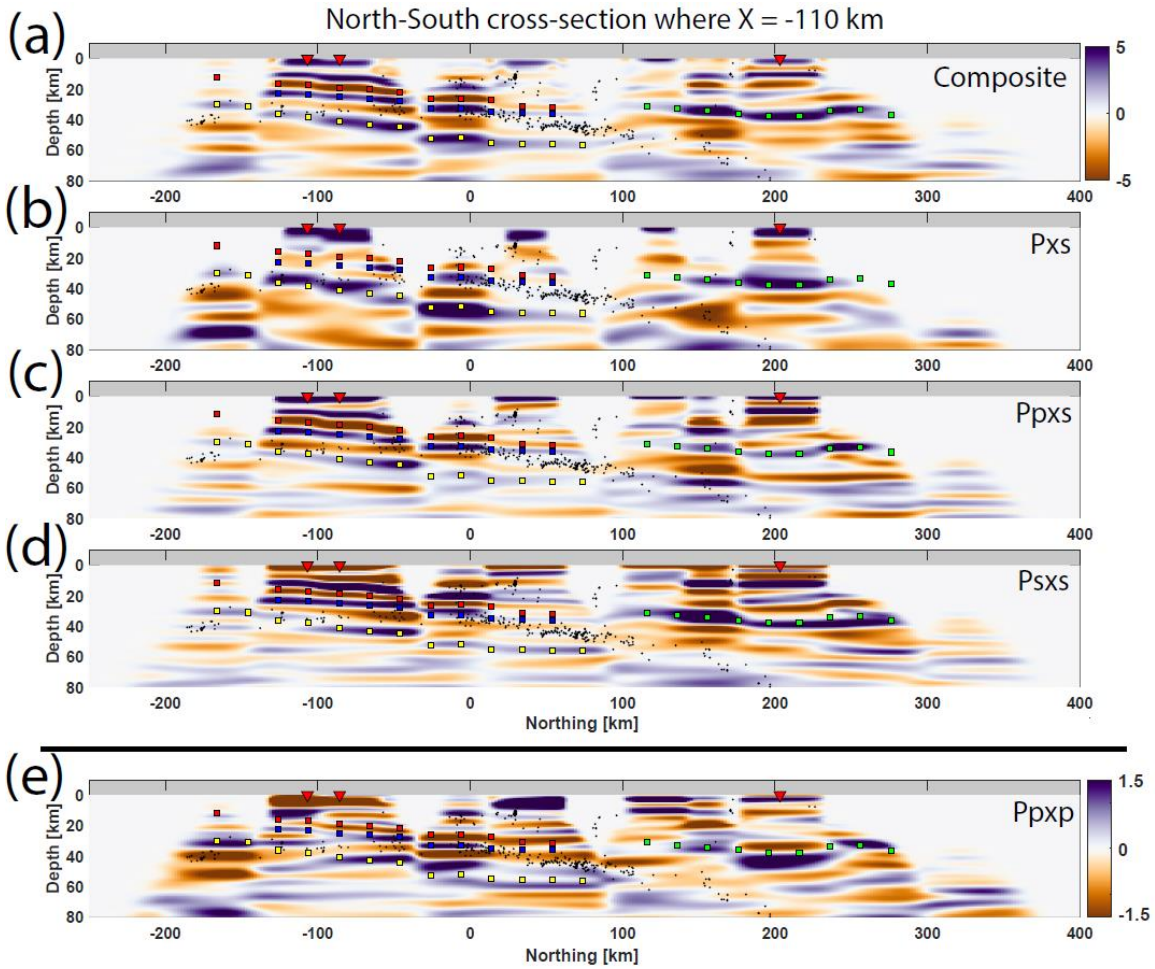

Figure C4. North-South cross sections from the composite and individual-mode CCP volumes where X = -110 km (Figure 3.8) highlighting the consistency of the Yakutat Moho and the plate interface LVL along-strike and down-dip. (b) CCP volume cross section only assuming energy is from Pxs (Figure 3.2b). (c) CCP volume cross section only assuming energy is from Ppxs. (d) CCP volume cross section only assuming energy is from Psxs. (e) CCP volume cross section through Ppxp CCP volume. All picked points are made on the composite CCP volume and plotted on each cross section (see **Section 3.4.5**).

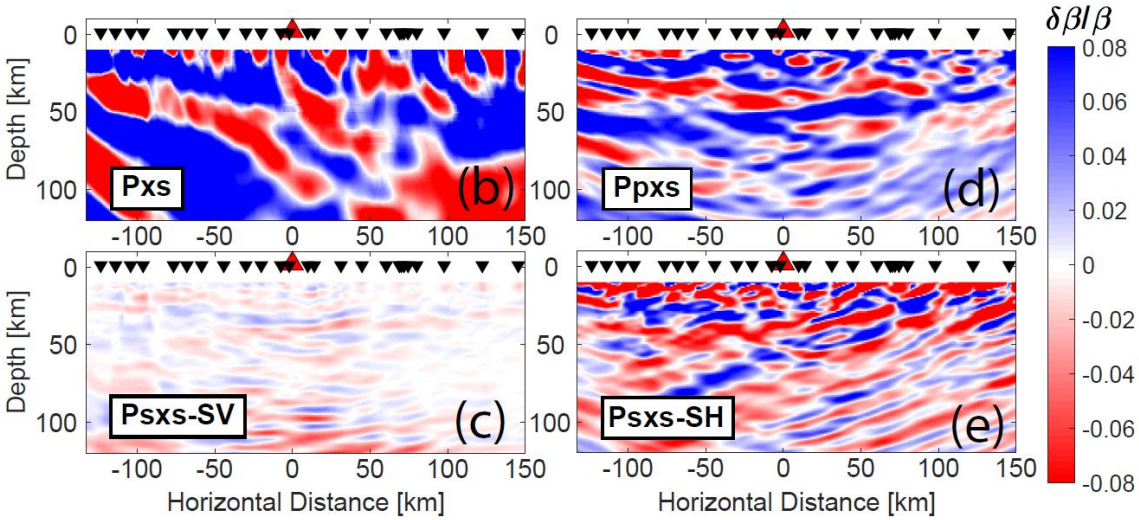

Figure C5. Individual-mode RF migration images.

Table C1. Table of teleseismic earthquakes that occurred during the WVLF deployment that were used to generate receiver functions (RF). If an event is used in the RF migration, it will have the RF modes (right 5 columns) that were selected marked with a 1 (RF mode included in migration) or a 0 (RF mode not included in migration), following Rondenay et al. (2001).

Latitude	Longitude	Depth (km)	Distance (Δ)	Back-Azimuth	Date	PS	PPXP	PPXS	PSXS-SV	PSXS-SH
12.92	-87.13	13.7	63	114	2016/06/10	0	1	0	1	0
26.95	130.25	12	64	280	2016/06/13	0	1	0	1	1
22.74	-44.95	12	74	71	2016/06/21	0	0	1	1	0
23.52	123.33	19.9	71	284	2016/06/23	0	1	0	0	0
39.47	73.43	16.9	74	331	2016/06/26	1	1	0	1	0
-16.02	167.36	37.7	87	226	2016/06/30	0	1	0	1	0
-15.06	-172.95	15.5	80	208	2016/07/10	0	1	1	1	1
0.48	-80.06	34	78	113	2016/07/11	1	0	0	1	1
0.58	-80	30.3	78	113	2016/07/11	0	0	0	0	0
47.68	146.91	423.2	40	282	2016/07/23	0	1	0	0	0
-2.97	148.18	12	82	249	2016/07/25	0	0	0	0	0
18.5	145.7	208.9	65	262	2016/07/29	0	1	1	1	1
24.98	141.91	522.7	61	269	2016/08/04	0	1	1	1	0
50.45	142.3	12.5	40	288	2016/08/14	0	0	0	0	0
40.33	143.91	12	47	278	2016/08/20	0	0	1	1	0
40.3	143.79	15	47	278	2016/08/20	1	1	1	1	0
42.64	13.22	12	74	17	2016/08/24	1	0	0	0	0
20.79	94.58	88.3	85	307	2016/08/24	0	1	1	1	0
30.69	137.78	473.2	58	276	2016/08/25	0	0	1	1	0

-3.58	**152.86**	**491**	**81**	**244**	**2016/08/31**	**0**	**1**	**1**	**1**	**0**
8.38	**125.85**	**19**	**83**	**274**	**2016/09/04**	**0**	**1**	**0**	**1**	**1**
30.53	**142.09**	**12**	**56**	**272**	**2016/09/20**	**0**	**1**	**1**	**1**	**0**
-19.77	**-178.15**	**606.8**	**86**	**212**	**2016/09/24**	**0**	**0**	**0**	**1**	**0**
-4.16	**150.4**	**452.6**	**83**	**246**	**2016/10/15**	**0**	**1**	**0**	**0**	**0**
-6.25	**148.92**	**52.2**	**85**	**247**	**2016/10/17**	**0**	**1**	**0**	**0**	**0**
44.07	**148.26**	**35.2**	**42**	**277**	**2016/10/23**	**0**	**0**	**0**	**0**	**0**
37.31	**141.46**	**12**	**51**	**277**	**2016/11/21**	**0**	**1**	**1**	**1**	**0**
-10.46	**161.12**	**45.5**	**84**	**234**	**2016/12/08**	**0**	**1**	**1**	**1**	**1**
-10.95	**161.06**	**12**	**84**	**234**	**2016/12/09**	**0**	**1**	**1**	**1**	**1**
-5.55	**153.76**	**52.8**	**82**	**243**	**2016/12/17**	**0**	**1**	**1**	**1**	**1**
-19.28	**176**	**17.3**	**87**	**217**	**2017/01/03**	**0**	**1**	**1**	**1**	**1**
4.57	**122.78**	**621.5**	**87**	**275**	**2017/01/10**	**0**	**1**	**1**	**1**	**1**
-10.21	**161.03**	**32**	**84**	**234**	**2017/01/10**	**0**	**1**	**1**	**1**	**1**
-10.4	**161.29**	**41.7**	**84**	**234**	**2017/01/19**	**0**	**1**	**1**	**1**	**1**
-6.03	**154.94**	**149.6**	**82**	**241**	**2017/01/22**	**0**	**1**	**1**	**1**	**1**
9.85	**125.49**	**12**	**82**	**275**	**2017/02/10**	**0**	**1**	**1**	**1**	**1**
-23.44	**-178.77**	**417.9**	**90**	**212**	**2017/02/24**	**0**	**1**	**1**	**1**	**1**
5.62	**127.4**	**29.5**	**84**	**271**	**2017/04/10**	**0**	**1**	**1**	**1**	**0**
7.74	**124.7**	**12**	**84**	**275**	**2017/04/11**	**0**	**1**	**1**	**1**	**1**
17.49	**-61.11**	**12**	**71**	**88**	**2017/04/17**	**0**	**0**	**0**	**0**	**0**
-2.77	**-75.37**	**21.6**	**83**	**110**	**2017/04/18**	**0**	**0**	**0**	**0**	**0**
5.49	**124.89**	**31.4**	**86**	**274**	**2017/04/28**	**0**	**1**	**1**	**1**	**1**

30.82	**131.43**	**25.9**	**61**	**281**	**2017/04/29**	**0**	**0**	**1**	**1**	**0**
39.51	**71.41**	**18**	**75**	**332**	**2017/05/05**	**1**	**0**	**0**	**0**	**0**
-14.55	**167.2**	**181.4**	**86**	**227**	**2017/05/09**	**0**	**1**	**1**	**1**	**1**
12.69	**-90.38**	**17.7**	**62**	**117**	**2017/05/12**	**0**	**1**	**0**	**1**	**1**
9.33	**124.02**	**544.6**	**83**	**276**	**2017/05/20**	**0**	**0**	**0**	**0**	**0**
17.64	**-105.41**	**18.5**	**52**	**131**	**2017/05/20**	**0**	**0**	**0**	**0**	**0**
17.17	**-94.1**	**147**	**57**	**119**	**2017/05/20**	**0**	**1**	**0**	**1**	**0**
19.1	**146.06**	**122.8**	**64**	**262**	**2017/05/31**	**0**	**0**	**0**	**0**	**0**
-4.23	**-80.66**	**51.6**	**82**	**116**	**2017/06/05**	**0**	**0**	**1**	**1**	**0**
38.81	**26.32**	**12**	**79**	**8**	**2017/06/12**	**1**	**0**	**1**	**1**	**0**
14.11	**-93.52**	**12**	**60**	**120**	**2017/06/14**	**0**	**0**	**0**	**1**	**0**
14.92	**-92.17**	**72.7**	**59**	**118**	**2017/06/14**	**0**	**1**	**0**	**1**	**0**
11.15	**124.68**	**12**	**81**	**276**	**2017/07/06**	**0**	**1**	**1**	**1**	**0**
-4.93	**153.19**	**34.1**	**82**	**243**	**2017/07/13**	**0**	**1**	**1**	**1**	**0**
-20.6	**-173.22**	**13.8**	**86**	**207**	**2017/07/16**	**0**	**1**	**0**	**1**	**0**
-20.55	**-173.24**	**12**	**86**	**207**	**2017/07/17**	**0**	**1**	**0**	**1**	**0**
36.79	**27.56**	**12**	**81**	**7**	**2017/07/20**	**1**	**1**	**1**	**1**	**0**
26.9	**130.13**	**12**	**65**	**280**	**2017/07/26**	**1**	**1**	**1**	**1**	**1**
13.42	**-49.39**	**28.7**	**80**	**80**	**2017/07/27**	**1**	**1**	**0**	**1**	**0**
46.1	**151.22**	**97.2**	**39**	**277**	**2017/07/30**	**1**	**1**	**0**	**0**	**0**
6.19	**125.29**	**82**	**85**	**274**	**2017/08/05**	**0**	**1**	**0**	**0**	**0**
33.21	**103.89**	**16.2**	**70**	**305**	**2017/08/08**	**1**	**1**	**1**	**1**	**0**
44.4	**82.74**	**27.6**	**67**	**326**	**2017/08/08**	**1**	**1**	**0**	**1**	**0**

14.03	**120.65**	**180.4**	**80**	**281**	**2017/08/11**	**0**	**1**	**1**	**1**	**1**
28.65	**127.89**	**205.5**	**64**	**283**	**2017/08/16**	**0**	**1**	**0**	**1**	**0**
-1.25	**148.15**	**15.9**	**81**	**250**	**2017/08/27**	**0**	**1**	**0**	**0**	**0**
15.38	**-94.66**	**44.8**	**58**	**120**	**2017/09/08**	**0**	**1**	**1**	**1**	**0**
18.59	**-98.63**	**51**	**54**	**123**	**2017/09/19**	**0**	**1**	**0**	**1**	**0**
38.02	**144.69**	**17.3**	**49**	**275**	**2017/09/20**	**0**	**1**	**1**	**1**	**1**
16.72	**-95.11**	**12.8**	**57**	**120**	**2017/09/23**	**0**	**1**	**0**	**1**	**0**
-6.36	**152.82**	**12**	**84**	**243**	**2017/09/25**	**0**	**1**	**0**	**0**	**0**
-23.79	**-176.47**	**110.7**	**90**	**209**	**2017/09/26**	**0**	**1**	**1**	**1**	**1**
37.48	**144**	**13.8**	**49**	**275**	**2017/10/06**	**0**	**0**	**0**	**0**	**0**
-20.72	**-173.29**	**16.9**	**86**	**207**	**2017/10/18**	**0**	**1**	**1**	**1**	**1**
18.79	**-106.57**	**14.7**	**50**	**132**	**2017/11/03**	**0**	**0**	**0**	**0**	**0**
-15.06	**-173.09**	**35**	**80**	**208**	**2017/11/04**	**0**	**1**	**1**	**1**	**0**
34.83	**45.84**	**17.9**	**83**	**352**	**2017/11/12**	**1**	**1**	**1**	**1**	**1**
9.45	**-84.58**	**29.6**	**68**	**113**	**2017/11/13**	**0**	**0**	**0**	**1**	**0**
10.09	**140.17**	**15.6**	**74**	**262**	**2017/12/08**	**0**	**1**	**1**	**1**	**1**
17.56	**-83.86**	**16.5**	**61**	**109**	**2018/01/10**	**0**	**1**	**1**	**1**	**0**
26.78	**-111.06**	**17.3**	**41**	**133**	**2018/01/19**	**0**	**1**	**0**	**0**	**0**
36.51	**70.72**	**205.3**	**78**	**332**	**2018/01/31**	**1**	**1**	**1**	**0**	**0**
13.66	**146.65**	**18.2**	**68**	**258**	**2018/02/11**	**0**	**1**	**1**	**1**	**1**
16.53	**-97.88**	**20**	**56**	**123**	**2018/02/16**	**0**	**1**	**0**	**1**	**1**
-6.29	**142.97**	**12**	**88**	**252**	**2018/02/25**	**0**	**1**	**1**	**1**	**1**
-5.69	**151.37**	**50**	**84**	**245**	**2018/03/26**	**0**	**1**	**1**	**1**	**1**

-5.67	**151.6**	**42.2**	**83**	**245**	**2018/03/29**	**0**	**1**	**1**	**1**	**1**
-5.95	**142.57**	**23.3**	**88**	**253**	**2018/04/07**	**0**	**0**	**1**	**1**	**0**
19.12	**-154.76**	**12**	**44**	**195**	**2018/05/04**	**0**	**0**	**0**	**0**	**0**
37.05	**71.25**	**126.1**	**77**	**332**	**2018/05/09**	**1**	**1**	**1**	**1**	**0**

Table C2. Table of teleseismic earthquakes that occurred during BEAAR deployment that were used to generate receiver functions (RF).

Latitude	Longitude	Depth (km)	Distance (Δ)	Back-Azimuth	Date
40.70	32.98	10	77	2	2000/06/06
36.82	135.51	2.3	54	282	2000/06/06
26.80	97.19	33	79	307	2000/06/07
-5.14	152.51	57.2	83	244	2000/06/09
23.86	121.19	35.6	71	286	2000/06/10
17.29	120.22	66.4	78	283	2000/06/14
-25.63	178.06	631.2	93	214	2000/06/14
46.61	152.61	49.7	38	276	2000/06/14
63.92	-20.47	10	47	30	2000/06/17
16.89	120.41	39.6	78	283	2000/06/19
14.02	120.63	130.9	80	281	2000/06/19
63.91	-20.74	10	47	30	2000/06/21
14.04	144.93	130.8	69	260	2000/06/21
1.25	126.27	65.3	89	270	2000/06/23
31.10	131.24	47	61	282	2000/06/25
34.13	139.51	6.9	54	277	2000/06/29
34.04	139.32	9.3	54	277	2000/06/29
12.97	144.52	47.8	70	260	2000/06/29
34.18	139.16	8.9	54	277	2000/07/01
34.12	139.24	16.9	54	277	2000/07/02
20.27	122.25	34	74	283	2000/07/04

34.16	**139.16**	**10**	**54**	**277**	**2000/07/08**
-16.23	**-177.63**	**33**	**83**	**212**	**2000/07/09**
46.85	**145.38**	**352.7**	**41**	**282**	**2000/07/10**
-18.32	**-175.50**	**214.1**	**84**	**210**	**2000/07/13**
34.34	**139.24**	**13.1**	**54**	**277**	**2000/07/15**
-7.02	**128.94**	**227.7**	**95**	**264**	**2000/07/15**
-7.78	**150.89**	**27.5**	**86**	**244**	**2000/07/16**
-4.18	**138.95**	**24.3**	**88**	**257**	**2000/07/16**
-12.43	**166.54**	**41.6**	**84**	**228**	**2000/07/16**
36.27	**70.96**	**114.3**	**78**	**332**	**2000/07/17**
17.88	**120.79**	**37.9**	**77**	**283**	**2000/07/18**
36.49	**140.94**	**51**	**52**	**277**	**2000/07/20**
9.42	**-85.32**	**42.2**	**67**	**114**	**2000/07/21**
35.18	**141.06**	**30.1**	**53**	**276**	**2000/07/21**
18.29	**-98.97**	**66.2**	**54**	**124**	**2000/07/21**
34.22	**139.39**	**2.6**	**54**	**277**	**2000/07/27**
-12.39	**166.41**	**81.4**	**84**	**228**	**2000/07/28**
23.41	**120.93**	**1.6**	**72**	**286**	**2000/07/28**
33.92	**139.35**	**12**	**54**	**277**	**2000/07/30**
33.90	**139.38**	**8.4**	**54**	**277**	**2000/07/30**
-29.56	**-176.26**	**57.4**	**95**	**208**	**2000/07/31**
-12.14	**166.42**	**73**	**84**	**229**	**2000/08/03**
31.11	**131.33**	**46.7**	**60**	**281**	**2000/08/03**

28.80	**139.60**	**416.9**	**59**	**273**	**2000/08/06**
-15.72	**167.98**	**29.8**	**86**	**226**	**2000/08/09**
18.16	**-102.58**	**16.2**	**52**	**128**	**2000/08/09**
-16.87	**174.34**	**67.4**	**85**	**220**	**2000/08/09**
12.07	**-82.90**	**10**	**66**	**110**	**2000/08/13**
-9.37	**153.87**	**10**	**86**	**241**	**2000/08/14**
43.03	**146.77**	**48.1**	**44**	**278**	**2000/08/15**
-22.02	**-174.65**	**38.7**	**88**	**208**	**2000/08/17**
34.17	**139.19**	**19.2**	**54**	**277**	**2000/08/18**
7.43	**126.47**	**189.4**	**83**	**273**	**2000/08/20**
-17.63	**-178.89**	**478.4**	**84**	**213**	**2000/08/27**
22.18	**143.79**	**103.1**	**62**	**265**	**2000/08/27**
-5.05	**133.62**	**25.2**	**91**	**261**	**2000/09/02**
-19.95	**-179.08**	**650.3**	**87**	**213**	**2000/09/02**
43.06	**146.79**	**49**	**44**	**278**	**2000/09/03**
7.19	**122.13**	**37.9**	**86**	**277**	**2000/09/08**
-22.78	**-175.33**	**33**	**88**	**209**	**2000/09/09**
-1.11	**129.38**	**38.3**	**89**	**266**	**2000/09/10**
-15.91	**-173.66**	**116.9**	**81**	**209**	**2000/09/11**
35.37	**99.37**	**12**	**70**	**309**	**2000/09/12**
-15.84	**179.90**	**35.9**	**83**	**215**	**2000/09/14**
-22.63	**-176.28**	**107.8**	**89**	**210**	**2000/09/14**
-1.99	**-80.62**	**34.4**	**80**	**115**	**2000/09/20**

-17.26	**-173.88**	**67.8**	**83**	**209**	**2000/09/26**
29.51	**129.44**	**26.4**	**63**	**282**	**2000/10/02**
31.89	**-40.92**	**10**	**68**	**63**	**2000/10/05**
13.73	**120.75**	**161.8**	**80**	**281**	**2000/10/21**
-5.22	**153.07**	**34.2**	**82**	**243**	**2000/11/16**
-6.79	**146.42**	**10**	**87**	**249**	**2001/06/05**
-22.05	**-179.48**	**594.9**	**89**	**213**	**2001/06/14**
-6.68	**152.11**	**10**	**84**	**244**	**2001/07/08**
28.75	**-43.44**	**10**	**70**	**67**	**2001/07/13**
-5.17	**132.37**	**39.7**	**92**	**262**	**2001/07/22**
1.49	**126.35**	**51.4**	**89**	**270**	**2001/07/31**
40.70	**32.98**	**10**	**77**	**2**	**2000/06/06**
36.82	**135.51**	**2.3**	**54**	**282**	**2000/06/06**

Table C3. Table of teleseismic earthquakes that occurred during MOOS deployment that were used to generate receiver functions (RF).

Latitude	Longitude	Depth (km)	Distance (Δ)	Back-Azimuth	Date
13.72	-90.57	66	61	117	2007/06/13
-3.14	138.72	38.7	87	257	2007/06/16
-7.96	154.62	17.9	84	241	2007/06/28
-7.93	-74.32	152.4	88	112	2007/07/12
-15.42	168.62	23.5	86	225	2007/07/15
37.56	138.48	7.4	52	280	2007/07/16
-8.09	-71.21	633.7	89	109	2007/07/21
2.89	127.57	39.8	87	270	2007/07/26
-21.50	170.98	22.2	91	221	2007/07/27
19.31	95.59	16.8	86	305	2007/07/30
-15.67	167.70	149.5	86	226	2007/08/01
-13.38	-76.56	41.2	92	116	2007/08/15
-9.83	159.46	9.5	84	236	2007/08/16
-5.28	129.47	42.4	93	264	2007/08/17
-13.81	-76.30	33.4	92	116	2007/08/18
6.11	127.45	23.8	84	272	2007/08/20
8.13	-39.25	0.7	90	73	2007/08/20
-17.48	-174.33	128.3	83	209	2007/08/26
24.99	-109.66	9.8	44	132	2007/09/01
-11.59	165.82	37.5	83	229	2007/09/02
45.80	150.10	100.6	40	278	2007/09/03

24.34	**122.25**	**58.2**	**70**	**285**	**2007/09/06**
3.00	**-77.90**	**29**	**76**	**110**	**2007/09/10**
3.79	**126.46**	**24.4**	**86**	**271**	**2007/09/13**
-5.04	**153.44**	**31.8**	**82**	**243**	**2007/09/26**
-21.14	**169.38**	**19.9**	**91**	**223**	**2007/09/27**
22.01	**142.71**	**253.5**	**63**	**266**	**2007/09/28**
10.54	**145.80**	**18.5**	**72**	**257**	**2007/09/30**
-25.20	**179.45**	**521.3**	**92**	**213**	**2007/10/05**
46.06	**154.18**	**14.2**	**38**	**275**	**2007/10/25**
-2.34	**-77.79**	**123.6**	**81**	**112**	**2007/11/16**
-21.21	**-178.67**	**558.9**	**88**	**212**	**2007/11/19**
14.99	**-61.22**	**147.3**	**73**	**89**	**2007/11/29**
-26.10	**-177.36**	**149.8**	**92**	**210**	**2007/12/09**
-15.27	**-172.32**	**33.3**	**80**	**208**	**2007/12/13**
-2.37	**139.11**	**36.1**	**86**	**257**	**2007/12/22**
37.26	**22.70**	**83.8**	**80**	**11**	**2008/01/06**
-0.77	**134.12**	**28.7**	**87**	**262**	**2008/01/07**
32.40	**85.26**	**27.7**	**78**	**319**	**2008/01/09**
-6.07	**146.75**	**44.9**	**86**	**249**	**2008/01/24**
10.73	**-41.90**	**4.1**	**86**	**74**	**2008/02/08**
16.43	**-94.24**	**85.7**	**57**	**120**	**2008/02/12**
36.52	**21.67**	**31.5**	**81**	**12**	**2008/02/14**
20.01	**121.34**	**34.6**	**75**	**284**	**2008/03/03**

13.42	**125.72**	**26**	**78**	**277**	**2008/03/03**
6.21	**126.98**	**30.8**	**84**	**272**	**2008/03/20**
35.55	**81.51**	**10**	**76**	**323**	**2008/03/20**
-20.04	**168.91**	**31.4**	**90**	**223**	**2008/04/09**
-17.39	**-179.01**	**556.2**	**84**	**213**	**2008/04/18**
63.96	**-20.99**	**10**	**47**	**30**	**2008/05/29**
20.15	**121.37**	**33.2**	**74**	**284**	**2008/06/01**
-10.44	**161.31**	**92.1**	**84**	**234**	**2008/06/03**
37.96	**21.45**	**15.8**	**79**	**12**	**2008/06/08**
39.15	**140.74**	**11.6**	**50**	**279**	**2008/06/13**
11.00	**91.84**	**27.6**	**95**	**305**	**2008/06/27**
10.87	**91.73**	**27.9**	**95**	**305**	**2008/06/28**
53.95	**152.86**	**646.1**	**33**	**285**	**2008/07/05**
27.56	**128.37**	**49.9**	**65**	**282**	**2008/07/08**
35.92	**27.80**	**64.9**	**82**	**7**	**2008/07/15**
37.54	**142.26**	**28.3**	**50**	**277**	**2008/07/19**
-11.07	**164.53**	**29.2**	**83**	**231**	**2008/07/19**
-17.40	**-177.28**	**389.2**	**84**	**212**	**2008/07/19**
39.80	**141.50**	**113.1**	**49**	**279**	**2008/07/23**
50.93	**157.51**	**45.3**	**33**	**278**	**2008/07/24**
32.08	**104.73**	**10.4**	**71**	**303**	**2008/08/01**
-5.93	**130.31**	**188.5**	**93**	**263**	**2008/08/04**
32.81	**105.50**	**10.8**	**70**	**303**	**2008/08/05**

-7.66	**-74.37**	**153.9**	**88**	**112**	**2008/08/26**
-6.14	**147.37**	**67.6**	**86**	**248**	**2008/08/30**
-13.52	**166.98**	**124.7**	**85**	**227**	**2008/09/08**
1.89	**127.45**	**97.3**	**88**	**270**	**2008/09/11**
-30.10	**-177.63**	**35**	**96**	**209**	**2008/09/29**
39.56	**73.79**	**29**	**74**	**331**	**2008/10/05**
29.84	**90.38**	**6.4**	**78**	**314**	**2008/10/06**
14.54	**-92.33**	**83.5**	**60**	**118**	**2008/10/16**
-21.88	**-173.80**	**30.7**	**87**	**207**	**2008/10/19**
30.59	**67.37**	**18.8**	**84**	**333**	**2008/10/28**
13.72	**-90.57**	**66**	**61**	**117**	**2007/06/13**
-3.14	**138.72**	**38.7**	**87**	**257**	**2007/06/16**

APPENDIX C REFERENCES

Brocher, T. M. (2005). Empirical Relations between Elastic Wavespeeds and Density in the Earth's Crust. *Bulletin of the Seismological Society of America, 95*(6), 2081–2092. https://doi.org/10.1785/0120050077

Christensen, N. I. (1996). Poisson's ratio and crustal seismology. *Journal of Geophysical Research: Solid Earth, 101*(B2), 3139–3156. https://doi.org/10.1029/95JB03446

Feng, Lili, & Ritzwoller, M. H. (2019). A 3-D Shear Velocity Model of the Crust and Uppermost Mantle Beneath Alaska Including Apparent Radial Anisotropy. *Journal of Geophysical Research: Solid Earth, 124*(10), 10468–10497. https://doi.org/10.1029/2019JB018122

Kennett, B. L. N., & Engdahl, E. R. (1991). Traveltimes for global earthquake location and phase identification, *Geophys. J. Int. 105*, 429-465.

Kim, Y., Abers, G.A., Li, J., Christensen, D., Calkins, J., Rondenay, S., 2014. Alaska Megathrust 2: Imaging the megathrust zone and Yakutat/Pacific plate interface in the Alaska subduction zone. *J. Geophys. Res. Solid Earth 119*, 1924–1941. https://doi.org/10.1002/2013JB010581

Miller, M. S., & Moresi, L. (2018). Mapping the Alaskan Moho. *Seismological Research Letters, 89*(6), 2430–2436. https://doi.org/10.1785/0220180222

Ratchkovski, N.A. & Hansen, R.A. (2002). New Evidence for Segmentation of the Alaska Subduction Zone. *Bulletin of the Seismological Society of America 92*, 1754–1765. https://doi.org/10.1785/0120000269

Rondenay, S., Bostock, M. G., & Shragge, J. (2001). Multiparameter two-dimensional inversion of scattered teleseismic body waves 3. Application to the Cascadia 1993 data set. *Journal of Geophysical Research: Solid Earth, 106*(B12), 30795–30807. https://doi.org/10.1029/2000JB000039

Rossi, G., Abers, G. A., Rondenay, S., & Christensen, D. H. (2006). Unusual mantle Poisson's ratio, subduction, and crustal structure in central Alaska. *Journal of Geophysical Research*, *111*(B9), B09311. https://doi.org/10.1029/2005JB003956

Veenstra, E., Christensen, D. H., Abers, G. A., & Ferris, A. (2006). Crustal thickness variation in south-central Alaska. *Geology*, *34*(9), 781. https://doi.org/10.1130/G22615.1

Zhu, L., & Kanamori, H. (2000). Moho depth variation in southern California from teleseismic receiver functions. *Journal of Geophysical Research: Solid Earth*, *105*(B2), 2969–2980. https://doi.org/10.1029/1999JB900322